Titre: Title:	Floating Solar-Driven Photocatalysts for the Removal of Contaminants of Emerging Concern
Auteur: Author:	Nila Davari
Date:	2026
Type:	Mémoire ou thèse / Dissertation or Thesis
Référence: Citation:	Davari, N. (2026). Floating Solar-Driven Photocatalysts for the Removal of Contaminants of Emerging Concern [Thèse de doctorat, Polytechnique Montréal]. PolyPublie. https://publications.polymtl.ca/76570/

URL de PolyPublie: PolyPublie URL:	https://publications.polymtl.ca/76570/
Directeurs de recherche: Advisors:	Daria Camilla Boffito, & Viviane Yargeau
Programme: Program:	Génie chimique

POLYTECHNIQUE MONTRÉAL

affiliée à l'Université de Montréal

Floating Solar-Driven Photocatalysts for the Removal of Contaminants of Emerging Concern

NILA DAVARI

Département de génie chimique

Thèse présentée en vue de l'obtention du diplôme de *Philosophiæ Doctor*

Génie chimique

Avril 2026

POLYTECHNIQUE MONTRÉAL

affiliée à l'Université de Montréal

Cette thèse intitulée :

Floating Solar-Driven Photocatalysts for the Removal of Contaminants of Emerging Concern

présentée par **Nila DAVARI**

en vue de l'obtention du diplôme de *Philosophiæ Doctor*

a été dûment acceptée par le jury d'examen constitué de :

Marc LAVERTU, président
Daria Camilla BOFFITO, membre et directrice de recherche
Viviane YARGEAU, membre et codirectrice de recherche
Zahra KORDJAZI, membre
David DEWEZ, membre externe

DEDICATION

*To my beloved family: **Baba**, **Maman**, and **Dadash**, my home and my heart.*

This work, and everything I have achieved, is because of you. With all my love!

*I also dedicate this work to my beautiful, brave people in **Iran** who are fighting for freedom with courage, dignity, and hope despite every hardship.*

ACKNOWLEDGEMENTS

First and foremost, I would like to express my deepest gratitude to my supervisors, Prof. Daria C. Boffito and Prof. Viviane Yargeau from McGill University, for their invaluable guidance, support, and encouragement throughout my Ph.D. journey.

I extend my sincere thanks to Prof. Claudia L. Bianchi and Prof. Ermelinda Falletta from the University of Milan for their valuable collaboration and contributions to the SUNFLOAT project.

I am deeply thankful to Mr. Marco Pineda from McGill University and Dr. Alexandra Furtos from the University of Montreal for their assistance with analytical laboratory work.

My sincere thanks go to Dr. Mojtaba Malayeri and Mr. Javad Vahabzadeh Pasikhani for their valuable assistance in the design and construction of my photoreactor setup.

I would like to thank the technicians of the Chemical Engineering Department, especially Miss Martine Lamarche, Mr. Gino Robin, Mr. Jean Ghantous, Mr. Alejandro Velez Garcia, Mr. Alexis Thivierge, and Mr. Santini Pace, for their technical expertise and support throughout my Ph.D. project.

I gratefully acknowledge the Velux Stiftung Foundation for its financial support through project 1381, “SUNFLOAT - Water decontamination by sunlight-driven floating photocatalytic systems”. I also acknowledge the financial support provided by the Natural Sciences and Engineering Research Council of Canada (NSERC). In addition, I am grateful for the *Bourse d'excellence Neil R. Mitchell et Danièle Dumais* awarded by Polytechnique Montreal.

I am especially thankful to my beloved Javad Vahabzadeh Pasikhani for his love, kindness, and encouragement. Thank you for standing by me through every stage of this academic journey, and for the countless hours you generously spent listening to my stories about floating photocatalysts!

Last but not least, I would like to express my heartfelt gratitude to my beloved family: Baba, Maman, and Dadash. Your unconditional love, unwavering belief in me, and constant support have always been a source of strength and motivation in my Ph.D. journey. I am deeply grateful for your sacrifices and support throughout my life. I couldn’t have done my Ph.D. without you! Thank you and love you, from the bottom of my heart! ♥

RÉSUMÉ

La présence de contaminants émergents (CECs), tels que les perturbateurs endocriniens (PE), les colorants, les pesticides et les produits pharmaceutiques, dans les environnements aquatiques pose des risques critiques en raison de leur persistance, de leur bioaccumulation et de leur potentiel à provoquer des effets mutagènes et cancérigènes. Ces contaminants sont introduits dans les systèmes aquatiques par les eaux usées municipales, le ruissellement agricole et les effluents industriels, et sont souvent insuffisamment éliminés par les procédés conventionnels de traitement de l'eau. Par conséquent, le développement de méthodes de traitement efficaces pour éliminer les CECs des eaux contaminées est essentiel afin de protéger l'environnement et la santé publique. La photocatalyse flottante est apparue comme une approche prometteuse qui imite la photosynthèse naturelle en utilisant l'énergie lumineuse pour entraîner des réactions d'oxydoréduction destinées à la dégradation des contaminants. Cette stratégie permet une exposition directe à la lumière, améliore le transfert d'oxygène depuis l'air et facilite la récupération du photocatalyseur. Cette recherche doctorale visait à développer des photocatalyseurs flottants nanostructurés pour la dégradation des CECs sous irradiation solaire simulée. Des photocatalyseurs de TiO_2 nanotubulaire unidimensionnel ont été fabriqués par l'ingénierie de nanostructures semi-conductrices de type n dans des matériaux avancés, au moyen d'une méthode hydrothermale assistée par ultrasons. Une mousse de polyuréthane à structure alvéolaire ouverte a été utilisée comme support flottant pour le dépôt de photocatalyseurs sous forme de poudre, via une nouvelle méthode de dépôt chimique en phase humide. Ce photocatalyseur flottant innovant (TNTs@PUF) a été appliqué pour éliminer une gamme de polluants organiques, tels que le bisphénol A (BPA), le méthyl orange (MO), le bleu de méthylène (MB), le bentazone (BZ), l'isoproturon (IPU), le sulfaméthoxazole (SMZ) et la carbamazépine (CBZ), sous irradiation solaire simulée (lampe solaire commerciale de 300 W et intensité de 35 W/m^2). L'activité photocatalytique des TNTs@PUF flottants a également été évaluée en présence de composants de matrice aqueuse et dans des systèmes contenant plusieurs polluants. De plus, la modification des TNTs@PUF flottants par dopage non métallique a été étudiée afin d'améliorer la dégradation photocatalytique du BPA. Plus intéressant encore, des photocatalyseurs flottants intelligents capables d'assurer une dégradation du BPA 24 heures sur 24 ont été développés en intégrant un stockage d'énergie basé sur des chalcogénures WS_2 dans des nanotubes de TiO_2 à fort rapport d'aspect, au sein d'une hétérojonction de type Z-scheme. Dans cette thèse, les photocatalyseurs flottants synthétisés ont été caractérisés de manière approfondie à

l'aide d'analyses SEM, TEM, EDX, XRD, XPS, TGA, BET, FTIR, DRS, PL et voltamétriques afin d'étudier leur morphologie, leur composition élémentaire, leur phase cristalline, leur structure chimique et leur état de valence, leur stabilité thermique, leurs propriétés texturales, leurs groupes fonctionnels, leurs propriétés optiques ainsi que leurs caractéristiques photoélectrochimiques. En outre, les concentrations de polluants ont été mesurées par spectrophotométrie UV-Visible et par LC-MS. Les produits de transformation formés lors de la dégradation photocatalytique ont été identifiés par HPLC-MS. Les mécanismes de dégradation des polluants et les contributions des espèces réactives à la dégradation photocatalytique ont également été étudiés au moyen d'expériences de piégeage des radicaux libres et d'analyses par résonance paramagnétique électronique (EPR). Dans ce travail doctoral, l'optimisation des paramètres opératoires, la réutilisabilité et la stabilité des photocatalyseurs flottants, la cinétique des réactions photocatalytiques ainsi que les voies potentielles de dégradation ont été étudiées. Cette thèse est structurée en quatre sections, chacune traitant d'un objectif de recherche spécifique et correspondant à un article publié ou soumis à une revue scientifique à comité de lecture. La première section débute par une comparaison de l'activité photocatalytique des nanotubes de TiO_2 et des nanoparticules de TiO_2 dans un système flottant pour l'élimination du BPA sous irradiation solaire simulée. Les résultats ont démontré que la morphologie du TiO_2 a influencé son activité photocatalytique dans l'élimination du BPA. Plus précisément, 0,1 g de nanoparticules flottantes de TiO_2 ont permis d'éliminer 45 % du BPA (10 mg/L), tandis que la structure nanotubulaire du TiO_2 flottant a permis une élimination complète du BPA après 180 minutes. Les TNTs@PUF flottants ont montré une stabilité sur cinq cycles de réutilisation, et l'espèce réactive principale responsable de la dégradation du BPA a été identifiée comme étant h^+. La deuxième section évalue l'activité photocatalytique des TNTs@PUF flottants pour l'élimination des CECs sous irradiation solaire simulée. Le photocatalyseur synthétisé présentait une structure biphasique anatase/TiO_2(B), une taille de cristallite de 26 nm, une énergie de bande interdite de 3,0 eV, une surface spécifique de 110 m^2/g et une densité de photocourant de 0,2 mA/cm^2. Lorsque les contaminants étaient traités individuellement (20 mg/L), les rendements d'élimination ont atteint 98 % pour le BPA, 98 % pour le MO, 85 % pour le MB, 98 % pour le BZ, 98 % pour l'IPU, 98 % pour le SMZ et 97 % pour la CBZ après 4 h d'irradiation. Les composants de la matrice aqueuse ont réduit l'élimination du BPA à 80 % en présence d'acide humique, à 86 % avec l'acide citrique et à 30 % avec l'acide oxalique. Les anions inorganiques ont également inhibé l'activité photocatalytique des TNTs@PUF flottants,

réduisant l'élimination du BPA à 80 % avec le bicarbonate, 86 % avec le chlorure et 90 % avec le sulfate. Par ailleurs, 80 % du BPA a été éliminé à partir d'un mélange de CECs. La troisième section présente le développement d'une nouvelle méthode solvothermale assistée par ultrasons pour la synthèse de nanotubes de TiO_2 dopés au soufre (S-TNT). L'utilisation de la thiourée comme précurseur de soufre a permis l'incorporation de soufre anionique (S^{2-}) et cationique (S^{4+}, S^{6+}) dans des TNT à double paroi, entraînant la formation de nanodots de soufre d'un diamètre de 3 nm. Le photocatalyseur S-TNT-1@PUF, contenant 1 % massique de dopant soufre, a présenté des propriétés optiques optimales, une génération accrue de charges photoinduites et une séparation efficace des paires électron-trou. La surface spécifique de S-TNT-1 a augmenté jusqu'à 267 m^2/g et son énergie de bande interdite a diminué à 2,48 eV. La densité de photocourant de S-TNT-1 a atteint 0,6 mA/cm^2, soit trois fois plus que celle du TNT non dopé. Sous irradiation solaire simulée pendant 75 minutes à pH 8, avec 0,2 g de S-TNT-1@PUF, plus de 96 % du BPA (10 mg/L) ont été dégradés. La dégradation photocatalytique a suivi une cinétique du premier ordre avec une constante apparente de vitesse de 0,05 min^{-1}, et le radical $^{\bullet}OH$ a été identifié comme principale espèce réactive (31 %). Le S-TNT-1@PUF flottant est resté stable après cinq cycles de réutilisation. La quatrième section présente la dégradation photocatalytique du BPA en continu (24 h/24) à l'aide d'une hétérojonction intelligente de type Z-scheme basée sur le photocatalyseur flottant WS_2-TNT@PUF. Cette configuration a permis une séparation efficace des charges via l'hétérojonction Z-scheme. Le WS_2-TNT-1@PUF optimisé, avec un rapport massique WS_2: TNT de 1:1, présentait une surface spécifique de 192 m^2/g et une absorption accrue de la lumière visible, caractérisée par une énergie de bande interdite de 2,8 eV. Sous irradiation solaire simulée, le WS_2-TNT-1@PUF flottant a dégradé plus de 97 % du BPA (10 mg/L) en 60 minutes à pH 8, suivant une cinétique du premier ordre avec une constante apparente de 0,069 min^{-1}. Le WS_2-TNT-1@PUF flottant a maintenu son activité photocatalytique après cinq cycles de réutilisation, et l'espèce réactive dominante impliquée dans la dégradation du BPA était $^{\bullet}O_2^-$ (41,2 %). Le WS_2-TNT-1@PUF a stocké jusqu'à 1 µmol d'électrons photogénérés, permettant une dégradation de 89 % du BPA en absence de lumière. Les électrons stockés dans WS_2-TNT-1@PUF ont entraîné la dégradation du BPA pendant la phase sombre, comme confirmé par les mesures photoélectrochimiques et les résultats EPR. Cette recherche doctorale établit un lien entre la photocatalyse à l'échelle du laboratoire et les applications en conditions réelles en proposant une stratégie visant à atteindre une indépendance énergétique solaire continue et un traitement

photocatalytique des eaux usées fonctionnant 24 heures sur 24. Le système photocatalytique flottant développé démontre un fort potentiel pour l'élimination des CECs des eaux polluées, mettant en évidence son applicabilité pour le traitement réel des eaux usées.

Mots-clés: Photocatalyse flottante, nanotubes de TiO_2, mousse de polyuréthane, dopage non métallique, hétérojonction Z-scheme, contaminants émergents (CECs), bisphénol A (BPA), dégradation continue 24 h/24.

ABSTRACT

The presence of contaminants of emerging concern (CECs), such as endocrine-disrupting chemicals (EDCs), dyes, pesticides, and pharmaceuticals, in aquatic environments poses critical risks due to their persistence, bioaccumulation, and potential to cause mutagenic and carcinogenic effects. These contaminants are introduced into water systems via municipal sewage, agricultural runoff, and industrial wastewater and are often inadequately removed by conventional treatment processes. Consequently, the development of effective treatment methods for removing CECs from contaminated water is essential to protecting environmental and public health. Floating photocatalysis has emerged as a promising approach that mimics natural photosynthesis by utilizing light energy to drive redox reactions for contaminant degradation. This strategy enables direct exposure to light, improves oxygen transfer from the air, and facilitates a straightforward photocatalyst. This doctoral research aimed to develop floating nanostructured photocatalysts for the degradation of CECs under simulated sunlight irradiation. One-dimensional nanotubular TiO_2 photocatalysts were fabricated by engineering n-type semiconductor nanostructures in advanced materials using an ultrasound-assisted hydrothermal method. Polyurethane foam with an open-cell structure served as a floating carrier for the deposition of powder photocatalysts via a novel wet chemical deposition method. This innovative floating photocatalyst (TNTs@PUF) was applied to remove a range of organic pollutants, such as bisphenol A (BPA), methyl orange (MO), methylene blue (MB), bentazon (BZ), isoproturon (IPU), sulfamethoxazole (SMZ), and carbamazepine (CBZ), under simulated sunlight (300 W commercial solar lamp and 35 W/m^2 intensity). The photocatalytic activity of floating TNTs@PUF was further evaluated in the presence of water matrix components and within mixed-pollutant systems. Additionally, the modification of floating TNTs@PUF with non-metal doping was investigated to enhance the photocatalytic degradation of BPA. Most interestingly, smart floating photocatalysts capable of round-the-clock degradation of BPA were developed by integrating WS_2 chalcogenide-based energy storage into high-aspect-ratio TiO_2 nanotubes within a Z-scheme heterojunction. In this dissertation, the synthesized floating photocatalysts were comprehensively characterized using SEM, TEM, EDX, XRD, XPS, TGA, BET, FTIR, DRS, PL, and voltammetry analyses to investigate their morphology, elemental composition, crystalline phase, chemical structure and valence state, thermal stability, textural properties, functional groups, optical properties, and photoelectrochemical characterizations. Additionally, pollutant concentrations were measured using UV-Visible spectrophotometry and

LC-MS. Transformation products formed during photocatalytic degradation were identified by HPLC-MS. The mechanisms of pollutant degradation and the contributions of reactive species to photocatalytic degradation were also examined through free radical scavenging experiments and EPR analysis. In this doctoral work, the optimization of operating parameters, the reusability and stability of floating photocatalysts, the kinetics of photocatalytic reactions, and potential degradation pathways were explored. This dissertation is structured into four sections, each addressing a specific research objective and corresponding to an article published or submitted to a peer-reviewed journal. The first section begins with a comparison of the photocatalytic activity of TiO_2 nanotubes and TiO_2 nanoparticles in a floating system for BPA removal under simulated sunlight irradiation. The results demonstrated that TiO_2 morphology affected its photocatalytic activity in BPA removal. Specifically, 0.1 g of floating TiO_2 nanoparticles removed 45% BPA (10 mg/L), while the nanotubular structure of floating TiO_2 achieved complete BPA removal after 180 min. Floating TNTs@PUF showed stability over five reuse cycles, and the primary reactive species responsible for BPA degradation was identified as h^+. The second section evaluates the photocatalytic activity of floating TNTs@PUF for the removal of CECs under simulated sunlight irradiation. The synthesized photocatalyst exhibited a biphasic anatase/TiO_2(B) structure with a crystallite size of 26 nm, a bandgap energy of 3.0 eV, a surface area of 110 m^2/g, and a photocurrent density of 0.2 mA/cm^2. When individual contaminants were treated (20 mg/L), removal efficiencies reached 98% for BPA, 98% for MO, 85% for MB, 98% for BZ, 98% for IPU, 98% for SMZ, and 97% for CBZ after 4 h irradiation. Water matrix components decreased BPA removal to 80% with humic acid, 86% with citric acid, and 30% with oxalic acid. Inorganic anions further inhibited the photocatalytic activity of floating TNTs@PUF, lowering BPA removal to 80% with bicarbonate, 86% with chloride, and 90% with sulfate. Additionally, 80% of BPA was removed from a mixture of CECs. The third section shows the development of a novel ultrasound-assisted solvothermal method for synthesizing sulfur-doped TiO_2 nanotubes (S-TNT). Employing thiourea as a sulfur precursor enabled the incorporation of anionic sulfur (S^{2-}) and cationic sulfur (S^{4+}, S^{6+}) into double-walled TNT, resulting in sulfur nanodots with a diameter of 3 nm. S-TNT-1@PUF photocatalyst, containing 1 wt.% sulfur dopant, exhibited optimal optical properties, enhanced photo-induced charge generation, and effective electron-hole pair separation. The specific surface area of S-TNT-1 increased to 267 m^2/g, and its bandgap energy decreased to 2.48 eV. The photocurrent density of S-TNT-1 reached 0.6 mA/cm^2, which was threefold higher than that of

undoped TNT. Under simulated sunlight irradiation for 75 min at pH 8, with 0.2 g S-TNT-1@PUF, more than 96% of 10 mg/L BPA was degraded. The photocatalytic degradation followed first-order kinetics with an apparent rate constant of 0.05 min^{-1}, with $^{\bullet}OH$ identified as the main reactive species (31%). Floating S-TNT-1@PUF was stable after five reuse cycles. The fourth section presents the round-the-clock photocatalytic degradation of BPA using a smart Z-scheme heterojunction based on floating WS_2-TNT@PUF. This configuration facilitated efficient charge separation through the Z-scheme heterojunction. The optimized WS_2-TNT-1@PUF, with a 1:1 WS_2-TNT weight ratio, exhibited a specific surface area of 192 m^2/g and enhanced visible-light absorption, characterized by a bandgap energy of 2.8 eV. Under simulated sunlight irradiation, floating WS_2-TNT-1@PUF degraded more than 97% of BPA (10 mg/L) within 60 min at pH 8, following first-order kinetics with an apparent rate constant of 0.069 min^{-1}. Floating WS_2-TNT-1@PUF maintained photocatalytic activity after five reuse cycles, and the dominant reactive species involved in BPA degradation was $^{\bullet}O_2^-$ (41.2%). WS_2-TNT-1@PUF stored up to 1 μmol of photogenerated electrons, enabling 89% BPA degradation in the absence of light. The stored electrons in WS_2-TNT-1@PUF drove dark-phase BPA degradation, as confirmed by photoelectrochemical measurements and EPR results. This doctoral research bridges laboratory-scale photocatalysis and real-world applications by proposing a strategy to achieve continuous solar-energy independence and round-the-clock photocatalytic wastewater treatment. The developed floating photocatalytic system demonstrates strong potential for removing CECs from polluted water, highlighting its applicability for real-world wastewater treatment.

Keywords: Floating Photocatalysis, TiO_2 Nanotubes, Polyurethane Foam, Non-metal Doping, Z-scheme Heterojunction, Contaminants of Emerging Concern (CECs), Bisphenol A (BPA), Round-the-clock Degradation

TABLE OF CONTENTS

LIST OF TABLES

LIST OF FIGURES

LIST OF SYMBOLS AND ABBREVIATIONS

a, *b*, *c*	Lattice parameters
ABS	Absorbance
AO	Ammonium oxalate
AOPs	Advanced oxidation processes
ATZ	Atrazine
BET	Brunauer-Emmett-Teller
BPA	Bisphenol A
BZ	Bentazon
BZQ	Benzoquinone
C	Pollutant concentration (mg/L)
C_0	Initial pollutant concentration (mg/L)
CB	Conduction band
CBZ	Carbamazepine
CECs	Contaminants of emerging concern
COF	Covalent organic frameworks
CSTR	Continuous stirred-tank reactor
D	Crystallite size (nm)
$d_{(hkl)}$	Distance between the crystal planes of (hkl)

DRS	Diffuse reflectance spectroscopy
e^-	Electrons
E_a	Electron affinity
E_{app}	Absolute applied potential (V)
E_{CB}	Conduction band energy level (eV)
E_e	Energy of free electrons on the hydrogen scale
E_g	Bandgap energy (eV)
E_{ion}	First ionization energy
E_{meas}	Measured electrode potential of photoanode (V)
E_{OCP}	Open-circuit potential of photoanode (V)
E°_{rev}	Standard changeable potential (V)
E_{VB}	Valence band energy level (eV)
EDCs	Endocrine-disrupting chemicals
EDS	Energy-dispersive X-ray spectroscopy
EDTA	Ethylenediaminetetraacetic acid
EIS	Electrochemical impedance spectroscopy
EPA	Environmental Protection Agency
EPR	Electron paramagnetic resonance spectrometer
f_A	Weight fraction of anatase/rutile phase

F(R)	Kubelka-Munk function
FESEM	Field-emission scanning electron microscopy
FLIR	Forward looking infrared
FLZ	Fluconazole
FTIR	Fourier transform infrared
FTO	Fluorine doped tin oxide
FWHM	Full width at half maximum
GFZ	Gemfibrozil
h^+	Holes
H^+	Hydrogen ions
h, k, l	Indices of crystal planes
h	Planck constant
HESI	Heated electrospray ionization
HPLC-MS	High-performance liquid chromatography-mass spectrometry
HR	High-resolution
HR-TEM	High-resolution transmission electron microscopy
I_0	Intensity of the incident light
I_A	Intensity of the strongest reflection for anatase phase
I_R	Intensity of the strongest reflection for rutile phase

IBP	Ibuprofen
ICBs	Industrial chemicals and by-products
ICP-OES	Inductively coupled plasma-optical emission spectroscopy
IFCT	Interfacial charge transfer
IPA	Isopropyl alcohol
IPU	Isoproturon
IR	Infrared
J_p	Photocurrent density (mA/cm^2)
K	Shape factor
k_{app}	Apparent rate constant
LC-HESI-MS	Liquid chromatography heated electrospray ionization mass spectrometry
LC-MS	Liquid chromatography-mass spectrometry
LDV	Laser doppler vibrometry
LECA	Light-expanded clay
LOD	Limit of detection
LOQ	Limit of quantification
LSPR	Local surface plasmon resonance
LSV	Linear sweep voltammetry
MB	Methylene blue

MO	Methyl orange
MPs	Microplastics
n	Photocatalytic reaction order
NHE	Normal hydrogen electrode
Ns	Nanomaterials
$^{\bullet}OH$	Hydroxyl radicals
$^{\bullet}OOH$	Hydroperoxyl radicals
$^{\bullet}O_2^-$	Superoxide anions
OCP	Open-circuit potential
OP	Oxidation photocatalyst
PAN	Polyacrylonitrile
PFAS	Per- and poly-fluoroalkyl substances
PFM	Piezoresponse force microscopy
PFOA	Perfluorooctanoic acid
PFR	Plug flow reactor
PL	Photoluminescence spectroscopy
ppb	Parts per billion
PPCPs	Pharmaceuticals and personal care products
PPI	Pores per inch

PU	Polyurethane
PUF	Polyurethane foam
PVA	Polyvinyl alcohol
PVDF	Polyvinylidene fluoride
PZC	Point of zero charge
QCs	Quality controls
r	Rate of pollutant removal/degradation
R	Reflectance
R^2	Correlation coefficient
RHE	Reversible hydrogen electrode
ROS	Reactive oxygen species
RP	Reduction photocatalyst
SAED	Selected area electron diffraction
SMZ	Sulfamethoxazole
t	Time (min)
TEM	Transmission electron microscopy
TGA	Thermogravimetric analysis
TiO_2-NPs	TiO_2 nanoparticles
TiO_2-NTs	TiO_2 nanotubes

TMDs	Transition metal dichalcogenides
TNPs	TiO_2 nanoparticles
TNTs	TiO_2 nanotubes
TPR	Transient photocurrent responses
TPs	Transformation products
TRL	Technology readiness level
UV	Ultraviolet
v_i	Number of elements
VB	Valence band
X	Electronegativity
x_i	Mulliken's electronegativity of element i
XPS	X-ray photoelectron spectroscopy
XRD	X-ray diffractometer

Greek letters

β	Full width at half maximum of peak (radians)
η	Photoconversion efficiency
θ	Half of the Bragg angle (degrees)
λ	Wavelength (nm)
ϑ	Frequency of radiation (Hz)

LIST OF APPENDICES

CHAPTER 1 INTRODUCTION

1.1 Background and problem identification

Rapid population growth and accelerated industrialization have contaminated global water cycles, leading to rising demand for clean water while reducing the availability of safe drinking water. As a result, water pollution and freshwater scarcity have emerged as critical global challenges that threaten both environmental sustainability and public health [1].

In recent years, significant attention has been directed toward contaminants of emerging concern (CECs) detected in surface water, groundwater, and wastewater systems [2]. These compounds, including pharmaceuticals, dyes, pesticides, and endocrine-disrupting chemicals (EDCs), are of particular concern due to their persistence, potential for bioaccumulation, and their ability to induce mutagenic and carcinogenic effects on human health and aquatic environments [3]. CECs are introduced into aquatic environments through multiple pathways, primarily municipal wastewater discharge, agricultural runoff, and industrial effluents [4].

Conventional wastewater treatment processes are generally ineffective at completely removing or substantially reducing CECs in water systems [5]. Therefore, there is an increasing need to develop innovative and sustainable treatment technologies capable of effectively degrading these contaminants. Among the advanced treatment methods, advanced oxidation processes (AOPs) have attracted considerable attention, particularly photocatalysis. Photocatalysis mimics natural photosynthesis by harnessing photon energy from light irradiation to drive redox reactions that generate reactive species capable of degrading organic contaminants [6].

Photocatalytic systems used for wastewater treatment are commonly categorized as either suspended or immobilized reactors. Suspended photocatalytic systems often exhibit high photocatalytic activity due to the large surface area of dispersed particles; however, they suffer from several limitations. These include difficulties in photocatalyst recovery and reuse following treatment, the requirement for continuous stirring to prevent particle agglomeration, and the potential release of nanoparticles into treated water, which may pose additional environmental concerns [7, 8].

To address these limitations, floating photocatalysts have emerged as an innovative category of immobilized photocatalytic systems. In such systems, photocatalysts are either intrinsically buoyant or immobilized on floating substrates [9]. Floating photocatalytic systems facilitate easy recovery and reuse of photocatalysts while minimizing photocatalyst loss during operation [10]. Furthermore, the formation of an air-solid-water triphase interface enhances photocatalytic efficiency by enabling direct exposure of the photocatalyst to light without attenuation by water and by improving oxygen transfer from air to the reaction interface [11, 12]. When driven by solar irradiation, floating photocatalysts also offer the advantage of utilizing renewable energy, making them suitable for sustainable water treatment applications [13].

Despite these advantages, several challenges remain for floating photocatalytic systems. Major issues include achieving effective photocatalyst loading onto floating supports, ensuring the chemical and mechanical stability of floating carriers, and minimizing light-blocking effects that reduce photocatalytic activity. Additionally, the potential detachment or release of photocatalyst particles from floating substrates into treated water remains a serious issue. Moreover, conventional photocatalytic systems, whether floating or suspended, rely on continuous light irradiation, which restricts treatment performance during dark periods. To overcome this limitation, selecting photocatalyst materials with intrinsic energy storage capability is a key design criterion. In this dissertation, we address these research gaps by developing a smart floating photocatalyst heterostructure capable of round-the-clock degradation of CECs under simulated sunlight irradiation, as outlined in the following objectives.

1.2 Research objectives

The main objective of this dissertation is to develop floating nanostructured photocatalysts for the degradation of contaminants of emerging concern (CECs) under simulated sunlight irradiation. To achieve this, we consider four specific objectives that resulted in four articles published or submitted to peer-reviewed journals. The specific objectives of this dissertation are outlined as follows:

1) To fabricate novel floating TiO_2 nanotube photocatalysts supported on polyurethane foam for Bisphenol A removal

In this specific objective, we evaluate the comparative photocatalytic activity of TiO_2 nanotubes with TiO_2 nanoparticles in both floating and suspended systems under simulated sunlight irradiation for the removal of Bisphenol A as a model of CECs. By engineering an n-type semiconductor in advanced nanostructured materials and without adding metallic or non-metallic dopants, we synthesize a one-dimensional nanotubular structure of TiO_2 photocatalysts that enhances photocatalytic activity through their high specific surface area and rapid electron migration. We fabricate an innovative floating TiO_2 photocatalyst system using polyurethane foam, which improves light exposure without water attenuation, oxygen transfer from air, and reactive oxygen species generation by forming an air-solid-water triphase interface in floating TiO_2. This specific objective is addressed in the first article of this dissertation (Chapter 3).

2) To remove CECs by floating TiO_2 nanotube photocatalysts in the presence of water matrix components and in a mixed-pollutant system

In this specific objective, we evaluate the photocatalytic activity of novel floating double-walled TiO_2 nanotube photocatalysts for the removal of various CECs, including endocrine-disrupting chemicals, dyes, pesticides, pharmaceuticals, and per- and poly-fluoroalkyl substances under simulated sunlight irradiation. In addition, the effects of water matrix components, such as natural organic matter and inorganic anions, on the photocatalytic efficiency of this floating system are investigated using Bisphenol A as a model resistant organic pollutant. Moreover, we examine the removal of Bisphenol A from a mixed-contaminant system containing sulfamethoxazole, carbamazepine, fluconazole, atrazine, ibuprofen, and gemfibrozil. This specific objective is addressed in the second article of this dissertation (Chapter 4).

3) To increase the photocatalytic activity of floating TiO_2 nanotubes by a non-metal doping for Bisphenol A degradation

In this specific objective, we explore a novel floating photocatalytic system engineered by anchoring sulfur nanodots onto double-walled TiO_2 nanotube photocatalysts immobilized on floating polyurethane foam for the degradation of Bisphenol A under simulated sunlight irradiation. We develop a novel dual sulfur-doping method, embedding both anionic and cationic sulfur in TiO_2 nanotubes via ultrasound-assisted solvothermal synthesis, which improves visible-light

absorption and electron excitation, thus increasing photocatalytic activity for the efficient and fast degradation of Bisphenol A. This specific objective is addressed in the third article of this dissertation (Chapter 5).

4) To synthesize a smart Z-scheme heterojunction of floating TiO_2 nanotubes and WS_2 nanospheres for round-the-clock Bisphenol A degradation

In this specific objective, we investigate the round-the-clock degradation of Bisphenol A using a novel energy storage floating photocatalyst under simulated sunlight irradiation. We fabricate an innovative Z-scheme heterojunction between WS_2 chalcogenides, possessing an electron storage capacity, and high-aspect-ratio TiO_2 nanotube photocatalysts, which enhance photocatalytic activity by suppressing rapid charge carrier recombination and provide round-the-clock degradation of Bisphenol A without the need for light irradiation, unlike conventional photocatalytic systems. This specific objective is addressed in the fourth article of this dissertation (Chapter 6).

Regarding the specific objectives outlined above, the synthesized floating photocatalysts were comprehensively characterized in terms of morphology, elemental composition, crystalline phase, chemical structure and valence state, thermal stability, textural properties, functional groups, and optical properties using SEM, TEM, EDX, XRD, XPS, TGA, BET, FTIR, DRS, and PL analyses. Additionally, the photocurrent density, photo-response, and photoconversion efficiency of the floating photocatalysts were evaluated by voltammetry analyses.

To address wastewater treatment as part of the above-mentioned specific objectives, various analytical techniques were investigated. The concentrations of pollutants were measured by UV-Visible spectrophotometry and LC-MS analyses. In addition, the possible mechanisms of pollutant degradation and the contributions of reactive species involved in photocatalytic degradation were examined using free radical scavenger experiments and EPR spectroscopy. Transformation products of pollutants were also identified by HPLC-MS analysis. Moreover, the optimization of key operating parameters, the kinetics of photocatalytic reactions, possible degradation pathways, and the reusability and stability of the prepared floating photocatalysts were explored in this dissertation.

1.3 Dissertation structure

This paper-based dissertation consists of six articles that have been published or submitted to peer-reviewed journals. The chapters are organized as follows:

Chapter 1: Introduction. This chapter presents the background and problem identification of this dissertation and outlines the research objectives and dissertation structure.

Chapter 2: Literature Review. This chapter discusses the fundamentals of photocatalysis, with a focus on TiO_2-based photocatalysts for wastewater treatment, and reviews previous studies on the removal of CECs.

Chapter 3: "TiO_2 Nanotubes Immobilized on Polyurethane Foam as a Floating Photocatalyst for Water Treatment". This chapter introduces the first article of this dissertation, published in *Catalysis Today*.

Chapter 4: "Photocatalytic Removal of Contaminants of Emerging Concern by Double-Walled TiO_2 Nanotubes Supported on Floating Polyurethane Foam". This chapter details the findings of the second article of this dissertation, submitted to *Discover Nano.*

Chapter 5: "Enhanced Photo-Induced Charge Generation of Floating Sulfur-Doped TiO_2 Double-Walled Nanotubes for Efficient Sunlight-Driven Photocatalytic Degradation of Bisphenol". This chapter presents the third article of this dissertation, published in *Ceramics International*.

Chapter 6: "Round-the-Clock Photocatalysis via Electron-Storing Floating Z-Scheme WS_2-TiO_2 Nanotube Heterostructures". This chapter reports the results of the fourth article of this dissertation, submitted to *Separation and Purification Technology*.

Chapter 7: General Discussion. This chapter discusses the key findings of this dissertation.

Chapter 8: Conclusion and Recommendation. This final chapter summarizes the overall conclusions derived from the results of this dissertation and provides recommendations for future research.

Appendix A presents the fifth article, "Comparing the Photocatalytic Activity of Suspended and Floating Ag-decorated TiO_2 for Dye Removal", published in *Tetrahedron Green Chem*. In this article, we report a novel two-step synthesis method for fabricating floating TiO_2 and Ag-decorated

TiO_2 photocatalysts and compare their photocatalytic activity in the removal of Methyl Orange as a dye pollutant.

Appendix B contains the sixth article, "Recent Progress on Ti-based Piezo-photocatalysts for Wastewater Treatment", published in *Current Opinion in Chemical Engineering*. In this article, we provide a concise review of recent advances in Ti-based piezo-electric semiconductors for wastewater treatment, focusing on studies between 2020 and 2025.

1.4 List of peer-reviewed publications and conferences

The findings of this doctoral research have been published in several peer-reviewed journals and presented at many conferences and events. The corresponding publications and conferences are listed below.

1.4.1 Peer-reviewed articles

1) Davari, N., Vahabzadeh Pasikhani, J., Falletta, E., Bianchi, C. L., Yargeau, V., and Boffito D. C., "Round-the-Clock Photocatalysis via Electron-Storing Floating Z-Scheme WS_2-TiO_2 Nanotube Heterostructures", Submitted to Separation and Purification Technology.

2) Davari, N., Falletta, E., Bianchi, C. L., Yargeau, V., and Boffito D. C., "Photocatalytic Removal of Contaminants of Emerging Concern by Double-Walled TiO_2 Nanotubes Supported on Floating Polyurethane Foam", Submitted to Discover Nano.

3) Davari, N., Vahabzadeh Pasikhani, J., Issa Hamoud, H., Falletta, E., Bianchi, C. L., Yargeau, V., and Boffito D. C., "Enhanced photo-induced charge generation of floating sulfur-doped TiO_2 double-walled nanotubes for efficient sunlight-driven photocatalytic degradation of bisphenol A", Ceramics International, vol. 51, no. 27(Part B), pp. 53519-53534, 2025. https://doi.org/10.1016/j.ceramint.2025.09.100

4) Davari, N., Vahabzadeh Pasikhani, J., Bianchi, C. L., Yargeau, V., and Boffito D. C., "Recent progress on Ti-based piezo-photocatalysts for wastewater treatment", Current Opinion in Chemical Engineering, vol. 47, pp. 101090, 2025. https://doi.org/10.1016/j.coche.2025.101090

5) Davari, N., Falletta, E., Bianchi, C. L., Yargeau, V., Rodriguez-Seco1, C., and Boffito D. C., "Comparing the Photocatalytic Activity of Suspended and Floating Ag-

decorated TiO_2 for Dye Removal", Tetrahedron Green Chem, vol. 5, pp. 100059, 2025. https://doi.org/10.1016/j.tgchem.2024.100059

6) Davari, N., Falletta, E., Bianchi, C. L., Yargeau, V., and Boffito D. C., "TiO_2 Nanotubes Immobilized on Polyurethane Foam as a Floating Photocatalyst for Water Treatment", Catalysis Today, vol. 436, pp. 114725, 2024. https://doi.org/10.1016/j.cattod.2024.114725

1.4.2 Conference presentations

1) Davari, N., Yargeau, V., and Boffito, D. C., "Sunlight-Driven Removal of Methyl Orange Using Floating TiO_2 Nanotubes Photocatalysts", 10 Years of the GCI Symposium: Thinking Green(er) in Daily Life, University of Toronto, Toronto (Canada), 7-9 May 2025.

2) Davari, N., Yargeau, V., and Boffito, D. C., "Sunlight-Driven Removal of Methyl Orange Using Floating TiO_2 Nanotubes Photocatalysts", Chemical Engineering Research Day, Montréal (Canada), 31 March 2025.

3) Davari, N., and Boffito, D. C., "Photocatalytic Removal of Pollutants from Surface Water by a Sunlight-driven Floating Reactor", UNESCO Chair in Green and Sustainable Electronics (GSE) and Tamale Technical University, Montréal (Canada), 17 June 2024.

4) Davari, N., Yargeau, V., and Boffito, D. C., "Solar Light Photoactive Floating Sulfur-doped TiO_2 Nanotubes for Degradation of Bisphenol A", Chemical Engineering Research Day, Montréal (Canada), 27 March 2024.

5) Davari, N., Galloni, M. G., Falletta, E., Bianchi, C. L., Yargeau, V., and Boffito D. C., "Application of Floating Titanium Nanotube Photocatalyst for Bisphenol A Degradation", 10^{th} International Symposium on Group Five Elements, Montréal (Canada), 25-28 June 2023.

6) Davari, N., Gar Alalm, M., Mokhtarifar, M., Bianchi, C. L., Falletta, E., Yargeau, V., and Boffito, D. C., "Photocatalytic activity of g-C_3N_4 immobilized on floating Polyurethane foam", ISCRE 27: Chemical Reaction Engineering for Sustainable Development, Québec City (Canada), 11-14 June 2023.

7) Davari, N., Yargeau, V., and Boffito, D. C., "Fabrication of floating g-C_3N_4@rGO photocatalyst for dye wastewater treatment", Chemical Engineering Research Day, Montréal (Canada), 17 March 2023.

8) Davari, N., Mokhtarifar, M., Bianchi, C. L., Falletta, E., and Boffito, D. C., "Ultrasound-assisted and spray-drying synthesis of floating TiO_2-Ag@polyurethane photocatalyst for methyl orange degradation under simulated sunlight", Canadian Chemical Engineering Conference (CCEC), Vancouver (Canada), 23-26 October 2022.

9) Davari, N., Gar Alalm, M., Bianchi, C. L., Falletta, E., and Boffito, D. C., "A floating TiO_2-Ag@PU photocatalyst for methyl orange removal under simulated sunlight", ECS Montréal Student Symposium, Montréal (Canada), 22 April 2022.

10) Davari, N., Mokhtarifar, M., Bianchi, C. L., Falletta, E., and Boffito, D. C., "Ultrasound-assisted synthesis of TiO_2-2%Ag photocatalyst supported on floating Polyurethane foam for water treatment", Chemical Engineering Research Days, Montréal (Canada), 17-18 March 2022.

1.4.3 Other contributions

1) Yasmeen, S., **Davari, N.**, Prosposito, P., and Boffito D. C., "Synthesis and Characterizations of Novel Composites for the Photocatalytic Degradation of Emerging Contaminants", Under Preparation.

2) Hoseinizadeh, M., **Davari, N.**, Gouda, A., Hyat H., Sain, M., Boffito D. C., and Santato, C., "Ultrasound-Assisted Deposition of Sepia Melanin and Multiwalled Carbon Nanotubes on Carbon Cloth: Toward Sustainable Surface Engineering for Flexible Supercapacitors", Advanced Sustainable Systems, vol. 8, pp. 2400302, 2024. https://doi.org/10.1002/adsu.202400302

3) Niaz Talkhouncheh, S., **Davari, N.**, Omanovic, S., and Boffito, D. C., "Synthesis of Magnéli Phase Titanium Suboxide Photoanodes for Photoelectrochemical Degradation of Persistent Micropollutants", 14th IWA Micropol & Ecohazard Conference, Toronto (Canada), 31 May-4 June 2026.

4) Galloni, M. G., Falletta, E., **Davari, N.**, Boffito D. C., and Bianchi, C. L., "Advanced sustainable floating photocatalysts for wastewater remediation", NanoInnovation Conference and Exhibition, Italy (Rome), 18-22 September 2023.

5) Falletta, E., Galloni, M. G., Mahdi, M., Bortolotto, V., **Davari, N.**, Boffito, D. C., and Bianchi, C. L., "Sunlight-driven degradation of non-steroidal anti-inflammatory drugs by innovative floating photocatalysts", 7th Green and Sustainable Chemistry Conference, Dresden (Germany), 22-23 May 2023.

6) Lika, A., Galloni, M. G., Ferrara, E., **Davari, N.**, Boffito, D. C., Falletta, E., and Bianchi, C. L., "Photocatalysis challenges the obstacles to sustainability: advanced floating materials for wastewater remediation", The 6th Global Public Health Conference (GLOBEHEAL 2023), 23-24 February 2023 (Selected as the winner of the Poster Award competition).

7) Bianchi, C. L., Falletta, E., Bruni, A., Sartirana, M., Gar Alalm, M., **Davari, N.**, and Boffito, D. C., "Floating photocatalysts for a sustainable environmental remediation exploiting sunlight", Virtual International Conference on Hierarchically Structured Materials (ICHSM), 8-10 April 2021.

CHAPTER 2 LITERATURE REVIEW

2.1 Contaminants of emerging concern (CECs)

Water is a fundamental resource required to sustain life [14]. Water is one of the most abundant natural resources that covers 71% of the Earth. Nevertheless, only 2.5% of global water is freshwater. Approximately 1% of this limited proportion is readily accessible to humans through rivers, streams, lakes, and groundwater aquifers [15].

In recent decades, water pollution and freshwater scarcity have become critical global challenges, primarily resulting from accelerated industrial development, rapid population growth, unregulated urban expansion, and increased agricultural activity [16, 17]. Since 2000, more than 2.4 billion people have lived in countries experiencing water scarcity. Every day, approximately 1,000 children die from diseases associated with water pollution [18].

Contaminants of Emerging Concern (CECs), also known as emerging contaminants, are a wide range of chemicals and substances that have attracted attention recently due to their persistence, bioaccumulation, and potential detrimental effects, such as toxicity, carcinogenicity, and mutagenicity [15, 19]. These contaminants are designated as "emerging" since they are not routinely monitored or regulated in the environment [14, 20]. Recent advancements in analytical detection methods and a deeper understanding of their ecological and toxicological effects have further underscored their significance as a growing concern.

CECs are introduced into the environment through various pathways associated with human activities and industrial processes, such as industrial discharges, agricultural runoff, sewage systems, atmospheric deposition, improper disposal and leaching, as well as the use of household and commercial products [21]. Figure 2.1 shows several categories of CECs, including pharmaceuticals and personal care products (PPCPs), endocrine-disrupting chemicals (EDCs), polyfluoroalkyl substances (PFAS), microplastics (MPs), nanomaterials (Ns), and industrial chemicals and by-products (ICBs). These contaminants are classified according to their origin, intended use, and chemical properties [21, 22]. Bisphenol A (BPA) is identified as an EDC in Figure 2.1.

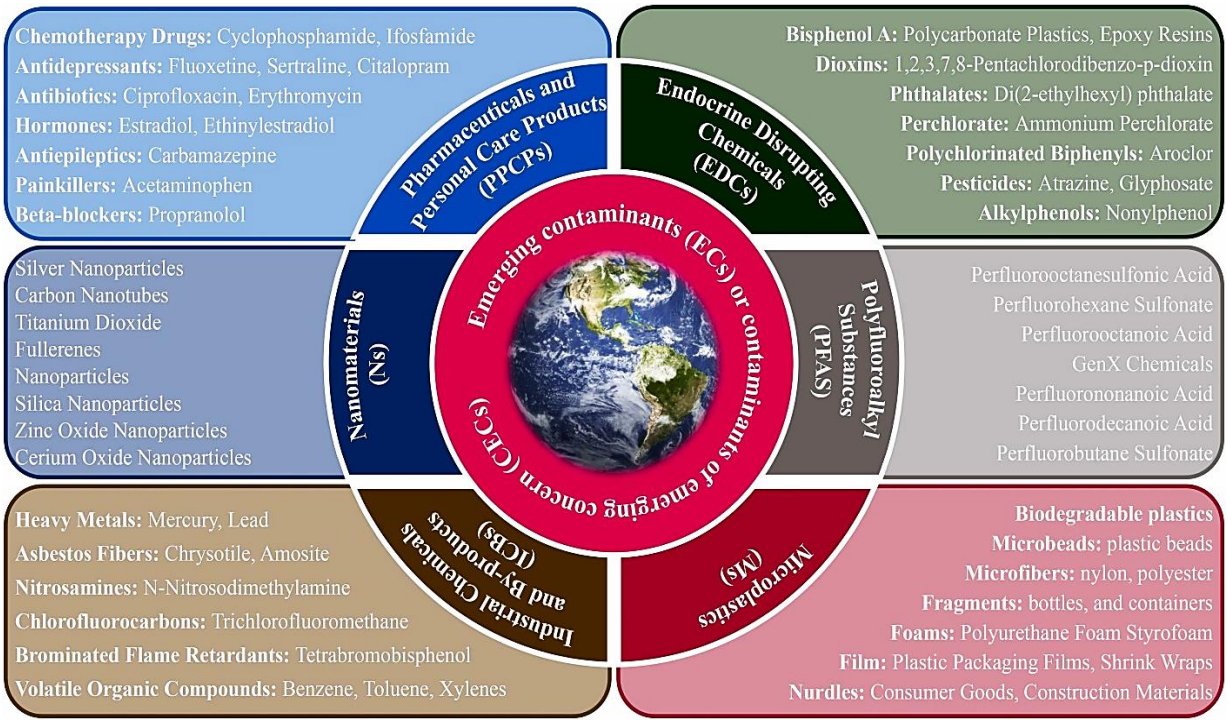

Figure 2.1 Types of CECs (adapted with permission from [21])

2.2 Bisphenol A (BPA)

BPA is utilized in the manufacture of epoxy resins, polycarbonates, plastic bottles, and food packaging [23-25]. BPA is released into water systems through various routes, including industrial discharges, landfill leachate, agricultural runoff, and effluents from municipal wastewater treatment plants. In addition, human exposure to BPA occurs via the consumption of contaminated water and food [26]. Figure 2.2 presents the potential sources of BPA contamination.

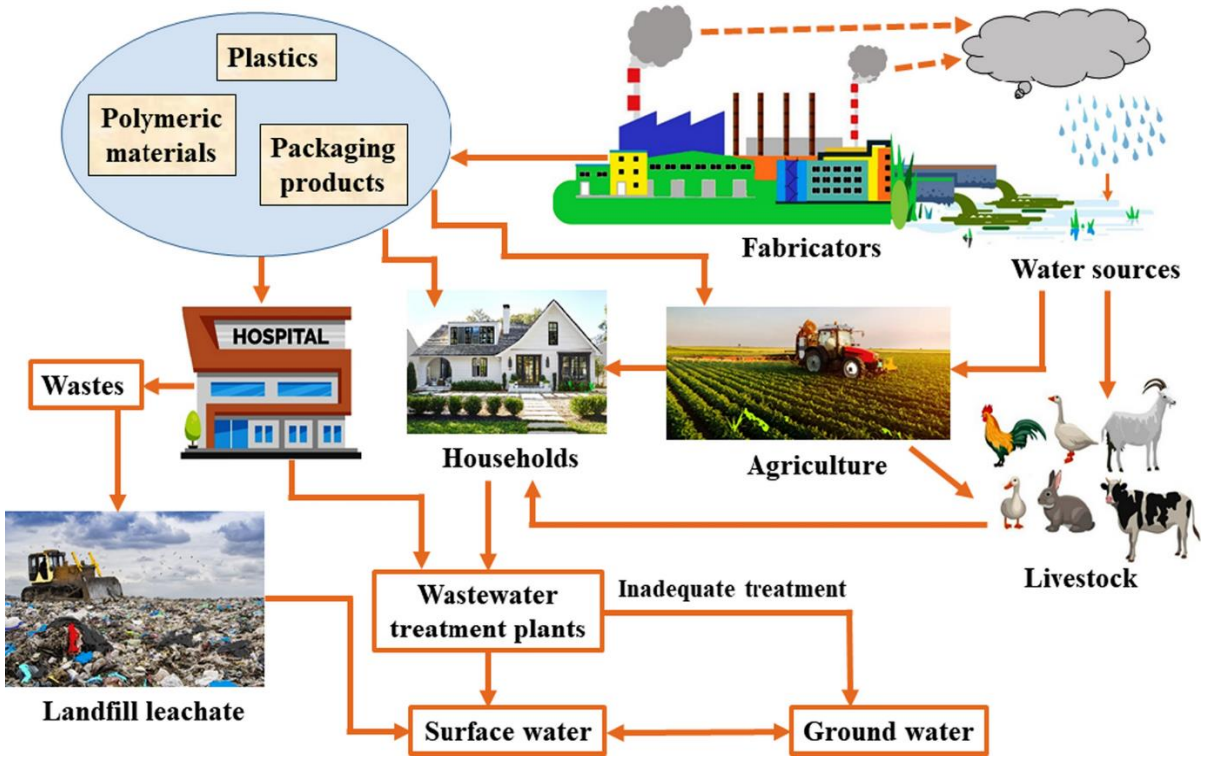

Figure 2.2 Potential sources of BPA contamination (adapted with permission from [26])

According to the United States Environmental Protection Agency (EPA), the annual release of BPA into the environment is greater than one million pounds [27]. BPA poses serious risks to the environment and human health, including carcinogenic effects, changes in lipid levels and dyslipidemia, and potential damage to the reproductive, nervous, and immune systems, even at trace levels [28-30].

Figure 2.3 shows the molecular structure of BPA, and its physicochemical properties are listed in Table 2.1.

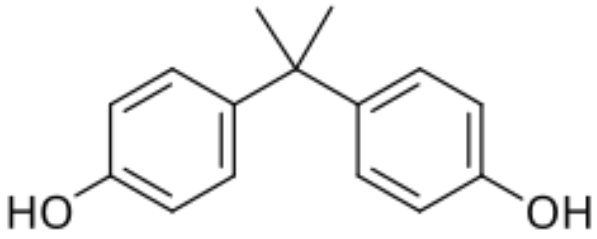

Figure 2.3 Molecular structure of BPA (adapted with permission from [31])

Table 2.1 Physicochemical properties of BPA [32]

Property	Value
Chemical name	2,2-Bis (4-hydroxyphenyl) propane
Molecular formula	$C_{15}H_{16}O_2$
Molar mass	228.3 g/mol
Water solubility	0.298 g/L at 25 ˚C
pK_a	9.8-10.4

BPA is a resistant organic pollutant detected in aquatic environments at concentrations ranging from nanograms per liter to micrograms per liter [33, 34]. Conventional wastewater treatment methods, including coagulation, flocculation, sedimentation, filtration, and disinfection, are ineffective at removing BPA [25, 35]. In addition, advanced treatment methods, such as reverse osmosis, membrane filtration, and adsorption, often require high energy input and complex infrastructure. These processes typically transfer pollutants to another phase rather than achieving complete degradation, potentially leading to the formation of secondary pollutants [36]. Consequently, there is a critical need to develop a promising method to remove aqueous BPA and to protect environmental health. Advanced oxidation processes (AOPs) offer effective and environmentally friendly solutions for eliminating BPA from contaminated water without generating secondary pollutants [26, 37].

2.3 Advanced oxidation processes (AOPs)

AOPs were first introduced by Glaze et al. in 1987 [38] for wastewater treatment. This process is based on the in-situ generation of strong oxidants, such as hydroxyl radicals (•OH), to degrade resistant organic contaminants under ambient temperature and pressure conditions. Figure 2.4 shows the classification of AOPs as homogeneous and heterogeneous processes. The difference between homogeneous and heterogeneous AOPs is the use of a solid-phase catalyst or promoter in heterogeneous AOPs [39]. Homogeneous AOPs utilize radical generators, such as hydrogen peroxide and ozone, as well as combinations of oxidants, Fenton's reagent, and photo-Fenton. These processes are classified into three types: photochemical (including photo-Fenton, UV/O_3, UV/H_2O_2, $UV/H_2O_2/O_3$, UV photolysis, and UV ultrasound), physical (such as sonolysis, electron beam, solar radiation, plasma, microwave, and gamma radiation), and chemical (including O_3/OH^-

, O_3/H_2O_2, Fe^{2+}/H_2O_2, ultrasound/H_2O_2, supercritical water oxidation, and wet air oxidation) [40]. Heterogeneous AOPs are categorized into photochemical (e.g., UV/O_3/catalyst, UV/H_2O_2/catalyst) and chemical (e.g., electro-Fenton) processes [40].

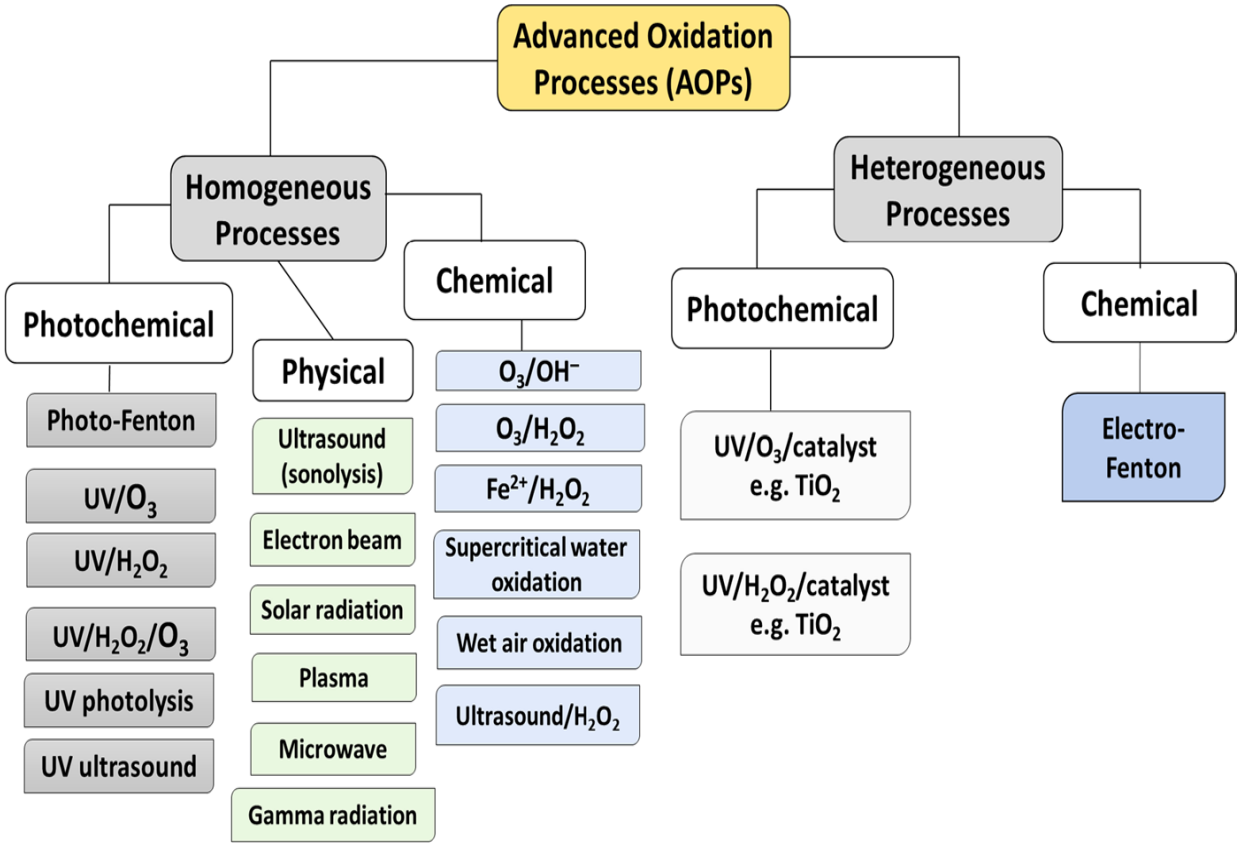

Figure 2.4 Classification of advanced oxidation processes (adapted with permission from [40])

2.4 Heterogeneous photocatalysis

Heterogeneous photocatalysis inspired by natural photosynthesis has drawn attention in AOPs. In this process, a semiconductor absorbs photon energy from light irradiation to drive redox reactions, converting light energy into chemical energy to degrade contaminants [41, 42]. Solar light is a renewable, sustainable, and cost-free source of light radiation for photocatalysis [8, 43]. As shown in Figure 2.5, the solar spectrum is mainly composed of infrared (IR) radiation, which accounts for 49% of the total energy. The visible region (400-700 nm) contributes 46%, while ultraviolet (UV) radiation with wavelengths below 400 nm has only 5% of the solar spectrum [44].

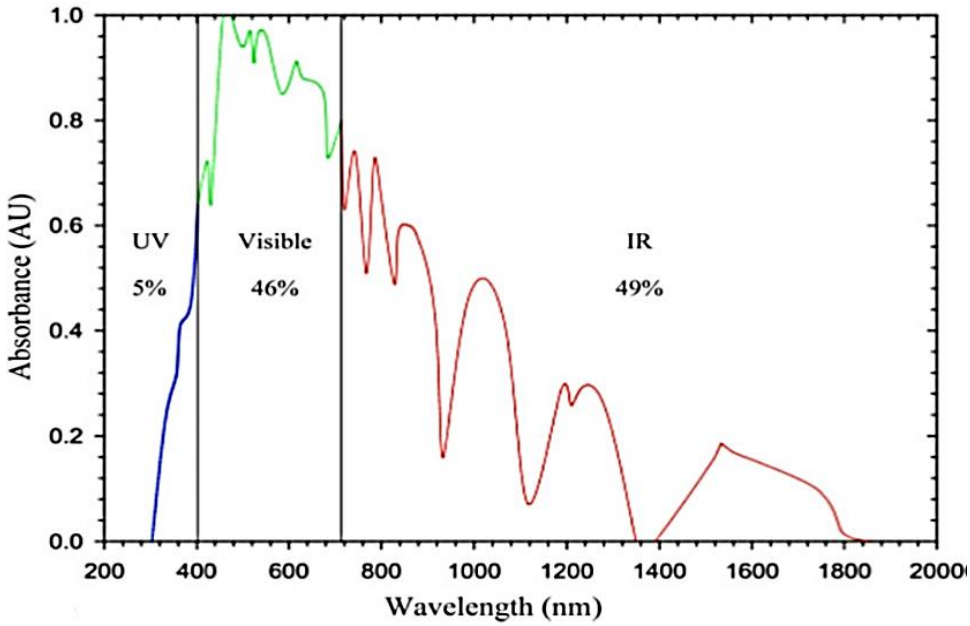

Figure 2.5 Solar light spectrum (adapted with permission from [44])

Figure 2.6 summarizes the bandgap energies and band positions of various photocatalysts [45]. For visible-light-driven photocatalysis, the photocatalyst must have an appropriate bandgap energy (~2.3-2.8 eV), enabling efficient absorption of solar light photons and the subsequent generation of charge carriers required for photocatalytic reactions. Additionally, the conduction band of the photocatalyst must be more negative than the $O_2/^{\bullet}O_2^-$ redox potential for converting dissolved oxygen to superoxide anions ($^{\bullet}O_2^-$) through a reduction reaction. Conversely, the valence band of the semiconductor must have a more positive potential than the $^{\bullet}OH/H_2O$ redox potential to participate in an oxidation reaction for converting water into hydroxyl radicals ($^{\bullet}OH$) [46]. Among commonly used photocatalysts, titanium dioxide (TiO_2) exhibits a favorable band-edge alignment with these redox potentials. Therefore, TiO_2 remains effective for degrading resistant organic pollutants under UV radiation ($\lambda \leq 400$ nm) [47].

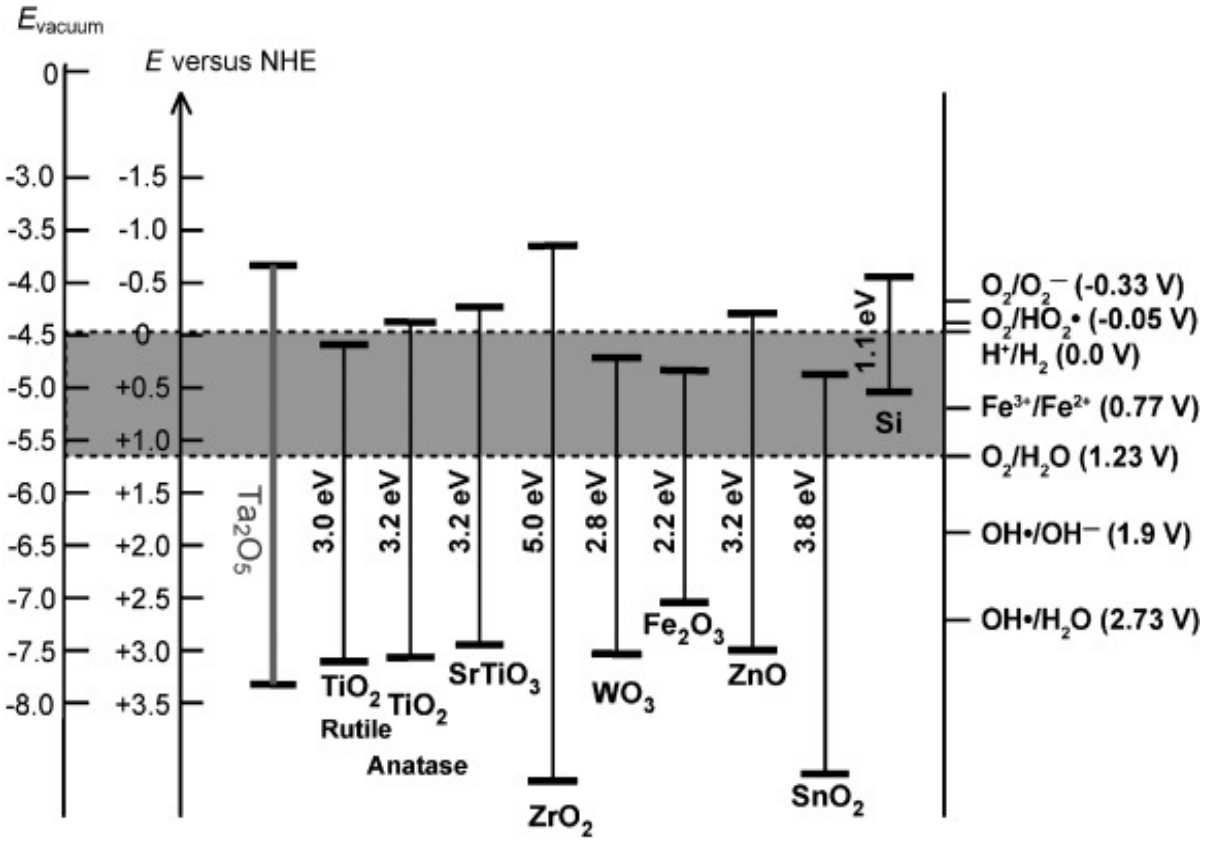

Figure 2.6 Bandgap energies and band positions of various photocatalysts vs. natural hydrogen electrode (NHE) at pH 0 (adapted with permission from [45])

2.5 TiO_2 photocatalyst

Heterogeneous photocatalysis using TiO_2 (titania) was initially introduced by Fujishima and Honda in the early 1970s [48]. They explored hydrogen production through water splitting by irradiating TiO_2 electrodes with UV light. In the late 1970s, Frank and Bard were the first to apply TiO_2 for the photocatalytic degradation of cyanide ions in aqueous solutions [49]. The photo-oxidation of cyanide to cyanate was achieved in the presence of oxygen under both artificial and natural sunlight. TiO_2 has attracted attention for photocatalytic degradation of contaminants owing to its non-toxicity, abundance, low cost, hydrophilicity, chemical and thermal stability, corrosion resistance, optical properties, and high photocatalytic activity under UV light [20, 50].

2.6 TiO_2 photocatalytic mechanism

Figure 2.7 presents the mechanism of TiO_2 photocatalysis. When TiO_2 is exposed to a light source with photon energy equal to or greater than its bandgap energy ($h\vartheta \geq E_g$), electrons in the valence band of TiO_2 are excited and moved to the conduction band [51]. This process generates positively charged electron holes in the valence band (h^+_{VB}) and negatively charged electrons in the conduction band (e^-_{CB}) of TiO_2 (Reaction 2.1). The pollutant degradation mechanism includes both direct and indirect photocatalytic reactions. In direct reactions, h^+_{VB} reacts with pollutants, forming intermediates that are ultimately converted to CO_2 and H_2O (Reaction 2.2). In indirect reactions, h^+_{VB} possesses a more positive band energy than $^{\bullet}OH/H_2O$. This allows h^+_{VB} to participate in oxidation reactions that convert water into $^{\bullet}OH$ (Reaction 2.3), which further contributes to pollutant degradation (Reaction 2.4). On the other hand, e^-_{CB} has a more negative band energy than $O_2/^{\bullet}O_2^-$, which converts dissolved oxygen to $^{\bullet}O_2^-$ through reduction reactions (Reaction 2.5) [20, 50]. The generated $^{\bullet}O_2^-$ then degrades pollutants through two mechanisms. $^{\bullet}O_2^-$ degrades pollutants into their intermediates, which leads to CO_2 and H_2O (Reaction 2.6). Additionally, $^{\bullet}O_2^-$ reacts with hydrogen ions (H^+) to generate hydroperoxyl radicals ($^{\bullet}OOH$) and hydrogen peroxide (H_2O_2) (Reactions 2.7 and 2.8) [52, 53]. The resulting H_2O_2 reacts with e^-_{CB} for generating $^{\bullet}OH$ (Reaction 2.9), which further degrades pollutants (Reaction 2.10).

$$TiO_2 + h\vartheta \rightarrow h^+_{VB} + e^-_{CB} \quad \text{(Reaction 2.1)}$$

$$h^+_{VB} + Pollutant \rightarrow Pollutant\ intermediates \rightarrow CO_2 + H_2O \quad \text{(Reaction 2.2)}$$

$$h^+_{VB} + H_2O \rightarrow \bullet OH + H^+ \quad \text{(Reaction 2.3)}$$

$$\bullet OH + Pollutant \rightarrow Pollutant\ intermediates \rightarrow CO_2 + H_2O \quad \text{(Reaction 2.4)}$$

$$e^-_{CB} + O_2 \rightarrow \bullet O_2^- \quad \text{(Reaction 2.5)}$$

$$\bullet O_2^- + Pollutant \rightarrow Pollutant\ intermediates \rightarrow CO_2 + H_2O \quad \text{(Reaction 2.6)}$$

$$\bullet O_2^- + H^+ \rightarrow \bullet OOH \quad \text{(Reaction 2.7)}$$

$$\bullet OOH + \bullet OOH \rightarrow H_2O_2 + O_2 \quad \text{(Reaction 2.8)}$$

$$H_2O_2 + e^-_{CB} \rightarrow \bullet OH + OH^- \quad \text{(Reaction 2.9)}$$

$$\bullet OH + Pollutant \rightarrow Pollutant\ intermediates \rightarrow CO_2 + H_2O \quad \text{(Reaction 2.10)}$$

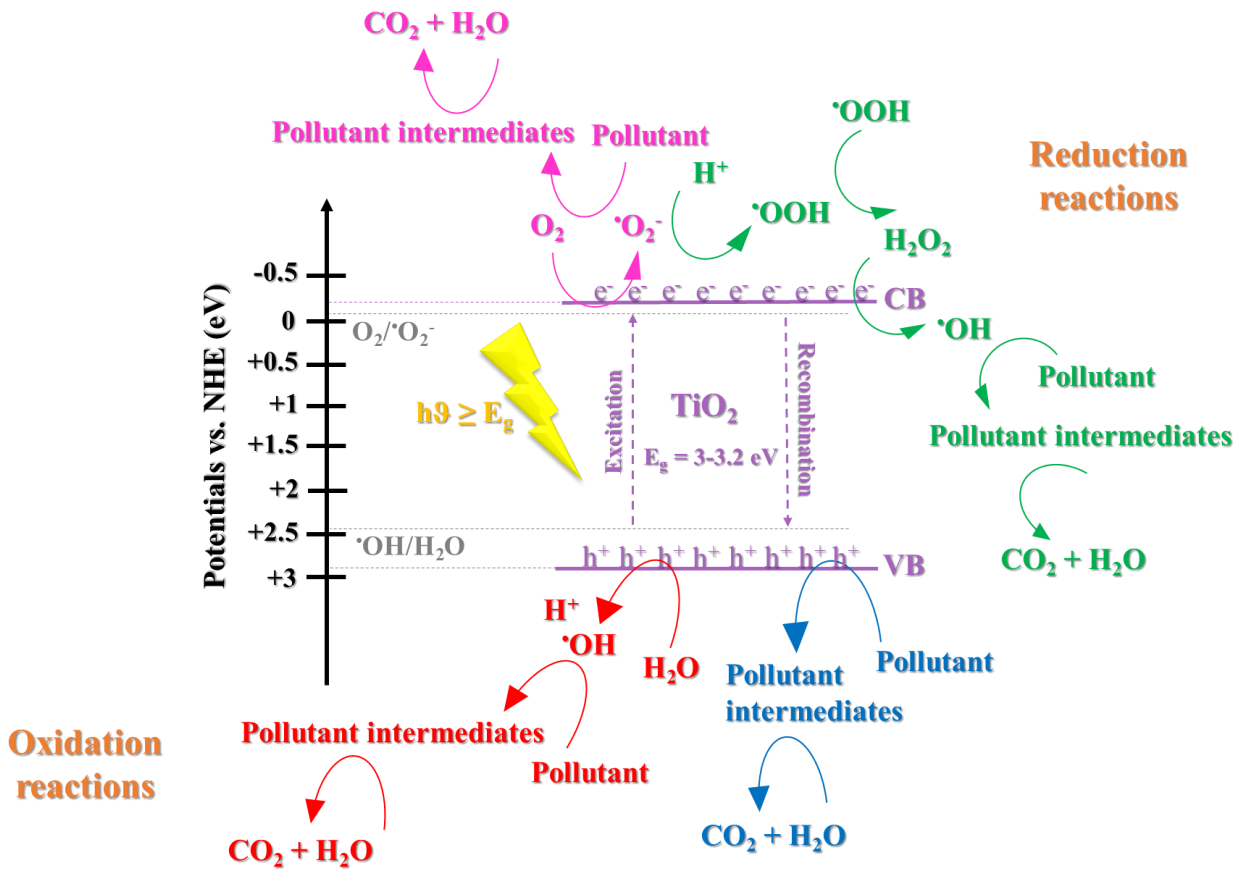

Figure 2.7 Mechanism of TiO_2 photocatalysis

2.7 TiO_2 structure

TiO_2 exists in four crystalline phases, including rutile, anatase, brookite, and TiO_2-B [54]. Figure 2.8 presents the crystal structures of rutile (tetragonal), anatase (tetragonal), brookite (orthorhombic), and TiO_2 (B) (monoclinic) [55]. Anatase is composed of corner-sharing TiO_6 octahedra, whereas rutile contains edge-sharing octahedra, and brookite has both corner- and edge-sharing octahedral crystals, which makes it less symmetric than anatase and rutile [56]. Among all TiO_2, rutile is thermodynamically the most stable phase, while anatase and brookite are metastable phases that persist at ambient conditions for long durations [57]. Brookite exhibits greater stability and superior photocatalytic activity than anatase [58]. TiO_2 (B) demonstrates good thermal stability and is characterized by its low density, high specific capacity, and open structural framework [59]. The physical properties of TiO_2 are listed in Table 2.2.

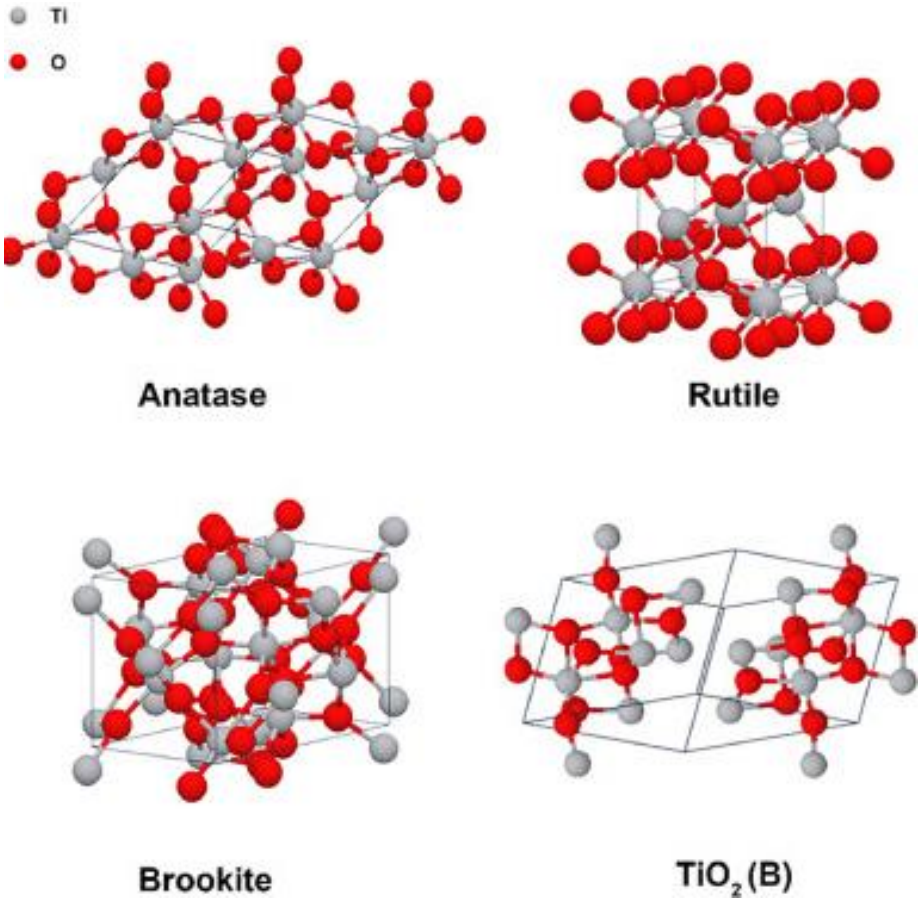

Figure 2.8 Crystal structures of TiO_2 (adapted with permission from [55])

Table 2.2 Physical properties of TiO_2 [54, 60]

Phase	Lattice parameters	Bandgap energy (eV)	Density (g/cm^3)
Anatase	a = b = 3.784 Å; c = 9.515 Å V = 136.24 $Å^3$	3.2	3.84
Rutile	a = b = 4.594 Å; c = 2.959 Å V = 62.45 $Å^3$	3.0	4.26
Brookite	a = 9.148 Å; b = 5.447 Å; c = 5.145 Å V = 257.38 $Å^3$	3.3	4.11
TiO_2 (B)	a = 12.179 Å; b = 3.741 Å; c = 6.525 Å; β = 107.054 V = 284.22 $Å^3$	3.29	3.64

2.8 TiO_2 modification

Although TiO_2 demonstrates high photocatalytic activity, it has several limitations. Pristine TiO_2 has a wide bandgap energy (3.0 eV for rutile and 3.2 eV for anatase), which restricts light absorption to the UV region. In addition, TiO_2 undergoes rapid recombination of charge carriers, thereby reducing its photocatalytic efficiency for the elimination of contaminants [61, 62]. Various modification strategies have been used to improve the photocatalytic activity of TiO_2 for pollutant degradation, such as doping with metals and non-metals and constructing heterojunctions with secondary semiconductors [63].

2.8.1 Metal and non-metal doping

Modification of TiO_2 with metals has been investigated, including the use of noble metals (Ag, Au, Rh, Pt, Pd, Ir, Os), transition metals (Cr, Cu, Co, Ni, Fe, Mo, V, W, Zr, Mn, Nb, Zn, Ru, Y), and rare earth metals (Nd, Tb, Ce, Yb, Er, La, Eu) [64-66]. Additionally, several non-metal elements, such as B, F, N, S, I, P, and C, have been studied to modify TiO_2 [61, 67, 68].

Doping TiO_2 with metal and non-metal elements enhances its photocatalytic activity by introducing new energy levels within the bandgap. Figure 2.9 shows the bandgap energies of pure, metal doped, and non-metal doped TiO_2. The bandgap energy of pure TiO_2 is approximately 3.2 eV. Metal doping involves substituting a Ti atom in the lattice, thereby forming a low-energy conduction band. This new energy band narrows the bandgap of TiO_2, which increases its photocatalytic efficiency. In contrast, non-metal doping substitutes an O atom in the lattice, generating a new energy level above the valence band. This modification also reduces the bandgap of TiO_2, thereby improving its photocatalytic activity [69, 70].

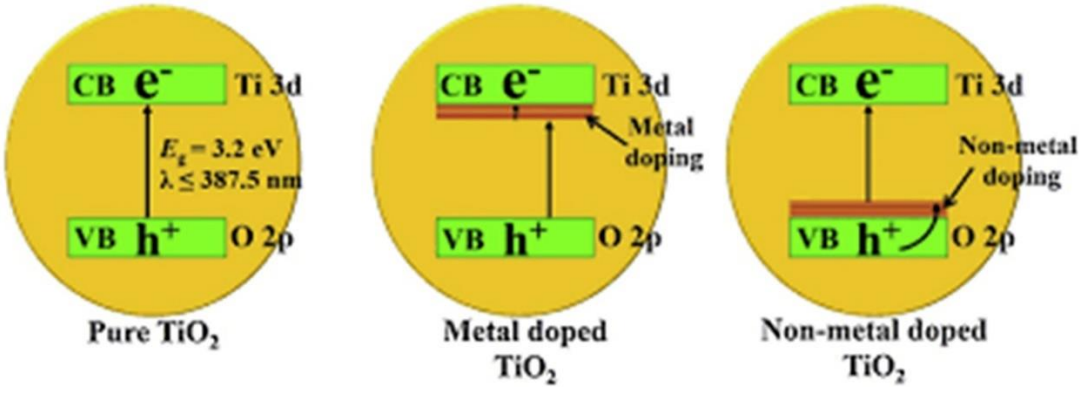

Figure 2.9 Modification of pure TiO_2 with metal and non-metal dopants (adapted with permission from [70])

2.8.2 Heterojunctions

Coupling TiO_2 with other semiconductors, such as metal oxides (e.g., WO_3, CeO_2, In_2O_3, V_2O_5), metal-free materials (e.g., g-C_3N_4), chalcogenides (e.g., FeS_2, CdS), and carbon-based materials (e.g., GO, rGO), has been investigated [20, 41, 50, 71-73]. The formation of a heterojunction between TiO_2 and a secondary semiconductor enhances the separation of photogenerated charge carriers or the separation of reduction and oxidation sites. This increases the lifetime of electron-hole pairs and thus enhances photocatalytic activity [41]. Several types of heterostructures have been reported, including p-n junctions, S-schemes, Z-schemes, and traditional heterojunctions, as shown in Figure 2.10 [74].

Traditional heterojunctions are categorized as type I, type II, and type III, corresponding to straddling, staggered, and broken energy gaps, respectively. In a type I heterojunction, the conduction band of semiconductor I is higher than that of semiconductor II, while its valence band is lower. Therefore, type I heterojunctions fail to properly separate electron-hole pairs as both electrons and holes accumulate in a single semiconductor (Figure 2.10(a)). In a type-II heterojunction, the conduction band and valence band of semiconductor I are higher than those of semiconductor II. This configuration leads to spatial separation of electron-hole pairs, with holes moving to semiconductor I and electrons migrating to semiconductor II under light irradiation (Figure 2.10(b)). In addition, a type-III heterojunction cannot separate electron-hole pairs due to the lack of overlap between the bandgaps. Thus, there is no transfer or separation of electrons and holes between semiconductors I and II (Figure 2.10(c)) [75, 76].

As shown in Figure 2.10(d), a p-n heterojunction occurs between p-type and n-type semiconductors. An n-type semiconductor has electrons as the major charge carriers, while holes are the major charge carriers in a p-type semiconductor [41]. Before illumination, the diffusion of majority carriers at the junction creates a space-charge region that establishes an internal electric field. This drives electrons and holes generated by light in opposite directions. The interplay of the internal electric field and band alignment enables p-n heterojunctions to achieve more efficient charge separation than type II heterojunctions [77].

Figure 2.10(e) shows a Z-scheme heterojunction, where both semiconductors in direct contact are excited by light irradiation. Electrons in the conduction band of semiconductor I directly recombine with holes in the valence band of semiconductor II. Consequently, the remaining electrons in the conduction band of semiconductor II and the holes in the valence band of semiconductor I become spatially separated, thereby maintaining a high redox potential. This separation increases the efficiency of redox reactions [78, 79].

S-scheme heterojunctions consist of two semiconductors: a reduction photocatalyst (RP) with a lower work function and an oxidation photocatalyst (OP) with a higher work function [80, 81]. Upon contact between the OP and RP, electrons transfer from RP to OP, creating a positive charge at the RP interface and a negative charge at the OP interface. This establishes an internal electric field that facilitates electron transfer from OP to RP (Figure 2.10(f)). As the interfaces between OP and RP align, the Fermi energy levels equalize on both sides, leading to band bending. This bending promotes the recombination of electrons from the conduction band of OP with holes in the valence band of RP. The electrons in the conduction band of OP are likely to recombine with holes in the valence band of RP because of Coulombic attraction between oppositely charged particles. This recombination process is influenced by Coulombic attraction, internal electric field, and band bending, which removes less effective charge carriers while maintaining the more effective electrons in the conduction band of RP and holes in the valence band of OP [82].

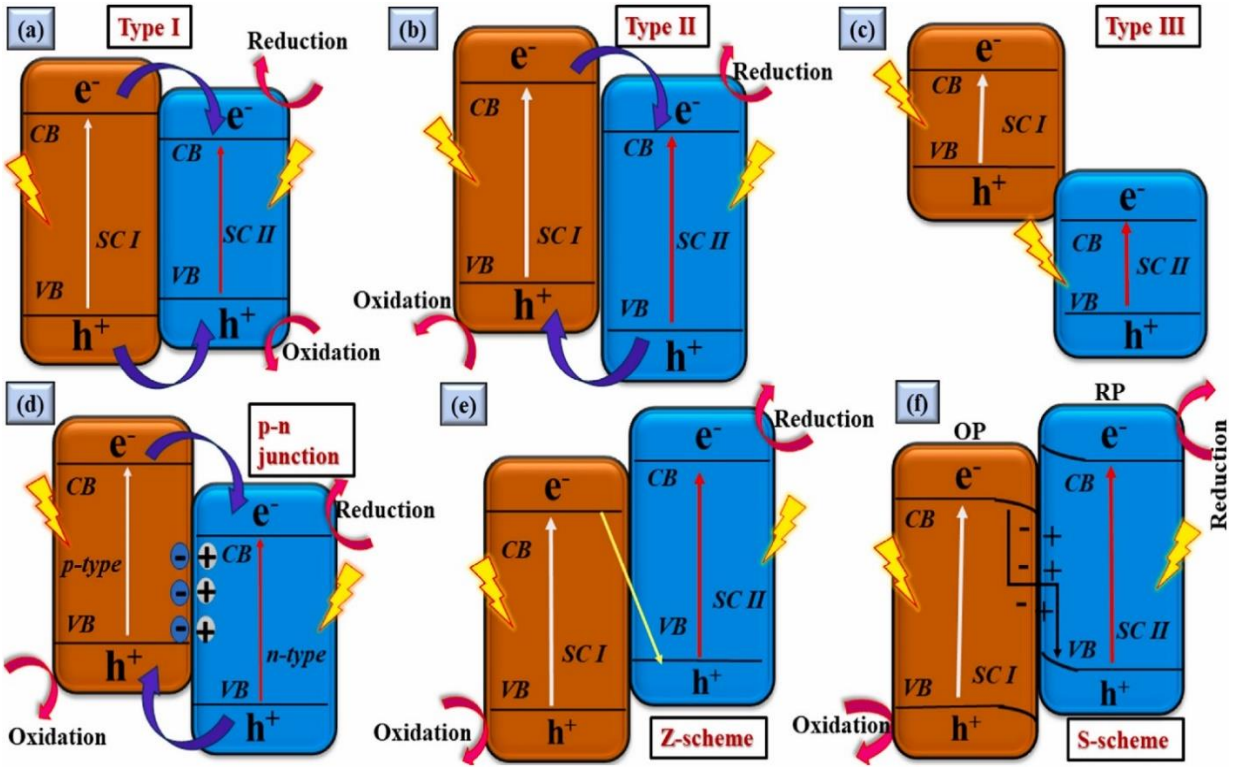

Figure 2.10 Schematic of various heterojunctions (a) type-I, (b) type-II, (c) type-III, (d) p-n junction, (e) Z-scheme, (f) S-scheme (adapted with permission from [74])

2.8.3 Energy storage photocatalysts

Another restriction of TiO_2 in photocatalytic wastewater treatment is its reliance on continuous light irradiation. Without light, the photocatalytic activity of TiO_2 stops completely, limiting its practical applications [42]. To tackle this issue, coupling TiO_2 with a secondary semiconductor with energy storage capacity has been proposed [83]. Photocatalysts possessing energy storage capacity store a portion of the photon energy during light irradiation and then maintain their photocatalytic activity in the absence of light, which is referred to as an "all-day-active photocatalyst" or "round-the-clock photocatalyst" [84]. Energy storage photocatalysts are classified into oxidative and reductive types.

Oxidative energy storage photocatalysts, such as $Ni(OH)_2$, NiO, and MnO_x, store photogenerated holes [84, 85]. The mechanism of oxidative photocatalysts includes p-n junction and mediator models [85]. As depicted in Figure 2.11(a), TiO_2, as an n-type semiconductor, forms a heterojunction with a p-type semiconductor, such as Ni $(OH)_2$, which creates an internal electric field. Upon light irradiation, electron-hole pairs are generated in both semiconductors (Reaction

2.11). The photogenerated holes move from the valence band of TiO_2 to $Ni(OH)_2$ through the built-in electric field (Reaction 2.12), and $Ni(OH)_2$ is oxidized by holes (Reaction 2.13). Meanwhile, the photogenerated electrons accumulate in the conduction band of TiO_2 and react with oxygen (Reaction 2.14). In the absence of light, the intermediate $NiO_x(OH)_{2-x}$ undergoes further oxidation reactions (Reaction 2.15) [84, 85].

$$TiO_2 + h\vartheta \rightarrow TiO_2^*(e^-) + TiO_2^*(h^+) \quad \text{(Reaction 2.11)}$$

$$TiO_2^*(h^+) \rightarrow Ni(OH)_2(h^+) \quad \text{(Reaction 2.12)}$$

$$Ni(OH)_2 + xh^+ + x\,OH^-_{(H_2O\ or\ electrolyte)} \rightarrow NiO_x(OH)_{2-x} + xH_2O \quad \text{(Reaction 2.13)}$$

$$O_2 + 2H^+ + 2e^- \rightarrow H_2O_2 \quad \text{(Reaction 2.14)}$$

$$NiO_x(OH)_{2-x} + substance \rightarrow Ni(OH)_2 + oxidation\ products \quad \text{(Reaction 2.15)}$$

As shown in Figure 2.11(b), an electron mediator, such as a Fe^{3+}/Fe^{2+} redox couple, is used in the mediator model. Photogenerated electrons in $Ni(OH)_2$ move fast to the conduction band of TiO_2 via the electron mediator. The remaining photogenerated holes in the valence band of $Ni(OH)_2$ oxidize itself (Reaction 2.13), thereby enabling oxidative energy storage [84, 85].

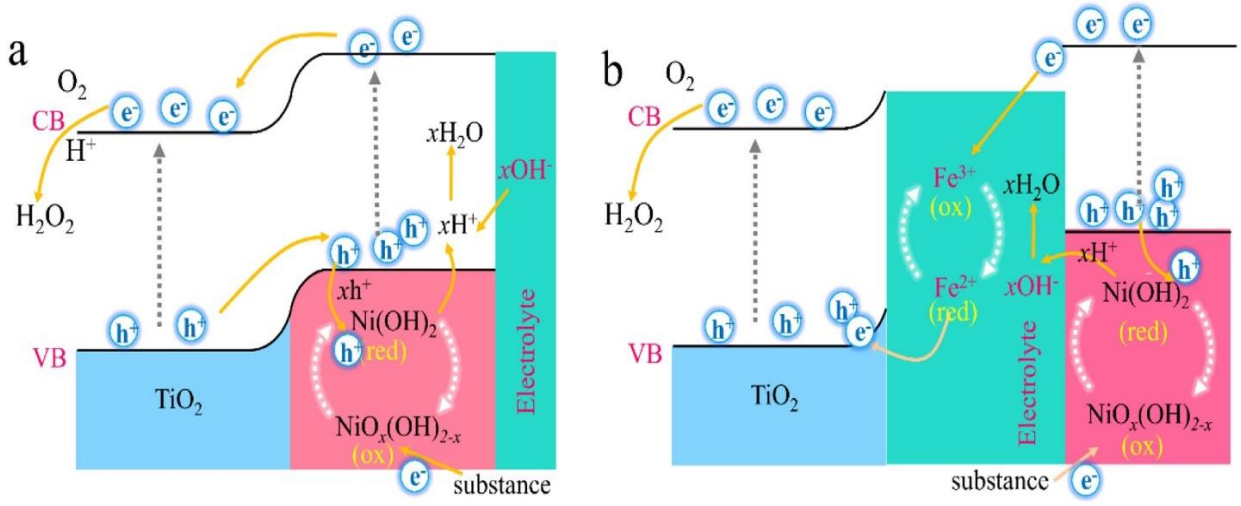

Figure 2.11 Oxidative energy storage mechanism in (a) p-n junction model and (b) mediator model (adapted with permission from [85])

Reductive photocatalysts, such as WO_3, MoO_3, Cu_2O, and V_2O_5, store photogenerated electrons [84, 85]. Figure 2.12 shows the mechanism of electron storage in the TiO_2-WO_3 system in the presence and absence of light [84]. In this system, TiO_2 is a photoactive material that absorbs light and generates electrons, while WO_3 acts as an electron storage medium. Under light irradiation, photo-induced charge carriers are generated in TiO_2 (Reaction 2.16). The photogenerated electrons are transferred to the conduction band of WO_3 through interfacial effects (Reaction 2.17). Simultaneously, water is oxidized by photogenerated holes, driving the oxygen evolution reaction and producing H^+ (or M^+ ions) and OH^- (Reaction 2.18). The transferred photogenerated electrons are subsequently trapped by H^+ (Reaction 2.19). In the dark, the trapped photogenerated electrons are released (Reaction 2.20) and react with oxygen to generate $^{\bullet}O_2^-$ (Reaction 2.21) [84, 85].

$$TiO_2 + h\vartheta \rightarrow TiO_2^*(e^-) + TiO_2^*(h^+) \quad \text{(Reaction 2.16)}$$

$$TiO_2^*(e^-) \rightarrow WO_3(e^-) \quad \text{(Reaction 2.17)}$$

$$3H_2O\ (or\ electrolyte) + 4h^+ \rightarrow 5H^+\ (or\ M^+) + O_2 + OH^- \quad \text{(Reaction 2.18)}$$

$$WO_3 + xe^- + xH^+\ (or\ M^+) \rightarrow H_xW_x^{5+}W_{1-x}^{6+}O_3\ (or\ M_xWO_3) \quad \text{(Reaction 2.19)}$$

$$H_xW_x^{5+}W_{1-x}^{6+}O_3\ (or\ M_xWO_3) \rightarrow WO_3 + xe^- + xH^+\ (or\ M^+) \quad \text{(Reaction 2.20)}$$

$$e^- + O_2 \rightarrow \bullet O_2^- \quad \text{(Reaction 2.21)}$$

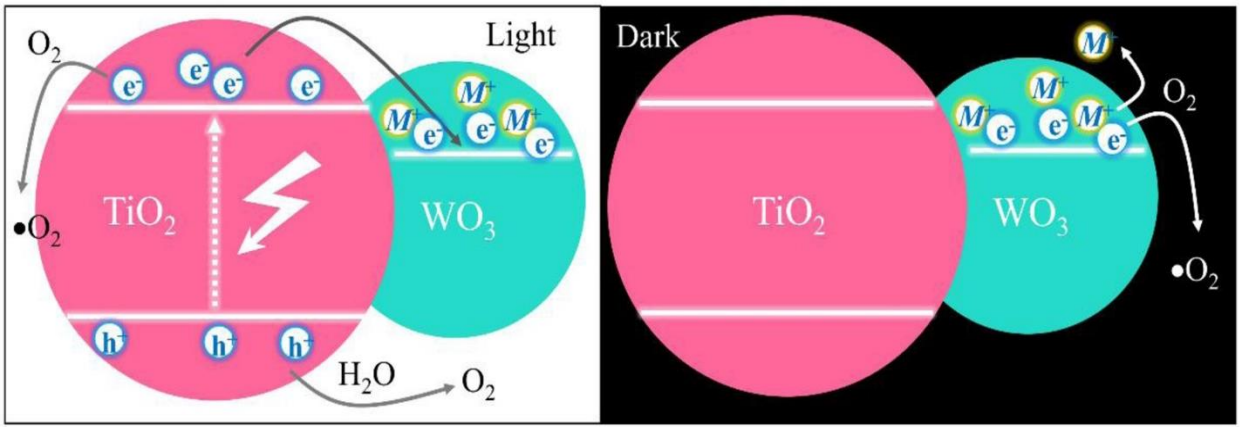

Figure 2.12 Reductive energy storage mechanism in the TiO_2-WO_3 system (adapted with permission from [84])

2.9 TiO_2 morphology

The morphology of TiO_2 is a critical factor influencing its photocatalytic activity [86]. TiO_2 nanostructures have been synthesized in diverse morphologies, including 0D (e.g., quantum dots), 1D (e.g., nanofibers, nanowires, nanotubes, nanorods), 2D (e.g., nanosheets, nanoflakes), and 3D (e.g., nanoflowers, nanospheres) [55], as shown in Figure 2.13. TiO_2 fabrication methods reported in the literature include hydrothermal, solvothermal, sonochemical, and sol-gel techniques, as well as template-assisted processes, precipitation method, simple mixing, direct oxidation, chemical vapor deposition, electrodeposition, and microwave-assisted synthesis [87]. The term one-dimensional (1D) nanostructure refers to nanocrystals whose elongation exceeds approximately 10 nm and is confined to a single direction [88].

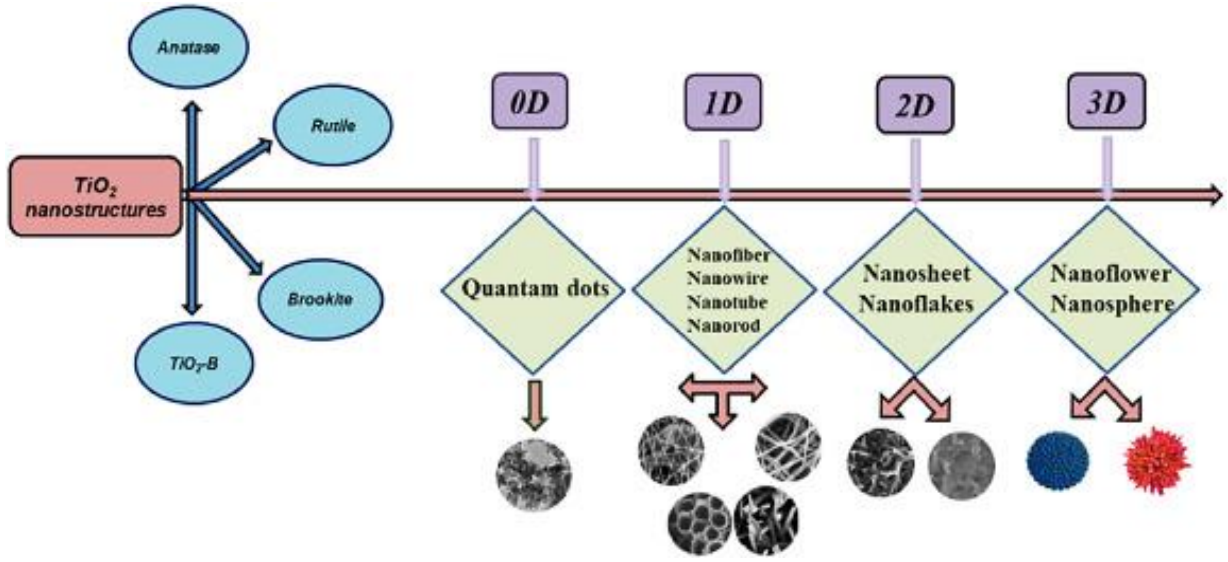

Figure 2.13 Classification of TiO_2 nanostructures according to phase and dimensionality (adapted with permission from [55])

2.10 TiO_2 nanotubes

1D TiO_2 nanotubes have attracted considerable attention among TiO_2 nanostructures due to their radial directional confinement and high aspect ratio [89]. These characteristics improve light harvesting and promote electron migration [89, 90]. Compared with TiO_2 nanoparticles, TiO_2 nanotubes show higher specific surface area, improved light absorption, and more directional charge mobility [91]. Figure 2.14 presents the electron transfer pathways in nanoparticles and

nanotubes. In particular, vertically oriented TiO_2 nanotubes facilitate current flow along their tubular architecture, thereby enabling superior charge-carrier transfer compared to nanoparticles [92].

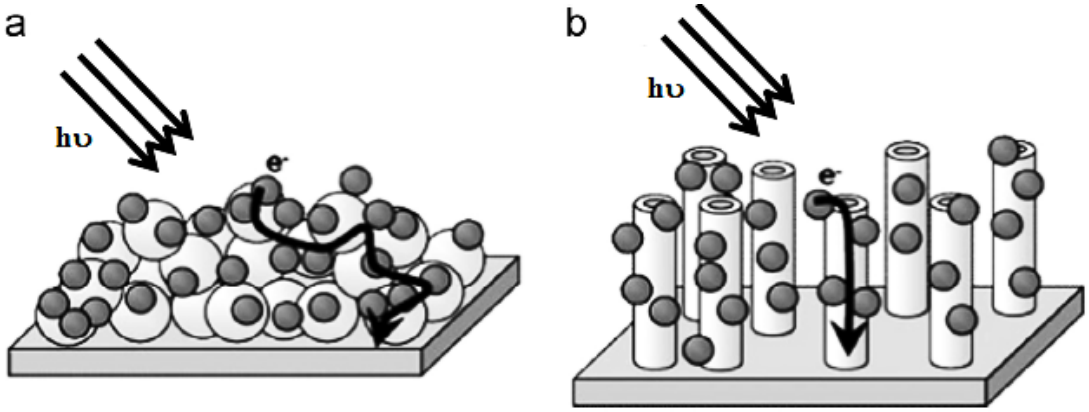

Figure 2.14 Schematic diagram of electron transfer in (a) nanoparticles and (b) nanotubes (adapted with permission from [92])

TiO_2 nanotubes have been synthesized using several methods, including electrochemical anodization of titanium, template-assisted techniques, the sol-gel process, and the hydrothermal method [93, 94]. The hydrothermal method is commonly used to convert TiO_2 nanoparticles into TiO_2 nanotubes [94]. Figure 2.15 presents the morphological phase diagrams of TiO_2 nanotubes based on NaOH concentration, hydrothermal treatment temperature, and TiO_2 precursors. The diagrams highlight distinct regions where different TiO_2 morphologies, such as nanoparticles, nanotubes, and nanoribbons, form during hydrothermal processing of anatase, rutile, and Degussa P25 [94, 95]. The results indicate that the morphology of TiO_2 can be controlled by adjusting hydrothermal conditions, offering insights into optimizing synthesis methods to produce TiO_2 nanostructures with tailored properties for specific applications.

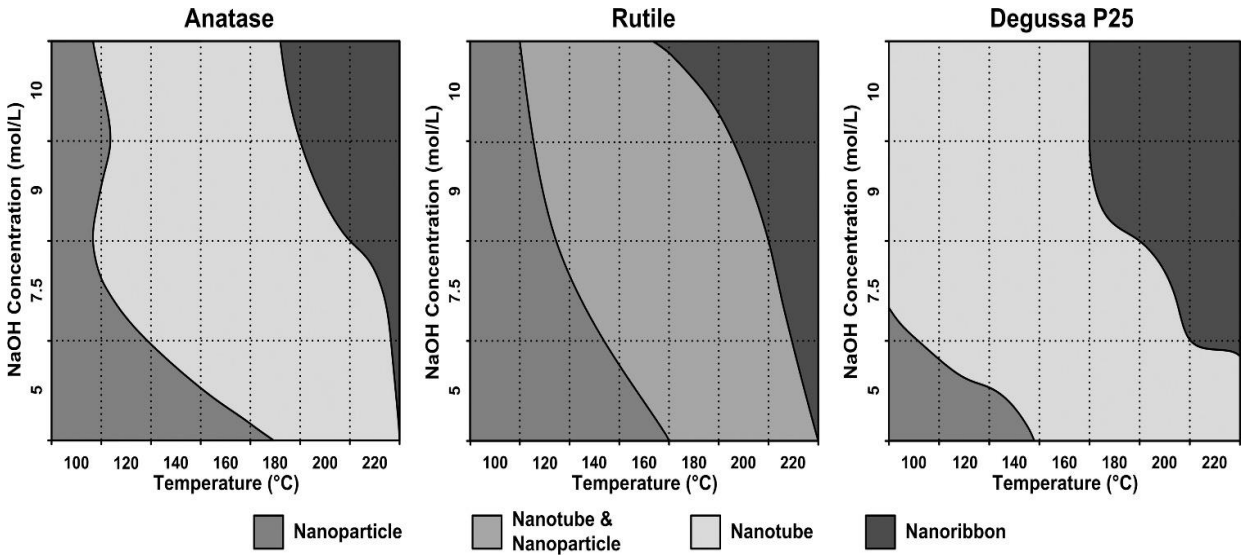

Figure 2.15 Morphological phase diagrams of hydrothermally treated anatase, rutile, and Degussa P25 (adapted with permission from [95])

Titanates with layered structures are produced under alkali hydrothermal synthesis. The transformation mechanism of TiO_2 nanoparticles into TiO_2 nanotubular structures occurs through the scrolling or consecutive wrapping of titanate nanosheets [94, 96]. Figure 2.16 presents the schematic diagrams of possible mechanisms for the hydrothermal formation of TiO_2 nanotubes. In Figure 2.16(a), a continuous spiral is formed through the helical scrolling of a single-layer nanosheet that results in a tube with two ends. Figure 2.16(b) shows an onion-like morphology resulting from the scrolling of a multiple-layer nanosheet, with a seam marking the transition to a tubular structure.

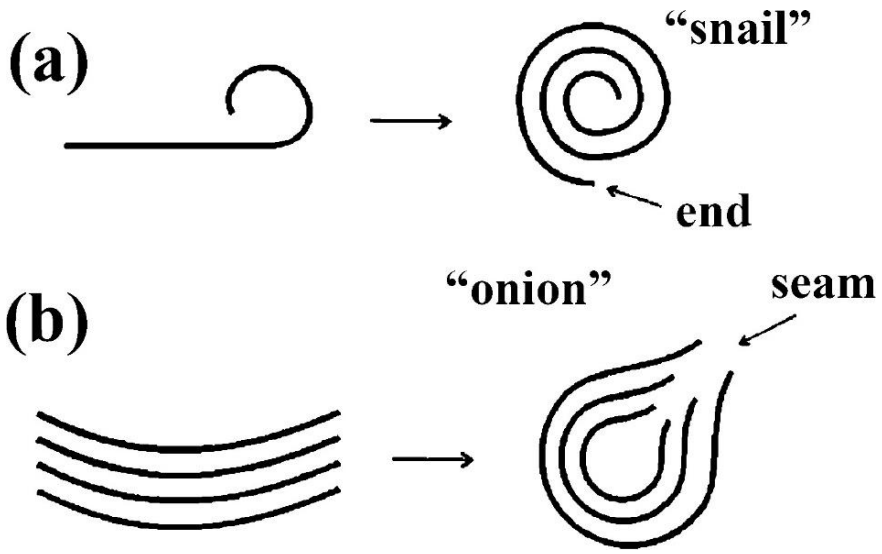

Figure 2.16 Schematic illustration of possible mechanisms for the hydrothermal formation of TiO_2 nanotubes (a) the helical scrolling of a single-layer nanosheet, (b) the curving of several conjoined nanosheets (adapted with permission from [94])

2.11 Photocatalytic systems

Photocatalytic reactors used in wastewater treatment are typically categorized as suspended or immobilized systems. In immobilized configurations, photocatalysts are deposited on solid supports or incorporated into floating carriers, designated as supported and floating systems, respectively. Figure 2.17 presents various configurations of photocatalysts.

As shown in Figure 2.17(a), in suspended systems, powder photocatalysts are evenly distributed throughout the water. This increases the contact area between the photocatalyst surface and the aqueous pollutant, thereby improving photocatalytic reactions in suspended configurations. However, suspended photocatalytic systems are hindered by some limitations. In real conditions, light irradiation cannot reach the photocatalyst beyond 0.5 m from the surface, leading to the deactivation of some fractions of the photocatalyst. Suspended systems also require strong stirring during photocatalytic reactions to prevent particle agglomeration. In addition, the recovery and reusability of suspended photocatalysts are complicated and costly. Moreover, nanoparticles remaining in water after photocatalytic treatment can pose environmental and health risks if no appropriate filtration step is included [8, 12, 97, 98].

In supported photocatalytic systems, photocatalysts are immobilized on solid substrates, such as wood, glass, or metallic plates (Figure 2.17(b)). Compared to suspended systems, supported systems facilitate photocatalyst recovery, but they exhibit reduced photocatalytic efficiency due to photocatalyst deposition [8, 12].

When sunlight is utilized as the irradiation source, floating photocatalytic systems are the most promising. As depicted in Figure 2.17(c), floating photocatalysts are free to move within the water, leading to higher photocatalytic efficiency compared with supported photocatalytic systems [99].

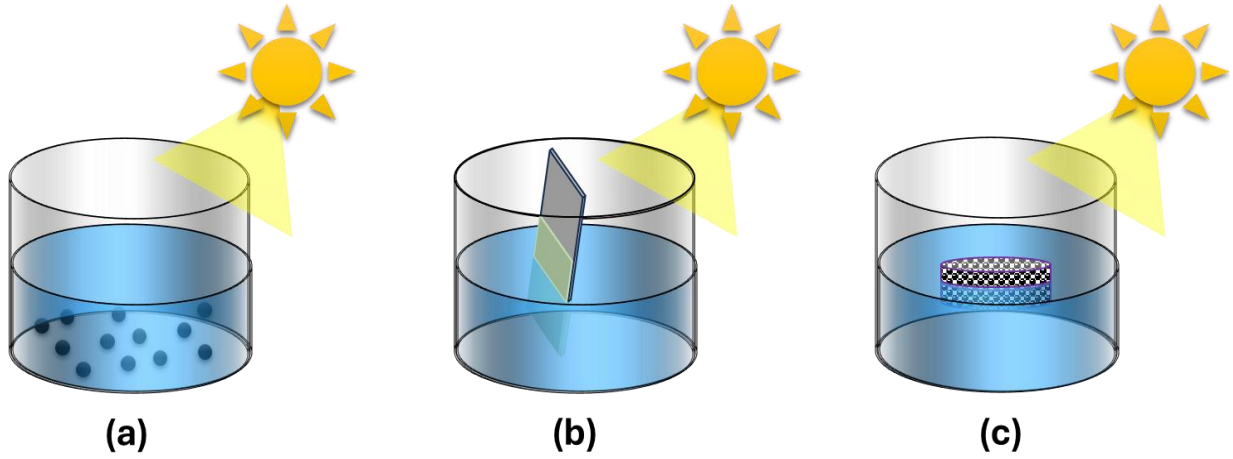

Figure 2.17 Configuration of photocatalysts for wastewater treatment (a) suspended, (b) supported, and (c) floating systems

2.12 Floating photocatalysts

Floating photocatalysts possess a density of 0.1-0.5 g/cm^3, which is lower than that of water (1 g/cm^3) [100]. As a result, these photoactive materials remain floating at the water surface. In floating photocatalytic systems, photoactive materials are utilized in a self-floating form or immobilized on buoyant carriers [9]. Compared to self-floating photocatalysts, immobilized floating photocatalysts reduce the amount of photoactive material required in synthesis [101] and eliminate the need for advanced synthesis techniques and their associated high costs [102]. Additionally, immobilized floating photocatalysts enable greater flexibility in depositing diverse photocatalysts onto floating carriers [100].

A wide range of materials have been reported as carriers for floating photocatalysts, including perlite, polymers, glass beads, cork, graphite, vermiculite, silica, alginate, aerogel, light-expanded clay aggregate, autoclaved cellular concrete, palm trunk, canvas, foam, sponge, fabric, cotton, fiber, cellulose, zeolite, fly-ash, and wood, as shown in Figure 2.18 [9, 100, 103].

Several fabrication techniques have been explored to deposit photoactive materials onto floating carriers, including dip coating, spin coating, spray coating, suspension coating, sol-gel, hydrothermal, solvothermal, solvent casting, strewing solvent casting, impregnating solvent casting, chemical vapor deposition, surface modification with strong acid or alkali treatment, liquid-phase deposition, direct hydrolysis precipitation, and three-dimensional printing [11, 100].

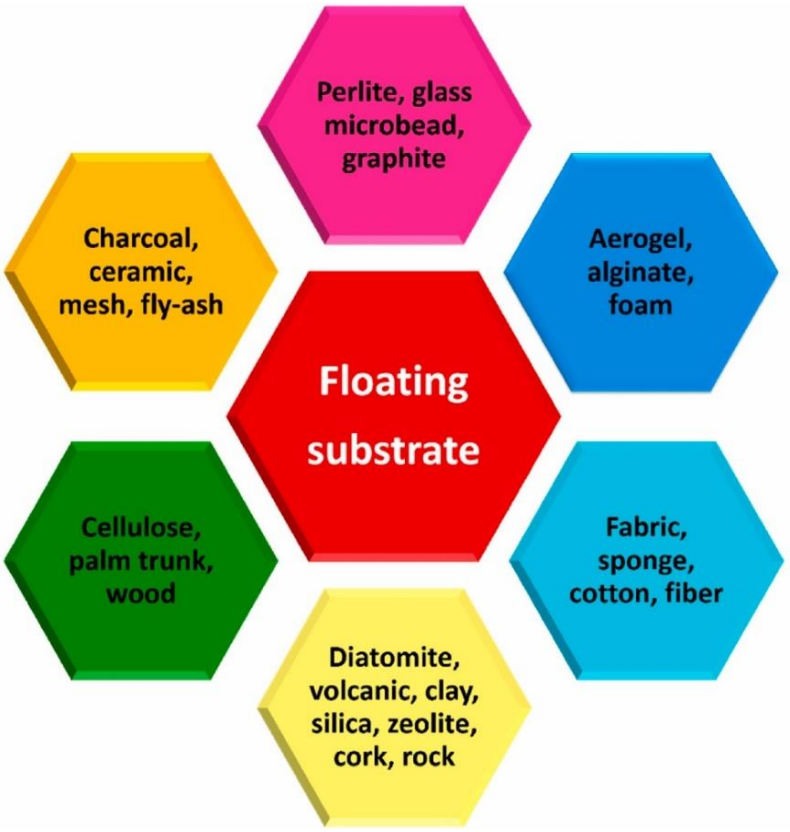

Figure 2.18 Various substrates used for floating photocatalysts (adapted with permission from [100])

Floating photocatalytic systems present several benefits for wastewater treatment as follows:

1) Unlike conventional immobilized photocatalysts that operate at a solid/water diphase interface, floating photocatalysts establish an air-solid-water triphase interface. This configuration in floating photocatalysts enables direct light irradiation of the photocatalyst surface, without attenuation by water, thereby increasing photon absorption and photoinduced charge carrier generation [11, 104].

2) The air-solid-water triphase interface formed in floating photocatalysts increases oxygen transfer from the air, which improves photocatalytic reactions through enhanced formation of reactive oxygen species (ROS) [10].

3) Compared with suspended photocatalysts, floating photocatalytic systems facilitate the easy recovery of photocatalysts and minimize photoactive material loss after wastewater treatment [10, 105].

2.13 State-of-the-Art literature review

Recent studies on TiO_2-based photocatalysts for BPA degradation are summarized in Table 2.3. Several suspended photocatalytic systems exhibited unsatisfactory degradation efficiency of BPA [32, 106-109]. For example, Krishnan et al. [106] fabricated TiO_2 and co-doped Cu-N/TiO_2 photocatalysts for degrading 10 mg/L BPA in a suspended system. BPA was degraded around 20% and 43% using suspended TiO_2 and Cu-N/TiO_2 photocatalysts after 120 min of visible light, respectively. In another study [107], only 30% of 20 mg/L BPA was degraded by suspended N-doped carbon/TiO_2 photocatalysts after 210 min exposed to UV light. In addition, the synthesized TiO_2 nanotubes achieved 42% BPA degradation under UV radiation for 80 min [108].

Some suspended photocatalysts showed low reusability after consecutive cycles. For instance, the photocatalytic activity of commercial TiO_2 P25 nanoparticles based on natural zeolite clinoptilolite decreased by 30% in degrading BPA after four reuse cycles [110]. Similar results were reported for suspended co-doped Cu-N/TiO_2 photocatalysts after three recovery cycles [106].

The literature indicates that the contribution of reactive species to the photocatalytic degradation of BPA remains underexplored [109, 111]. In addition, several studies have not investigated the photoelectrochemical characterization of photocatalysts [106, 107, 110, 112]. There is also a lack of kinetic studies on BPA removal in the existing literature [109]. Moreover, no research has been

conducted on the round-the-clock degradation of BPA with an energy storage floating photocatalyst.

To date, no studies have reported BPA degradation in a floating catalyst photoreactor under simulated sunlight irradiation. As listed in Table 2.3, only two studies have investigated floating photocatalysts for degrading BPA under UV and visible light. Li et al. [111] prepared floating photocatalysts by depositing commercial TiO_2 benchmark on polyurethane foam. The fabricated floating photocatalyst degraded 71% of BPA under UV irradiation after 120 min. In another study, Cai et al. [109] utilized cellulose nanofibrous as a floating carrier for TiO_{2-x} photocatalysts. Floating TiO_{2-x}@cellulose removed about 27% of BPA after 60 min of visible light irradiation. Additionally, co-doped magnetic N-TiO_{2-x}/rGO photocatalysts immobilized on floating cellulose nanofibrous were examined [109]. Approximately 96% of BPA was degraded by floating N-TiO_{2-x}-rGO/Fe_3O_4@cellulose photocatalysts after 60 min of visible light irradiation.

Table 2.3 Recent studies on TiO_2-based photocatalysts for BPA degradation

Photocatalyst	TiO_2 morphology	Photocatalytic system	Photocatalyst dosage	BPA concentration	Light and irradiation time	BPA degradation	Ref.
TiO_2 P25/PU	Nanoparticles	Floating	2 g/L	20 mg/L	UV 120 min	71%	[111]
TiO_{2-x}@cellulose	Nanoparticles	Floating	0.5 g/L	10 mg/L	Visible 60 min	~27%	[109]
TiO_2	Nanoparticles	Suspension	0.5 g/L	10 mg/L	Visible 120 min	~20%	[106]
TiO_2	Nanotubes	Suspension	1 g/L	10 mg/L	UV 80 min	42%	[108]
Cr-doped TiO_2	Nanoparticles	Suspension	0.5 g/L	10 mg/L	Visible 240 min	99%	[113]
Cu-doped TiO_2	Nanoparticles	Suspension	1 g/L	5 mg/L	Visible 360 min	~96%	[114]
Pt-doped TiO_2	Nanorods	Suspension	0.125 g/L	10 mg/L	Visible 240 min	100%	[32]
Au-doped TiO_2	Nanorods	Suspension	0.125 g/L	10 mg/L	Visible 240 min	50%	[32]
Ag-doped TiO_2	Nanorods	Suspension	0.125 g/L	10 mg/L	Visible 240 min	80%	[32]
B-doped TiO_2	Nanoparticles	Suspension	1 g/L	10 mg/L	Sunlight 66.5 min	88%	[115]
N-doped TiO_2	Nanoparticles	Suspension	1 g/L	10 mg/L	Sunlight 66.5 min	94%	[115]
P-doped TiO_2	Nanoparticles	Suspension	1 g/L	10 mg/L	Sunlight 66.5 min	93%	[115]
I-doped TiO_2	Nanoparticles	Suspension	1 g/L	10 mg/L	Sunlight 66.5 min	100%	[115]

Table 2.3 Recent studies on TiO_2-based photocatalysts for BPA degradation (cont'd)

Photocatalyst	TiO_2 morphology	Photocatalytic system	Photocatalyst dosage	BPA concentration	Light and irradiation time	BPA degradation	Ref.
N-TiO_{2-x}-rGO/Fe_3O_4@cellulose	Nanoparticles	Floating	0.5 g/L	10 mg/L	Visible 60 min	~96%	[109]
Cu-N/TiO_2	Nanoparticles	Suspension	0.5 g/L	10 mg/L	Visible 120 min	~43%	[106]
N-doped C/TiO_2	Microsphere	Suspension	1 g/L	20 mg/L	UV 210 min	30%	[107]
Mn/Co-TiO_2	Nanoparticles	Suspension	3 g/L	10 mg/L	Simulated sunlight 120 min	~95%	[116]
C-doped TiO_2/C-doped α-Fe_2O_3	Nanorods	Suspension	0.5 g/L	10 mg/L	Simulated solar 270 min	79%	[117]
TiO_2@g-C_3N_4	Spherical	Suspension	0.4 g/L	20 mg/L	UV 90 min	71%	[118]
Cu_7S_4-TiO_2-Conjugated polymer	Nanosheets	Suspension	0.4 g/L	20 mg/L	Visible 45 min	100%	[119]
TiO_2/g-C_3N_4/rGO	Nanoparticles	Suspension	1 g/L	10 mg/L	Visible 180 min	~96%	[120]
TiO_2/graphene oxide	Nanoparticles	Suspension	0.75 g/L	50 mg/L	UV 60 min	~89%	[112]
TiO_2 P25/natural zeolite	Nanoparticles	Suspension	2 g/L	5 mg/L	Simulated solar 180 min	100%	[110]

CHAPTER 3 ARTICLE 1: TiO_2 NANOTUBES IMMOBILIZED ON POLYURETHANE FOAM AS A FLOATING PHOTOCATALYST FOR WATER TREATMENT

Nila Davari[1], Ermelinda Falletta[2,3], Claudia L. Bianchi[2,3], Viviane Yargeau[4], Daria C. Boffito[1,5*]

[1] Department of Chemical Engineering, Polytechnique Montréal, Montréal, Canada

[2] Department of Chemistry, University of Milan, Milan, Italy

[3] Consorzio Interuniversitario Nazionale per la Scienza e Tecnologia dei Materiali (INSTM), via Giusti 9, 50121, Florence, Italy

[4] Department of Chemical Engineering, McGill University, Montréal, Canada

[5] Canada Research Chair in Engineering Process Intensification and Catalysis

The article was published in Catalysis Today, Volume 436, 15 April 2024, 114725.

Author contributions

Nila Davari: Conceptualization, Data curation, Formal analysis, Investigation, Methodology, Validation, Visualization, Writing – original draft. Ermelinda Falletta: Data curation, Investigation, Methodology, Writing – review & editing. Claudia L. Bianchi: Data curation, Funding acquisition, Investigation, Methodology, Project administration, Writing – review & editing. Viviane Yargeau: Data curation, Investigation, Methodology, Project administration, Supervision, Writing – review & editing. Daria Camilla Boffito: Data curation, Funding acquisition, Investigation, Methodology, Project administration, Resources, Supervision, Writing – review & editing.

3.1 Abstract

We investigated the photocatalytic activity of TiO_2 nanoparticles (TiO_2-NPs) and TiO_2 nanotubes (TiO_2-NTs) supported on a floating polyurethane (PU) foam for removing Bisphenol A (BPA) as a model pollutant. We fabricated TiO_2-NPs by the sol-gel method and TiO_2-NTs by the ultrasound-assisted hydrothermal method. Subsequently, the photocatalysts were immobilized onto the PU foam through the wet chemical deposition process. The synthesized photocatalysts were characterized by contact angle, SEM-EDS, TEM, XRD, DRS, and BET analyses. TiO_2-NPs and TiO_2-NTs were successfully deposited onto the PU foam, creating floating photocatalysts denoted as TiO_2-NPs@PU and TiO_2-NTs@PU. Our findings indicated that the nanotubular structure of floating TiO_2 photocatalysts enhanced the removal efficiency of BPA relative to the nanoparticles, resulting in the complete removal of the pollutant over 180 min of simulated sunlight irradiation. TiO_2-NTs@PU was also stable after five reuse cycles. Moreover, h^+ was the main scavenging reactive species during the photocatalysis of BPA with TiO_2-NTs@PU.

Keywords: Photocatalyst, Floating TiO_2 nanoparticles, Floating TiO_2 nanotubes, PU Foam, Bisphenol A, Sunlight

3.2 Introduction

The application of TiO_2 semiconductors has been investigated in solar cells, fuel cells, Li-ion batteries, H_2 production, air purification, CO_2 conversion, NO_x gases conversion, heavy metals reduction, gas sensors, water splitting, and especially wastewater treatment with photocatalytic processes [121, 122]. Photocatalysis by TiO_2 that mimics natural photosynthesis employs TiO_2 semiconductors as photocatalysts for light-driven photocatalytic removal of hazardous organic pollutants from wastewater [123, 124].

TiO_2 photocatalysts have drawn attention due to their characteristics, including hydrophilicity, thermal and chemical stability, optical properties, corrosion resistance, and photocatalytic activity under light irradiation [125-128].

However, TiO_2 has limitations originating from the low electron transfer rate and light absorption, as well as the rapid recombination of photogenerated electron-hole pairs in the photocatalyst.

Furthermore, employing TiO_2 in the powder format is another obstacle, making TiO_2 recovery challenging after the photocatalytic process [7, 129].

To modify the photocatalytic activity of TiO_2, TiO_2 nanostructures can be engineered into nanotubes, which results in enhanced electron migration and reduced electron-hole recombination [90, 130, 131]. TiO_2 nanotubes (TiO_2-NTs) have a large surface area, higher light absorption, and oriented charge mobility in comparison to TiO_2 nanoparticles (TiO_2-NPs) [91, 97]. Several research has been reported on the synthesis of TiO_2-NTs photocatalysts, including the template-assisted method, sol-gel process, electrochemical anodization of titanium, and hydrothermal method [93, 94]. Among these methods, hydrothermal is a common approach to converting TiO_2 powder as a precursor to the 1D nanotubular structure (TiO_2-NTs) [94].

Floating TiO_2 photocatalysts can be considered a promising approach to tackle the recovery and reusability issues of suspended ones and prevent environmental toxicity from releasing nanoparticles to treated water. Compared with suspended systems, floating TiO_2 photocatalysts can benefit from more accessibility to the water-air interface, resulting in better solar light harnessing. This can boost the removal efficiency of contaminants from wastewater [109, 111, 132, 133].

Floating substrates, including perlite, vermiculite, glass microbead, cork, graphite, polymer, light-expanded clay aggregate, silicone, and autoclaved cellular concrete, have been employed in immobilized floating TiO_2-based photocatalysts for water purification [9]. Polyurethane (PU) foam is a macroporous polymer with a three-dimensional structure. The open-pore structure of the PU foam increases porosity and surface area, which improves the adsorption ability of pollutants. Therefore, the removal efficiency of aqueous contaminants can be enhanced [134, 135]. In addition, PU foam has low density (< 1000 kg/m^3), making it a suitable floating support [136]. According to the literature, Zhang et al. [135] synthesized well-ordered mesoporous TiO_2 photocatalysts onto floating PU foam. Based on the results, the heavy metal ions in the mixed solution were completely removed, and the removal efficiency of the dye was greater than 90% under sunlight irradiation after 2 h. Zhang et al. [137] described preparing ordered mesoporous SiO_2-TiO_2 photocatalysts based on a PU foam. Floating SiO_2-TiO_2/PUF photocatalyst was applied in a photocatalytic circulating-bed biofilm reactor where phenol and 2,4,5-trichlorophenol were completely removed under 3 h and 6 h of UV irradiation (365 nm, 8 W), respectively. Ni et al. [134] fabricated floating photocatalysts based on polyurethane foams with Ag/TiO_2/graphene

nanoparticles. The photocatalytic activity of floating PU-Ag/TiO_2/graphene was investigated for diesel degradation under visible light irradiation (500 W, Halogen tungsten lamp). The results reported 76% of diesel degradation during 16 h. In another study, Li et al. [111] synthesized a floating photocatalyst, which was TiO_2 P25 nanoparticles supported on a polyurethane foam to degrade BPA. The degradation efficiency with TiO_2 P25/PU was achieved at 71% after 120 min UV irradiation.

To the best of our knowledge, no study has been reported to remove pollutants from wastewater using mesoporous TiO_2-NTs photocatalysts immobilized on a macroporous PU foam as a floating macro/mesoporous photocatalyst carrier. Herein, we investigated for the first time the photocatalytic performance of the floating nanocomposite foam (TiO_2-NTs@PU) to eliminate Bisphenol A (BPA), a model organic pollutant in wastewater, when exposed to simulated solar irradiation. In addition, this work was the first to report the effect of the nanotubular structure of TiO_2 on the activity of floating TiO_2 photocatalysts in degrading BPA under simulated sunlight. Furthermore, the mechanism of BPA degradation with floating TiO_2-NTs@PU was examined by capturing free radical species.

3.3 Materials and Methods

3.3.1 Chemicals

We used Ti(IV)-butoxide ($C_{16}H_{36}O_4Ti$, reagent grade, 97%, Sigma Aldrich), Ethanol (C_2H_6O, 95%, Commercial Alcohols), Sodium hydroxide (NaOH, 98%, Thermo Scientific), Hydrochloric acid (HCl, 37% w/w, Fisher Scientific), Polyvinyl alcohol (low molecular weight, 98-99% hydrolyzed, Thermo Scientific Chemicals), Bisphenol A (≥99%, Sigma Aldrich), and DMPO (5,5-Dimethyl-1-pyrroline N-oxide, Sigma-Aldrich). Porous Polyurethane foam (Porosity: Medium, 20 PPI) was purchased from Amtra. We prepared all solutions with deionized water.

3.3.2 Fabrication of photocatalysts

3.3.2.1 TiO_2-NPs

We synthesized TiO_2-NPs by the sol-gel method [138]. First, we mixed $C_{16}H_{36}O_4Ti$ (25 mL) and ethanol (80 mL) for 4 h at 25 °C with a magnetic stirrer. After that, we kept the solution for aging

for 12 h at room temperature. The sample was then dried at 80 °C in an oven and calcined in a furnace at 400 °C for 2 h (heating rate of 5 °C/min under air atmosphere).

3.3.2.2 TiO_2-NTs

We synthesized TiO_2-NTs by the ultrasound-assisted hydrothermal method [139]. First, we added the previously synthesized TiO_2-NPs (1 g) to NaOH solution (10 M, 50 mL) under 30 min stirring at room temperature to make a suspension. To homogenize the suspension, the sample was then kept under ultrasonication (110 W, 30 min). Afterwards, the homogenized suspension was transferred into a Teflon-lined autoclave (100 mL), heated to 160 °C with a heating rate of 5 °C/min and maintained for 24 h in an oven. After cooling to room temperature, the as-obtained white precipitate was filtered and washed with deionized water and HCl solution (0.1 M). This process was repeated until the pH of the solution was nearly neutral. In the next step, the prepared sample underwent drying at 80 °C, and finally, the as-synthesized TiO_2-NTs were calcined at 400 °C for 2 h by a furnace (heating rate of 5 °C/min under air atmosphere).

3.3.2.3 Floating TiO_2-NPs@PU and TiO_2-NTs@PU

To prepare floating TiO_2-NPs@PU and TiO_2-NTs@PU, we coated TiO_2-NPs and TiO_2-NTs photocatalysts onto PU foam through the wet chemical deposition method. We applied porous PU foam (size: 4 cm x 1 cm, porosity: 85%) as a floating support for powder photocatalysts. To immobilize TiO_2-NPs and TiO_2-NTs onto the PU foam, we employed Polyvinyl alcohol (PVA) as a binder [140] with a weight percentage of 1 (i.e., 99 wt.% photocatalysts and 1 wt.% of PVA). First, PVA (1 wt.%) was dissolved in deionized water (30 mL) in a three-neck flask (100 mL). The solution was heated to 95 °C for 3 h using a hot plate stirrer. Next, TiO_2-NPs and TiO_2-NTs photocatalysts (0.5 g) were added to the three-neck flask, followed by heating at 95 °C for another 2 h. The obtained solution was then transferred into a beaker (50 mL) and cooled to 80 °C. Finally, the PU foam was immersed in the aqueous suspension containing the photocatalysts and PVA and then dried in an oven at 80 °C to obtain TiO_2-NPs@PU and TiO_2-NTs@PU.

3.3.3 Characterization

We studied the wettability properties of the photocatalysts, hydrophobicity and hydrophilicity, by a Contact Angle System (OCA25, DataPhysics Instruments). The morphology and elemental compositions of the photocatalysts were investigated by a Field-Emission Scanning Electron

Microscopy (FESEM, JSM-7600TFE, JEOL) equipped with Energy-Dispersive X-ray Spectroscopy (EDS). We utilized Transmission Electron Microscopy (TEM) and High-resolution Transmission Electron Microscopy (HR-TEM) to further investigate the morphology and structure of the photocatalysts (JEM-2100F, JEOL). The size of the synthesized photocatalysts was measured by Digimizer version 5.3.5 software. The crystalline phase of the photocatalysts was characterized by an X-ray Diffractometer (XRD, D8 advance, Bruker). The crystallite size of the photocatalysts was determined by the Scherrer Equation [141].

$$D = \frac{K\lambda}{\beta cos\theta} \tag{3.1}$$

In Equation 3.1, D is the crystallite size (nm), K is a constant (shape factor = 0.94), λ is the wavelength of the X-ray radiation source (Cu-Kα = 0.15406 nm), β is the full width at half maximum (FWHM) of the peak (in radian), and θ is half of the Bragg angle (in degrees).

The optical properties of the photocatalysts were examined by a Diffuse Reflectance UV-Visible Spectrophotometer (DRS, Evolution™ 220, Thermo Fisher Scientific). The bandgap energy of the photocatalysts (E_g) was calculated by plotting $[F(R) \times hv]^{0.5}$ vs. hv, where $F(R)$ is the Kubelka-Munk function obtained from Equation 3.2 and R is the reflectance [142, 143].

$$F(R) = \frac{(1-R)^2}{2R} \tag{3.2}$$

Nitrogen adsorption-desorption isotherms applying the Brunauer-Emmett-Teller method (BET) measured the specific surface area, total pore volume, and mean pore diameter of the photocatalysts by means of N_2 adsorption at 77 K (Autosorb-1 device, Quantachrome Instruments). For chemical compositions and valence states of the photocatalysts, X-ray photoelectron spectroscopy (XPS) analysis was performed by an X-ray photoelectron spectrometer microprobe (VG ESCALAB 250Xi, Thermo Scientific). Fourier Transform infrared (FTIR) spectra were performed using an FTIR Spectrometer (Thermo Scientific™, Nicolet™ iS™ 5).

3.3.4 Floating photocatalytic system

We evaluated the photocatalytic activity of floating TiO_2-NPs@PU and TiO_2-NTs@PU to remove BPA in a batch floating catalyst photoreactor under simulated sunlight irradiation. The experimental conditions for the removal of BPA were as follows: BPA concentration (10 mg/L), photocatalyst amount coated onto the floating PU foam (0.1 g), pH (natural, 5.7), and irradiation

time (180 min). The TiO_2-NPs@PU and TiO_2-NTs@PU photocatalysts were floated in BPA solution (200 mL). The light source was a 300 W commercial solar lamp (Ultra-Vitalux, Osram) with a wavelength of 360-800 nm and an intensity of 35 W/m^2, placed 20 cm above the reactor. Before being exposed to irradiation, each sample was kept in the dark for 60 min to reach absorption-desorption equilibrium. We repeated the photocatalytic experiments three times for 180 min of simulated sunlight irradiation. Every 30 min, the BPA concentration was monitored by a UV-Vis Spectrophotometer (Evolution™ 220, Thermo Fisher Scientific) at λ_{max} = 276 nm.

3.3.5 Scavenging reactive species experiments

We carried out scavenging experiments to investigate the main reactive species in removing BPA with floating TiO_2-NPs@PU and TiO_2-NTs@PU photocatalysts. We applied the following scavengers: Ammonium oxalate (AO) for photogenerated holes (h^+), Tert-butanol (t-BuOH) for hydroxyl radicals ($^{\bullet}OH$), Silver nitrate ($AgNO_3$) for electrons (e^-), and Benzoquinone (BZQ) for superoxide anions ($^{\bullet}O_2^-$). Scavenging experiments were conducted by adding 1 mM of each scavenger into the floating catalyst photoreactor under the same conditions for BPA photocatalysis experiments, as described in Section 3.3.4. In addition, we utilized an Electron Paramagnetic Resonance Spectrometer (EPR, Magnettech ESR5000, Bruker) with the DMPO technique to detect reactive species under simulated sunlight irradiation. Moreover, we identified intermediates during the photocatalytic degradation of BPA using High-performance Liquid Chromatography-mass Spectrometry (HPLC-MS). Samples were taken from the floating catalyst photoreactor before and after 180 min of the photocatalytic reaction.

3.4 Results and Discussion

3.4.1 Wettability properties of TiO_2-NPs@PU and TiO_2-NTs@PU

Figure 3.1 presents the dynamic water contact angle for pristine PU foam, TiO_2-NPs@PU, and TiO_2-NTs@PU. We examined the wettability properties of samples over 5 s ($t \geq 5$ s), with t = 0 s when the water droplet was initially formed and t = 1 s representing the time when the water droplet contacted the PU foam. As shown in Figure 3.1(a), the water droplet could not pass the non-coated PU foam and remained on the PU foam for over 5 s, indicating that the pristine PU foam was hydrophobic. Interestingly, introducing TiO_2-NPs on the PU foam enhanced the hydrophilicity, causing the water droplet to rapidly go through the photocatalyst and then vanish after 5 s (Figure

3.1(b)). Consequently, floating TiO_2-NPs@PU exhibited hydrophilicity. Similarly, immobilizing TiO_2-NTs into the PU foam significantly affected hydrophilic properties. TiO_2-NTs@PU also resulted in a hydrophilic floating photocatalyst, as presented in Figure 3.1(c). Our findings suggest that the deposition of TiO_2 photocatalysts onto the PU foam as a floating support induced changes in the PU foam's wettability characteristics owing to the inherent hydrophilic traits of TiO_2 [144], which has potential applications in water purification.

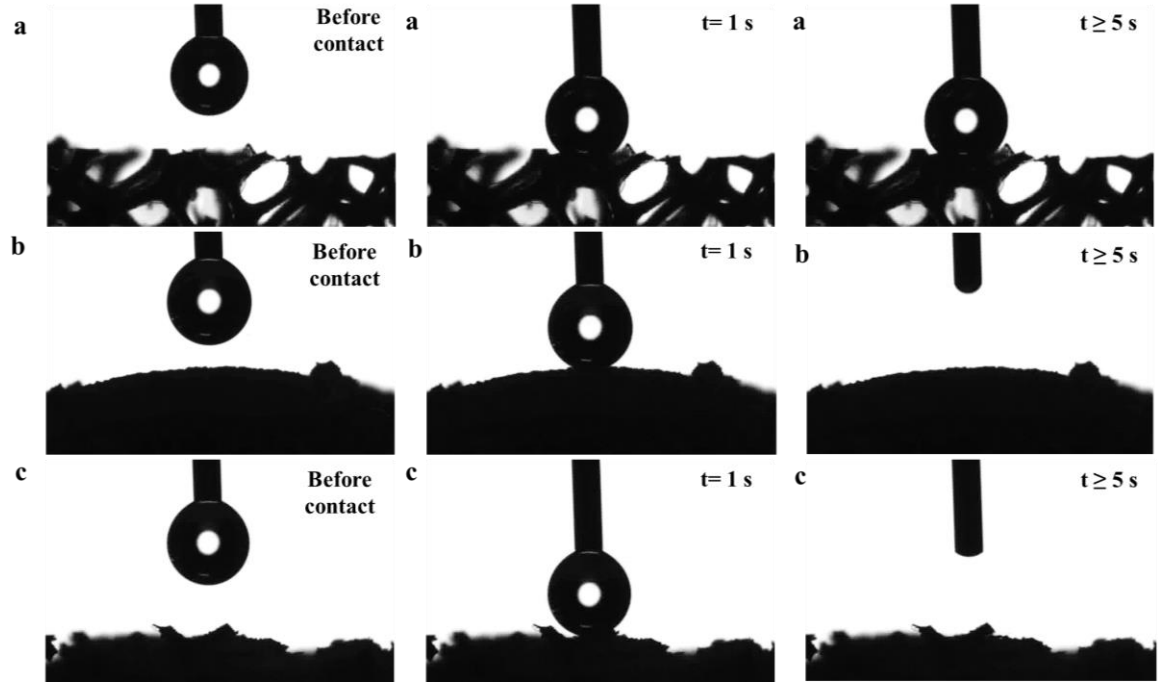

Figure 3.1 Dynamic water contact angle for (a) pristine PU foam, (b) TiO_2-NPs@PU, and (c) TiO_2-NTs@PU

3.4.2 Morphology and elemental compositions of TiO_2-NPs@PU and TiO_2-NTs@PU

EDS analysis detected the elements of Ti (61%) and O (39%) in TiO_2-NPs (Figure 3.2(a)). Figure 3.2(b) also indicates the presence and amount of Ti, O, and Na in TiO_2-NTs ranked in the order of 67.8%, 31.9%, and 0.3%. Moreover, the elements were uniformly dispersed in TiO_2-NPs and TiO_2-NTs, as shown in Figures 3.2(c) and 3.2(d).

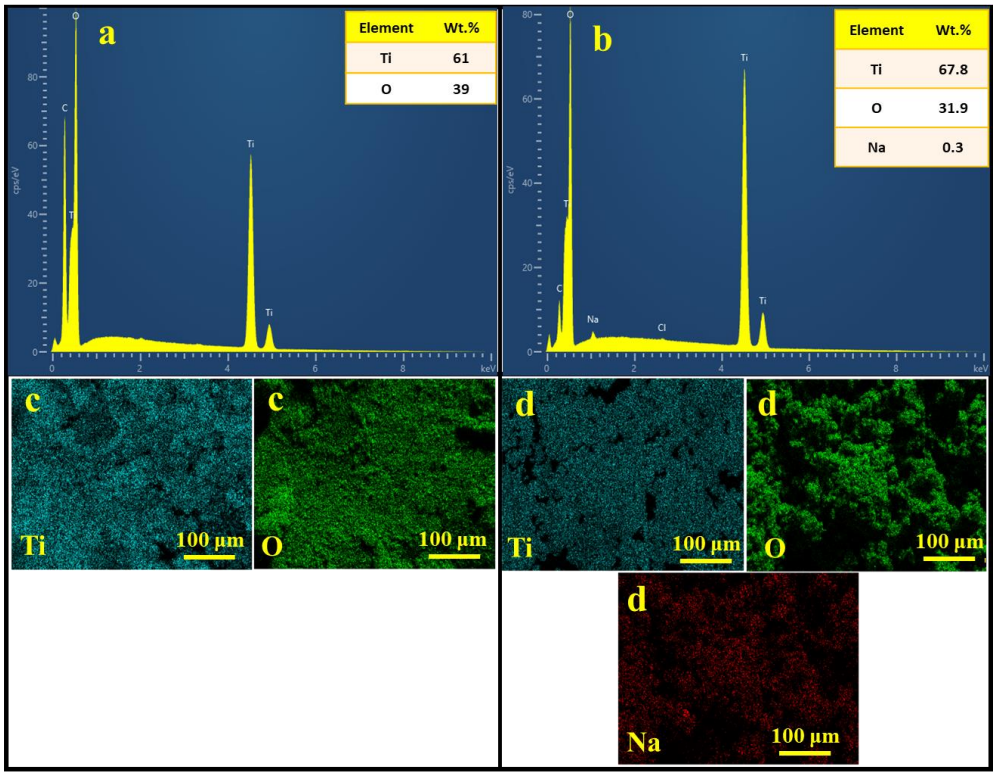

Figure 3.2 EDS spectra of (a) TiO_2-NPs and (b) TiO_2-NTs; EDS mappings of (c) TiO_2-NPs and (d) TiO_2-NTs

Figure 3.3(a) shows the SEM image of PU foam, indicating the smooth surface of the pristine PU foam before immobilizing TiO_2-NPs and TiO_2-NTs onto it. The SEM image of TiO_2-NPs@PU presents that TiO_2-NPs were uniformly coated into the PU foam (Figure 3.3(b)). As depicted in Figure 3.3(c), the shape of the TiO_2-NPs photocatalyst synthesized by the sol-gel method was spherical. Moreover, Figure 3.3(d) proves the successful deposition of TiO_2-NTs onto the PU foam (TiO_2-NTs@PU). Figure 3.3(e) shows the morphology of TiO_2-NTs, confirming that the hydrothermal synthesis method successfully fabricated the nanotubular structure of TiO_2.

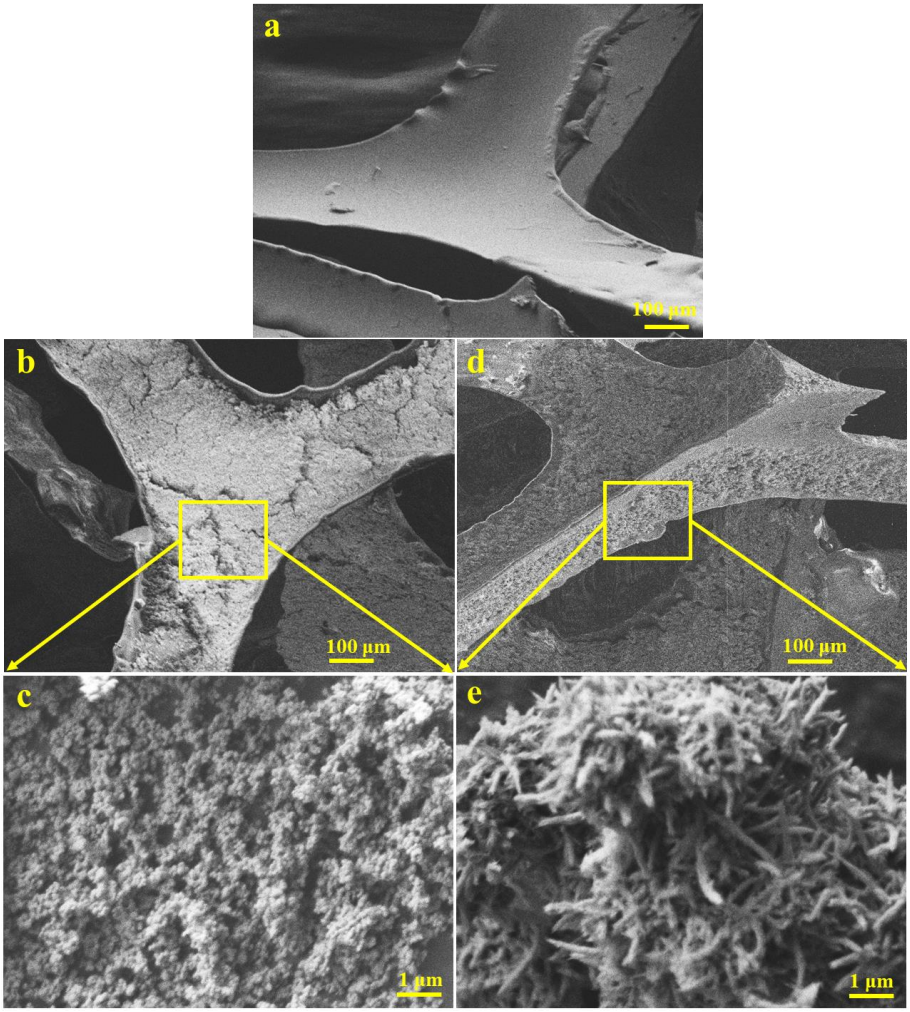

Figure 3.3 SEM images of (a) pristine PU foam, (b) TiO_2-NPs@PU, (c) TiO_2-NPs, (d) TiO_2-NTs@PU, and (e) TiO_2-NTs

Figure 3.4(a) shows the morphology of TiO_2-NPs analyzed by TEM. The TEM image indicates that the as-prepared TiO_2 photocatalyst was formed in approximately spherical nanoparticles, with an average diameter of about 32 nm measured using the Digimizer software. The internal crystalline structure of TiO_2-NPs was determined by the HR-TEM image, as depicted in Figure 3.4(c). The results confirmed the existence of TiO_2 anatase planes, namely (101), (004), and (200), corresponding to the d-spacing values of 0.349 nm, 0.237 nm, and 0.188 nm, respectively (Reference code: 01-071-1166). In addition, Figure 3.4(b) shows that TiO_2 photocatalysts had a hollow nanotubular structure, confirming the synthesis of TiO_2-NTs. By comparing Figure 3.4(b) with Figure 3.4(a), we observed that TiO_2-NPs were transformed into TiO_2-NTs through the hydrothermal synthesis method. The transformation of TiO_2-NPs to TiO_2-NTs was reported as a

sheet folding mechanism [145, 146]. In the primary stage, TiO_2-NPs are dissolved, and Ti-O-Ti bonds are broken by the concentrated alkaline solution, forming Ti-O-Na and Ti-OH. In the next stage, the replacement of Na^+ and H^+ ions results in the formation and growth of layered nanosheets of sodium titanates. In the last stage, the variation of surface charge caused by ion exchange of Na^+ with H^+ arising from HCl treatment causes nanosheet exfoliation and increases curling tendency, leading to the formation of nanotubes. [147]. According to the HR-TEM image of TiO_2-NTs (Figure 3.4(d), we measured the external diameter and internal diameter of the fabricated nanotubes, as well as the wall thickness as 7.5 nm, 5.2 nm, and 1.15 nm, respectively. Our results are consistent with previous work, including Yang et al. [148], Kubo and Nakahira [149], Hosseini and Vahabzadeh Pasikhani [139], Alkanad et al. [150], and Gilani et al. [151] who synthesized TiO_2-NTs in the same hydrothermal conditions, resulting in hollow tube-like nanostructures with an average diameter of in the range of 5 to 7 nm.

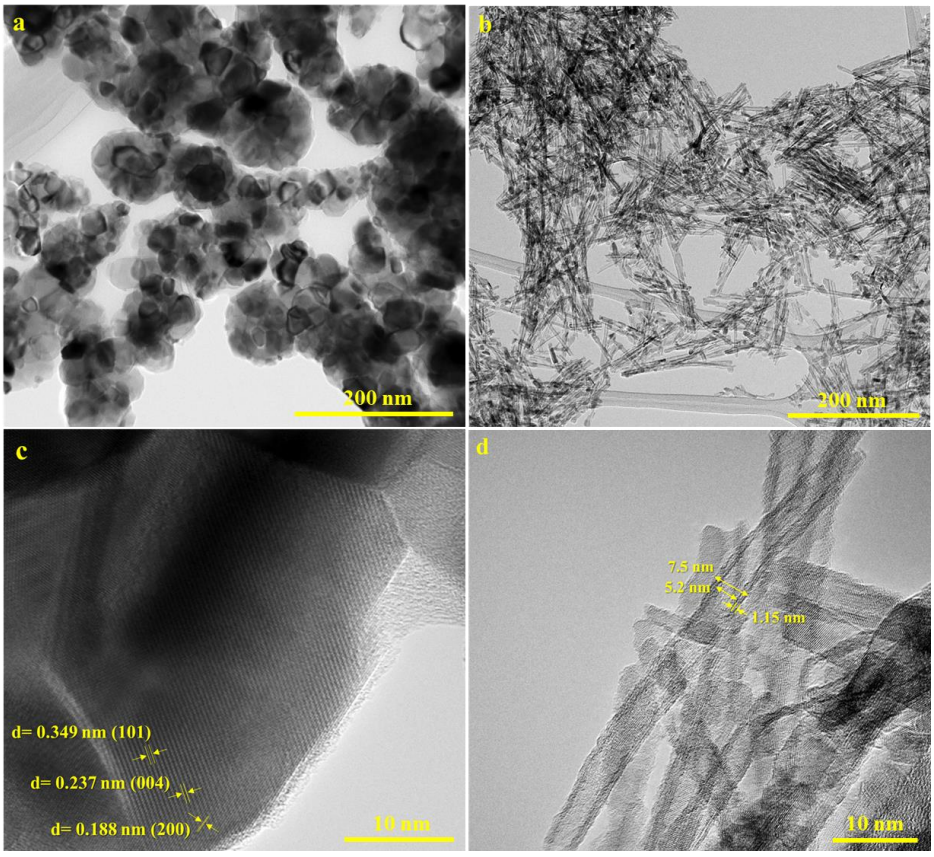

Figure 3.4 TEM images of (a) TiO_2-NPs and (b) TiO_2-NTs; HR-TEM images of (c) TiO_2-NPs and (d) TiO_2-NTs

3.4.3 Functional group detection of TiO_2-NPs@PU and TiO_2-NTs@PU

Figure 3.5 shows the FTIR spectra of PU foam, TiO_2-NPs, TiO_2-NTs, TiO_2-NPs@PU, and TiO_2-NTs@PU. In the FTIR spectrum of PU foam, the peaks at around 1526 cm^{-1} and 3320 cm^{-1} were related to the in-plane bending vibration of N-H and the symmetric and asymmetric stretching vibrations of N-H, respectively. Also, the peak at near 1222 cm^{-1} indicated asymmetric stretching vibration of C-O. The vibration of C=C was identified at about 1604 cm^{-1}, and the bending vibration of C-H was observed in the range of 767-917 cm^{-1}. The peak at about 1380 cm^{-1} originated from the symmetric bending vibration of CH_3, and the peak at approximately 1083 cm^{-1} showed bond C-O-C stretch. The stretching vibrations of C-H in methyl and methylene groups were observed at about 2979 cm^{-1}, 2929 cm^{-1}, and 2873 cm^{-1} [152, 153]. Regarding the FTIR spectra of TiO_2-NPs and TiO_2-NTs, the broad peaks at 700-800 cm^{-1} and 433-490 cm^{-1} corresponded to the asymmetric stretching, symmetric stretching, and the bending modes of Ti-O-Ti bonds [139]. In addition, the presence of peaks around 3420 cm^{-1} was attributed to O-H stretching of the hydroxyl group to Ti atoms (Ti-OH), and peaks observed at 1630 cm^{-1} were indexed to the stretching vibrations of H-O-H bond from water molecules adsorbed at the surface of photocatalysts [154]. As shown in Figure 3.5, the FTIR spectra of TiO_2-NPs@PU and TiO_2-NTs@PU were primarily composed of the peaks of TiO_2 photocatalysts and PU foam. In addition, a shift to the high wavenumber in the FTIR spectra of TiO_2-NPs@PU and TiO_2-NTs@PU was observed owing to the hydrogen bonds formed between TiO_2 photocatalysts and PU foam [155]. Furthermore, some peaks were observed at about 790-1000 cm^{-1} in the FTIR spectra of TiO_2-NPs@PU and TiO_2-NTs@PU, which can be attributed to the vibration of Ti-O-C [139, 156, 157].

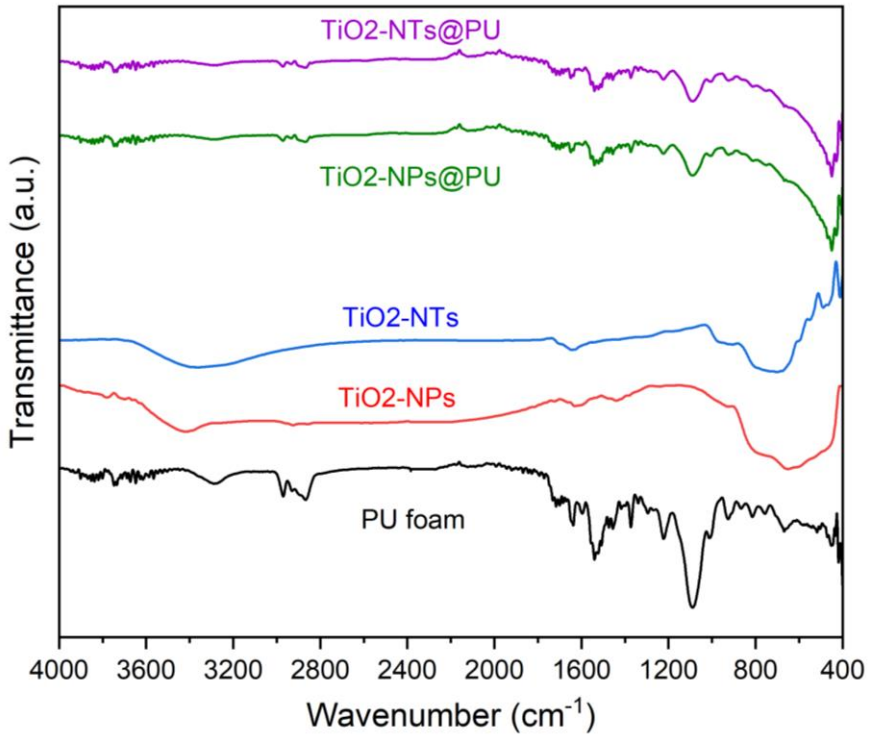

Figure 3.5 FTIR spectra of PU foam, TiO_2-NPs, TiO_2-NTs, TiO_2-NPs@PU, and TiO_2-NTs@PU

3.4.4 Chemical compositions and valence states of TiO_2-NTs and TiO_2-NTs@PU

Figure 3.6(a) shows the XPS analysis of TiO_2-NTs, indicating the presence of Ti and O elements in the fabricated photocatalyst. Based on the high-resolution spectrum of Ti 2p (Figure 3.6(b)), two evident peaks were observed at binding energies of 464.6 eV and 458.9 eV, which were related to Ti $2p_{1/2}$ and Ti $2p_{3/2}$ of Ti^{4+} in TiO_2, respectively [123]. In addition, Figure 3.6(c) shows a sharp peak at a binding energy of 530.4 eV associated with the formation of lattice oxygen (Ti-O) in TiO_2 [158]. No peak related to Na was observed in XPS, implying the negligible concentration of Na in TiO_2-NTs.

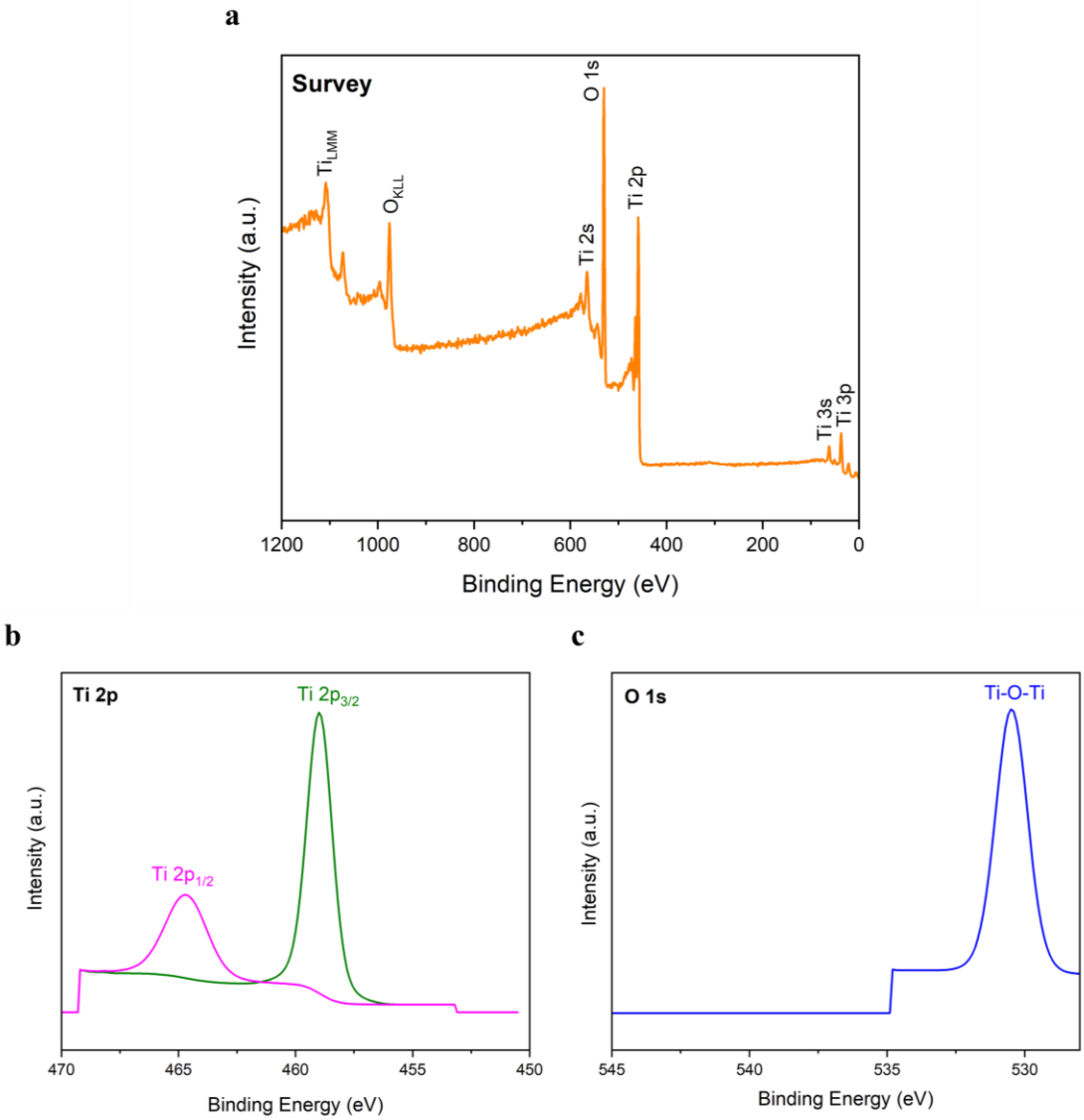

Figure 3.6 XPS analysis (a) Survey spectrum of TiO_2-NTs; Spectra of (b) Ti 2p and (c) O 1s

Figure 3.7 shows the XPS analysis of TiO_2-NTs@PU. In comparison with Figure 3.6, the peaks of O 1s (530.5 eV), C 1s (284.8 eV), and N 1s (399.9 eV) were detected as characteristic of PU foam [159, 160], as shown in Figure 3.7(a). Also, the same high-resolution spectrum was observed for Ti 2p (Figure 3.7(b)). Regarding the spectrum of O 1s (Figure 3.7(c)), the peak at a binding energy of 529.8 eV was related to Ti-O-Ti [159]. The peaks at 532.5 eV referred to C-O, and 533.6 eV related to O*-C=O [159, 161]. In addition, the peak observed at 531.8 eV confirmed the formation of Ti-O-C [159, 162-164]. Figure 3.7(d) shows the spectrum of N 1s, with a peak at 399.8 eV for the O=C-N group [165]. Figure 3.7(e) shows the high-resolution spectrum of C 1s. The peaks at 284.7 eV, 285.6 eV, 286.3 eV, 287.7 eV, and 289.3 eV were attributed to C-C, C-N, C-O, C=O,

and N-(C=O)-O, respectively [159, 162]. Moreover, there was a peak at 285.2 eV, referred to as Ti-O-C bonds [164].

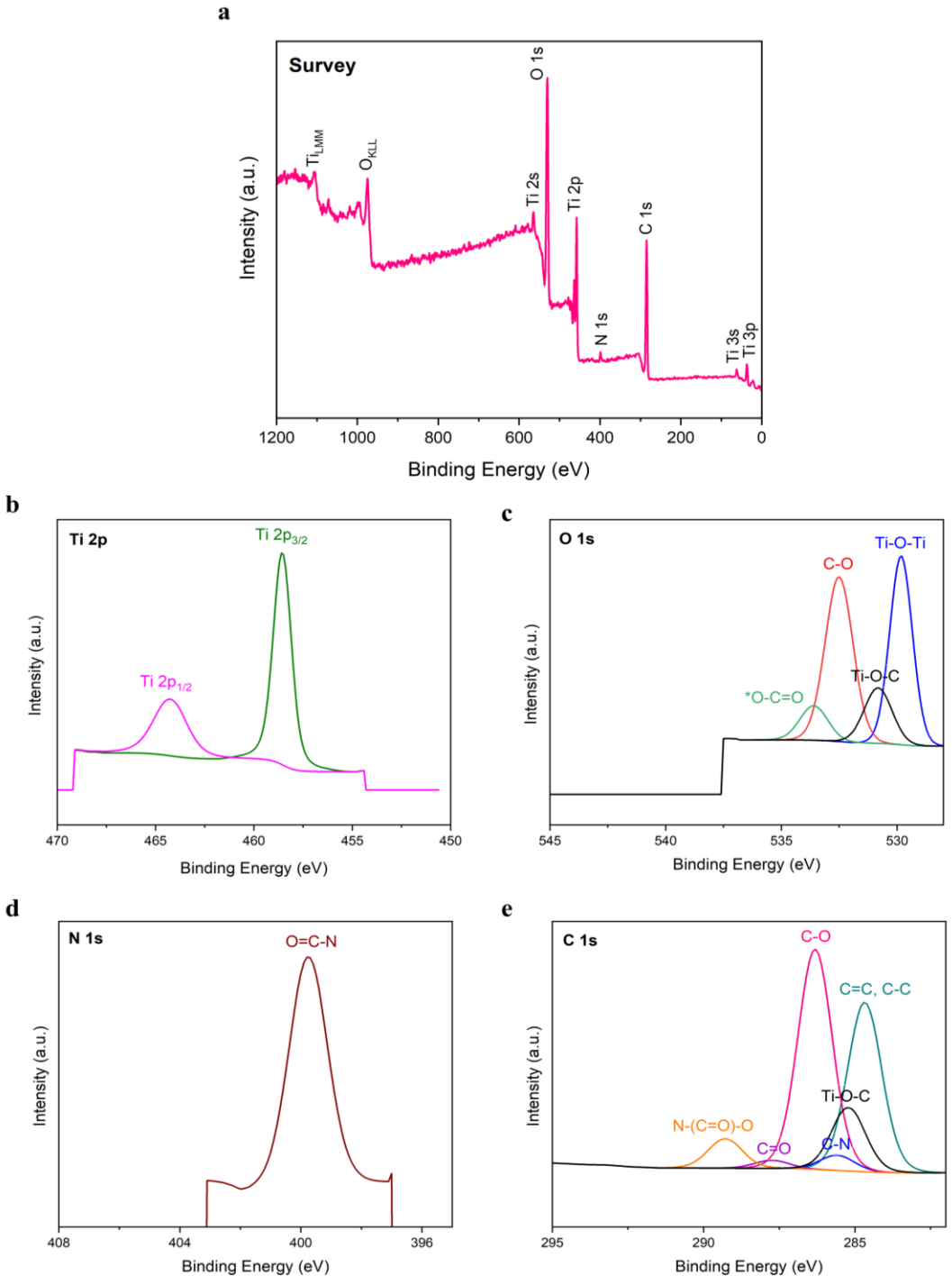

Figure 3.7 XPS analysis (a) Survey spectrum of TiO_2-NTs@PU; Spectra of (b) Ti 2p, (c) O 1s, (d) N 1s, and (e) C 1s

3.4.5 Crystalline phase of TiO_2-NPs and TiO_2-NTs

Figure 3.8 depicts the XRD pattern of TiO_2-NPs and TiO_2-NTs, indicating that TiO_2 photocatalysts exhibit a crystallized anatase structure. Figure 3.8(a) confirmed the anatase phase of TiO_2-NPs based on the peaks at 2θ values of 25.48°, 37.04°, 37.95°, 38.67°, 48.21°, 53.92°, 55.22°, 62.84°, and 68.88° assigned to Miller indexes of (101), (103), (004), (112), (200), (105), (211), (204), and (220), respectively (JCPDS card No. 21-1272) [123, 166]. Similarly, TiO_2-NTs showed the anatase phase, as confirmed by the peaks at 25.36°, 37.90°, 48.15°, 53.98°, 55.27°, and 62.86° ranked in the order of the Miller indexes of (101), (004), (200), (105), (211), (204), and (220), as shown in Figure 3.8(b). In addition, some peaks were observed in the XRD pattern of TiO_2-NTs at 2θ values of 15.1°, 28.6°, and 43.5°, corresponding to (001), (002), and (003) planes of TiO_2(B) phase (JCPDS No. 46-1237) [167, 168]. Moreover, the crystallite size of TiO_2-NPs was 30 nm, while it was 26 nm for TiO_2-NTs, obtained by the Scherrer Equation from the anatase peak of (101). The reduction in the crystallite size of TiO_2-NTs can be justified by the hydrothermal synthesis method, which avoids the growth of TiO_2 nanocrystals [169].

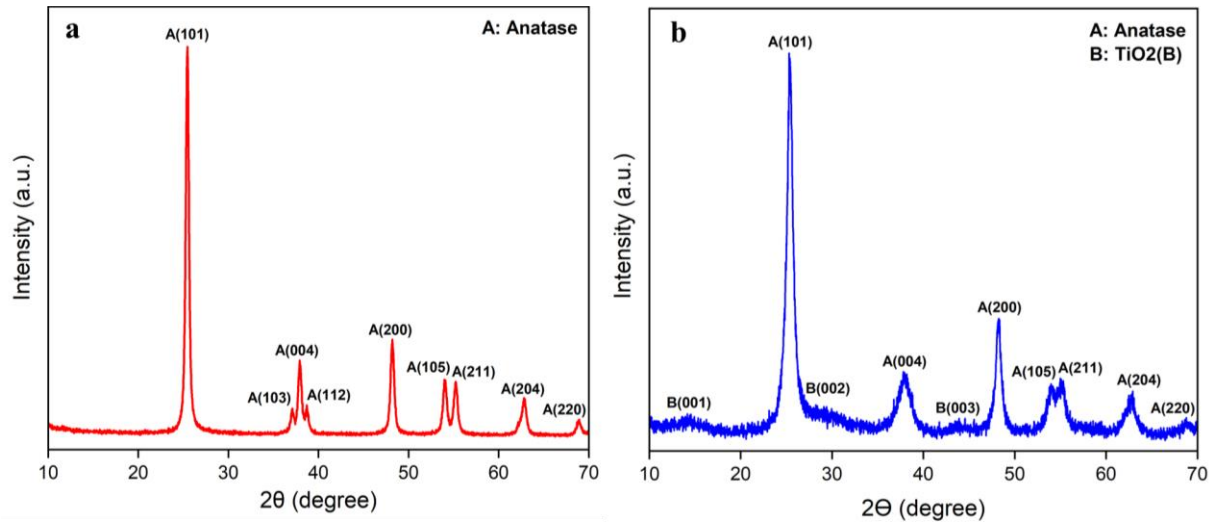

Figure 3.8 XRD patterns of (a) TiO_2-NPs and (b) TiO_2-NTs

3.4.6 Optical features of TiO_2-NPs and TiO_2-NTs

Figure 3.9 reports the DRS analyses of TiO_2-NPs and TiO_2-NTs. The absorption spectra of TiO_2 nanocrystals showed an intense absorption peak in the UV region, which can be related to the electron excitation from the conduction band of TiO_2 (2p orbitals of O^{2-}) to its valence band (3d orbitals of Ti^{4+}) [170, 171]. According to Figure 3.9(a), TiO_2-NPs had an absorption edge of about

400 nm, and the bandgap energy calculated by the Kubelka-Munk function was 3.1 eV, as shown in Figure 3.9(c). Moreover, a redshift was observed in the absorption spectrum of TiO_2-NTs in which the absorption edge was around 415 nm (Figure 3.9(b)), and the bandgap energy was calculated at 3 eV (Figure 3.9(d)). The reduced bandgap energy can result from the decreased crystallite size of TiO_2-NTs (26 nm) that leads to the redshift in the absorption spectrum (Figure 3.9(b)) and broadening of anatase peaks in the XRD pattern (Figure 3.8(b)) [169]. Besides the crystal size, synthesizing nanotubes with an average inner diameter of 5 nm can assist in decreasing the bandgap energy to 3 eV. The same results were observed in References [172, 173]. In addition, the synthesized TiO_2-NTs by alkaline hydrothermal methods led to the formation of anatase-TiO_2-B phases. Biphasic anatase-TiO_2-B phases also decreased the bandgap energy, which is reported by Peng et al. [174].

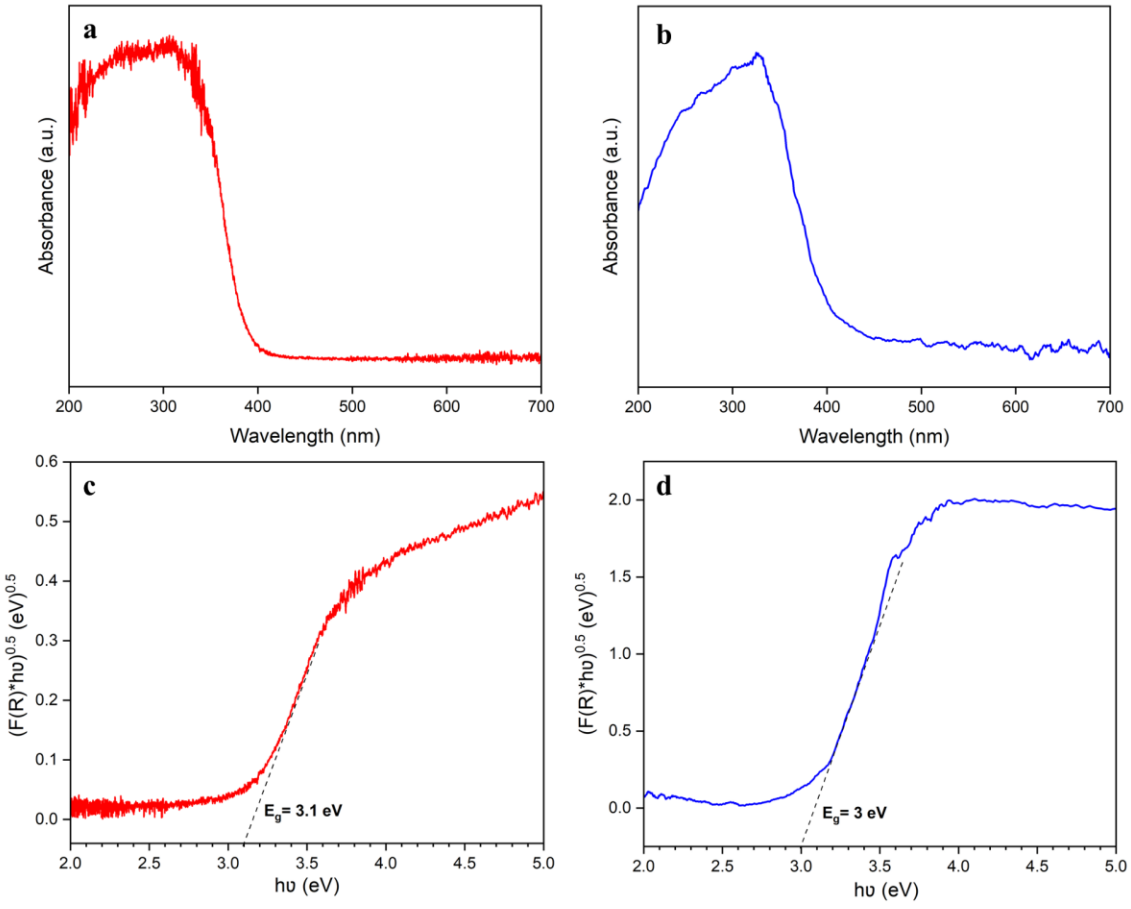

Figure 3.9 DRS analysis for the absorption spectra of (a) TiO_2-NPs and (b) TiO_2-NTs; Bandgap energies of (c) TiO_2-NPs and (d) TiO_2-NTs

3.4.7 Textural properties of TiO_2-NPs and TiO_2-NTs

Figures 3.10(a) and 3.10(b) show N_2 adsorption-desorption isotherms of TiO_2-NPs and TiO_2-NTs, respectively. Both TiO_2 photocatalysts presented type IV isotherms with H3 hysteresis loops based on the IUPAC classification [175]. The results indicated the slit-like mesoporous geometry of TiO_2-NPs (mean pore diameter of 37 nm) and TiO_2-NTs (mean pore diameter of 24 nm). The formation of the slit-like pore geometry by TiO_2 photocatalysts can be attributed to their aggregation, which is expected for mesoporous materials [139].

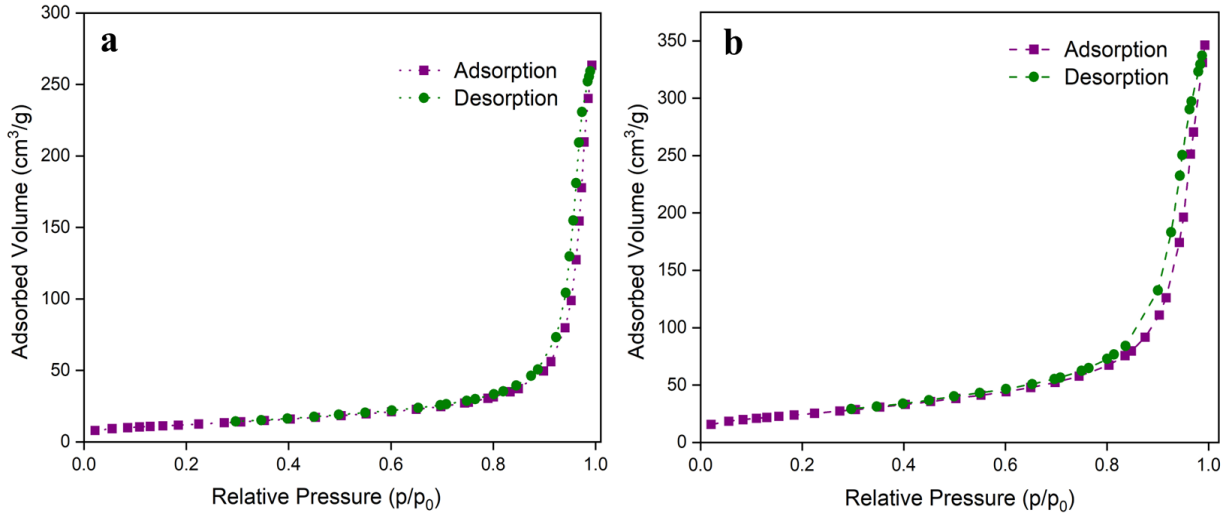

Figure 3.10 N_2 adsorption-desorption isotherms of (a) TiO_2-NPs and (b) TiO_2-NTs

Table 3.1 presents BET surface area, total pore volume, and mean pore diameter of TiO_2-NPs and TiO_2-NTs. The BET surface area of TiO_2-NTs (89 m^2/g) was around two times higher than that of TiO_2-NPs (43 m^2/g). Also, as shown in Table 3.1, TiO_2-NTs had a total pore volume of 0.6 cm^3/g, which was greater than that of TiO_2-NPs (0.5 cm^3/g). According to the results, TiO_2-NTs fabricated by the hydrothermal method had a larger surface area than TiO_2-NPs obtained from the sol-gel method. This can be related to mesoporous walls and tube openings of TiO_2-NTs [147]. Our results are consistent with previous work. There are many studies in the literature, such as work reported by Zaki et al. [176], Rashad et al. [177], and Gilani et al. [151], which applied 160 °C to prepare the anatase phase TiO_2 precursor in 10 mol/L NaOH and obtained a BET surface area in the 80-90 m^2/g range.

Table 3.1 BET results of TiO_2-NPs and TiO_2-NTs

Photocatalyst	BET Surface area (m^2/g)	Total pore volume (cm^3/g)	Mean pore diameter (nm)
TiO_2-NPs	43	0.5	37
TiO_2-NTs	89	0.6	24

3.4.8 Photocatalytic activity of TiO_2-NPs and TiO_2-NTs for BPA removal in suspended and floating systems

Figures 3.11(a) and 3.11(b) report the photocatalytic activity of TiO_2-NPs and TiO_2-NTs under simulated sunlight irradiation in suspended and floating systems, respectively. The error bars in the Figures indicate the standard deviation of replicate experiments (n = 3). For all Figures, the change in BPA concentration over the first 60 min in the dark was due to the adsorption-desorption equilibrium of BPA on the surface of photocatalysts. After the first 60 min, the light was turned on, and the change in BPA concentration correspond to the photocatalytic removal of BPA. As shown in Figure 3.11(a), the adsorption of BPA in the suspension system was negligible, and 4% and 6% of BPA were adsorbed on TiO_2-NPs and TiO_2-NTs, respectively. Under 180 min of simulated solar light irradiation, TiO_2-NTs had better activity than TiO_2-NPs and increased the removal of BPA from 51% to 100%. The improvement in photocatalytic activity is a consequence of engineering the optical and structural properties of TiO_2 by converting nanoparticles to 1D nanotubes [91]. As reported in Table 3.1, TiO_2-NTs had a surface area about two times greater than TiO_2-NPs (89 m^2/g), providing more active sites for the photocatalytic degradation of BPA. Following DRS results (Figures 3.9(b) and 3.9(d)), the bandgap energy of TiO_2-NTs decreased to 3 eV, indicating improved light harvesting in the visible region, thus increasing the photocatalytic activity. Moreover, the smaller crystallite size of TiO_2-NTs (26 nm) compared to TiO_2-NPs could accelerate electron migration, resulting in efficient electron-holes separation and improved BPA removal. The same trend was observed for the floating system, in which TiO_2-NTs@PU exhibited better activity than TiO_2-NPs@PU. As depicted in Figure 3.11(b), the BPA adsorption efficiencies over floating TiO_2-NTs@PU and TiO_2-NPs@PU were 12% and 10%, respectively. Also, the photocatalytic activity of TiO_2-NTs@PU was approximately two times higher than TiO_2-NPs@PU. BPA was completely removed by TiO_2-NTs@PU after 180 min of light irradiation, while TiO_2-

NPs@PU removed only 45% of BPA under the same conditions. The results indicated that the nanotubular TiO_2 photocatalysts boosted the photocatalytic efficiency of TiO_2 for BPA removal.

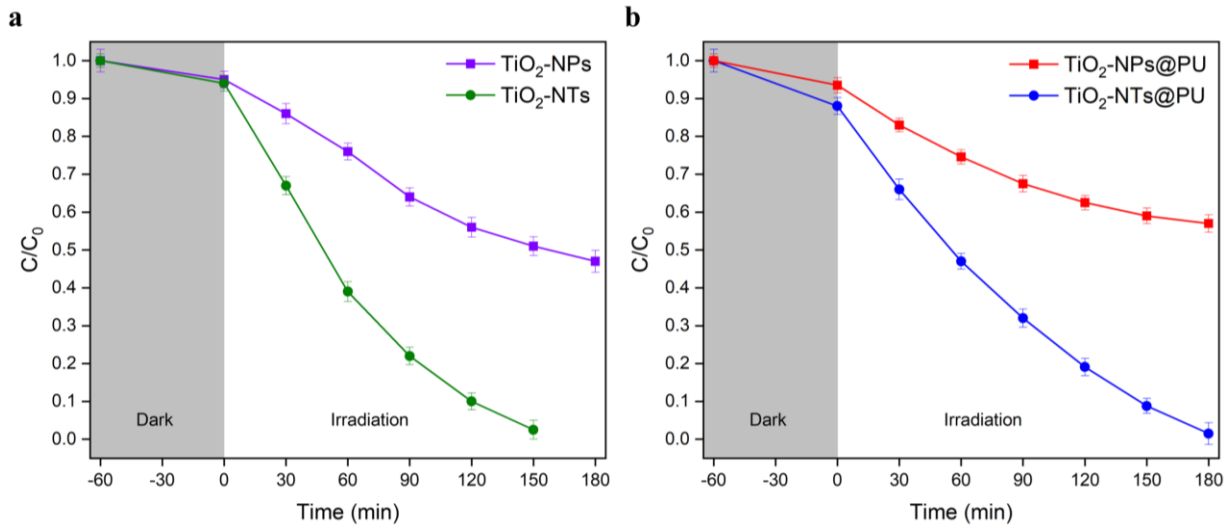

Figure 3.11 BPA removal with TiO_2-NPs and TiO_2-NTs under simulated sunlight irradiation for (a) suspended and (b) floating systems

The comparison between Figure 3.11(a) and Figure 3.11(b) shows that both TiO_2-NPs and TiO_2-NTs had 7% and 5% better photocatalytic activity in the suspension system than in the floating system due to the higher contact area in the suspended form [97]. Nevertheless, a floating photocatalyst is a promising system that can facilitate the recovery of photocatalysts after the process, resulting in lower operation costs and reduced runoff of materials into waters [132]. In addition, the synergistic effect of adsorption and photocatalytic degradation can contribute to the practical removal of BPA by a floating photocatalytic system. Recent studies have shown that a floating system can cause a temperature gradient at the air-water interface, which is called photothermal effect [104, 178, 179]. The photothermal effect increases oxygen absorption from the air and enhances photocatalytic reactions by increasing the concentration of reactive oxygen species in the submerged part in liquid. In addition, as shown in Figure 3.11(b), the photothermal effect can promote the diffusion and adsorption of BPA molecules on the floated photocatalysts' surface during the process [104].

We investigated the kinetics of BPA photocatalysis with TiO_2-NPs and TiO_2-NTs in suspended and floating systems. Equation 3.3 shows the kinetics study for BPA photocatalytic removal as follows [123, 170]:

$$r = -\frac{dC}{dt} = k_{app}C^n \quad (3.3)$$

Where k_{app} is the apparent rate constant, C is BPA concentration, t is irradiation time, and n is the photocatalytic reaction order.

For zero-order kinetics (n = 0), Equation 3.3 can be simplified to Equation 3.4.

$$C = -k_{app}t + C_0 \quad (3.4)$$

Moreover, Equations 3.5 and 3.6 present the first-order kinetics (n = 1) and the second-order kinetics (n = 2), respectively.

$$Ln\frac{C}{C_0} = -k_{app}t \quad (3.5)$$

$$\frac{1}{C} = k_{app}t + \frac{1}{C_0} \quad (3.6)$$

Where C_0 is the initial concentration of BPA.

Table 3.2 reports the correlation coefficients and apparent rate constants obtained based on kinetics models for BPA removal under simulated sunlight irradiation. According to Table 3.2, floating TiO_2-NPs@PU and TiO_2-NTs@PU photocatalysts followed the first-order kinetics ($R^2 \geq 0.98$). Also, the apparent rate constant (k_{app}) was 0.0032 min^{-1} for TiO_2-NPs@PU, and TiO_2-NTs@PU had a k_{app} of 0.016 min^{-1}. Regarding the suspended photocatalytic system, BPA photocatalysis with TiO_2-NPs and TiO_2-NTs was aligned with first-order kinetics with a k_{app} of 0.0045 min^{-1} and 0.0209 min^{-1}, respectively.

Table 3.2 Correlation coefficients and apparent rate constants for kinetics models of BPA removal

Sample	Kinetics model					
	Correlation coefficient (R^2)			Apparent rate constant (k_{app})		
	n = 0	n = 1	n = 2	n = 0	n = 1	n = 2
TiO_2-NPs@PU	0.98	0.99	0.97	0.0226	0.0032	0.0005
TiO_2-NTs@PU	0.96	0.98	0.70	0.047	0.016	0.0115
TiO_2-NPs	0.96	0.99	0.97	0.0307	0.0045	0.0006
TiO_2-NTs	0.95	0.97	0.62	0.0615	0.0209	0.0212

3.4.9 Reusability of TiO_2-NPs and TiO_2-NTs for BPA removal in suspended and floating systems

According to Figure 3.12(a), the photocatalytic activity of suspended TiO_2-NPs and TiO_2-NTs decreased from 51% to 32% and from 100% to 86% after five cycles, mainly due to the photocatalyst loss and poisoning of active sites with degraded products [63, 170]. As shown in Figure 3.12(b), the BPA removal by floating TiO_2-NTs@PU declined to 93% after five cycles, which can be due to the poisoning of active sites in the photocatalyst with degraded products [170]. Regarding floating TiO_2-NPs@PU, the photocatalyst maintained its activity after five recycling steps, with an 8% decrease in BPA removal efficiency. Floating photocatalysts can be reused several consecutive times without significant decrease in photocatalytic activity as opposed to the suspension system [133].

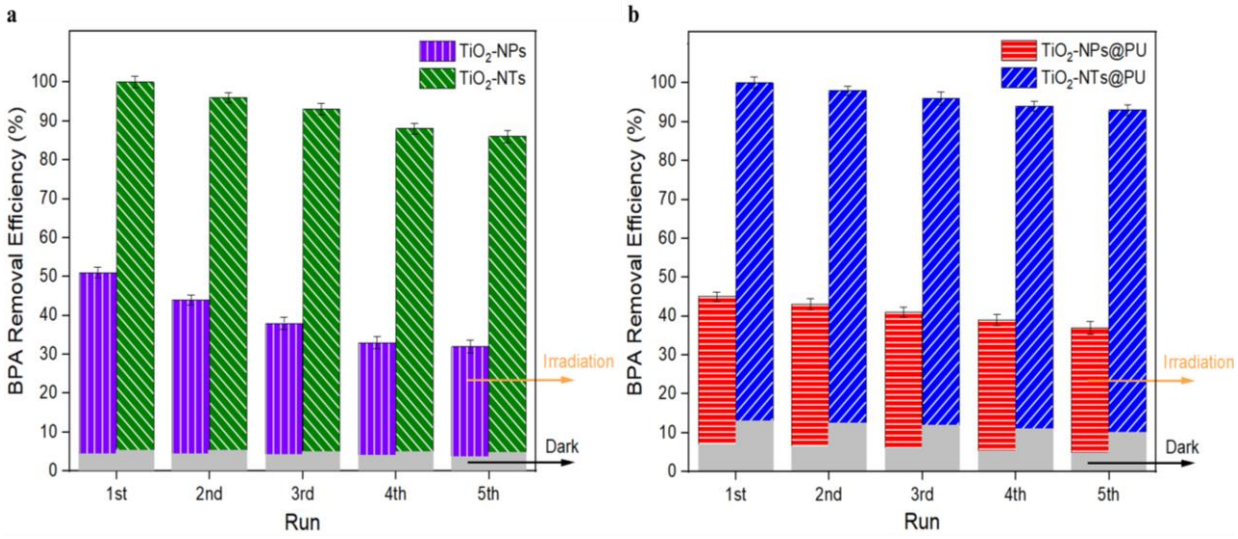

Figure 3.12 Reusability of TiO_2-NPs and TiO_2-NTs for BPA removal in (a) suspended and (b) floating systems

We investigated the structure and morphology of floating TiO_2-NPs@PU and TiO_2-NTs@PU photocatalysts after five reuse cycles. Figures 3.13(a) and 3.13(b) show no change in the XRD patterns of fresh and used photocatalysts. Thus, the results confirmed the structural stability of TiO_2-NPs@PU and TiO_2-NTs@PU after five cycles. In addition, Figures 3.13(c) and 3.13(d) show that the nanotubular structure of TiO_2-NTs did not change after five cycles, implying its chemical stability. Only a few particles appeared on the surface of TiO_2-NTs, which corresponds to the

poisoning of active sites with degraded products based on EDS results (i.e., the presence of C elements after the process), which can explain the decline in the photocatalytic activity.

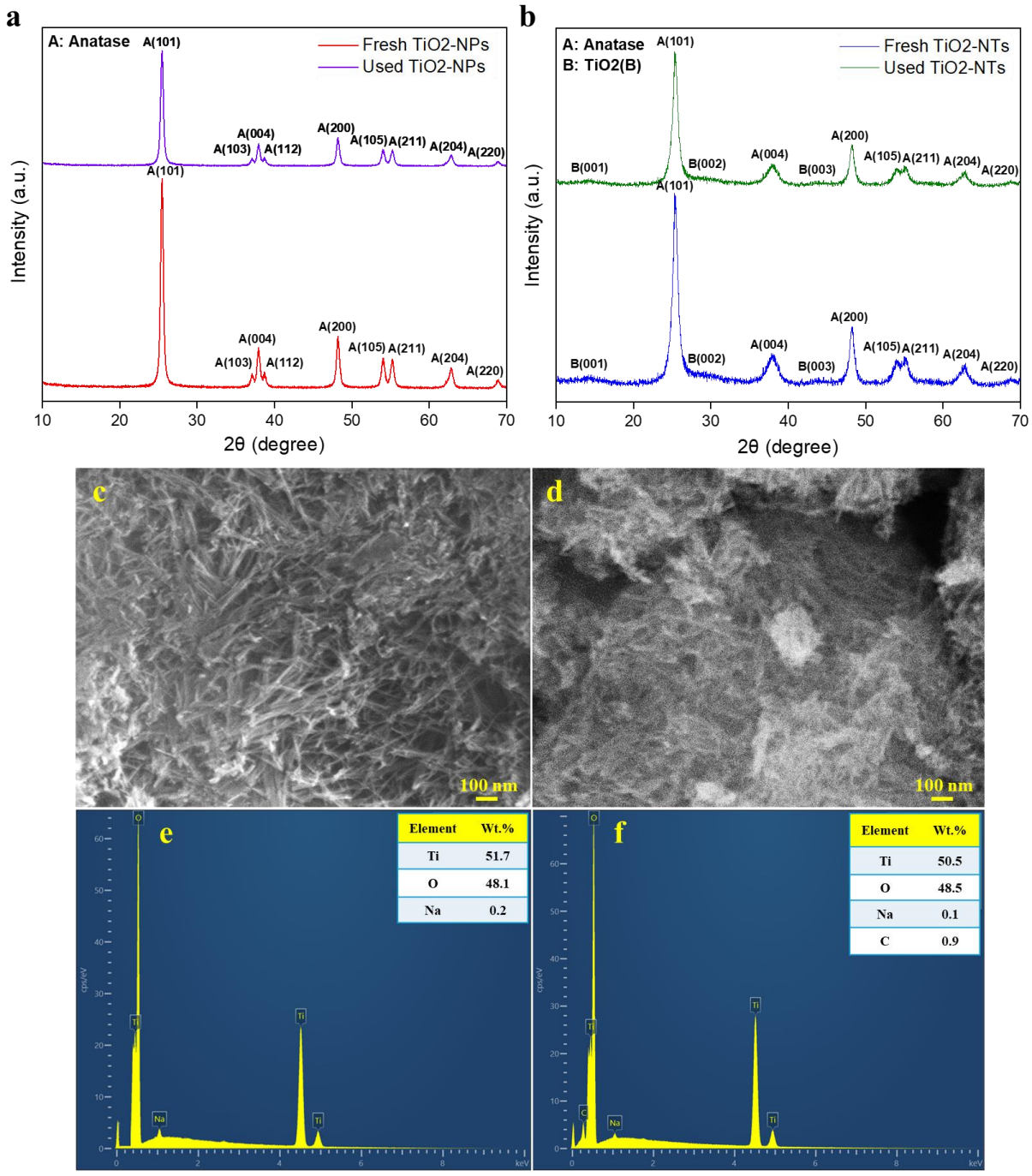

Figure 3.13 XRD patterns of (a) fresh and used TiO_2-NPs@PU and (b) fresh and used TiO_2-NTs@PU; SEM images of (c) fresh TiO_2-NTs@PU and (d) used TiO_2-NTs@PU after five cycles; EDS spectra of (e) fresh TiO_2-NTs@PU and (f) used TiO_2-NTs@PU after five cycles

3.4.10 Mechanism of BPA removal by floating TiO_2-NPs@PU and TiO_2-NTs@PU

Figure 3.14(a) shows the results of free radical scavenging of h^+, $^{\bullet}OH$, e^-, and $^{\bullet}O_2^-$ generated during BPA photocatalysis with TiO_2-NPs@PU and TiO_2-NTs@PU under simulated sunlight irradiation. Regarding TiO_2-NTs@PU, adding ammonium oxalate (AO) as h^+ scavengers to the floating photocatalytic system significantly decreased BPA removal from 100% to 35%. This indicates that h^+ was the main reactive species in the BPA photocatalysis compared to other scavengers. Besides, we determined the contribution of each reactive species (h^+, $^{\bullet}OH$, e^-, and $^{\bullet}O_2^-$) affecting BPA removal over TiO_2-NTs@PU and TiO_2-NPs@PU, as it is shown in Figures 3.14(b) and 3.14(c), respectively. According to Figure 3.14(b), the contribution of h^+ (direct) in the photocatalytic removal of BPA with TiO_2-NTs@PU was 42%. Also, $^{\bullet}OH$, e^-, and $^{\bullet}O_2^-$ were the other reactive species, which accounted for 20%, 28%, and 10% of the BPA removal, respectively. Moreover, Figure 3.14(c) presents the same trend for TiO_2-NPs@PU in the photocatalytic removal of BPA. As it is shown in Figure 3.14(c), the dominant free radical scavenging in BPA photocatalysis with TiO_2-NPs@PU was h^+ (direct), with a contribution of 40%. In addition, $^{\bullet}OH$, e^-, and $^{\bullet}O_2^-$ had a 20%, 30%, and 10% contribution to the BPA removal, respectively.

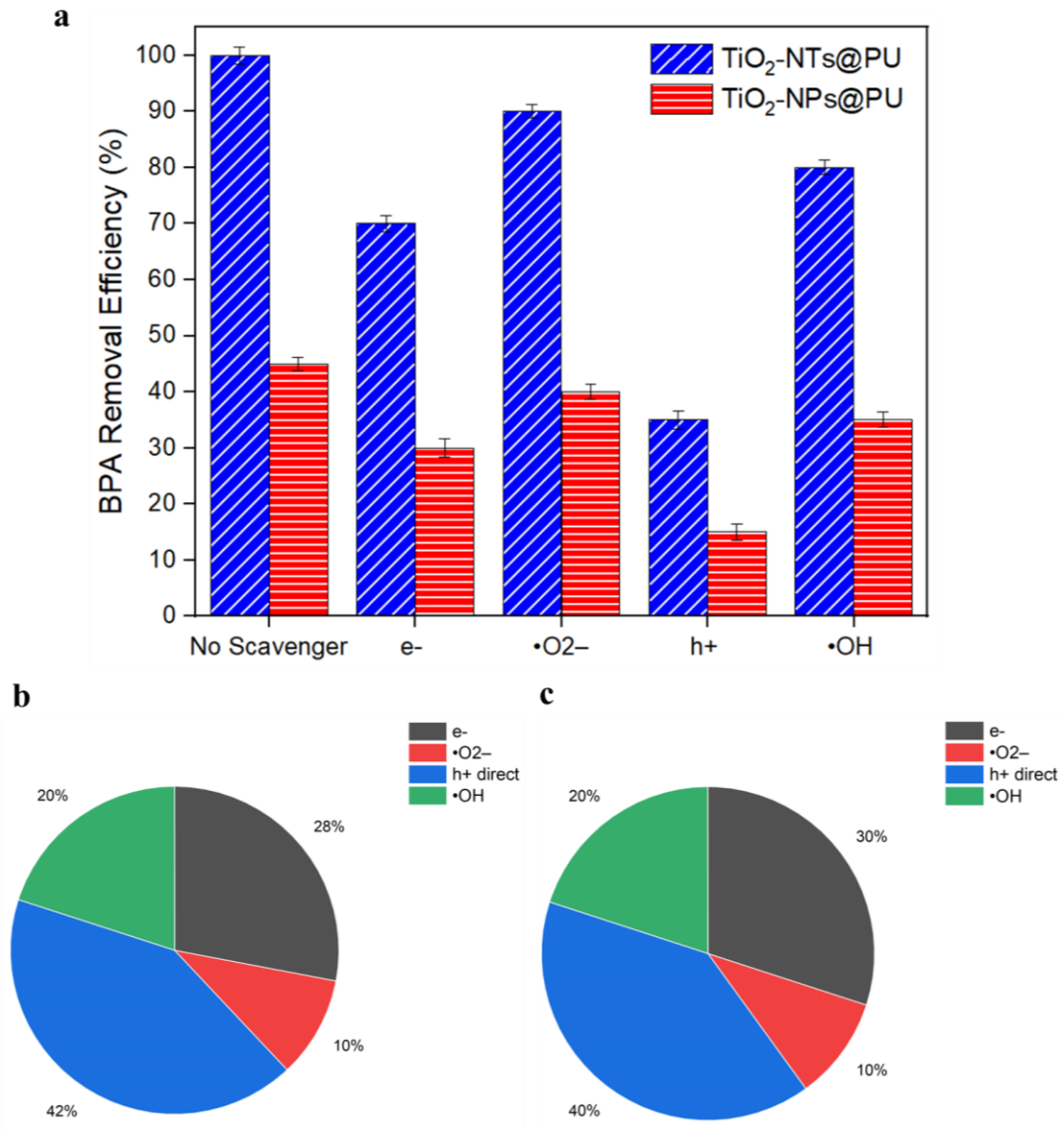

Figure 3.14 (a) Free radical scavenging experiments of TiO_2-NPs@PU and TiO_2-NTs@PU for BPA removal; Reactive species contribution on BPA removal with (b) TiO_2-NTs@PU and (c) TiO_2-NPs@PU

Further, Figure 3.15 shows that signals detected in the ESR, confirming the generation of $^{\bullet}OH$ and $^{\bullet}O_2^-$ [180] during the removal of BPA with floating TiO_2-NTs@PU under simulated sunlight irradiation.

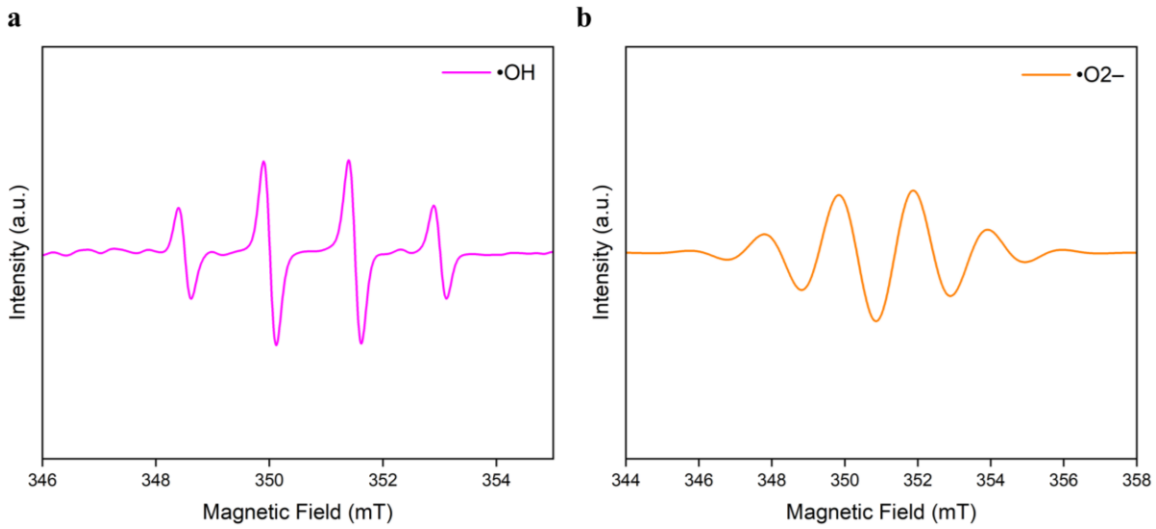

Figure 3.15 ESR spectra of (a) $^{\bullet}OH$ and (b) $^{\bullet}O_2^-$ generated during BPA removal with floating TiO_2-NTs@PU under simulated sunlight irradiation

Table 3.3 shows intermediates generated during the photodegradation of BPA with floating TiO_2-NTs@PU via HPLC-MS analysis. According to the detected intermediates, BPA photocatalytic degradation occurred based on oxidation and β-scission reactions [181]. The detected intermediate $C_{15}H_{16}O_4$ (m/z = 261) was a result of BPA oxidation [181]. The formation of $C_9H_{10}O$ (m/z = 135) and $C_6H_4O_2$ (m/z = 107) arose from the β-scission of BPA [182]. Further progress of the reaction can lead to the mineralization of these intermediates, producing CO_2 and H_2O [181, 182]. These results confirm that TiO_2-NTs@PU was able to degrade BPA under simulated sunlight irradiation.

Table 3.3 Identified intermediates from BPA degradation with TiO_2-NTs@PU

Compound	m/z	Molecular weight
$C_{15}H_{16}O_4$	$[M+H]^+$ 261	260
$C_6H_4O_2$	$[M-H]^-$ 107	108
$C_9H_{10}O$	$[M+H]^+$ 135	134

3.4.11 Comparison of floating TiO_2-NTs@PU with previous work

Table 3.4 shows the recent literature review on the photocatalytic removal of BPA. Only two works have been reported to remove BPA using floating photocatalytic systems. Li et al. [111] fabricated

floating photocatalysts based on a polyurethane foam with P25 nanoparticles, the commercial TiO_2 benchmark, to remove BPA. The removal of BPA was 71% after 120 min of UV irradiation based on a first-order kinetics. In another study [109], about 27% of BPA was removed by floating TiO_{2-x}@cellulose under visible light after 60 min irradiation. The literature seems to lack kinetic studies on BPA removal with floating TiO_{2-x}@cellulose. Further, the contribution of reactive species in the photocatalytic removal of BPA has not been investigated [109, 111]. Krishnan et al. [106] synthesized TiO_2 nanoparticles for BPA removal in suspended system, resulting in about 20% degradation under visible light (120 min). Also, the synthesized TiO_2 nanotubes by Doong and Tsai [108] reached 42% of BPA removal under UV irradiation for 80 min. In this work, for the first time, we investigated the effect of the TiO_2 nanotubular structure on the activity of floating photocatalytic systems for BPA removal under simulated sunlight. In addition, we compared the photocatalytic activity of floating systems with that of suspended ones. The BPA removal efficiency was 45% for floating TiO_2-NPs@PU, while it was 100% for floating TiO_2-NTs@PU after 180 min of simulated sunlight irradiation. Moreover, we examined the mechanism of BPA degradation with floating photocatalysts by determining reactive species contribution, which other researchers have not reported. Finally, floating TiO_2-NTs@PU photocatalysts constitute a promising approach to removing contaminants from water.

Table 3.4 Recent literature review on photocatalytic removal of BPA

Photocatalyst	Pollutant	Photocatalytic system	Light and irradiation time	Removal (%)	Kinetics	Reactive species contribution	Ref.
TiO_2 P25/PU (1 g per 500 mL)	BPA (20 mg/L)	Floating	UV (120 min)	71%	First order k_{app} = 0.0106 min^{-1}	h^+ : NA $^{\bullet}OH$: NA e^- : NA $^{\bullet}O_2^-$: NA	[111]
TiO_{2-x}@cellulose (0.5 g/L)	BPA (10 mg/L)	Floating	Visible (60 min)	~27%	NA	h^+ : NA $^{\bullet}OH$: NA e^- : NA $^{\bullet}O_2^-$: NA	[109]
TiO_2 nanoparticles (0.5 g/L)	BPA (10 mg/L)	Suspension	Visible light (120 min)	~20%	NA	h^+ : NA $^{\bullet}OH$: NA e^- : NA $^{\bullet}O_2^-$: NA	[106]
TiO_2 nanotubes (1 g/L)	BPA (10 mg/L)	Suspension	UV (80 min)	42%	Pseudo first order k_{app} = 0.0074 min^{-1}	h^+ : NA $^{\bullet}OH$: NA e^- : NA $^{\bullet}O_2^-$: NA	[108]
TiO_2-NPs@PU (0.1 g per 200 mL)	BPA (10 mg/L)	Floating	Simulated sunlight (180 min)	45%	First order k_{app} = 0.0032 min^{-1}	h^+ : 40% $^{\bullet}OH$: 20% e^- : 30% $^{\bullet}O_2^-$: 10%	Present work
TiO_2-NTs@PU (0.1 g per 200 mL)	BPA (10 mg/L)	Floating	Simulated sunlight (180 min)	100%	First order k_{app} = 0.016 min^{-1}	h^+ : 42% $^{\bullet}OH$: 20% e^- : 28% $^{\bullet}O_2^-$: 10%	Present work

3.5 Conclusions

We synthesized floating photocatalysts TiO_2-NPs@PU by the sol-gel method and TiO_2-NTs@PU by the ultrasound-assisted hydrothermal method, followed by wet chemical deposition. The results confirmed the successful anchoring of TiO_2-NPs and TiO_2-NTs onto the porous PU foam, resulting in hydrophilic floating photocatalysts. Morphological characterizations indicated that the hydrothermal synthesis method successfully fabricated the nanotubular TiO_2 photocatalysts. The synthesized photocatalysts were crystalline anatase TiO_2 with a crystallite size of 26 nm for TiO_2-NTs. DRS results showed a reduced bandgap energy of 3 eV for TiO_2-NTs. The nanotubular structure of TiO_2 photocatalysts prepared by the hydrothermal method increased the surface area to 89.6 m^2/g. According to the results, 0.1 g of TiO_2-NTs@PU eliminated 10 mg/L of BPA after 180 min of exposure to simulated sunlight (300 W commercial solar lamp and intensity of 35 W/m^2), while the photocatalytic removal of BPA was 45% with TiO_2-NPs@PU. The fabricated photocatalysts remained stable after five consecutive cycles. In addition, the dominant free radical scavenging during BPA photocatalysis was identified as h^+.

3.6 Acknowledgments

The authors thank Velux Stiftung Foundation for the financial support through the project 1381 “SUNFLOAT - Water decontamination by sunlight-driven floating photocatalytic systems”. We also appreciate the support of Bourse d’excellence Neil R. Mitchell et Danièle Dumais.

CHAPTER 4 ARTICLE 2: PHOTOCATALYTIC REMOVAL OF CONTAMINANTS OF EMERGING CONCERNS BY DOUBLE-WALLED TiO_2 NANOTUBES SUPPORTED ON FLOATING POLYURETHANE FOAM

Nila Davari[1], Ermelinda Falletta[2,3], Claudia L. Bianchi[2,3], Viviane Yargeau[4], Daria C. Boffito[1,5*]

[1] Department of Chemical Engineering, Polytechnique Montréal, Montréal, Canada

[2] Department of Chemistry, University of Milan, via C. Golgi 19, 20133, Milan, Italy

[3] Consorzio Interuniversitario Nazionale per la Scienza e Tecnologia dei Materiali (INSTM), via Giusti 9, 50121, Florence, Italy

[4] Department of Chemical Engineering, McGill University, Montréal, Canada

[5] Canada Research Chair in Engineering Process Intensification and Catalysis

The article was submitted to Discover Nano, 2 March 2026.

Author contributions

Nila Davari: Conceptualization, Investigation, Methodology, Validation, Visualization, Writing – original draft. Ermelinda Falletta: Methodology, Writing – review & editing. Claudia L. Bianchi: Funding acquisition, Methodology, Project administration, Writing – review & editing. Viviane Yargeau: Methodology, Project administration, Resources, Supervision, Writing – review & editing. Daria Camilla Boffito: Funding acquisition, Methodology, Project administration, Resources, Supervision, Writing – review & editing.

4.1 Abstract

We fabricated TiO_2 nanotubes (TNTs) by ultrasound-assisted hydrothermal synthesis and deposited the photocatalyst onto floating polyurethane foam (PUF) through wet chemical deposition. The synthesis method yielded TiO_2 double-walled nanotubes with a surface area of 110 m^2/g and a bandgap energy of 3.0 eV. The synthesized photocatalyst exhibited a biphasic anatase/TiO_2(B) structure with a crystallite size of 26 nm and a photocurrent density of 0.2 mA/cm^2. The photocatalytic activity of floating TNTs@PUF was evaluated for the removal of contaminants of emerging concern (CECs) under simulated sunlight irradiation. When individual contaminants were treated, removal efficiencies were 98% (bisphenol A), 98% (methyl orange), 85% (methylene blue), 98% (bentazon), 98% (isoproturon), 98% (sulfamethoxazole), and 97% (carbamazepine) after 4 h of irradiation. The presence of natural organic matter and inorganic anions in the BPA solution was also examined. Water matrix components had inhibitory effects on the photocatalytic activity of floating TNTs@PUF, decreasing BPA removal to 80%, 86%, and 30% for humic acid, citric acid, and oxalic acid, respectively. Similarly, inorganic anions reduced BPA removal to 80% with bicarbonate, 86% with chloride, and 90% with sulfate. In a mixture of CECs, the removal of BPA was 80%.

Keywords: Floating Photocatalysis, Bisphenol A, Contaminants of Emerging Concern (CECs), Matrix Effects, CECs Mixture

4.2 Introduction

Contaminants of emerging concern (CECs) in aquatic environments, such as endocrine-disrupting chemicals (EDCs), pharmaceuticals, pesticides, and dyes [183-185], are of increasing concern due to their persistence, bioaccumulation, and potential harmful effects, such as toxicity, carcinogenicity, and mutagenicity [183, 185, 186]. These pollutants enter water bodies through industrial wastewater, agricultural runoffs, and municipal sewage, and they are resistant to conventional treatment processes [42, 185, 186]. Thus, developing an efficient wastewater treatment method is crucial for successfully removing these contaminants and protecting environmental and public health.

Among current wastewater treatment methods, photocatalysis has emerged as a promising and environmentally friendly approach to eliminate CECs [37, 107]. Photocatalysis offers a chemical-free and energy-efficient alternative that operates effectively under moderate pressure and temperature conditions [72, 187]. In the photocatalytic process, exposure of a photocatalyst to a suitable light source induces the generation of electron-hole pairs. These pairs can directly degrade organic pollutants or facilitate their removal by generating reactive oxygen species (ROS) in aqueous environments [47, 139, 188-190].

In our recent studies [191, 192], we fabricated and tested a floating one-dimensional (1D) TiO_2 photocatalyst, i.e., TiO_2 nanotubes (TNTs) supported on a polyurethane foam (PUF), for the degradation of bisphenol A (BPA) under simulated sunlight irradiation. By engineering n-type semiconductor nanostructures in advanced materials without the incorporation of metallic or non-metallic dopants, floating TNTs@PUF exhibited high photocatalytic activity for BPA degradation, achieving over 96% removal after 180 min. This novel floating photocatalyst forms an air-solid-water triphase interface, enabling direct light exposure without water attenuation and thereby improving photon absorption and charge carrier generation. In addition, enhanced oxygen transfer from the air through the air-solid-water triphase interface in the floating photocatalyst facilitates ROS generation, further increasing photocatalytic efficiency. Despite these promising results, our floating photocatalytic system was limited to addressing only a single pollutant, BPA. Additionally, the efficiency of this system in removing BPA from a mixture of pollutants or in targeting other contaminants was not investigated. Moreover, the photocatalytic activity of floating TNTs@PUF in the presence of different natural organic matter and inorganic anions remained unexamined.

Natural organic matter and inorganic anions commonly found in aquatic environments have either promoting or inhibitory effects on the photocatalytic degradation of organic contaminants [20, 120, 193-195]. The presence of water matrix components can lead to the generation of secondary reactive species during photocatalytic degradation, which contributes to oxidation reactions and thereby improves photocatalytic activity. On the other hand, these components can scavenge reactive species involved in the photocatalytic degradation or compete for active sites on the photocatalyst, thus inhibiting photocatalytic activity for contaminant degradation [196]. Some previous studies reported the effects of water matrix constituents on the degradation of BPA. Various inorganic anions, including sulfate (SO_4^{2-}), chloride (Cl^-), bicarbonate (HCO_3^-) [20, 120,

193-195, 197-204], carbonate (CO_3^{2-}), nitrate (NO_3^-) [20, 120, 194, 195, 197, 199-201], monohydrogen phosphate ($H_2PO_4^-$) [120, 194, 198, 200], and phosphate (PO_4^{3-}) [195, 199], were investigated for BPA degradation. Some researchers also explored how different inorganic cations, including magnesium (Mg^{2+}), manganese (Mn^{2+}) [193], sodium (Na^+), calcium (Ca^{2+}), potassium (K^+) [197, 198], and iron (Fe^{3+}) [198], affect the degradation of BPA. Additionally, the impacts of natural organic matter, such as humic acid [195, 198-200, 203, 205] and organic acids [203, 204], on BPA degradation were examined.

Herein, we investigate for the first time the photocatalytic activity of floating TNTs@PUF for the removal of different organic pollutants under simulated sunlight irradiation. Target contaminants include BPA as an EDC, methyl orange (MO) and methylene blue (MB) as dyes, bentazon (BZ) and isoproturon (IPU) as pesticides, sulfamethoxazole (SMZ) and carbamazepine (CBZ) as pharmaceuticals, and perfluorooctanoic acid (PFOA) as a representative per- and poly-fluoroalkyl substances (PFAS). To the best of our knowledge, no previous study has examined the effects of water matrix components, such as natural organic matter and inorganic anions, on BPA removal using a floating TNTs@PUF system. Additionally, the present study is the first to report the removal of BPA from a specific mixture of CECs, including SMZ, CBZ, fluconazole (FLZ), atrazine (ATZ), ibuprofen (IBP), and gemfibrozil (GFZ), using a floating TNTs@PUF photocatalyst.

4.3 Materials and Methods

4.3.1 Chemicals and materials

We applied titanium (IV) butoxide ($C_{16}H_{36}O_4Ti$, 97%, Sigma Aldrich), ethanol (C_2H_6O, 95%, Commercial Alcohols), sodium hydroxide (NaOH, 98%, Thermo Scientific), hydrochloric acid (HCl, 37% w/w, Fisher Scientific), polyvinyl alcohol (low molecular weight, 98-99% hydrolyzed, Thermo Scientific Chemicals), bisphenol A ($C_{15}H_{16}O_2$, ≥99%, Sigma Aldrich), methyl orange ($C_{14}H_{14}N_3NaO_3S$, 85%, Sigma Aldrich), methylene blue ($C_{16}H_{18}ClN_3S.xH_2O$, ≥97%, Sigma Aldrich), bentazon ($C_{10}H_{12}N_2O_3S$, analytical standard, Sigma Aldrich), isoproturon ($C_{12}H_{18}N_2O$, analytical standard, Sigma Aldrich), sulfamethoxazole ($C_{10}H_{11}N_3O_3S$, analytical standard, Sigma Aldrich), carbamazepine ($C_{15}H_{12}N_2O$, ≥98%, Sigma Aldrich), fluconazole ($C_{13}H_{12}F_2N_6O$, ≥98%, Santa Cruz Biotechnology), atrazine ($C_8H_{14}ClN_5$, analytical standard, Fluka), ibuprofen ($C_{13}H_{18}O_2$,

>95%, TRC), gemfibrozil ($C_{15}H_{22}O_3$, Sigma Aldrich), perfluorooctanoic acid ($CF_3(CF_2)_6COOH$, 95%, Sigma Aldrich), sodium bicarbonate ($NaHCO_3$, ≥99.7%, Sigma Aldrich), sodium chloride (NaCl, ≥99%, Sigma Aldrich), sodium sulfate (Na_2SO_4, ≥99%, Sigma Aldrich), citric acid ($C_6H_8O_7$, ≥99.5%, Sigma Aldrich), oxalic acid ($C_2H_2O_4$, ≥99%, Sigma Aldrich), and humic acid (technical grade, Sigma Aldrich). Additionally, we purchased a commercial polyurethane foam from Amtra (medium-porous, 20 pores per inch). All solutions were prepared with deionized water.

4.3.2 Synthesis of photocatalysts

TNTs photocatalyst was fabricated by the ultrasound-assisted hydrothermal method, as reported in our previous work [191]. First, 1 g of TiO_2 nanoparticles (TNPs) was dispersed in NaOH solution (10 M, 50 mL) and stirred for 30 min at room temperature. After that, the mixture was sonicated by an ultrasonic bath (Branson 2800, 23 cm (L) × 14 cm (W) × 10 cm (D), 1.8 L, 110 W) for 30 min. Using a mild ultrasonication prior to the hydrothermal method can facilitate the uniform dispersion of TNPs and control the morphology of TNTs, yielding longer TNTs than those obtained by the conventional hydrothermal method [94]. After sonication, the homogenized suspension was transferred to a Teflon-lined autoclave (100 mL) and placed in an oven for 24 h at 160 °C. Upon cooling to room temperature, the resulting white precipitate was collected by filtration and thoroughly washed with deionized water and HCl solution (0.1 M) until the pH was close to neutral. The obtained material was then dried at 80 °C in an oven and subsequently calcined at 400 °C for 2 h in a furnace with a heating rate of 5 °C/min.

A floating TNTs@PUF photocatalyst was prepared using a wet chemical deposition method. We utilized a porous PUF (4 cm (d) × 1 cm (t), 85% porosity) as a floating substrate. Notably, this PUF is commonly used in aquarium filters, making it a safe, inert, and non-toxic substrate [206]. Additionally, polyvinyl alcohol (PVA) was applied as a binder [140] to deposit the powder TNTs onto the PUF. For fabrication, PVA (1 wt.%) was first dissolved in deionized water (30 mL) in a three-neck flask (100 mL) under stirring for 3 h at 95 °C. After that, 0.7 g of TNTs was added to the flask and kept at 95 °C for an additional 2 h. The resulting solution was subsequently cooled to 80 °C in a beaker. Finally, the PUF was immersed in the solution, followed by drying at 80 °C in an oven. Figure 4.1 shows the synthesis steps of TNTs and floating TNTs@PUF.

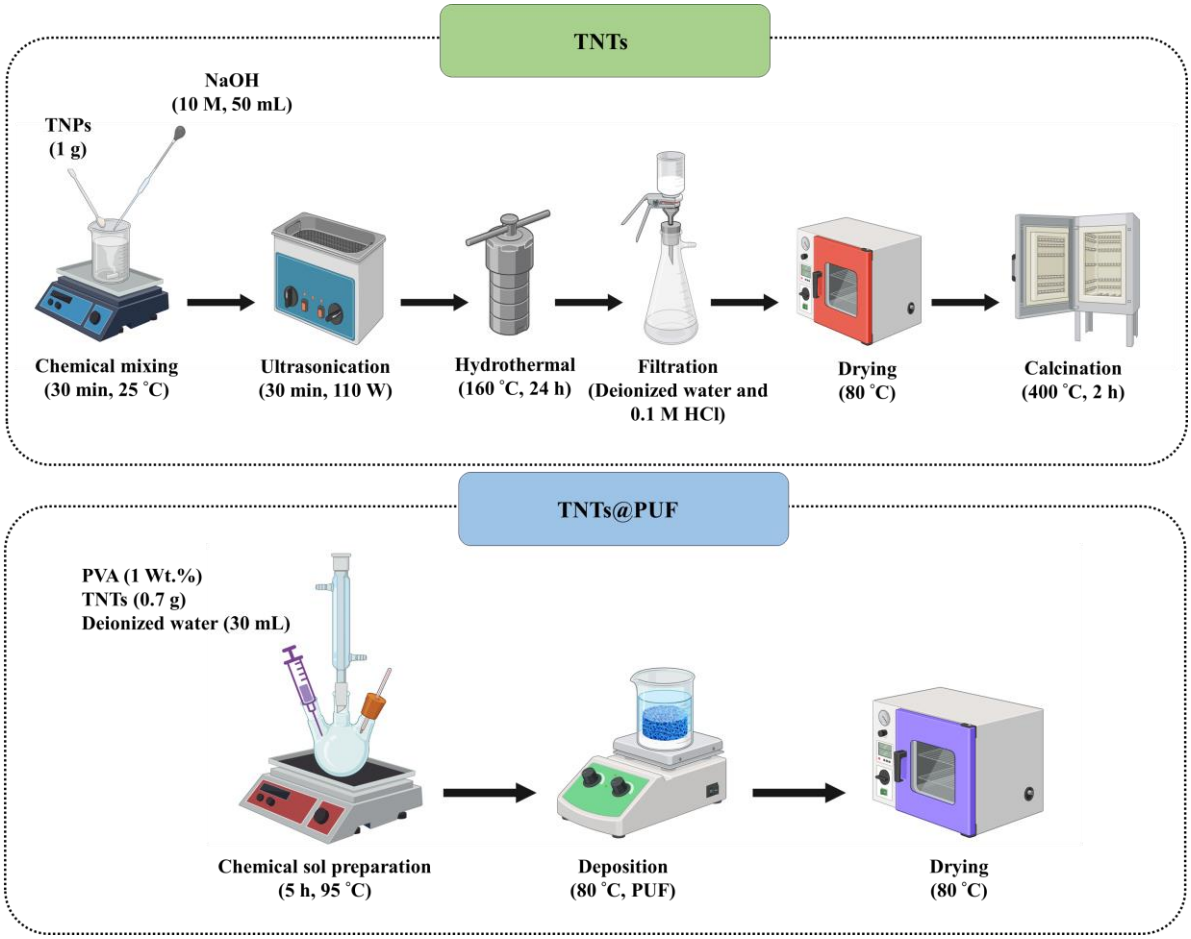

Figure 4.1 Schematic illustration of the synthesis methods of TNTs and floating TNTs@PUF

4.3.3 Characterizations of photocatalysts

The morphology and elemental composition were characterized using field-emission scanning electron microscopy (FESEM, JSM-IT800, JEOL) equipped with energy-dispersive X-ray spectroscopy (EDS). High-resolution transmission electron microscopy (HR-TEM, JEM-2100F, JEOL) was also employed to examine structural morphology, and the photocatalyst particle size was measured using Digimizer software (version 6.4.5). The chemical composition and valence states were analyzed by X-ray photoelectron spectroscopy (XPS) with an X-ray photoelectron spectrometer microprobe (VG ESCALAB 250Xi, Thermo Scientific). The crystalline structure was evaluated using X-ray diffraction (XRD, D8 Advance, Bruker), and the crystallite size was calculated using the Scherrer Equation [141].

$$D = \frac{K\lambda}{\beta cos\theta} \tag{4.1}$$

D represents the crystallite size (nm), K is the shape factor (0.94), λ denotes the wavelength of the X-ray source (Cu-Kα = 0.15406 nm), β corresponds to the full width at half maximum (FWHM) of the diffraction peak (in radians), and θ is half of the Bragg angle (in degrees).

The textural characteristics were evaluated through nitrogen adsorption-desorption isotherms at 77 K using the Brunauer-Emmett-Teller (BET) method (Autosorb 6100 FKM MP-MP, Anton Paar). The optical properties were examined using a diffuse reflectance UV-visible spectrophotometer (DRS, Evolution™ 220, Thermo Fisher Scientific). The photocatalyst bandgap energy (E_g) was estimated by plotting $[F(R) \times h\vartheta]^{0.5}$ versus $h\vartheta$, as described in Refs [142, 143].

$$F(R) = \frac{(1-R)^2}{2R} \tag{4.2}$$

$$h\vartheta = \frac{1240}{\lambda} \tag{4.3}$$

$F(R)$ is the Kubelka-Munk function, R represents the reflectance, $h\vartheta$ corresponds to the photon energy, and λ indicates the wavelength (nm).

The photoelectrochemical performance was evaluated using linear sweep voltammetry and chronoamperometry. We used a potentiostat/galvanostat (VersaSTAT3, AMETEK Scientific) as an electrochemical workstation, connected to a standard three-electrode photoelectrochemical cell. In this configuration, the photocatalyst coated on fluorine-doped tin oxide (FTO) glass served as the working electrode, platinum foil acted as the counter electrode, and an Ag/AgCl electrode was used as the reference electrode. Measurements were performed in a 0.01 M Na_2SO_4 electrolyte at a scan rate of 100 mV/s. Irradiation of the working electrode was provided by a 300 W commercial solar lamp (Ultra-Vitalux, Osram) with an intensity of 35 W/m^2. The photocurrent efficiency (η), which indicates the conversion of light photon energy into chemical energy, was calculated from the linear sweep voltammetry curve using Equation 4.4 [188].

$$\eta\% = J_p \left[\frac{E^{\circ}_{rev} - |E_{app}|}{I_0}\right] \times 100 \tag{4.4}$$

J_p represents the photocurrent density (mA/cm^2), I_0 is the incident light intensity, and E°_{rev} is the standard changeable potential (1.23 V vs. reversible hydrogen electrode [RHE]).

E_{app} is the absolute applied potential (V vs. Ag/AgCl), which was determined using Equation 4.5.

$$E_{app} = E_{meas} - E_{OCP} \quad (4.5)$$

E_{meas} corresponds to the measured electrode potential of the photoanode (V vs. Ag/AgCl), and E_{OCP} represents the open-circuit potential (OCP) of the photoanode (V vs. Ag/AgCl).

4.3.4 Experimental procedures

Photocatalytic experiments were performed in a batch photoreactor under simulated sunlight irradiation, provided by a 300 W commercial solar lamp (Ultra-Vitalux, Osram) with an intensity of 35 W/m^2 at 20 cm above the reactor. We evaluated the photocatalytic activity of floating TNTs@PUF in removing different organic contaminants, including BPA, MO, MB, BZ, IPU, SMZ, and CBZ. Each pollutant was tested individually at 20 mg/L for 4 h of irradiation in a 200 mL solution with a 0.2 g TNTs loading (the amount of TNTs deposited onto the PUF). In addition, we investigated the matrix effects, such as natural organic matter and inorganic anions, on BPA removal using floating TNTs@PUF. Humic acid (10 mg/L) was considered a representative of natural organic matter, and citric acid and oxalic acid (10 mM) were used as common organic acids. Notably, the concentrations of these compounds were selected based on previous studies [200, 203, 205, 207, 208]. We also selected a concentration of 10 mM for inorganic anions, including HCO_3^-, Cl^-, and SO_4^{2-}, based on previous reports [195, 201-204, 207]. The experimental conditions for the matrix effects were constant (BPA concentration of 20 mg/L, treated solution volume of 200 mL, TNTs loading of 0.2 g, irradiation of 4 h). Moreover, we examined the photocatalytic removal of BPA from a mixture of CECs, including SMZ, FLZ, CBZ, ATZ, IBP, and GFZ, by floating TNTs@PUF. All pollutants were present at 20 mg/L in a 200 mL mixture, with a TNTs loading of 0.2 g and an irradiation time of 4 h. Further experiments were conducted to assess the photocatalytic efficiency of our floating system in removing PFOA (10 mg/L) using floating TNTs@PUF (0.2 g) under 3 h of irradiation. For all experiments, prior to irradiation, TNTs@PUF was kept in the dark for 1 h to reach adsorption-desorption equilibrium between the pollutants and the photocatalyst's surface. Photolysis tests were also performed under simulated sunlight irradiation without the presence of TNTs@PUF.

4.3.5 Analytical methods

The concentrations of BPA, MO, MB, BZ, IPU, SMZ, and CBZ compounds were measured individually using a UV-Vis spectrophotometer (Evolution™ 220, Thermo Fisher Scientific). The

maximum wavelengths (λ_{max}) for each compound were as follows: 276 nm for BPA, 464 nm for MO, 664 nm for MB, 330 nm for BZ, 239 nm for IPU, 265 nm for SMZ, and 285 nm for CBZ.

The analysis of the CECs mixture was performed using liquid chromatography coupled to atmospheric pressure heated electrospray ionization tandem mass spectrometry (LC-HESI-MS). The system consisted of an Accela 600 HPLC coupled to an MSQ Plus mass spectrometer (Thermo Scientific, Waltham, MA, USA). The chromatographic separation was achieved using a 0.2 µm inline filter with a UHPLC Zorbax Eclipse Plus C18 guard column (5 mm × 2.1 mm, 1.8 µm) followed by a Zorbax Eclipse Plus C18 RRHD analytical column (50 mm × 2.1 mm, 1.8 µm), both from Agilent Technologies (Santa Clara, CA, USA). The mobile phase consisted of 0.1% acetic acid in water (Buffer A) and 10 mM ammonium acetate in acetonitrile with 0.1% acetic acid (Buffer B). The LC gradient started with a 2-min held at 5% B, followed by a linear increase to 50% B over 5.5 min. This was followed by a ramp to 100% B over 2 min, with a 3-min hold at 100% B to ensure complete elution of all analytes. The column was then returned to its initial condition (5% B) and re-equilibrated for 2.5 min, for a total run time of 15 min. The injection volume was 25 µL, with a constant flow rate of 150 µL/min. The column temperature was maintained at a constant 35 $^{\circ}$C throughout the run, while the samples were kept at 4 $^{\circ}$C in the autosampler. MS detection was carried out using a heated electrospray ionization (HESI) source operating in both positive and negative ionization modes (polarity switching), with a spray voltage of 3.5 kV. Source parameters were optimized by direct infusion of individual analytical standards at a flow rate of 10 µL/min to determine compound-specific cone voltages (Table 4.1). The ion source temperature was set to 350 $^{\circ}$C, with nitrogen used as both auxiliary and sweep gas. Data acquisition was performed in full scan mode over the m/z range 50-700, using a resolution of 0.7 mass units and a 2 m/z span window centered on each compound's monoisotopic mass. Quantification and instrument control were performed using Thermo Scientific Xcalibur. The analysis was performed using a seven-point external calibration curve with a concentration range from 5-250 ppb (µg/L). All target analytes exhibited linear responses with correlation coefficients (R^2) of ≥ 0.99.

Table 4.1 LC-MSQ method source parameters for CECs

Compound	Polarity	Cone V	m/z	Limit of detection ppb	Limit of quantification ppb
SMZ	+ve	45	254.06	5.71	17.30
FLZ	+ve	65	307.11	3.57	10.83
CBZ	+ve	45	237.09	2.16	6.54
ATZ	+ve	40	216	2.63	7.98
BPA	-ve	100	227.91	9.13	27.68
IBP	-ve	35	205.09	2.62	7.94
GFZ	-ve	40	249.16	1.82	5.52

The analytical method for PFOA samples was adapted from previous work [209]. PFOA concentration was determined using an Accela 600 HPLC system coupled to a MSQ Plus single quadrupole mass spectrometer (Thermo Scientific). Detection was performed in negative-ion mode using a HESI source to generate precursor ions at m/z. Mass spectrometry parameters for quantitation were optimized by direct injection of a 5 mg/mL standard solution at 1 mL/min and a 1:1 water-methanol mixture at 10 µL/min. Both solutions contained 0.1% acetic acid and 2 mM ammonium acetate. Nitrogen served as the gas source in static mode, and the capillary voltage was set to 3.0 kV. The ion transfer tube temperature was maintained at 275 °C, and no vaporization was applied during ionization. The resulting ions were focused on a beam using a cone voltage of -35 V. Data acquisition included a full scan range from 150 to 500 m/z, with a 2 m/z span, while single ion monitoring was done at 284.98 m/z using a 2 m/z span mode. An Alltima C18 column (53 mm × 7 mm, 3 µm) from Alltech (KY, USA) was installed on the divert valve to minimize interference and prevent precipitation of sulfate and chloride salts within the analytical column between the loading pump and the injector valve. Buffer exchange was conducted under isocratic conditions for 3 min at a flow rate of 1 mL/min, using 5% methanol in Milli-Q water as the mobile phase. After 0.1 min, the valve position was switched, and the loading flow was reduced to 0.1 mL/min for 15 min, before returning to 1 mL/min. Chromatographic separation was achieved using a column configuration consisting of an online filter cartridge (2.1 mm × 0.2 µm stainless steel filter), followed by an Eclipse Plus C18 RRHD guard column (5 mm × 2.1 mm, 1.8 µm) from Agilent Technologies (CA, USA) and an Alltima C8 analytical column (53 mm × 7 mm, 3 µm) from Alltech (KY, USA). Due to the persistence of PFOA within laboratory tubing and instrument

components, Hypersyl Gold aQ columns (20 mm × 2.1 mm, 12 μ pore size) from Thermo Scientific were installed between the pumps and both the injection and divert valves. Additionally, all tubing used in the system was stainless steel. Throughout the analysis, the column temperature was maintained at 40 °C. The mobile phase used for the analytical column consisted of Milli-Q water and methanol, each containing 0.1% acetic acid and 2 mM ammonium acetate, delivered at a constant flow rate of 1 mL/min. The flow gradient started at 5% organic solvent, was maintained for 4 min, and then ramped linearly to 100% over 2 min. This composition was then held for 8 min to clean the column. The system was subsequently returned to the initial 5% organic conditions and equilibrated for 2 min, resulting in a total run time of 16 min. Quantitative determination of the analyte was performed using an eight-point linear calibration curve, along with three quality controls (QCs) at low, medium, and high concentrations. Data analysis was conducted using Xcalibur Quan Browser software (version 4.4, Thermo Scientific).

4.3.6 Photocatalytic kinetic study

We examined the kinetics of pollutant removal in the floating TNTs@PUF system under simulated sunlight irradiation. The Langmuir-Hinshelwood kinetics model was followed (Equation 4.6) [190].

$$r = \frac{dC}{dt} = \frac{kKC}{1 + KC} \tag{4.6}$$

In this model, r is the rate of pollutant removal (mg/L.min), C is pollutant concentration (mg/L), t is irradiation time (min), k is the reaction rate constant (mg/L.min), and K is the pollutant adsorption constant (L/mg).

At low pollutant concentrations, Equation 4.6 simplifies to Equation 4.7 as first-order kinetics.

$$ln\left(\frac{C_0}{C}\right) = kKt = k_{app}t \tag{4.7}$$

k_{app} is the apparent first-order rate constant (min^{-1}).

4.4 Results and Discussion

4.4.1 Characterization of photocatalysts

Figure 4.2(a) presents a photograph of TNTs@PUF, confirming the successful deposition of TNTs onto the PUF substrate. Figure 4.2(b) shows the morphology of TNTs, confirming the nanotubular structure of TNTs photocatalysts. Based on the HR-TEM image (Figure 4.2(c)), TiO_2 double-walled nanotubes had an external diameter of 7.5 nm, an internal diameter of 5.2 nm, and a wall thickness of 1.15 nm on average, measured by Digimizer software. The SEM image of pristine PUF (Figure 4.2(d)) indicates its relatively smooth surface prior to TNTs deposition. Figures 4.2(e-h) present the elemental composition of TNTs@PUF. Ti and O elements were uniformly distributed in the PUF, with a composition of 29% C, 54% O, and 17% Ti.

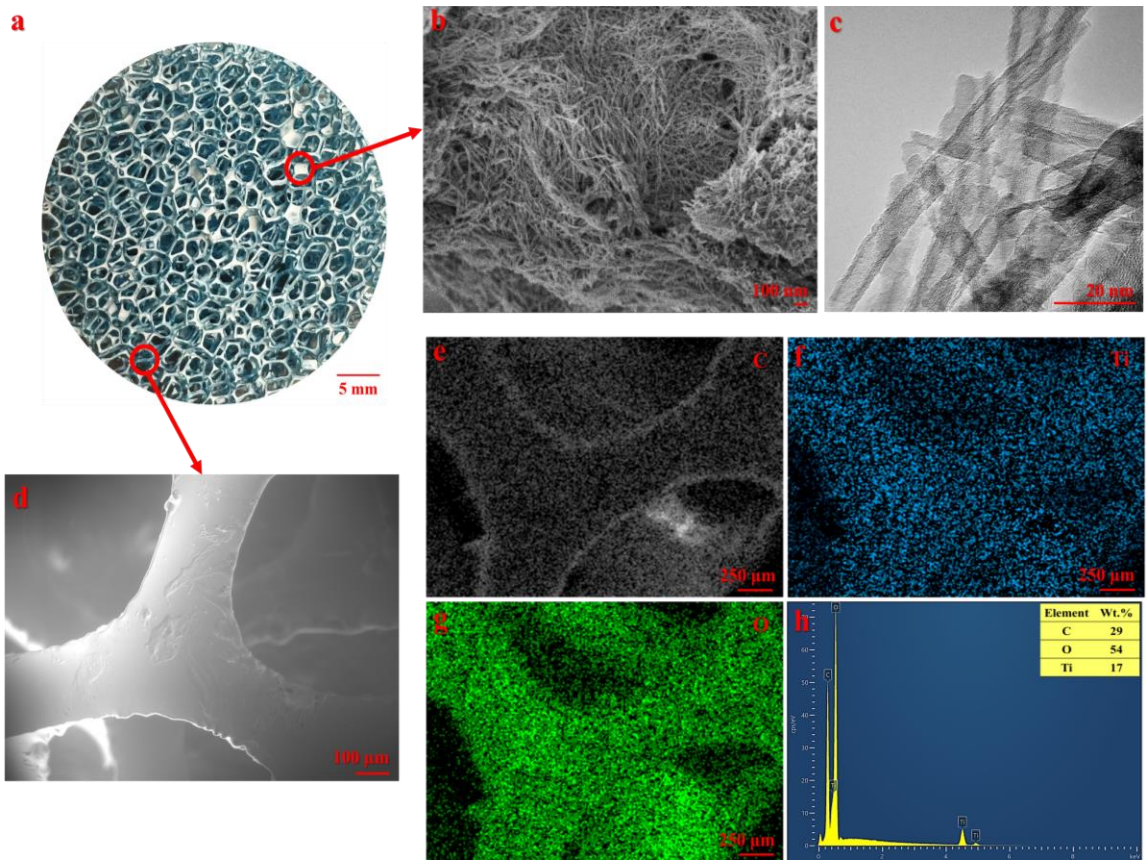

Figure 4.2 (a) Photograph of TNTs@PUF; (b) SEM image of TNTs; (c) HR-TEM image of TNTs; (d) SEM image of pristine PUF; (e-g) EDS mapping of TNTs@PUF for C, Ti, and O, respectively; (h) EDS spectrum of TNTs@PUF

Figures 4.3(a-c) show the XPS results, including the chemical compositions and valence states of TNTs. According to the XPS survey shown in Figure 4.3(a), the photocatalyst was composed of Ti and O elements. In the high-resolution XPS (HR-XPS) spectrum of Ti 2p (Figure 4.3(b)), two peaks were observed at binding energies of 464.7 eV for Ti $2p_{1/2}$ and 459 eV for Ti $2p_{3/2}$, with a peak separation of 5.7 eV, indicating the presence of Ti^{4+} [192, 210]. The HR spectrum of O 1s (Figure 4.3(c)) shows a peak at 530.5 eV attributed to lattice oxygen [158, 192], as well as an additional peak at 531.8 eV corresponding to oxygen vacancies [211, 212]. The formation of oxygen vacancies has been proven for enhancing photocatalytic activity [213, 214]. Rajendran and Vijayaraghavan [215] reported that oxygen vacancies in $BaSnO_3$, introduced by Cu doping, serve as trapping sites for photogenerated electrons, which enhances charge separation and promotes the generation of ROS. Consequently, the photocatalytic activity of Cu-doped $BaSnO_3$ for MB degradation increased, achieving 98.9% degradation after 30 min under visible light and sunlight. Similarly, in another study, oxygen vacancies also led to improved photocatalytic activity. The presence of oxygen vacancies in ultrathin $Bi_7Fe_2Ti_2O_{17}Cl$ nanosheets [216] creates a new donor level, thereby reducing the bandgap energy and enhancing the light absorption of the photocatalyst. Therefore, approximately 92.7% of rhodamine B was degraded after 90 min of visible light irradiation. Additionally, in Ag/TiO_2 nanoflowers [214], the existence of oxygen vacancies enhances photocatalytic efficiency by optimizing light absorption, resulting in a 92% degradation of rhodamine B after 120 min of irradiation. Zhang et al. [217] further demonstrated that lattice oxygen vacancies in carbon-doped TiO_2 nanofiber membranes form defect states that inhibit the recombination of photogenerated carriers. This effect resulted in a 90.8% degradation of tetracycline under visible light.

Figure 4.3(d) shows the XRD pattern of TNTs. The photocatalyst exhibited characteristic diffraction peaks at 2θ values of 25.3°, 37.9°, 48.1°, 53.9°, 55.2°, 62.8°, and 68.8°, corresponding to the Miller indices of (101), (004), (200), (105), (211), (204), and (220) planes, respectively (JCPDS card No. 21-1272) [72, 192]. The results indicated that TNTs were predominantly in the crystalline anatase phase. Additional peaks were observed at 15.1°, 28.6°, and 43.5°, assigned to (001), (002), and (003) planes of TiO_2(B) phase (JCPDS No. 46-1237) [167, 168]. Biphase anatase/TiO_2(B) exhibits superior photocatalytic activity compared to single-phase TiO_2 in pollutant degradation applications [54, 218-220]. For instance, Yang et al. [221] synthesized core-shell TiO_2(B)/anatase photocatalysts for the degradation of sulforhodamine B. Their results showed that mixed-phase

photocatalysts exhibited higher photocatalytic activity than pure anatase or TiO_2(B), achieving complete degradation of sulforhodamine B after 90 min of UV irradiation. This improvement is attributed to the interface between the two phases, which promotes photogenerated charge migration, reduces charge recombination, and thereby enhances the photocatalytic activity of TiO_2 (B)/anatase. Furthermore, the crystallite size of TNTs was 26 nm, calculated by Equation 4.1 at the anatase peak of (101).

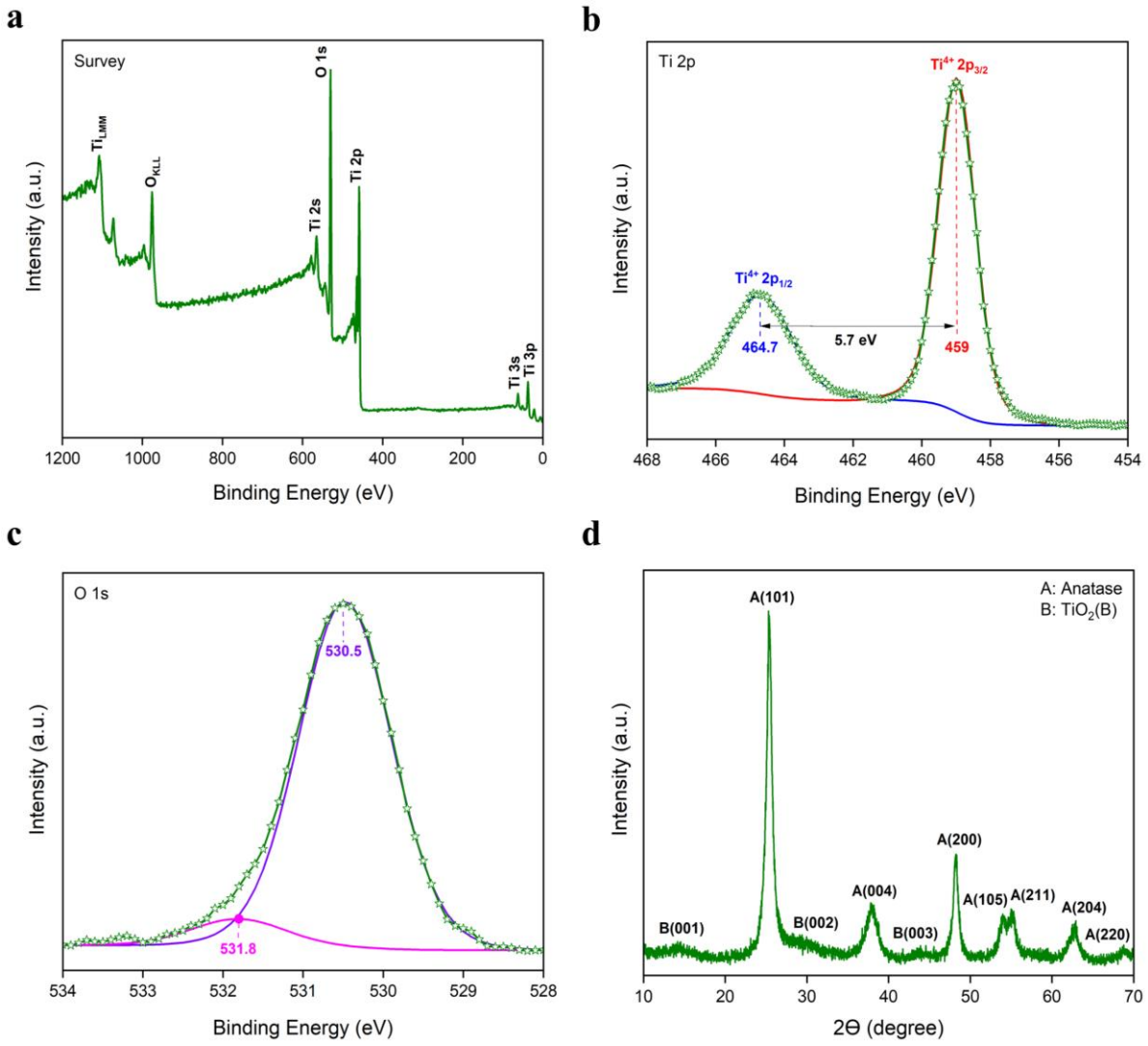

Figure 4.3 (a) XPS survey spectrum of TNTs; (b, c) HR-XPS spectra of Ti 2p and O 1s, respectively; (d) XRD pattern of TNTs

Figures 4.4(a) and 4.4(b) show the DRS results of TNTs. The absorption spectrum of TNTs exhibited an intense absorption peak in the UV region, corresponding to the electron excitation from the conduction band to the valence band of TNTs [170, 192]. TNTs had an absorption edge at approximately 415 nm (Figure 4.4(a)), and the bandgap energy was determined as 3.0 eV using Equations 4.2 and 4.3 (Figure 4.4(b)). As depicted in Figure 4.3(d), TNTs has a biphasic anatase/TiO_2(B) structure, where anatase exhibits a wider bandgap energy (3.2 eV) than TiO_2(B) (3.0 eV) [222]. Thus, the existence of TiO_2(B) causes a reduction in the bandgap energy of the photocatalyst [174, 191], resulting in a bandgap of 3.0 eV for TNTs. In addition, the introduction of oxygen vacancies into the TNTs lattice (Figure 4.3(c)) leads to the formation of localized mid-gap or vacancy states within the bandgap, which influence band energies and alter band widths [216, 223, 224]. This further narrows the bandgap energy of TNTs to 3.0 eV.

Figure 4.4(c) shows the adsorption-desorption isotherm of TNTs. According to the IUPAC classification [175], the photocatalyst exhibited a type IV isotherm with an H3 hysteresis loop, indicating a slit-like mesoporous geometry for TNTs [139] and a mean pore size of 31 nm. In addition, BET analysis determined a surface area of 110 m^2/g and a total pore volume of 0.57 cm^3/g for TNTs. Notably, 1D TiO_2 nanostructures, such as nanotubes, have been investigated for photocatalytic applications due to their large specific surface area [191, 225-227]. This characteristic provides more active sites available for photocatalytic reactions, thereby improving the photocatalytic activity of TNTs.

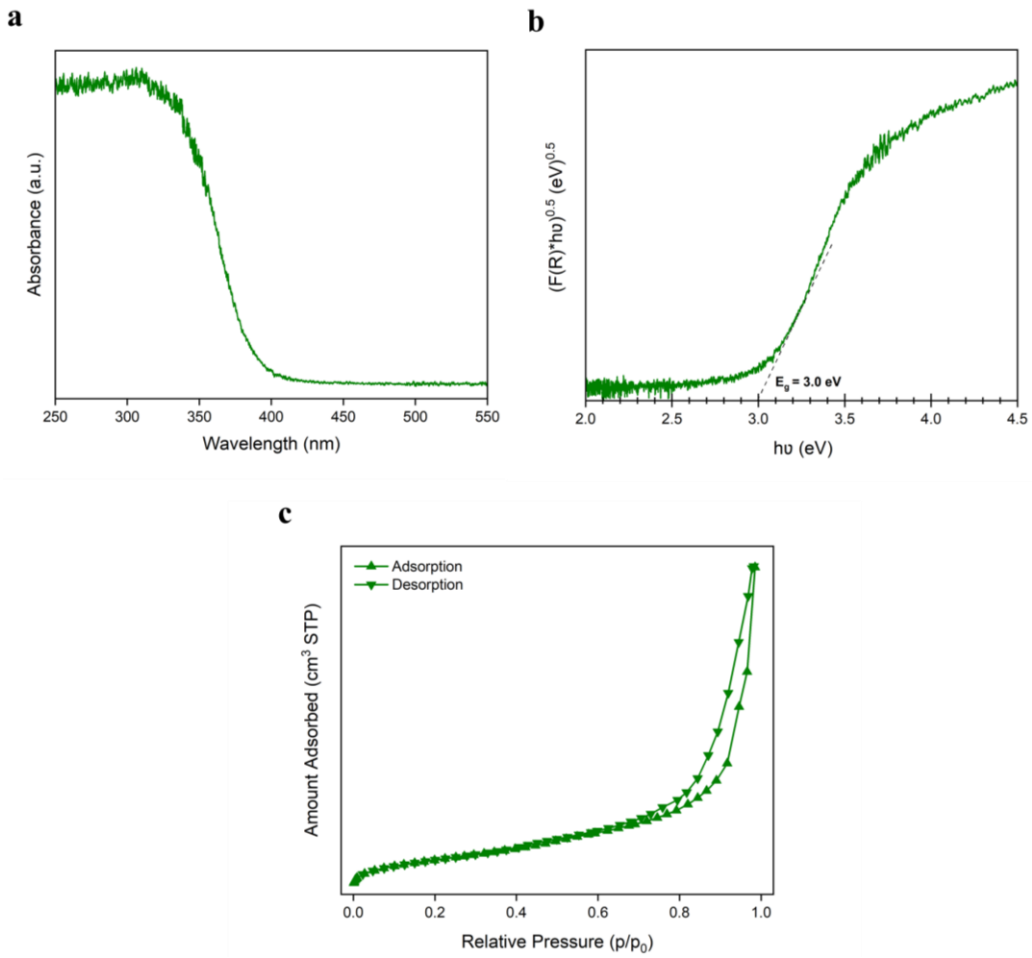

Figure 4.4 (a) Absorption spectrum of TNTs; (b) Bandgap energy of TNTs; (c) N_2 adsorption-desorption isotherm of TNTs

Figure 4.5 shows the photoelectrochemical properties of TNTs. The photocurrent density of TNTs was zero under dark conditions, indicating no electrochemical reactions (Figure 4.5(a)). Under simulated sunlight irradiation, TNTs generated a positive photocurrent density within the anodic potential range of 0.0–2.0 V (vs. Ag/AgCl). At a potential of 2.0 V, the photocurrent density of TNTs was recorded at 0.2 mA/cm^2. Figure 4.5(b) shows the chronoamperometry of TNTs at a constant potential of 0.0 V (vs. Ag/AgCl) through three cycles of on-off pulses, with an interval of 20 s. We selected 0.0 V to evaluate photo-response, as the photocatalytic experiments were performed without any external potential. The photocurrent density of TNTs remained at zero when the light was off. However, when exposed to light, the photocurrent density peaked at 0.2 mA/cm^2 and subsequently returned to zero once the light was turned off. The rapid response reflects the reproducibility of the electron-hole pairs generated in TNTs. Additionally, the photocurrent density

of 0.2 mA/cm^2 was maintained during the on pulses, indicating photocatalytic activity of TNTs in generating electron-hole pairs. Figure 4.5(c) shows that TNTs achieved a photoconversion efficiency of 0.24%, as calculated using Equations 4.4 and 4.5. The excellent photoelectrochemical properties of TNTs at zero potential, attributed to their 1D nanostructures, enhance photon energy absorption and accelerate electron excitation under simulated sunlight irradiation. Consequently, the photocatalytic activity of TNTs for redox reactions is improved. Tang et al. [228] reported a photocurrent transient response of 0.01 μA/cm^2 under visible light irradiation for titanate nanotubes. In another study [229], the photocurrent response and photoconversion efficiency of titanium dioxide nanotubes exposed to visible light were found to be 0.09 mA/cm^2 and 0.16%, respectively. Additionally, a photocurrent density of 20.7 μA/cm^2 was observed for titania nanotubes under solar light illumination [230]. Hajjaji et al. [231] examined the photoelectrochemical behavior of titanium dioxide nanotube arrays under simulated solar light, achieving a photoconversion efficiency of 0.16%. These comparisons indicate that the TNTs in the present study exhibit higher photocurrent density and photoconversion efficiency compared to previously reported titanate nanotubes.

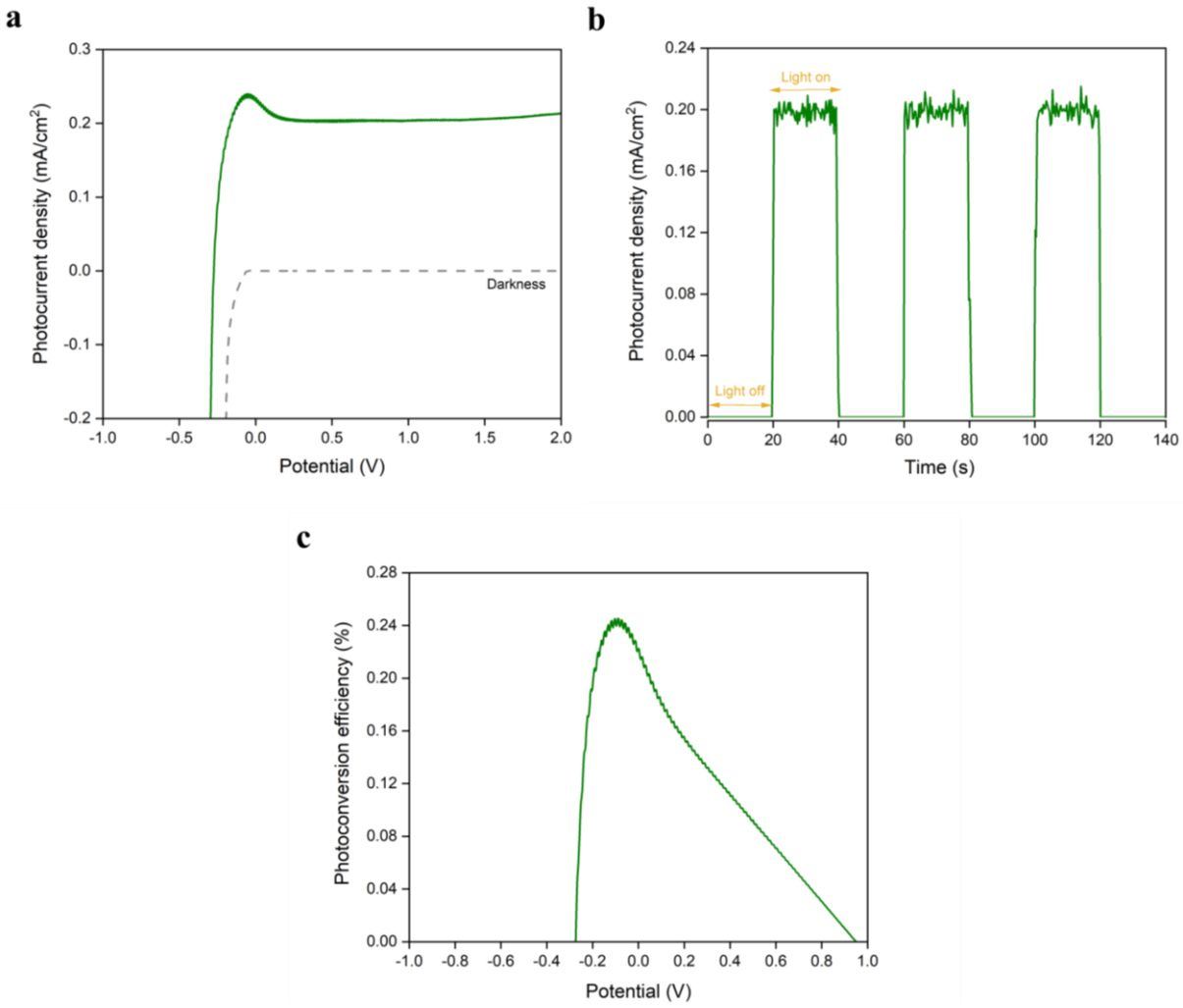

Figure 4.5 (a) Linear sweep voltammetry of TNTs; (b) Transient photocurrent response of TNTs; (c) Photoconversion efficiency of TNTs

4.4.2 Photocatalytic activity of floating TNTs@PUF towards organic pollutant removal

Figure 4.6 shows the photocatalytic activity of floating TNTs@PUF for the removal of different organic contaminants, including BPA, MO, MB, BZ, IPU, SMZ, and CBZ, under simulated sunlight irradiation. Error bars present the standard deviation of three replicates. The photolysis results revealed negligible removal of all pollutants after 4 h (approximately 2%). In addition, TNTs@PUF exhibited the highest adsorption for MB (12%) and IPU (11%). The adsorption was 10% for BPA, MO, and SMZ, and 9% for BZ and CBZ. As depicted in Figure 4.6, TNTs@PUF achieved removal efficiencies of 98% for BPA, 98% for MO, 85% for MB, 98% for BZ, 98% for

IPU, 98% for SMZ, and 97% for CBZ after 4 h of irradiation, including the initial adsorption. However, PFOA was not removed by TNTs@PUF after 3 h of irradiation. The results demonstrate the high efficiency of floating TNTs@PUF in removing most of the tested pollutants, except PFOA.

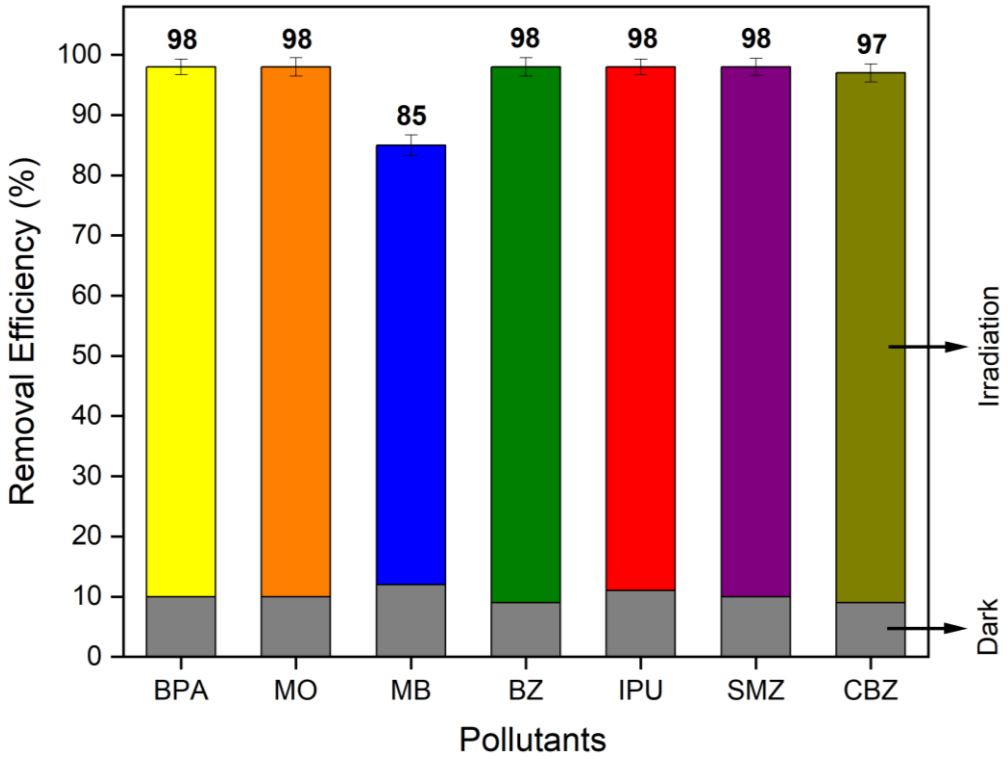

Figure 4.6 Removal efficiencies of BPA, MO, MB, BZ, IPU, SMZ, and CBZ by floating TNTs@PUF (individual contaminants, 20 mg/L pollutant concentration, 0.2 g TNTs loading, 4 h irradiation)

Figure 4.7 presents the apparent first-order rate constants (k_{app}) calculated from kinetic models (Equations 4.6 and 4.7) for the removal of BPA, MO, MB, BZ, IPU, SMZ, and CBZ under simulated sunlight irradiation. The correlation coefficients (R^2) were 0.99, confirming that the photocatalytic removal of these pollutants by floating TNTs@PUF followed first-order kinetics. The k_{app} values were 0.0156 min^{-1} for BPA (Figure 4.7(a)), 0.0149 min^{-1} for MO (Figure 4.7(b)), 0.0078 min^{-1} for MB (Figure 4.7(c)), 0.0162 min^{-1} for BZ (Figure 4.7(d)), 0.0152 min^{-1} for IPU (Figure 4.7(e)), 0.015 min^{-1} for SMZ (Figure 4.7(f)), and 0.0137 min^{-1} for CBZ (Figure 4.7(g)). Notably, MB exhibited the lowest k_{app} (0.0078 min^{-1}), while BZ had the highest one (0.0162 min^{-1}), indicating variation in removal rates among these compounds.

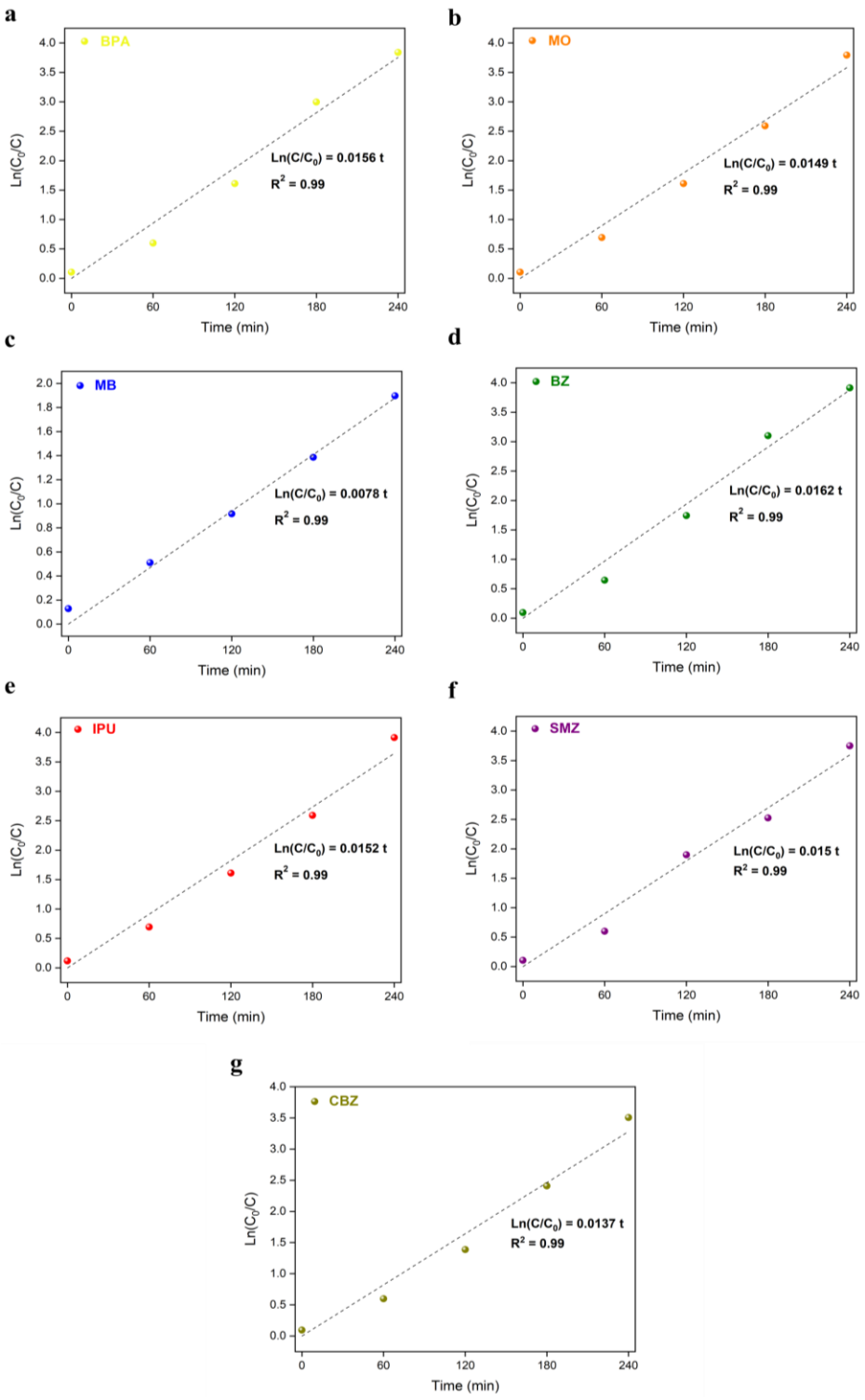

Figure 4.7 Apparent first-order rate constants for the removal of (a) BPA, (b) MO, (c) MB, (d) BZ, (e) IPU, (f) SMZ, and (g) CBZ using floating TNTs@PUF (individual contaminants, 20 mg/L pollutant concentration, 0.2 g TNTs loading, 4 h irradiation)

4.4.3 Matrix effects on BPA removal using floating TNTs@PUF

Figure 4.8(a) shows the effect of natural organic matter on BPA removal using floating TNTs@PUF under simulated sunlight irradiation. Error bars indicate the standard deviation from three replicates. The control test refers to the removal of BPA in the absence of natural organic matter, which was 98%. When humic acid was added to the BPA solution, the removal dropped to 80% after 4 h of irradiation. This reduction can be attributed to the scavenging of $^{\bullet}OH$ by humic acid [203]. This hinders the oxidation reaction and consequently diminishes the photocatalytic activity of TNTs@PUF for BPA removal. Additionally, the presence of phenolic hydroxyl and carboxyl groups in humic acid inhibits the interaction between BPA and the photocatalyst [200], further decreasing the photocatalytic activity of TNTs@PUF for BPA removal. Similar results regarding the inhibitory effect of humic acid on BPA degradation were reported by Latif et al. [203] using a different oxidative treatment. In their study, humic acid (10 mg/L) decreased BPA degradation from 92.2% to 77.7% in the Fe (III)/peroxymonosulfate system. Additionally, Hassani et al. [205] assessed $CoFe_2O_4$-reduced graphene oxide nanocomposite for degrading BPA in the presence of 10 mg/L humic acid. Their results indicated that humic acid caused a reduction of approximately 20% in BPA degradation. Another inhibitory effect of humic acid (10 mM) on BPA degradation was also observed by Ma et al. [200]. As shown in Figure 4.8(a), the presence of citric acid and oxalic acid resulted in a reduction in BPA removal, achieving 86% and 30%, respectively. These organic acids can trap photogenerated holes (h^+) [232-234] and prevent the generation of ROS, thereby inhibiting the photocatalytic activity of TNTs@PUF for the removal of BPA. The observed reduction in BPA removal efficiency in the presence of organic acids is consistent with previous studies. For instance, Latif et al. [203] investigated the effect of organic acids (10 mM) on BPA degradation using the Fe(III)/peroxymonosulfate system. Their results showed that BPA removal decreased from 92.2% to 86.9% with citric acid and to 66.1% with oxalic acid. Similarly, another study reported a decrease in BPA removal using 0.8 mM oxalic acid, with 76.2% of BPA being removed by $FeS_2@SiO_2$ [204].

Figure 4.8(b) presents the effect of inorganic anions, such as HCO_3^-, Cl^-, and SO_4^{2-}, on BPA removal with floating TNTs@PUF under simulated sunlight irradiation. The control test refers to the removal of BPA in the absence of inorganic anions (98%). Upon the addition of HCO_3^- to the BPA solution, the removal efficiency decreased from 98% to 80% after 4 h of irradiation. Similarly, inhibitory effects of Cl^- and SO_4^{2-} on BPA removal were observed, resulting in 86% for Cl^- and

90% for SO_4^{2-}. The reduction in BPA removal can be attributed to the formation of secondary reactive species, which have a more negative oxidation potential than $^{\bullet}OH$ (2.8 V vs. normal hydrogen electrode [NHE]) [235, 236], the most potent ROS in photocatalysis. As shown in Reactions 4.1 and 4.2, HCO_3^- reacts with $^{\bullet}OH$ and h^+, generating carbonate radicals ($^{\bullet}CO_3^-$) and bicarbonate radicals ($^{\bullet}HCO_3^-$) with a redox potential of 1.6-1.8 V vs. NHE [237, 238]. Similarly, the presence of Cl^- in the system leads to the generation of chlorine species ($^{\bullet}ClOH^-$ and $^{\bullet}Cl$; Reactions 4.3 and 4.4), which have a redox potential of 1.3 V vs. NHE [239]. For SO_4^{2-}, Reactions 4.5 and 4.6 show the formation of sulfate radicals ($^{\bullet}SO_4^-$) with a redox potential of 2.43 V vs. NHE [240]. Therefore, the more negative oxidation potential of the abovementioned secondary reactive species compared to $^{\bullet}OH$ causes a drop in the removal efficiency of BPA.

$$HCO_3^- + {}^{\bullet}OH \rightarrow H_2O + {}^{\bullet}CO_3^- \quad \text{(Reaction 4.1)}$$

$$HCO_3^- + h^+ \rightarrow {}^{\bullet}HCO_3^- \quad \text{(Reaction 4.2)}$$

$$Cl^- + {}^{\bullet}OH \rightarrow {}^{\bullet}ClOH^- \quad \text{(Reaction 4.3)}$$

$$Cl^- + h^+ \rightarrow {}^{\bullet}Cl \quad \text{(Reaction 4.4)}$$

$$SO_4^{2-} + {}^{\bullet}OH \rightarrow {}^{\bullet}SO_4^- + OH^- \quad \text{(Reaction 4.5)}$$

$$SO_4^{2-} + h^+ \rightarrow {}^{\bullet}SO_4^- \quad \text{(Reaction 4.6)}$$

The impacts of Cl^- and HCO_3^- on BPA degradation were investigated in a previous study [202]. Adding 10 mM Cl^- and HCO_3^- to graphene oxide-TiO_2 decreased BPA degradation from 88.9% to 85.2% for Cl^- and 60% for HCO_3^-. Similarly, in the Fe(III)/peroxymonosulfate system, 10 mM HCO_3^- and Cl^- resulted in a reduction of 13.1% and 6.5% in BPA degradation, respectively [203]. Diao et al. [204] also observed the negative effects of Cl^- and HCO_3^- on BPA removal using FeS_2@SiO_2. In their study, BPA removal was 81.5% in the presence of Cl^- and 67.6% with HCO_3^-, both at a concentration of 10 mM. Similar results were obtained for the impact of anions on the photocatalytic reaction of BPA using WO_3@MoS_2/Ag [201]. The removal of BPA decreased from 92.5% to 49.2%, 65.6%, and 88.4% in the presence of 10 mM HCO_3^-, Cl^-, and SO_4^{2-}, respectively. Another negative effect of 10 mM SO_4^{2-} on BPA removal was also reported by Abdul et al. [195].

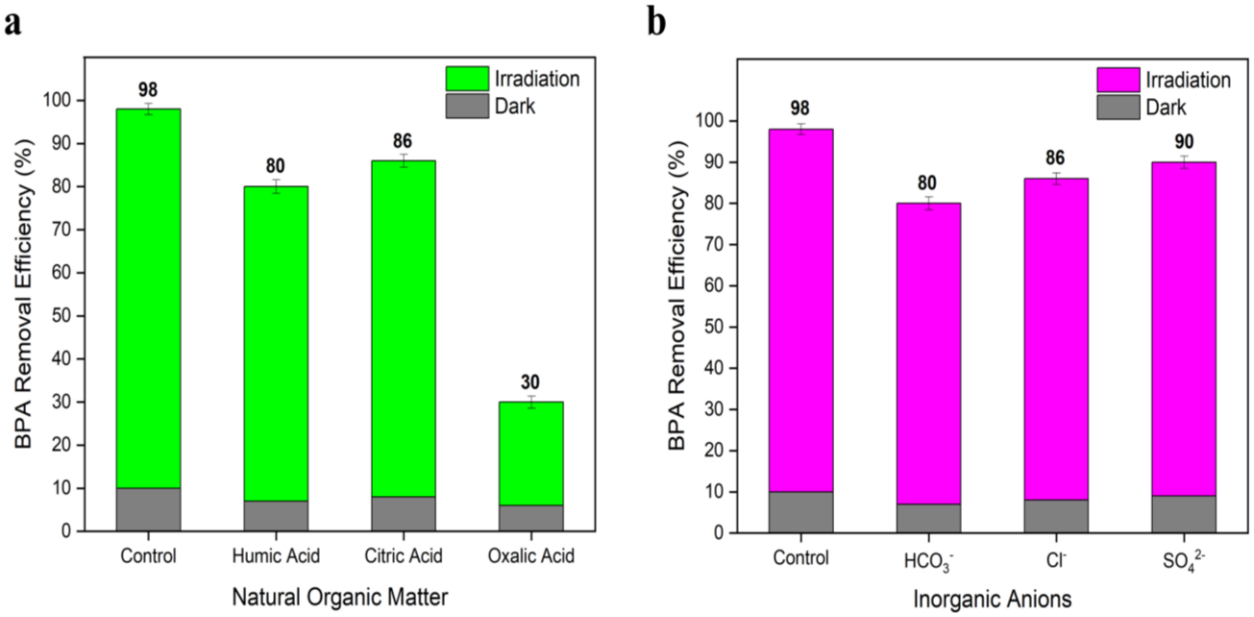

Figure 4.8 Effect of (a) natural organic matter and (b) inorganic anions on BPA removal by floating TNTs@PUF (20 mg/L BPA, 0.2 g TNTs loading, 4 h irradiation, 10 mg/L humic acid, 10 mM citric acid, 10 mM oxalic acid, 10 mM HCO_3^-, 10 mM Cl^-, 10 mM SO_4^{2-})

Figure 4.9 presents the effect of natural organic matter on apparent first-order rate constants for the removal of BPA using floating TNTs@PUF. The control experiment yielded a k_{app} of 0.0156 min^{-1}, as shown in Figure 4.9(a). The addition of natural organic matter to the BPA solution resulted in a reduction in k_{app}. The k_{app} value decreased to 0.0065 min^{-1} in the presence of humic acid (Figure 4.9(b)), 0.0078 min^{-1} with citric acid (Figure 4.9(c)), and 0.0015 min^{-1} with oxalic acid (Figure 4.9(d)). Among the natural organic matter tested, oxalic acid exhibited the lowest k_{app} (0.0015 min^{-1}).

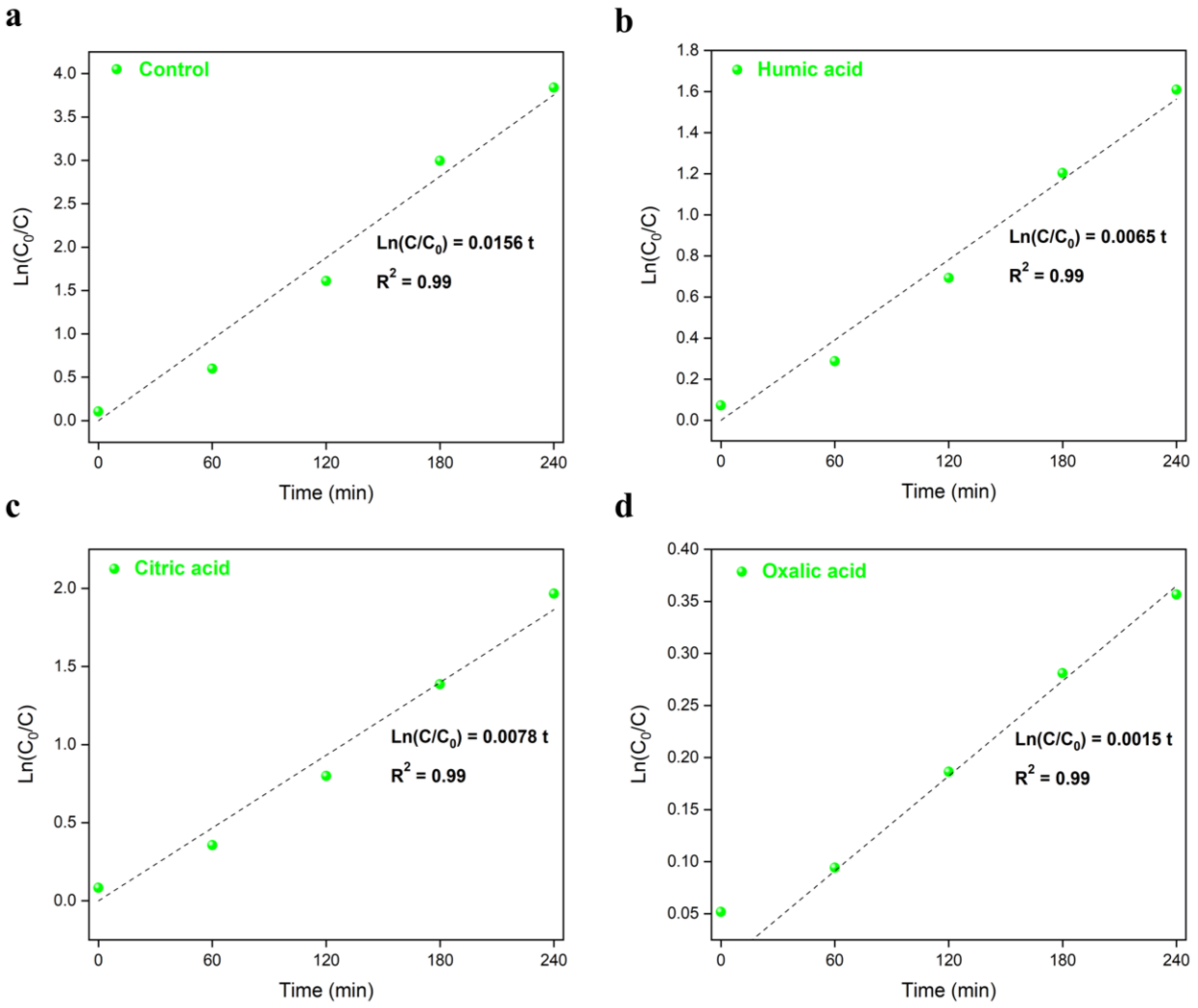

Figure 4.9 Effect of natural organic matter (a) control, (b) humic acid, (c) citric acid, (d) oxalic acid on apparent first-order rate constants for BPA removal using floating TNTs@PUF (20 mg/L BPA, 0.2 g TNTs loading, 4 h irradiation, 10 mg/L humic acid, 10 mM citric acid, 10 mM oxalic acid)

Figure 4.10 shows how inorganic anions affect the apparent first-order rate constants for BPA removal with floating TNTs@PUF. Without inorganic anions, k_{app} was 0.0156 min^{-1} (control test, Figure 4.10(a)). By adding HCO_3^- to the BPA solution, k_{app} decreased to 0.0063 min^{-1} (Figure 4.10(b)). The presence of Cl^- and SO_4^{2-} also decreased k_{app} to 0.0081 min^{-1} (Figure 4.10(c)) and 0.0089 min^{-1} (Figure 4.10(d)), respectively. Among the inorganic anions examined, HCO_3^- achieved the lowest k_{app} (0.0063 min^{-1}).

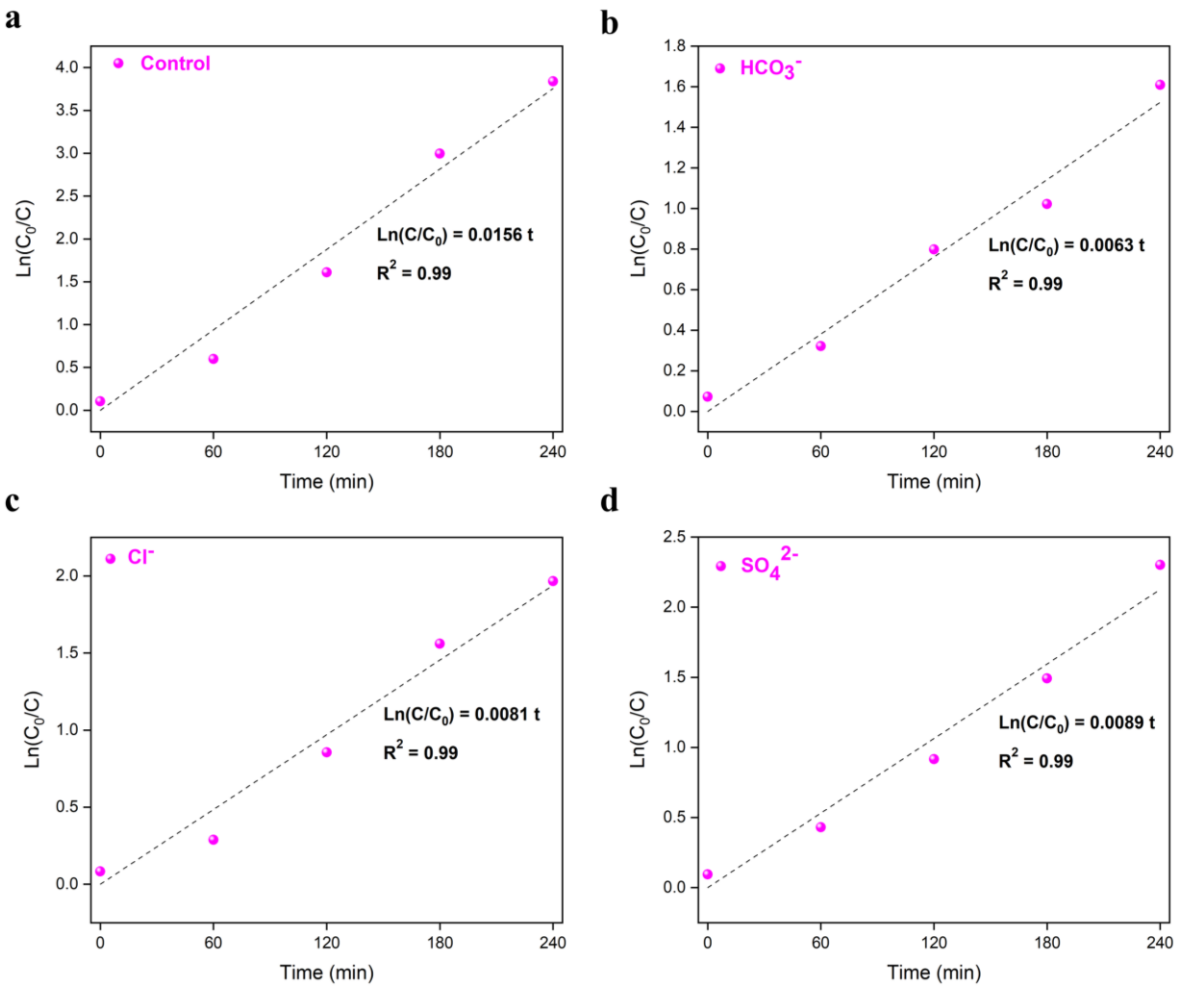

Figure 4.10 Effect of inorganic anions (a) control, (b) HCO_3^-, (c) Cl^-, (d) SO_4^{2-} on apparent first-order rate constants for BPA removal using floating TNTs@PUF (20 mg/L BPA, 0.2 g TNTs loading, 4 h irradiation, 10 mM HCO_3^-, 10 mM Cl^-, 10 mM SO_4^{2-})

4.4.4 Photocatalytic removal of BPA from a CECs mixture using floating TNTs@PUF

Figure 4.11(a) shows the photocatalytic activity of floating TNTs@PUF for the removal of BPA from a mixture of CECs, including SMZ, FLZ, CBZ, ATZ, IBP, and GFZ, under simulated sunlight irradiation. Error bars present the standard deviation of two replicates. TNTs@PUF achieved 80% removal of BPA from the CECs mixture after 4 h of irradiation. In comparison, when BPA was tested as a single pollutant, its removal reached 98%, as shown in Section 4.4.2. Similar results were observed for SMX and CBZ after 4 h. The removal of SMX from the mixture was 70%, while it was 98% when assessed individually. In addition, TNTs@PUF removed 71% of CBZ from the

mixture, compared to 97% in the single-pollutant system. The results indicated that the removal efficiency of pollutants decreased when they were present in the mixture compared with when treated individually. This reduction is likely attributable to competitive adsorption of pollutants (see dark in Figure 4.11(a)) on the photocatalyst's active sites or potential interactions within the mixture that restrict access to the photocatalyst surface, thereby decreasing the photocatalytic activity of TNTs@PUF in a mixed-pollutant system. For the other pollutants in the CECs mixture, removal efficiencies were 51% for FLZ, 26% for ATZ, 98% for IBP, and 92% for GFZ. Figure 4.11(b) presents the apparent first-order rate constant for BPA removal from the CECs mixture by floating TNTs@PUF. The k_{app} for BPA was 0.0062 min^{-1} in the CECs mixture, compared to 0.0156 min^{-1} when BPA was present as a single pollutant (Figure 4.7(a)).

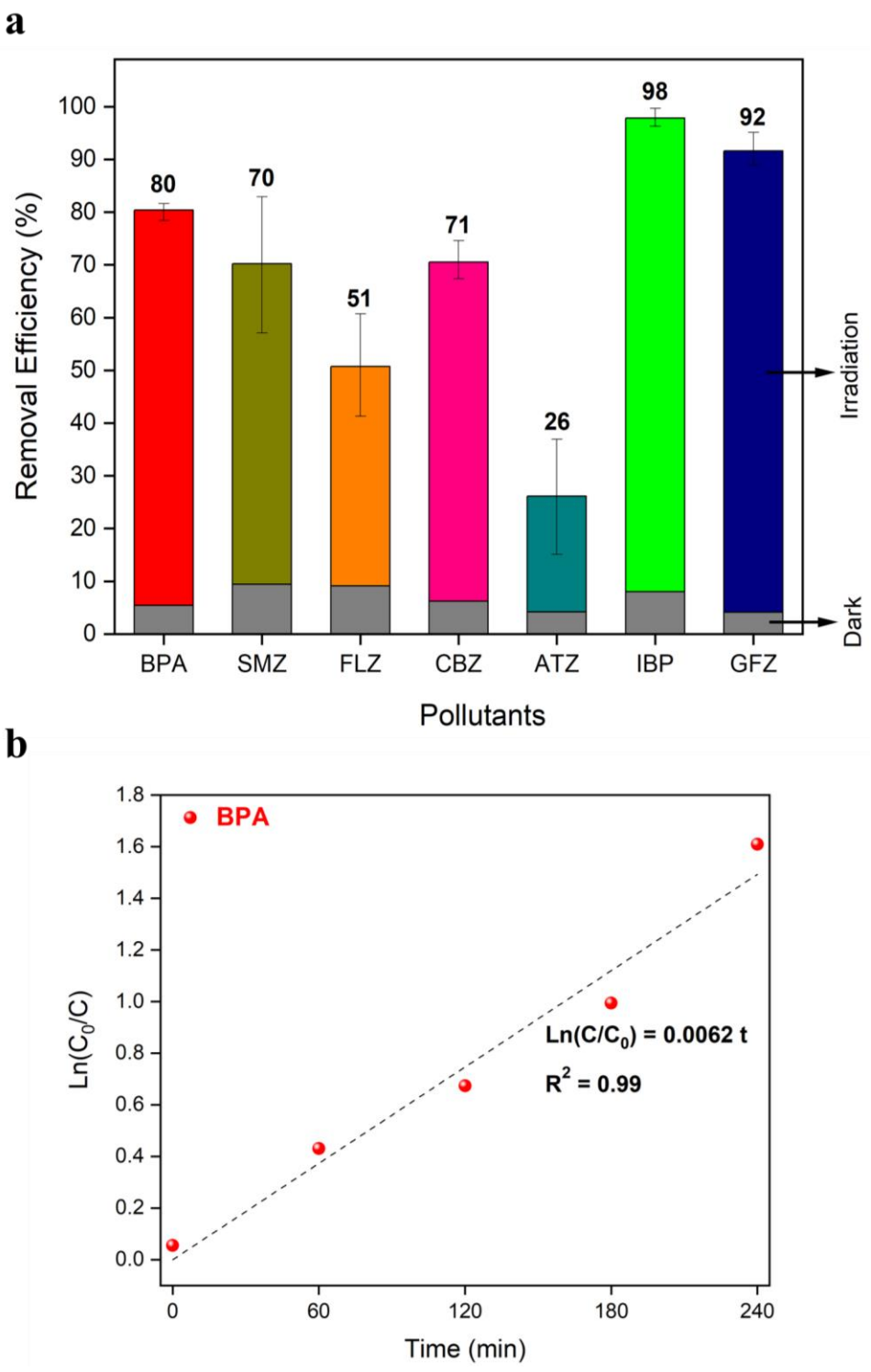

Figure 4.11 (a) Removal efficiency of BPA from a CECs mixture and (b) apparent first-order rate constant for BPA removal from a CECs mixture using floating TNTs@PUF (CECs mixture, 20 mg/L pollutant concentration, 0.2 g TNTs loading, 4 h irradiation)

4.5 Conclusion

We presented a floating photocatalytic system, TNTs@PUF, for the removal of different organic contaminants under simulated sunlight irradiation (300 W commercial solar lamp, 35 W/m^2 intensity). Removal efficiencies for individual contaminants after 4 h of irradiation were 98% (BPA), 98% (MO), 85% (MB), 98% (BZ), 98% (IPU), 98% (SMZ), and 97% (CBZ). When natural organic matter, such as humic acid, citric acid, and oxalic acid, was present in the BPA solution, the photocatalytic activity of floating TNTs@PUF was inhibited, reducing BPA removal to 80%, 86%, and 30%, respectively. Similarly, inorganic anions lowered BPA removal to 80% with HCO_3^-, 86% with Cl^-, and 90% with SO_4^{2-}. In addition, 80% of BPA was removed from a mixture of CECs (SMZ, CBZ, FLZ, ATZ, IBP, GFZ) using floating TNTs@PUF. Our results indicate that the floating TNTs@PUF photocatalyst is a promising approach for removing a range of organic pollutants, such as EDCs, dyes, pesticides, and pharmaceuticals. Our floating photocatalytic system effectively removes BPA from different water matrices and a CECs mixture, underscoring its potential for real-world wastewater treatment.

4.6 Acknowledgments

The authors thank the Velux Stiftung Foundation for the financial support through project 1381, “SUNFLOAT - Water decontamination by sunlight-driven floating photocatalytic systems”, and through the Natural Sciences and Engineering Research Council of Canada (NSERC). We also appreciate the support of Bourse d'excellence Neil R. Mitchell et Danièle Dumais from Polytechnique Montréal, Canada. Additionally, we extend our thanks to Mr. Marco Aurelio Pineda Castro for analyzing the CECs samples.

Funding

Daria C. Boffito and Claudia L. Bianchi reports financial support was provided by Velux Foundation. Daria C. Boffito reports was provided by Natural Sciences and Engineering Research Council of Canada.

Ethics, Consent to Participate, and Consent to Publish declarations

Not applicable.

CHAPTER 5 ARTICLE 3: ENHANCED PHOTO-INDUCED CHARGE GENERATION OF FLOATING SULFUR-DOPED TiO_2 DOUBLE-WALLED NANOTUBES FOR EFFICIENT SUNLIGHT-DRIVEN PHOTOCATALYTIC DEGRADATION OF BISPHENOL A

Nila Davari[1], Javad Vahabzadeh Pasikhani[2], Houeida Issa Hamoud[1], Ermelinda Falletta[3,4], Claudia L. Bianchi[3,4], Viviane Yargeau[5], Daria C. Boffito[1,6*]

[1] Department of Chemical Engineering, Polytechnique Montréal, Montréal, Canada

[2] Process Engineering Advanced Research Lab (PEARL), Department of Chemical Engineering, Polytechnique Montréal, Université de Montréal, PO Box 6079, Stn Centre-Ville, Montréal, QC, H3C 3A7, Canada

[3] Department of Chemistry, University of Milan, via C. Golgi, 19, 20133, Milan, Italy

[4] Consorzio Interuniversitario Nazionale per la Scienza e Tecnologia dei Materiali (INSTM), via Giusti 9, 50121, Florence, Italy

[5] Department of Chemical Engineering, McGill University, Montréal, Canada

[6] Canada Research Chair in Engineering Process Intensification and Catalysis

The article was published in Ceramics International, Volume 51, Issue 27, Part B, 6 September 2025, 53519-53534.

Author contributions

Nila Davari: Writing – original draft, Visualization, Validation, Methodology, Investigation, Conceptualization. Javad Vahabzadeh Pasikhani: Writing – review & editing, Visualization, Methodology, Investigation. Houeida Issa Hamoud: Writing – review & editing, Methodology. Ermelinda Falletta: Writing – review & editing, Methodology. Claudia L. Bianchi: Writing – review & editing, Project administration, Methodology, Funding acquisition. Viviane Yargeau: Writing – review & editing, Supervision, Project administration, Methodology. Daria C. Boffito:

Writing – review & editing, Supervision, Resources, Project administration, Methodology, Funding acquisition.

5.1 Abstract

Floating photocatalysts are an innovative class of immobilized semiconductors that can address the limitations of traditional photocatalysis by directly harvesting light, enhancing oxygen transfer from the air, and enabling easy photocatalyst recovery. In the present study, we developed a novel ultrasound-assisted solvothermal method to synthesize sulfur-doped TiO_2 nanotubes (S-TNT). The floating photocatalysts were prepared by immobilizing S-TNT onto buoyant polyurethane foam (PUF) with an open-cell structure using a wet chemical deposition method. The synthesis yielded double-walled TNT doped with 3 nm sulfur nanodots. The ultrasound-assisted solvothermal synthesis method using thiourea as a sulfur precursor resulted in the incorporation of anionic sulfur (S^{2-}) and cationic sulfur (S^{4+}, S^{6+}) into TNT. Among different sulfur dopants (0.5 to 2 wt.%), 1 wt.% (S-TNT-1) was optimal to achieve superior optical properties, enhanced photo-induced charge generation, and effective electron-hole pair separation. Compared to bare TNT, the specific surface area of S-TNT-1 increased from 110 to 267 m^2/g, while the bandgap energy decreased from 3 to 2.48 eV. The photocurrent density of S-TNT-1 (0.6 mA/cm^2) was threefold higher than that of TNT. Evaluating operating parameters indicated that >96% of 10 mg/L Bisphenol A (BPA) was degraded with 0.2 g S-TNT-1@PUF at pH = 8 after 75 min of simulated sunlight irradiation. This degradation followed first-order kinetics, with an apparent rate constant of 0.05 min^{-1}, in which $^{\bullet}OH$ was the reactive species that contributed most (31%).

Keywords: Floating TiO_2, Sulfur nanostructure, Photocatalytic degradation, Sunlight irradiation

5.2 Introduction

The growing scarcity of drinking water and the contamination of water resources with resistant organic pollutants underscore the urgent need for advanced water treatment technologies. Advanced oxidation processes (AOPs), particularly photocatalysis, offer a clean solution for eliminating the resistant organic contaminants from polluted water without generating secondary pollutants [37, 107, 241, 242]. In photocatalysis, exposure of a semiconductor to a light irradiation source, provided that the bandgap energy of the semiconductor is smaller than or equal to the photon energy of light, leads to the formation of electron-hole pairs within the semiconductor [47,

188]. The electron-hole pairs can interact with water and oxygen to generate reactive oxygen species (ROS) that degrade any resistant organic pollutants, such as Bisphenol A (BPA), an endocrine-disrupting compound (EDC) [28-30].

Photocatalytic wastewater reactors are generally categorized as suspended and immobilized systems. In the suspended systems, powder photocatalysts are dispersed in the medium to be treated. In contrast, in immobilized systems, photocatalysts are either coated on the reactor walls or supported on a specific substrate [142, 170, 243]. Immobilized systems have several advantages over suspension systems, including easier photocatalyst recovery with reduced loss and integration with continuous reactor configurations, such as continuous stirred-tank reactors (CSTR) and plug flow reactors (PFR) [244, 245]. Considering the immobilized photocatalytic systems, coating photocatalysts onto the surface of a buoyant substrate with a density below 1000 kg/m^3 leads to the flotation of photocatalysts at the water surface. Unlike conventional immobilized photocatalysts, which form a solid-water diphase interface, floating photocatalysts establish an air-solid-water triphase interface. This configuration allows direct light irradiation on the photocatalyst surface without attenuation from water, resulting in higher photon energy harvesting and photo-induced charge generation [10, 11, 104]. In addition, constructing the air-solid-water triphase in the floating photocatalytic system can increase oxygen transfer from the air and enhance photocatalytic reactions by raising ROS generation in the submerged part of the floating photocatalyst in water [10]. Furthermore, floating photocatalysts simplify the photocatalyst recovery after the wastewater treatment process [9-11, 105].

Selecting an appropriate buoyant substrate for the photocatalyst is critical to enhance its stability and reusability. TiO_2 nanostructures, common photocatalysts for wastewater treatment, have been supported on various substrates, including perlite, cork, vermiculite, glass microbead, graphite, silicone, light-expanded clay aggregate, autoclaved cellular concrete, palm trunk, canvas [9, 103], polymers [99, 190], aerogel [8], and alginate beads [246, 247]. Among these floating substrates, polyurethane foam (PUF) is a three-dimensional macroporous polymer with an open-cell structure that benefits from lightweight, high porosity and surface-to-volume ratio [135, 248]. These features make PUF a suitable substrate for floating photocatalytic wastewater treatment. In our previous work [191], we manufactured one-dimensional TiO_2 nanotubes (TNT) supported on a floating PUF substrate. Such a system degraded over 96% of BPA under 180 min of simulated sunlight

irradiation. Despite the high photocatalytic efficiency, the reaction rate was hindered by the intrinsic limitations of TiO_2, including its high bandgap energy, low photocurrent density, and insufficient photo-induced charge carrier separation. To address these challenges, modifying TiO_2 supported on PUF with metal or oxide dopants, such as Ag, SiC, SiO_2, Al_2O_3, W_xO_y, and Ru_xSe_y, has been proposed for improving the performance of TiO_2 in wastewater treatment [134, 137, 178, 249-252]. However, these modifications often suffer from high costs or low stability of metal dopants. Non-metallic modifications, such as graphene oxide, reduced graphene oxide, nitrogen, or graphite carbon nitride, offer an alternative approach to improve photocatalytic activity and overcome the issues associated with metal or metallic compound doping [104, 253].

Sulfur doping on TiO_2, as a non-metal dopant, narrows the bandgap energy of TiO_2 and causes a redshift toward the visible light region. Notably, unlike other non-metal dopants, sulfur can be incorporated into TiO_2 in multiple oxidation states (i.e. S^{2-}, S^{4+}, or S^{6+}) depending on the sulfur precursor and synthesis method [254]. In the cationic oxidation state, S^{4+} or S^{6+} is replaced by Ti^{4+}, forming S-O-Ti bonds, while the anionic oxidation state, S^{2-}, substitutes oxygen in TiO_2, leading to Ti-S bonds. Regardless of the oxidation state, both cationic and anionic sulfur can assist TiO_2 in increasing photo-induced charge generation and decreasing electron-hole pair recombination [255]. Despite these promising characteristics, the potential of sulfur-doped TNT (S-TNT) remains underexplored, particularly in the floating photocatalytic systems. Investigating sulfur doping in these configurations can pave the way for improving photocatalytic wastewater treatment and the applicability of floating systems under sunlight irradiation.

Herein, for the first time, we developed a new synthesis process to yield floating S-TNT supported on PUF (S-TNT@PUF). This innovative photocatalyst was tested to eliminate aqueous BPA under simulated sunlight irradiation. Firstly, S-TNT photocatalysts were synthesized by an ultrasound-assisted solvothermal method. Secondly, the as-prepared S-TNT photocatalysts were deposited on the PUF via a wet chemical deposition approach. The photocatalysts were then comprehensively characterized to determine their morphological features, elemental compositions, crystalline phase, chemical structures and valence states, thermal stability, zeta potential, and textural and optical properties. In addition, the photocurrent density, photo-response, and photoconversion efficiency over the synthesized floating photocatalysts were evaluated by voltammetry analyses. We also investigated the influence of key operating parameters, including photocatalyst loading, BPA

concentration, and pH, on BPA degradation using floating TNT@PUF and S-TNT@PUF photocatalysts. Moreover, the kinetics of the reaction, the reusability of the photocatalysts, the contribution of reactive species, and the possible mechanism of BPA degradation were investigated under optimal treatment conditions. Lastly, we identified BPA transformation products (TPs) and proposed possible degradation pathways under optimal treatment conditions.

5.3 Materials and Methods

5.3.1 Materials

The reagents included titanium(IV) butoxide ($C_{16}H_{36}O_4Ti$, 97%, Sigma Aldrich), ethanol (C_2H_6O, 95%, Commercial Alcohols), sodium hydroxide (NaOH, 98%, Thermo Scientific), hydrochloric acid (HCl, 37% w/w, Fisher Scientific), thiourea (CH_4N_2S, ≥ 99.0%, Sigma Aldrich), ethylene glycol ($C_2H_6O_2$, ≥ 99%, Sigma Aldrich), polyvinyl alcohol (low molecular weight, 98-99% hydrolyzed, Thermo Scientific Chemicals), ammonium oxalate ($(NH_4)_2C_2O_4$, ≥ 99%, Sigma Aldrich), tert-butanol ($C_4H_{10}O$, ≥ 99.5%, Sigma Aldrich), silver nitrate ($AgNO_3$, ≥ 99.9%, Sigma Aldrich), benzoquinone ($C_6H_4O_2$, ≥ 98%, Sigma Aldrich), and bisphenol A (≥ 99%, Sigma Aldrich). A commercial polyurethane foam (Medium porous, 20 pores per inch [PPI]) was purchased from Amtra. All solutions were prepared with deionized water.

5.3.2 Fabrication of photocatalysts

5.3.2.1 TNT

We synthesized TNT photocatalysts using a hydrothermal method reported by Kasuga et al. [256], with some modifications. In this method, 1 g of TiO_2 nanoparticles obtained from the sol-gel method [191] was added to a NaOH solution (10 M, 50 mL) under stirring for 30 min at room temperature. The mixture was then subjected to an ultrasonic bath (Branson 2800, 23 cm (L) × 14 cm (W) × 10 cm (D), 1.8 L, 110 W) for 30 min. Notably, ultrasonication before the hydrothermal method can uniformly disperse TiO_2 nanoparticles in the solution and control the morphology of TNT, resulting in the formation of longer TNT compared to the regular hydrothermal method [94]. Next, the homogenized suspension was transferred into a Teflon-lined autoclave (100 mL) and heated up to 160 $^{\circ}$C for 24 h in an oven. After cooling to room temperature, the white precipitate was filtered and washed with deionized water and 0.1 M HCl until reaching a neutral pH. The

sample was then dried at 80 °C in an oven, yielding TNT. Finally, TNT photocatalysts were calcined at 400 °C for 2 h in a muffle furnace with a heating rate of 5 °C/min under an air atmosphere.

5.3.2.2 S-TNT

We fabricated S-TNT photocatalysts using the previously synthesized TNT and CH_4N_2S as a sulfur precursor through the ultrasound-assisted solvothermal method. In this synthesis method, 0.5 g of TNT was mixed with C_2H_6O (40 mL) and $C_2H_6O_2$ (10 mL) under 30 min stirring at room temperature. CH_4N_2S with a weight percentage (wt.%) of 0.5, 1, and 2 was added to the mixture, followed by stirring for 90 min. The solution was then sonicated for 30 min (Branson 2800, 23 cm (L) × 14 cm (W) × 10 cm (D), 1.8 L, 110 W). Subsequently, the obtained suspension was placed in a Teflon-lined autoclave (100 mL) and maintained in an oven at 150 °C for 24 h. After cooling, the prepared sample was filtered and washed multiple times with deionized water to remove the solvent. Finally, the synthesized S-TNT samples underwent drying at 80 °C in the oven. We labelled the fabricated S-TNT photocatalysts as S-TNT-0.5, S-TNT-1, and S-TNT-2, corresponding to the nominal weight percentages of the sulfur precursor of 0.5, 1, and 2, respectively.

5.3.2.3 Floating TNT@PUF and S-TNT@PUF

We prepared floating photocatalysts, namely TNT@PUF, S-TNT-0.5@PUF, S-TNT-1@PUF, and S-TNT-2@PUF, by immobilizing powder TNT and S-TNT samples onto the PUF by the wet chemical deposition method. The deposition setup involved porous PUF as a floating substrate (4 cm (d) × 1 cm (h), 85% porosity) and polyvinyl alcohol (PVA) as a binder [140]. First, 1 wt.% of PVA was dissolved in 30 mL of deionized water, and the solution was heated to 95 °C for 3 h in a three-neck flask (100 mL). Afterwards, different amounts of TNT and S-TNT samples (0.5 g, 0.7 g, 1 g) were added to the flask and continuously heated at 95 °C for 2 h. The resulting solution was then cooled to 80 °C. Finally, the PUF was immersed in the suspension and dried at 80 °C in the oven to achieve floating TNT@PUF and S-TNT@PUF photocatalysts. Figure 5.1 shows the steps in the synthesis of TNT, S-TNT, and floating TNT@PUF and S-TNT@PUF.

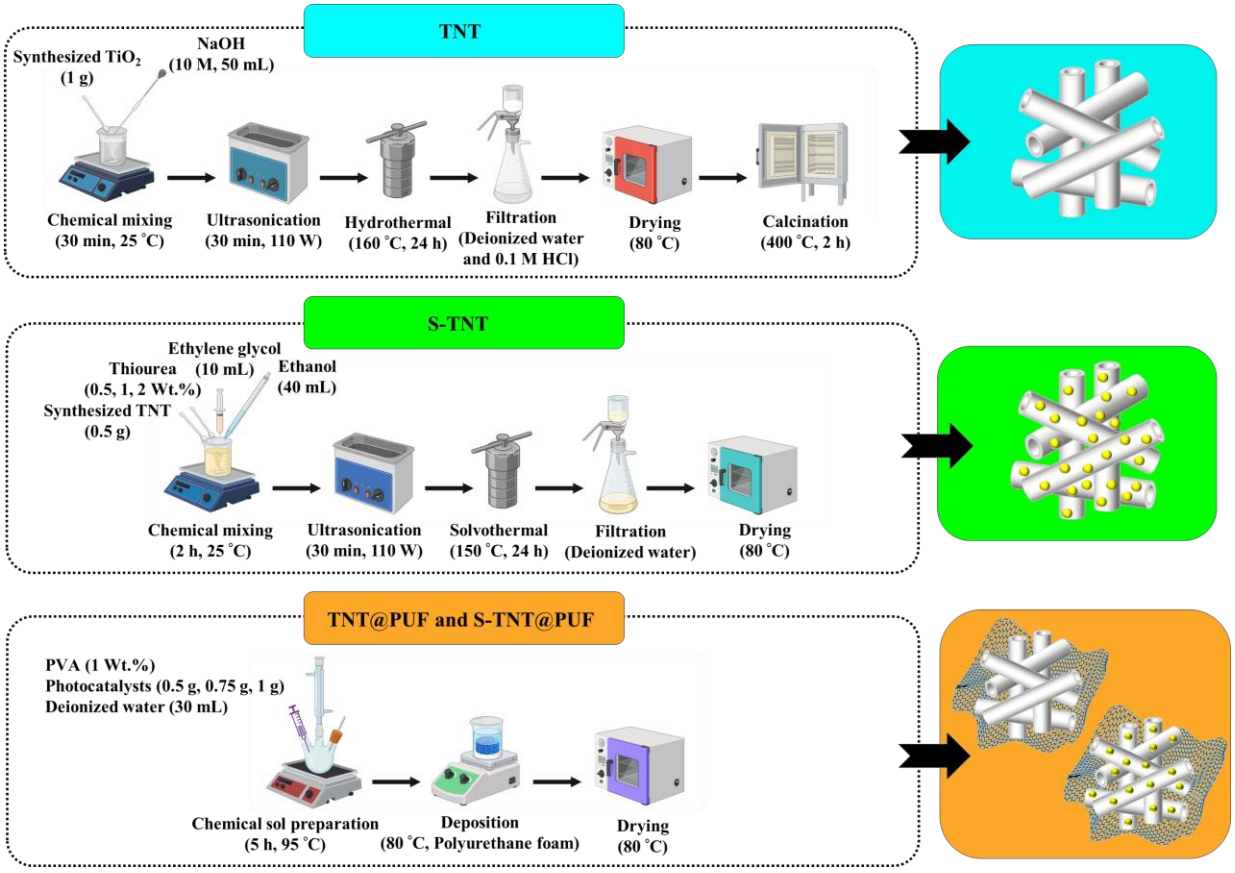

Figure 5.1 Schematic of the synthesis steps of TNT, S-TNT, and floating TNT@PUF and S-TNT@PUF

5.3.3 Characterization of photocatalysts

The morphology and elemental composition of the synthesized photocatalysts were investigated by field-emission scanning electron microscopy (FESEM, JSM-7600TFE, JEOL) equipped with energy-dispersive X-ray spectroscopy (EDS). We utilized transmission electron microscopy (TEM) and high-resolution transmission electron microscopy (HR-TEM) to further study the morphology and structure of the photocatalysts (JEM-2100F, JEOL). The size of the synthesized photocatalysts was measured by Digimizer software (version 5.3.5). The crystalline phase of the photocatalysts was characterized by an X-ray diffractometer (XRD, D8 Advance, Bruker). The crystallite size of the photocatalysts was calculated using the Scherrer Equation [141].

$$D = \frac{K\lambda}{\beta cos\theta} \tag{5.1}$$

In Equation 5.1, D is the crystallite size (nm), K is a constant (shape factor = 0.94), λ is the wavelength of the X-ray radiation source (Cu-Kα = 0.15406 nm), β is the full width at half maximum (FWHM) of the peak (in radian), and θ is half of the Bragg angle (in degrees).

We determined the optical features of the photocatalysts by diffuse reflectance spectroscopy (DRS) analysis using a UV-Vis spectrophotometer (Evolution™ 220, Thermo Fisher Scientific) and photoluminescence spectroscopy (PL, FL0905M016, Cary Eclipse). The bandgap energy of the photocatalysts (E_g) was calculated by plotting $[F(R) \times h\vartheta]^{0.5}$ vs. $h\vartheta$ using Equation 5.2 [142, 143].

$$F(R) = \frac{(1-R)^2}{2R} \tag{5.2}$$

Where $F(R)$ is the Kubelka-Munk function, R is reflectance, and $h\vartheta$ is photon energy.

The conduction band edge potential and valence band edge potential of the photocatalysts were estimated by Mulliken's electronegativity theory as follows: [72, 257]

$$E_{CB} = X - E^e - (0.5\, E_g) \tag{5.3}$$

$$E_{VB} = E_{CB} + E_g \tag{5.4}$$

In Equations 5.3 and 5.4, E_{CB} is the potential of the conduction band edge, E_{VB} is the potential of the valence band edge, E^e is the energy of free electrons on the hydrogen scale (about 4.5 eV), and X is the electronegativity of the photocatalysts calculated as follows:

$$X = \left(\prod_i^n x_i^{v_i}\right)^{\frac{1}{\sum_i^n v_i}} \tag{5.5}$$

$$x_i = \frac{E_a + E_{ion}}{2} \tag{5.6}$$

Where x_i is Mulliken's electronegativity of element i, v_i is the number of elements, E_a is the electron affinity, and E_{ion} is the first ionization energy (Equations 5.5 and 5.6).

For the chemical compositions and valence states of the photocatalysts, X-ray photoelectron spectroscopy (XPS) was performed by an X-ray photoelectron spectrometer microprobe (VG ESCALAB 250Xi, Thermo Scientific). Thermal stability and quantitative analysis of the photocatalysts were studied by thermogravimetric analysis (TGA, TA Instruments-550, USA) under an air atmosphere with a heating rate of 5 ˚C/min. Adsorption-desorption isotherms using the Brunauer-Emmett-Teller (BET) method were recorded to measure the textural properties of the

photocatalysts, including specific surface area, total pore volume, and mean pore size using Nitrogen adsorption at 77 K (Autosorb 6100 FKM MP - MP, Anton Paar). The zeta potential of S-TNT photocatalysts in deionized water was measured by a zeta potential analyzer (ZetaProbe, Colloidal Dynamics), with the pH adjusted by titration using nitric acid (HNO_3) and potassium hydroxide (KOH) solutions.

5.3.4 Photoelectrochemical characterization

The photo-induced charge generation, photo-response to sunlight irradiation, and photoconversion efficiency of the synthesized photocatalysts were evaluated by voltammetry analysis, including linear sweep voltammetry (LSV) and chronoamperometry. A potentiostat/galvanostat (VersaSTAT3, AMETEK Scientific, USA) served as an electrochemical workstation connected to a standard three-electrode photoelectrochemical cell. The cell configuration contained photocatalysts coated onto a fluorine-doped tin oxide (FTO) glass substrate as the working electrode, a platinum foil as the counter electrode, and an Ag/AgCl electrode as the reference electrode. The photoelectrochemical experiments were conducted in a 0.01 M sodium sulfate (Na_2SO_4) electrolyte at a scan rate of 100 mV/s. The working electrode was illuminated with a 300 W commercial solar lamp (Ultra-Vitalux, Osram) at an intensity of 35 W/m^2. We replicated all photoelectrochemical measurements three times to ensure the reliability of the experiments and presented the results as an average of these repetitions.

5.3.5 Floating photocatalytic experiments

We assessed the photocatalytic activity of floating TNT@PUF and S-TNT@PUF to degrade BPA in a batch floating catalyst photoreactor under simulated sunlight irradiation. The effects of operating parameters on BPA degradation were investigated, including photocatalyst loading (0.1 g, 0.2 g, 0.4 g), BPA concentration (10 mg/L, 20 mg/L, 40 mg/L), and pH (5.7, 8, 10) over the different synthesized photocatalysts (TNT@PUF, S-TNT-0.5@PUF, S-TNT-1@PUF, S-TNT-2@PUF). The loadings of 0.1 g, 0.2 g, and 0.4 g represent the amount of the photocatalysts deposited onto the floating PUF, and the initial BPA solution was 200 mL. The pH of the BPA solution was adjusted with NaOH (0.1 M), and the natural pH of the BPA solution was 5.7. We used a 300 W commercial solar lamp (Ultra-Vitalux, Osram) as a light source with an intensity of 35 W/m^2, placed 20 cm above the reactor. Before starting the photocatalytic reaction, each photocatalyst was kept in the dark for 60 min to reach adsorption-desorption equilibrium. Blank

tests (photolysis) were also performed under the light source without adding any photocatalysts. All photocatalytic experiments were replicated three times under the same reaction conditions. Additionally, we performed inductively coupled plasma-optical emission spectroscopy analysis (ICP-OES, Agilent, 5110-SVDV) to quantify the concentration of Ti and S elements leaching from the floating S-TNT-1@PUF photocatalyst under optimal treatment conditions (S-TNT-1@PUF loading = 0.2 g, BPA concentration = 10 mg/L, irradiation time = 75 min, and pH = 8).

5.3.6 Reusability experiments

The reusability and stability of the S-TNT@PUF photocatalyst for BPA degradation were evaluated under optimal treatment conditions (S-TNT-1@PUF loading = 0.2 g, BPA concentration = 10 mg/L, irradiation time = 75 min, and pH = 8). After each cycle, the photocatalyst was removed from the photoreactor, washed with deionized water, and then dried in an oven at 80 $^{\circ}$C prior to reuse. The experimental conditions were the same for each cycle.

5.3.7 Scavenging reactive species experiments

We investigated the main reactive species involved in the photocatalytic degradation of BPA under optimal treatment conditions (S-TNT-1@PUF loading = 0.2 g, BPA concentration = 10 mg/L, irradiation time = 75 min, and pH = 8). Scavenging experiments were carried out by adding 1 mM of ammonium oxalate (AO), tert-butanol (t-BuOH), silver nitrate ($AgNO_3$), and benzoquinone (BZQ) to the floating catalyst photoreactor as scavengers of photogenerated holes (h^+), hydroxyl radicals ($^{\bullet}OH$), electrons (e^-), and superoxide anions ($^{\bullet}O_2^-$), respectively. Also, an electron paramagnetic resonance spectrometer (EPR, Magnettech ESR5000, Bruker) was utilized with the spin trapping technique (50 mM of 5,5-Dimethyl-1-pyrroline N-oxide [DMPO], Sigma Aldrich) to detect reactive species formed during the photocatalytic degradation of BPA under optimal treatment conditions.

5.3.8 BPA analysis

Changes in BPA concentration were monitored by a UV-Vis spectrophotometer (Evolution™ 220, Thermo Fisher Scientific) within the wavelength range of 200–400 nm. During the photocatalytic reaction, 2 mL of BPA solution was withdrawn at 30-minute intervals. The collected sample was placed in a quartz cuvette and analyzed in a UV-Vis spectrophotometer to measure the absorbance

spectrum. The BPA degradation efficiency (η) was determined at the maximum wavelength of BPA (λ_{max} = 276 nm) by Equation 5.7.

$$\eta = \left(1 - \frac{C}{C_0}\right) \times 100\% \tag{5.7}$$

Where C_0 is the initial concentration of BPA and C is the concentration of BPA at time t.

The quantification of BPA was performed based on a calibration curve, which relates the absorbance peak at λ_{max} to BPA concentration. To do so, we prepared standard solutions of BPA ranging from 0.4 mg/L to 50 mg/L. The concentration of BPA in each sample was linearly correlated to the absorbance value at λ_{max} using Equation 5.8.

$$ABS = 0.017\, C_{BPA} + 0.0087 \tag{5.8}$$

In Equation 5.8, ABS is the absorbance, and C_{BPA} is the concentration of BPA.

The detection limit of the UV-Visible spectrophotometer measured for BPA was 0.4 mg/L. Therefore, by considering the initial concentration of 10 mg/L, we reported the degradation efficiency as >96% when BPA was undetectable by UV-Visible spectrophotometer.

TPs formed during the photocatalytic degradation of BPA under optimal treatment conditions were identified by high-performance liquid chromatography-mass spectrometry (HPLC-MS). The HPLC-MS analysis was performed using a Dionex UltiMate 3000 HPLC system (Thermo Scientific) coupled to a mass spectrometer (Thermo Scientific, Orbitrap Q-Exactive). The HPLC column was a Hypersil Gold C18 (100 mm × 2.1 mm, 1.9 µm, Thermo Scientific) maintained at 50 °C. The mobile phase consisted of HPLC-grade water with 0.1 mM ammonium fluoride (NH_4F) as solvent A and methanol with 0.1 mM NH_4F as solvent B. The mass spectrometer was operated in both positive and negative ionization modes (switch mode) with 50-500 m/z. The TPs of BPA were identified by exact monoisotopic mass with a mass tolerance of 10 ppm.

5.4 Results and Discussion

5.4.1 Characterization of photocatalysts

The SEM image of pristine PUF shows approximately a smooth surface with some roughness due to its open-cell structure before depositing the photocatalysts (Figure 5.2(a)). TNT and S-TNT-1 were successfully deposited onto the PUF (Figures 5.2(b) and 5.2(c)), fabricating floating

TNT@PUF and S-TNT-1@PUF photocatalysts (S-TNT-1@PUF represents the most efficient photocatalyst for eliminating BPA, as will be discussed in Section 5.4.2). As it is possible to observe, after the deposition of both TNT and S-TNT-1, PUF exhibits a rougher morphology. Figure 5.2(d) shows the EDS mapping of TNT@PUF, indicating uniform dispersion of Ti and O elements into PUF. Similarly, Ti, O, and S elements were evenly distributed in S-TNT-1@PUF (Figure 5.2(e)).

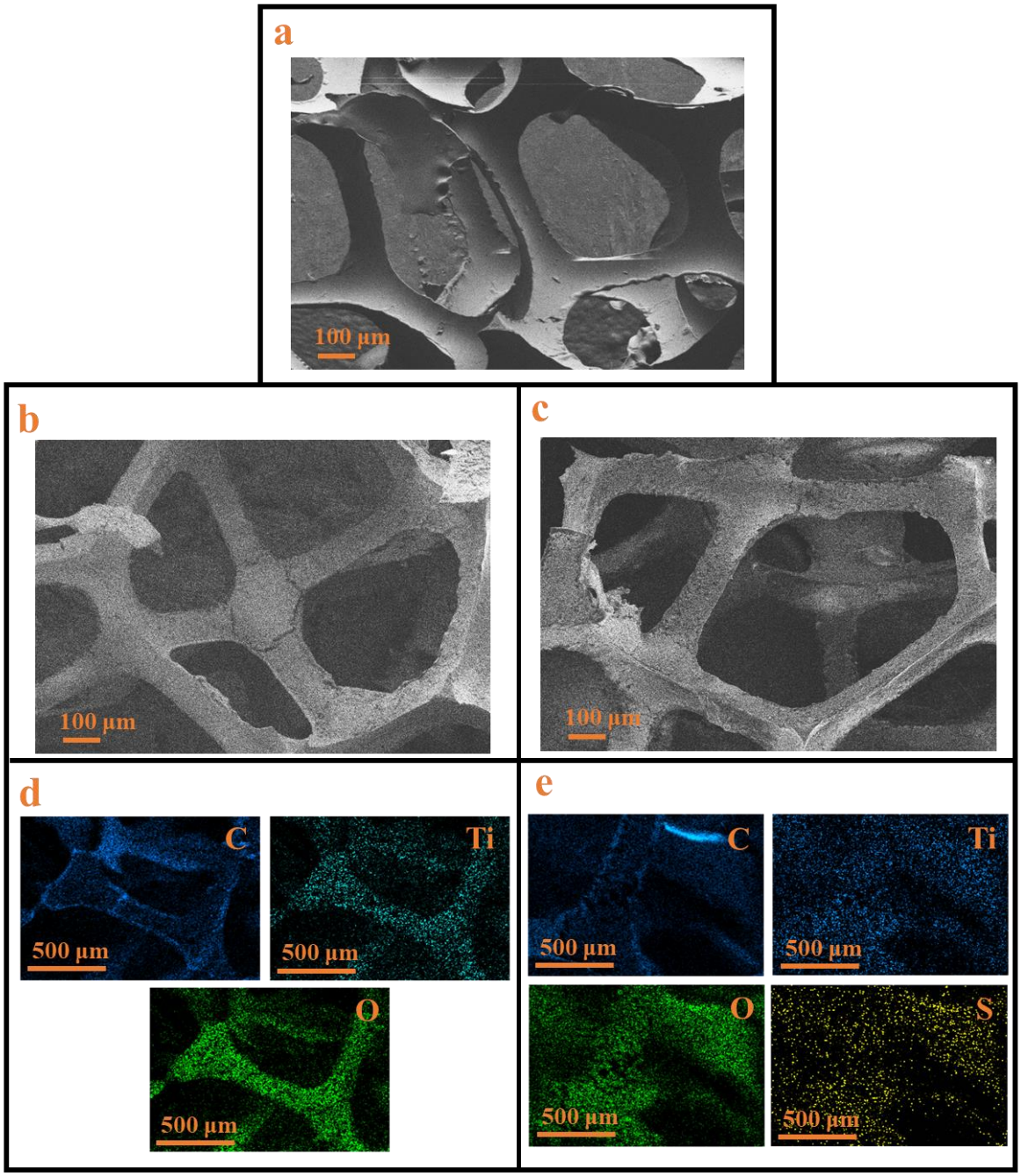

Figure 5.2 SEM images of (a) PUF, (b) TNT@PUF, and (c) S-TNT-1@PUF; EDS mappings of (d) TNT@PUF and (e) S-TNT-1@PUF

Figures 5.3(a) and 5.3(b) show the morphology of TNT and S-TNT-1, confirming the nanotubular structure of the photocatalysts. According to the TEM images, TNT was formed in a hollow nanotubular structure (Figure 5.3(c)), while S-TNT-1 exhibited a nanotube-shaped structure with sulfur nanospheres incorporated into TNT (Figure 5.3(d)). From the HR-TEM images, the external

diameter, internal diameter, and wall thickness of TNT were measured at 8.2 nm, 5.8 nm, and 1.2 nm on average, respectively. S-TNT-1 exhibited dimensions like those of TNT, with the incorporated spherical sulfur having an average diameter of 3 nm. In addition, the selected area electron diffraction (SAED) patterns of TNT and S-TNT-1 in Figures 5.3(c) and 5.3(d) present discontinuous rings corresponding to the crystalline anatase phase of TiO_2. The crystal plane spacing was measured at 0.351 nm, 0.237 nm, and 0.189 nm, indexed to the (101), (004), and (200) crystal planes of anatase TiO_2, respectively [258, 259]. Moreover, as depicted in Figure 5.3(e), the elemental composition of TNT was Ti (68 wt.%) and O (32 wt.%), while S-TNT-1 was composed of Ti (53.5 wt.%), O (45 wt.%), and S (1.5 wt.%) elements (Figure 5.3(f)). Figures 5.3(g) and 5.3(h) show that these elements were uniformly distributed on TNT and S-TNT-1.

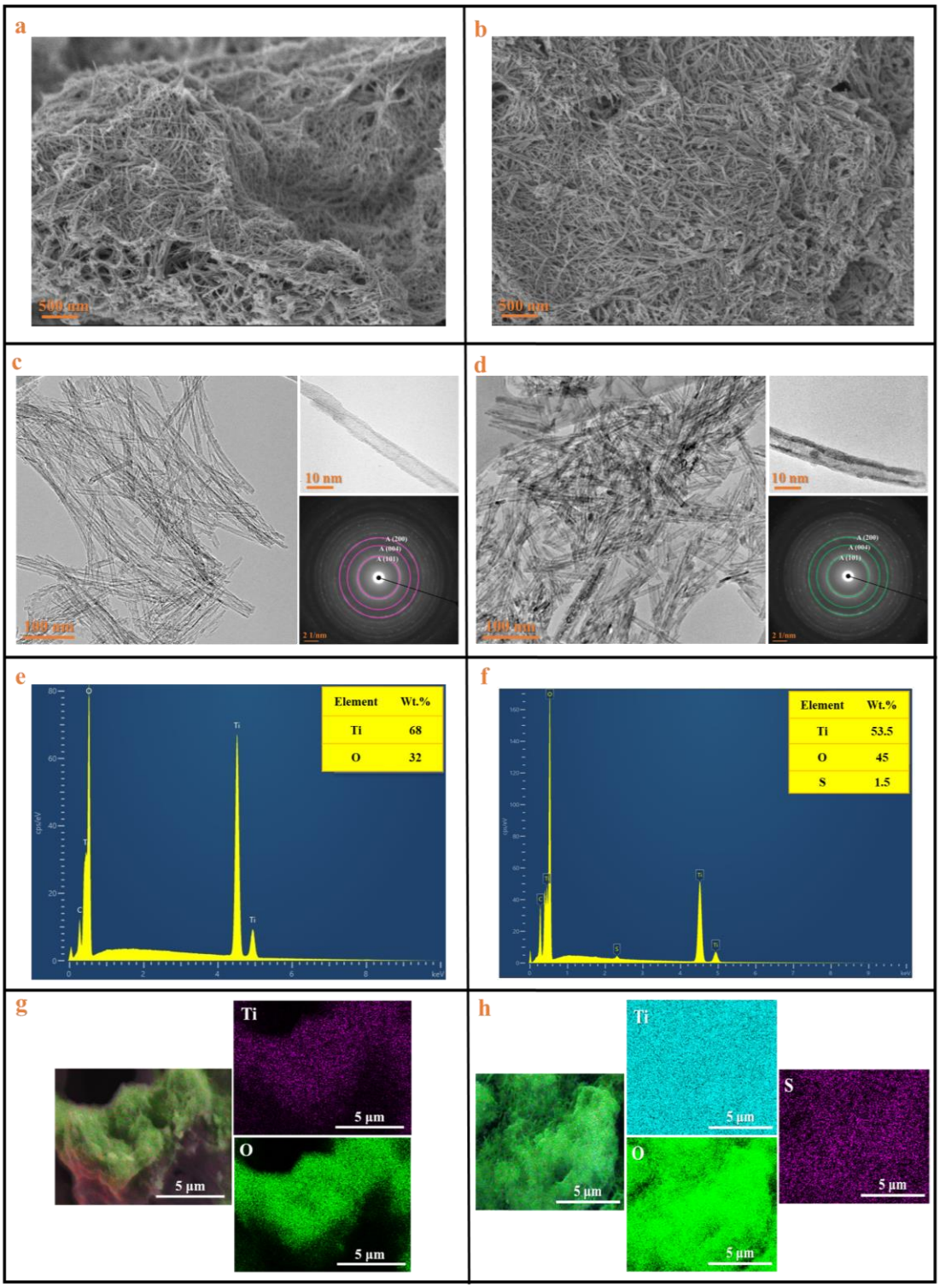

Figure 5.3 SEM images of (a) TNT and (b) S-TNT-1; TEM and HR-TEM images and SAED patterns of (c) TNT and (d) S-TNT-1; EDS spectra of (e) TNT and (f) S-TNT-1; EDS mappings of (g) TNT and (h) S-TNT-1

Figures 5.4(a–d) present the XPS results of TNT and S-TNT-1, indicating the presence of Ti and O elements in TNT, while S-TNT-1 contained Ti, O, and S elements (Figure 5.4(a)). S-TNT-1 exhibited two peaks at binding energies of 464.5 eV for Ti $2p_{1/2}$ and 458.8 eV for Ti $2p_{3/2}$ with a peak separation of 5.7 eV, corresponding to the existence of Ti^{4+} in S-TNT-1 (Figure 5.4(b)) [260, 261]. Figure 5.4(b) also presents a peak at 456.8 eV, related to the Ti^{4+} $2p_{3/2}$ in Ti-S bonds [262]. In addition, the Ti 2p spectrum of S-TNT-1 showed a 0.2 eV shift toward lower binding energy compared to TNT (Figure 5.4(b)), which can be related to the incorporation of sulfur into the TiO_2 lattice [254, 263]. Regarding the spectrum of O 1s (Figure 5.4(c)), a peak at a binding energy of 530.1 eV is attributed to the formation of lattice oxygen (Ti-O) in S-TNT-1 [263, 264]. Two peaks were observed at 168.6 eV for S $2p_{3/2}$ and 169.8 eV for S $2p_{1/2}$ (Figure 5.4(d)), referring to S^{6+} and S^{4+} species [260, 264]. The cation substitution of Ti^{4+} by sulfur in S^{4+} and bidentate SO_4^{2-} (S^{6+}) states resulted in the formation of S-O-Ti bonds in S-TNT-1, which confirms the successful incorporation of sulfur into the TNT structure [254, 265]. Additional peaks were detected at binding energies of 162.5 eV and 163.6 eV for S $2p_{3/2}$ and S $2p_{1/2}$, respectively, indicating that sulfur was also present as S^{2-} in S-TNT-1. The anionic state of sulfur results from some oxygen in the TiO_2 lattice being substituted by sulfur, leading to the formation of Ti-S bonds in S-TNT-1 [263, 266, 267].

Figure 5.4(e) shows the XRD patterns of TNT, S-TNT-1, S-TNT-2, and S-TNT-3, indicating a crystalline anatase structure for all photocatalysts. The anatase phase of the samples was confirmed by the peaks at 2θ values of 25.36°, 37.90°, 48.15°, 53.98°, 55.27°, and 62.86° corresponding to Miller indexes of (101), (004), (200), (105), (211), and (204), respectively (JCPDS card No. 21-1272) [72, 166]. The XRD results are consistent with the SAED patterns presented in Figures 5.3(c) and 5.3(d), suggesting the crystalline anatase phase of TiO_2. In addition, no sulfur peaks were detected in the XRD patterns of S-TNT photocatalysts, which is in line with previous reports [255, 260, 268-271]. Based on the XRD results, the crystallite size of the photocatalysts was calculated at the anatase peak of (101) using Equation 5.1. The crystallite size of TNT was 26 nm, and it was approximately 25 nm for S-TNT photocatalysts.

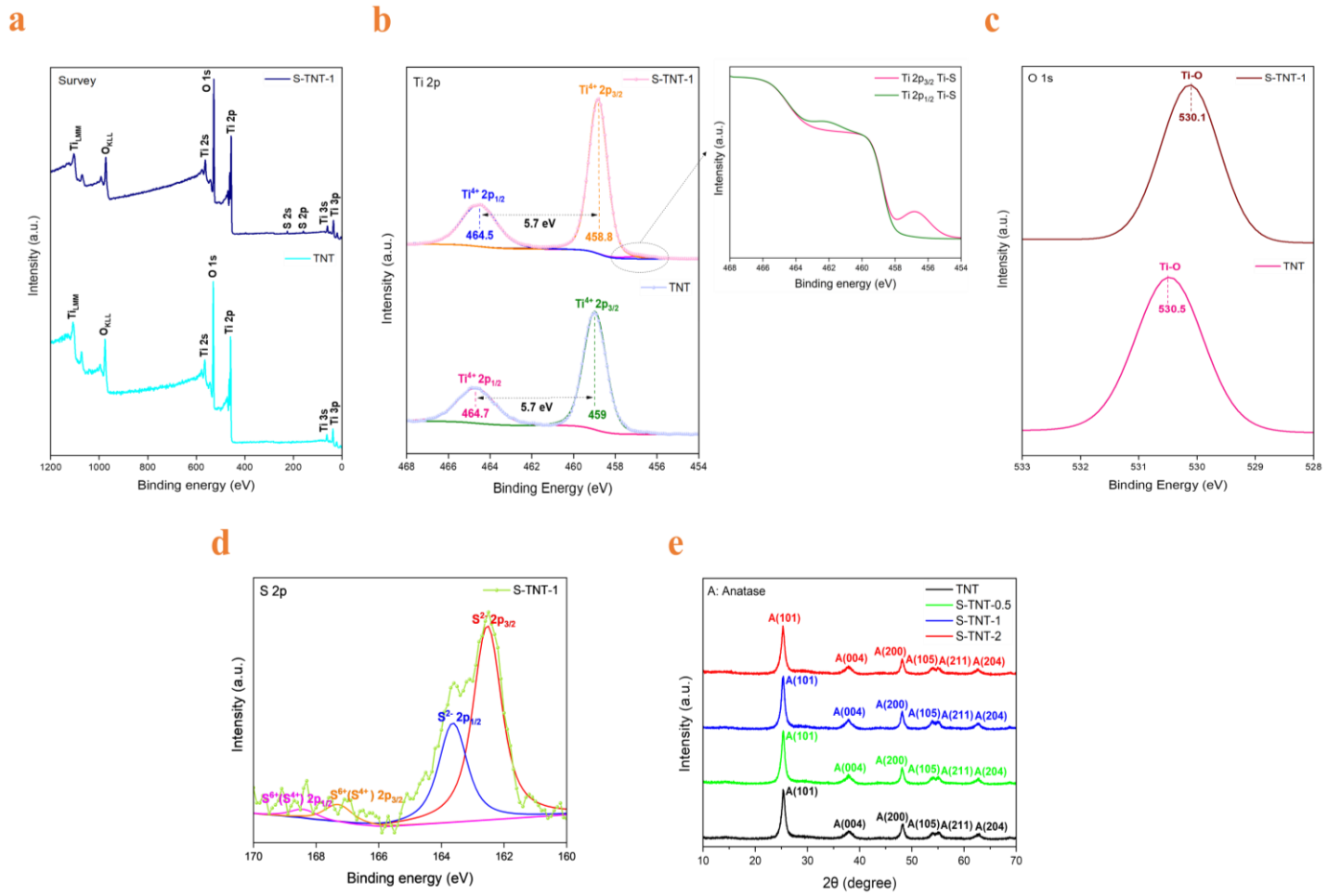

Figure 5.4 XPS spectra of TNT and S-TNT-1 (a) Full spectrum, (b-d) High-resolution spectra of Ti 2p, O 1s, and S 2p, respectively; (e) XRD patterns of TNT, S-TNT-0.5, S-TNT-1, and S-TNT-2

Figure 5.5(a) shows the TGA results of the fabricated photocatalysts over the temperature range of 25–800 ˚C. All samples exhibited about 2-3% weight loss below 250 ˚C, which can be attributed to the evaporation of moisture and crystalline water on the surface of the photocatalysts [139]. As depicted in Figure 5.5(a), a slight mass loss (0.3%) was observed for TNT above 250 ˚C, indicating the thermal stability of TNT [272]. Conversely, S-TNT samples exhibited a two-step weight loss. The first step, between 250 ˚C and 450 ˚C, is associated with the decomposition of sulfate groups (i.e., SO_4^{2-} and SO_2) [273, 274]. This aligns well with the XPS results, which confirmed the presence of S^{6+} and S^{4+} species in S-TNT photocatalysts. Figure 5.5(a) shows that S-TNT-0.5, S-TNT-1, and S-TNT-2 contained 4 wt.%, 5 wt.%, and 4.8 wt.% of sulfate groups, respectively. The second step of weight loss started at 450 ˚C and ended at 800 ˚C, corresponding to the decomposition of organic residues (less than 0.7 wt.%) [275]. Based on the results, 2 wt.% of the sulfur precursor did not further increase the sulfur content in the S-TNT photocatalyst, likely due to the saturation effect of sulfur doping [260, 276].

Figures 5.5(b) and 5.5(c) show the DRS analyses of TNT, S-TNT-0.5, S-TNT-1, and S-TNT-2. According to Figure 5.5(b), TNT had an intense absorption peak in the UV region, which can be due to the electron excitation from the conduction band of TNT to the valence band [170, 171]. TNT had an absorption edge of about 415 nm and a bandgap energy of 3 eV, calculated by Equation 5.2 (Figure 5.5(c)). In addition, a redshift was observed in the absorption spectra of S-TNT-0.5, S-TNT-1, and S-TNT-2, in which the absorption edge ranked in the order of around 425 nm, 500 nm, and 435 nm (Figure 5.5(b)). The redshift can result from sulfur doping into the TNT structure, which improves the light absorption in the visible range and reduces the photon energy required for electron excitation in the synthesized photocatalysts [277]. Moreover, all S-TNT photocatalysts had a smaller bandgap energy compared to undoped TNT. The bandgap energies of S-TNT-0.5, S-TNT-1, and S-TNT-2 were 2.92 eV, 2.48 eV, and 2.85 eV, respectively (Figure 5.5(c)). Increasing the sulfur content in S-TNT samples decreased the bandgap energy of the photocatalysts, improving the photocatalytic activity of S-TNT for visible light-driven photocatalysis [260, 271]. S-TNT-1 exhibited the lowest bandgap energy among all photocatalysts (2.48 eV) as it contained the highest amount of sulfate groups (5 wt.%) based on the TGA results.

The separation and recombination of the excited electron-hole pairs in TNT, S-TNT-0.5, S-TNT-1, and S-TNT-2 were investigated by PL (Figure 5.5(d)). The intense peak at about 424 nm is related to free excitons [278, 279]. In addition, the PL emission peaks at around 485 nm and 524

nm are assigned to oxygen vacancies of TiO_2 [278-280]. S-TNT-0.5, S-TNT-1, and S-TNT-2 exhibited lower PL intensities compared to TNT, suggesting that sulfur doping in TNT can reduce the recombination rate of photogenerated charge carriers and enhance the migration of excited electrons. As depicted in Figure 5.5(d), S-TNT-1 had the lowest PL intensity among all synthesized photocatalysts, which can improve the separation of electron-hole pairs and, thus, the photocatalytic activity.

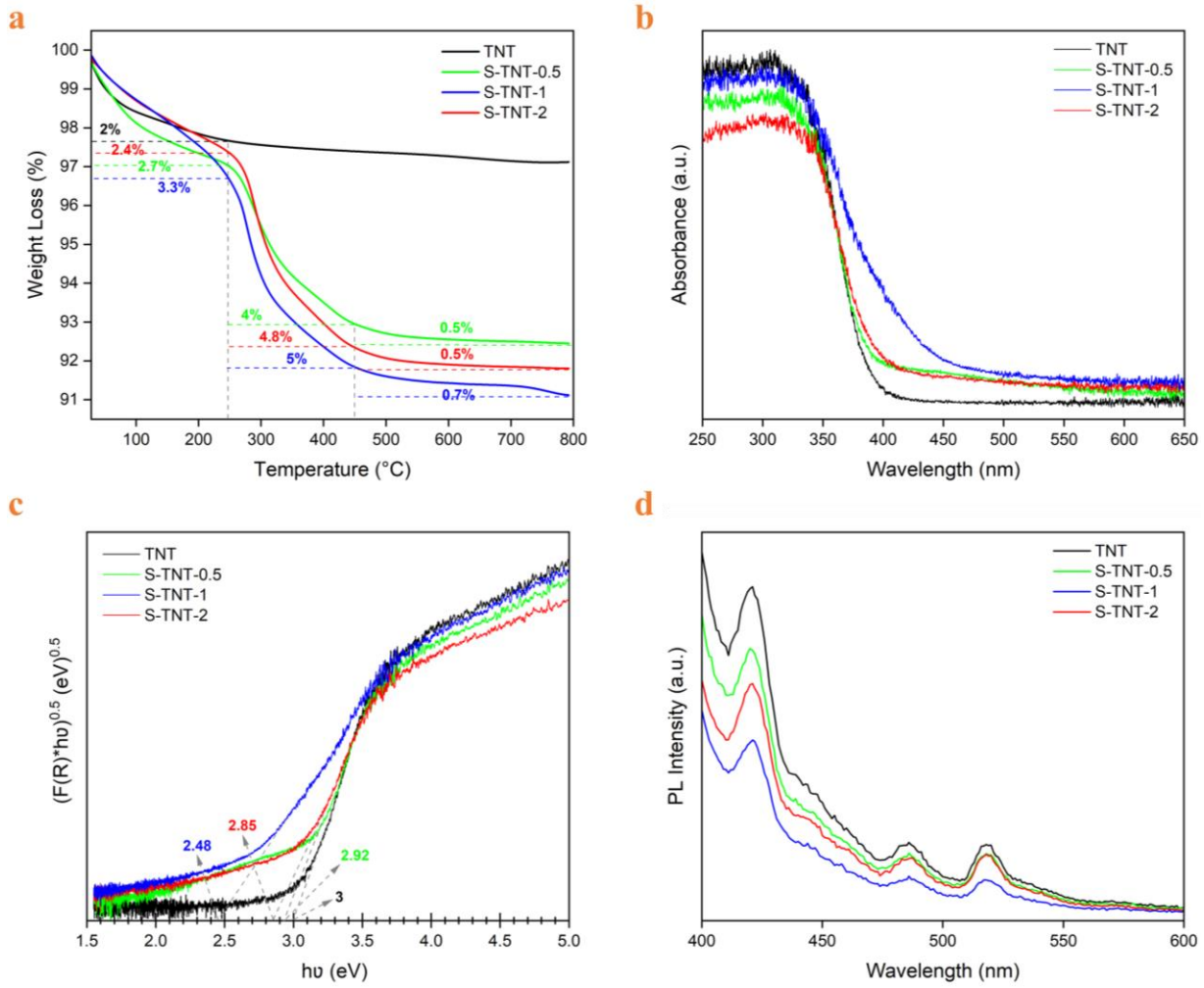

Figure 5.5 (a) TGA curves, (b) Absorption spectra, (c) Bandgap energies, and (d) PL spectra of TNT, S-TNT-0.5, S-TNT-1, and S-TNT-2

Figure 5.11 shows the adsorption-desorption isotherms of TNT and S-TNT photocatalysts. According to the IUPAC classification [175], all synthesized photocatalysts exhibited type IV isotherms with H3 hysteresis loops, suggesting a slit-like mesoporous structure [139]. Table 5.1 summarizes the BET surface area, total pore volume, and mean pore size of the synthesized

photocatalysts. The BET surface area of S-TNT-0.5 (252 m^2/g), S-TNT-1 (267 m^2/g), and S-TNT-2 (274 m^2/g) was about two times higher than that of TNT (110 m^2/g). This enhancement is attributed to the incorporation of sulfur nanodots, which decorate the TNT surface and interstitial regions, acting as nano-spacers that reduce aggregation and increase the accessible porous network. Moreover, sulfur doping may induce surface curvature and introduce structural defects, which further enhance the surface area [281]. These modifications collectively result in a higher density of adsorption sites and improved textural properties, thereby contributing to enhanced photocatalytic performance, as discussed in Section 5.4.2. This observation is consistent with previous works [254, 255, 270].

Table 5.1 BET results of TNT, S-TNT-0.5, S-TNT-1, and S-TNT-2

Photocatalyst	BET surface area (m^2/g)	Total pore volume (cm^3/g)	Mean pore size (nm)
TNT	110	0.57	30.7
S-TNT-0.5	252	0.58	31.0
S-TNT-1	267	0.59	31.1
S-TNT-2	274	0.60	31.2

Figure 5.6(a) shows the LSV results of the photocatalysts under dark conditions and simulated sunlight irradiation. In the absence of light, the photocurrent density of all photocatalysts was nearly zero, indicating that no electrochemical reactions occurred (see darkness in Figure 5.6(a)). Upon solar irradiation, all samples produced a positive current within the anodic potential range of 0–2 V (vs. Ag/AgCl). At the potential of 2 V, S-TNT-1 generated a photocurrent density of 0.60 mA/cm^2, which was three times higher than that of TNT (0.20 mA/cm^2). Other S-TNT photocatalysts also exhibited higher photocurrent densities compared to TNT across the potential range of -1–2 V (vs. Ag/AgCl). The photocurrent density of S-TNT-0.5 was recorded as 0.25 mA/cm^2, and it was 0.4 mA/cm^2 for S-TNT-2 at 2 V. In addition, Figure 5.6(a) shows that sulfur doping in S-TNT-1 shifted the open-circuit potential (OCP) of TNT from -0.27 V to -0.57 V (vs. Ag/AgCl). This negative shift suggests that S-TNT-1 requires a lower applied potential than TNT to generate photo-induced charge carriers and transfer them to the counter electrode via the external

circuit [170]. Thus, electron-hole pair separation in S-TNT-1 is enhanced, which is in line with PL results.

Figure 5.6(b) depicts the chronoamperometry of TNT and S-TNT photocatalysts at a constant potential of 0 V (vs. Ag/AgCl) through three pulses of solar lamp on-off cycles, each with 20-second intervals. The selection of 0 V to evaluate photo-response was due to photocatalytic experiments being conducted without an external potential. The photocurrent density for all samples was zero when the light was off. Upon light exposure, the photocurrent density surged to its maximum and dropped back to zero when the light source was interrupted. This rapid response indicates the excellent reproducibility of the electron-hole pairs in the synthesized photocatalysts. In addition, a consistent level of photocurrent density during the three pulses for each sample shows their good photocatalytic activity for the generation of electron-hole pairs. According to Figure 5.6(b), S-TNT-1 exhibited a photocurrent density of 0.60 mA/cm^2, which was higher than that of S-TNT-2 (0.40 mA/cm^2), S-TNT-0.5 (0.25 mA/cm^2), and TNT (0.20 mA/cm^2).

The photocurrent efficiency (η) represents the efficiency of converting light photon energy into chemical energy, derived from the LSV curve by the following Equation [188]:

$$\eta\% = J_p \left[\frac{E^{\circ}_{rev} - |E_{app}|}{I_0}\right] \times 100 \tag{5.9}$$

In Equation 5.9, J_p is the photocurrent density (mA/cm^2), I_0 is the intensity of the incident light, and E°_{rev} is the standard changeable potential (1.23 V vs. reversible hydrogen electrode [RHE]).

The E_{app} is attributed to the absolute value of the applied voltage, calculated by Equation 5.10:

$$E_{app} = E_{meas} - E_{OCP} \tag{5.10}$$

Where E_{meas} denotes the measured electrode potential of the photoanode (vs. Ag/AgCl), and E_{OCP} is the OCP of the photoanode (V vs. Ag/AgCl).

Figure 5.6(c) presents the photoconversion efficiency of the fabricated photocatalysts as 0.24%, 0.29%, 0.39%, and 0.35% for TNT, S-TNT-0.5, S-TNT-1, and S-TNT-2, respectively. The higher photoconversion efficiency of S-TNT-1 compared to TNT indicates that sulfur doping can enhance the light's photon harnessing and conversion to electron-hole pairs to participate in wastewater oxidation reactions. To sum up, the highest photoelectrochemical properties of S-TNT-1 at zero potential among all photocatalysts can be attributed to its superior optical properties. The narrower

bandgap energy and the lower PL intensity of S-TNT-1 compared with other photocatalysts can enhance photon energy absorption and accelerate electron excitation under sunlight irradiation. This indicates the potential of S-TNT-1 for superior photocatalytic activity compared to other photocatalysts.

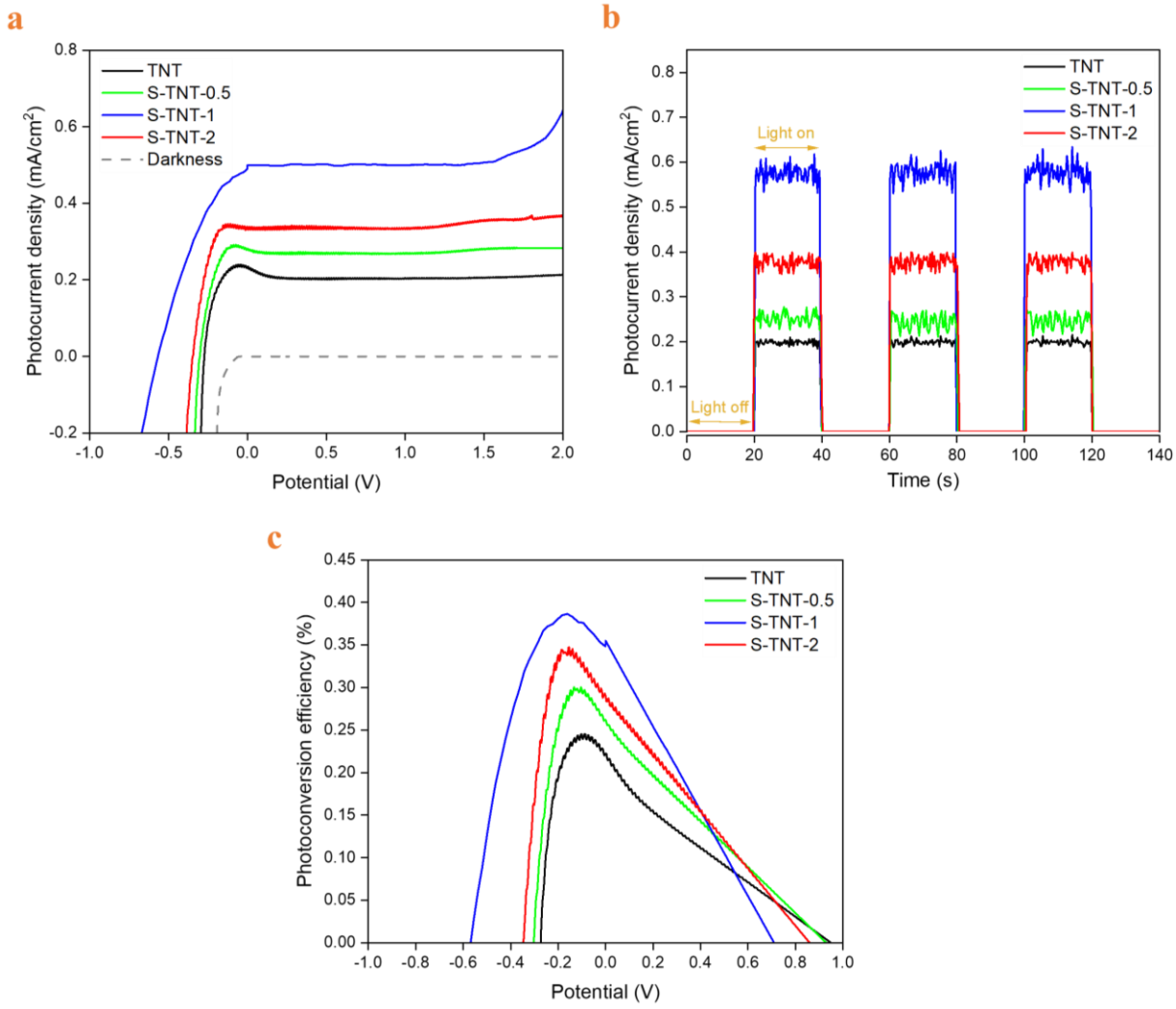

Figure 5.6 Photoelectrochemical properties of TNT, S-TNT-0.5, S-TNT-1, and S-TNT-2 (a) Linear-sweep voltammograms, (b) Transient photocurrent response, and (c) Photoconversion efficiency

5.4.2 Photocatalytic activity

Figure 5.7(a) shows the effect of the sulfur content in the photocatalysts (S-TNT-0.5@PUF, S-TNT-1@PUF, S-TNT-2@PUF) on BPA degradation under simulated sunlight irradiation (BPA concentration = 10 mg/L, photocatalyst loading = 0.1 g, pH = 5.7). Under simulated sunlight

irradiation (photolysis), about 2% of BPA was removed after 180 min, which was considered negligible. A change in BPA concentration was observed during the first 60 min in the dark, which is attributed to the adsorption-desorption equilibrium of BPA on the surface of the photocatalysts. A maximum of about 14% of BPA was adsorbed on S-TNT-1@PUF. The photocatalytic activity of TNT@PUF and S-TNT-0.5@PUF was similar for BPA degradation (>96% after 180 min irradiation, Figure 5.7(a)). In comparison, S-TNT-2@PUF degraded more than 96% of BPA over a shorter time (150 min irradiation). Among the synthesized photocatalysts with different sulfur content, S-TNT-1@PUF presented the highest photocatalytic activity for the degradation of BPA (over 96% after 120 min irradiation), which can be related to the photocatalytic properties of S-TNT-1. Based on the characterization results, S-TNT-1 exhibited the lowest bandgap energy (2.48 eV, Figures 5.5(b) and 5.5(c)) and the lowest PL intensity (Figure 5.5(d)), which improved the light harvesting in the visible region and reduced electron-hole pair recombination. In addition, the highest photocurrent density (0.6 mA/cm^2) and photoconversion efficiency (0.39%) were obtained for S-TNT-1 (Figure 5.6), enhancing photon trapping and conversion to electron-hole pairs for BPA degradation. Consequently, we employed the photocatalyst containing 1 wt.% of the sulfur precursor (S-TNT-1@PUF) in the following experiments.

We investigated the effect of S-TNT-1@PUF loading (0.1 g, 0.2 g, 0.4 g) on BPA degradation (Figure 5.7(b)). The experimental conditions remained constant (BPA concentration = 10 mg/L and pH = 5.7). As shown in Figure 5.7(b), 0.1 g of photocatalyst degraded more than 96% of BPA after 120 min of irradiation. Increasing the photocatalyst loading from 0.1 g to 0.2 g resulted in over 96% degradation at a shorter reaction time (90 min). This can be due to the availability of more active photocatalytic sites within the PUF that interact with light irradiation and contribute to the photocatalytic reaction [134, 190]. However, once the photocatalyst loading increased from 0.2 g to 0.4 g, BPA degradation decreased to 96% after 120 min of irradiation. This likely corresponds to decreased light penetration caused by the agglomeration of the photocatalyst in the PUF and the blockage of its pores [111, 134, 190, 282, 283]. Based on the results, 0.2 g S-TNT-1@PUF was selected as the optimum loading of the photocatalyst for further experiments.

The effect of BPA concentration (10 mg/L, 20 mg/L, 40 mg/L) on BPA degradation was examined with 0.2 g of S-TNT-1@PUF at pH = 5.7. Figure 5.7(c) shows that over 96% degradation occurred at 10 mg/L BPA after 90 min irradiation. However, by increasing BPA concentration from 10 mg/L to 20 mg/L, BPA degradation decreased to 90% after 120 min. Similarly, an increase in BPA

concentration to 40 mg/L caused a 20% reduction in BPA degradation after 120 min. The lower concentrations of BPA led to a higher percentage of removal, considering that BPA can readily interact with h^+ on the photocatalyst surface and ROS in bulk solution, facilitating BPA degradation. However, as BPA concentration increased, the accumulation of BPA and its TPs on the photocatalyst surface limited BPA degradation by reducing the number of active sites available for photocatalytic reactions [139, 284, 285]. Consequently, the optimal concentration of BPA was determined to be at the lowest concentration tested, 10 mg/L.

We evaluated the effect of pH (5.7, 8, 10) on BPA degradation using 0.2 g S-TNT-1@PUF and 10 mg/L BPA. Figure 5.7(d) shows that the lowest BPA degradation occurred at pH = 10, being 50% after 120 min of irradiation. This can be attributed to the surface charge properties of S-TNT-1@PUF. As depicted in Figure 5.12, the point of zero charge for S-TNT-1@PUF was 5.6 (pH_{PZC} = 5.6), indicating a negatively charged surface of S-TNT-1@PUF at pH = 10. Similarly, BPA was negatively charged in an alkaline environment due to its pk_a, which is 9.6 [286]. Therefore, this electrostatic repulsion between the negatively charged BPA and the negatively charged surface of S-TNT-1@PUF reduces the adsorption of BPA onto the photocatalyst surface, thereby decreasing BPA degradation. On the other hand, the highest BPA degradation (>96%) was observed at pH = 8 after 75 min irradiation. This is because the surface of S-TNT-1@PUF was negatively charged at pH = 8, while BPA was positively charged. Thus, this electrostatic attraction between the negatively charged photocatalyst surface and the positively charged BPA improves the adsorption of BPA onto the photocatalyst surface and hence increases BPA degradation. In addition, at the natural pH of the BPA solution (pH = 5.7), more than 96% of degradation was achieved after 90 min of irradiation. According to Figure 5.7(d), the photocatalytic degradation of BPA was predominant at pH = 8, with over 96% degradation at the shortest irradiation time (75 min), which can be due to the pH_{PZC} of S-TNT-1@PUF (pH_{PZC} = 5.6). As shown in Figure 5.12, the surface of S-TNT-1@PUF is strongly negatively charged at pH = 8 (zeta potential ~ -35 mV) than that of pH = 5.7 (zeta potential ~ -2 mV). Consequently, at pH = 8, the surface of S-TNT-1@PUF is more negatively charged to adsorb positively charged BPA and thus increases the degradation of BPA. Our results indicated that BPA (10 mg/L) was degraded (>96%) with floating S-TNT-1@PUF (0.2 g) exposed to simulated sunlight irradiation (75 min) at pH = 8.

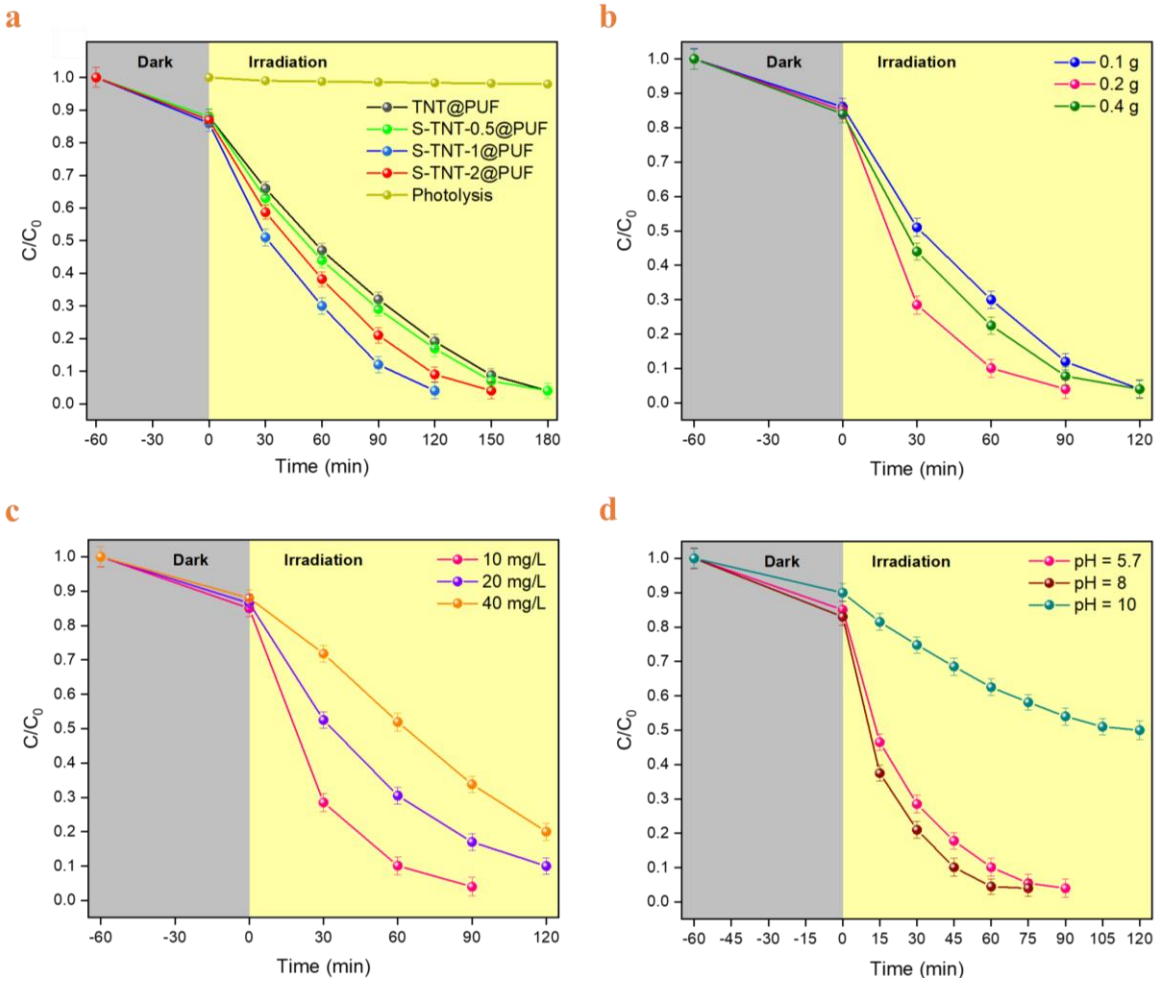

Figure 5.7 Effects of (a) the sulfur content in the S-TNT@PUF photocatalysts, (b) photocatalyst loading, (c) BPA concentration, and (d) pH on BPA degradation (Error bars represent the standard deviation of three replicates)

Optimal treatment conditions for the photocatalytic degradation of BPA under simulated sunlight irradiation were S-TNT-1@PUF loading of 0.2 g, BPA concentration of 10 mg/L, irradiation time of 75 min, and pH = 8. The UV-Vis absorption spectra of BPA degradation under optimal treatment conditions are shown in Figure 5.13(a). Over the 75 minutes of irradiation, the absorption peak of BPA at 276 nm decreased to nearly zero, resulting in over 96% degradation.

We investigated the leaching of Ti and S elements from the floating S-TNT-1@PUF photocatalyst by ICP-OES analysis under optimal treatment conditions. Based on the results, Ti and S were not observed in the BPA solution (limit of detection of 0.000028 µg/mL for Ti and 0.024 µg/mL for S), indicating that the elements were not released from the floating photocatalyst. In addition, the PUF support is commonly used in aquarium filters as a safe, inert, and non-toxic substrate. It is

designed to operate in aquatic environments without releasing harmful substances or undergoing significant abrasion [206].

We investigated the kinetics of BPA degradation with floating S-TNT-1@PUF under optimal treatment conditions. Equation 5.11 represents the degradation rate of BPA [72, 170]:

$$r = -\frac{dC}{dt} = k_{app}C^n \tag{5.11}$$

Where k_{app} is the apparent rate constant, C is the BPA concentration, t is the irradiation time, and n is the reaction order.

Correlation coefficients (R^2) and apparent rate constants (k_{app}) obtained from the kinetics models (Equations 5(12–14)) are presented in Table 5.3. R^2 in the first-order kinetics was more than 0.97 (R^2 = 0.99); thus, BPA degradation followed the first-order kinetics with a k_{app} of 0.05 min^{-1}, as shown in Figure 5.13(b).

5.4.3 Reusability of photocatalysts

We evaluated the reusability of S-TNT-1@PUF for BPA degradation in five consecutive cycles under optimal treatment conditions (S-TNT-1@PUF loading = 0.2 g, initial BPA concentration = 10 mg/L, irradiation time = 75 min, and pH = 8). Figure 5.8(a) shows that S-TNT-1@PUF maintained its photocatalytic activity after five reuse cycles, with a 2% reduction in BPA degradation. This reduction in BPA degradation efficiency can be attributed to the poisoning of active sites in the photocatalyst by BPA degradation products [191]. In addition, the structure and morphology of S-TNT-1@PUF were investigated after five reuse runs. There was no significant change in the XRD patterns or the morphology of fresh and used S-TNT-1@PUF (see Figures 5.8(b–d)), confirming the stability of S-TNT-1@PUF for the degradation of BPA.

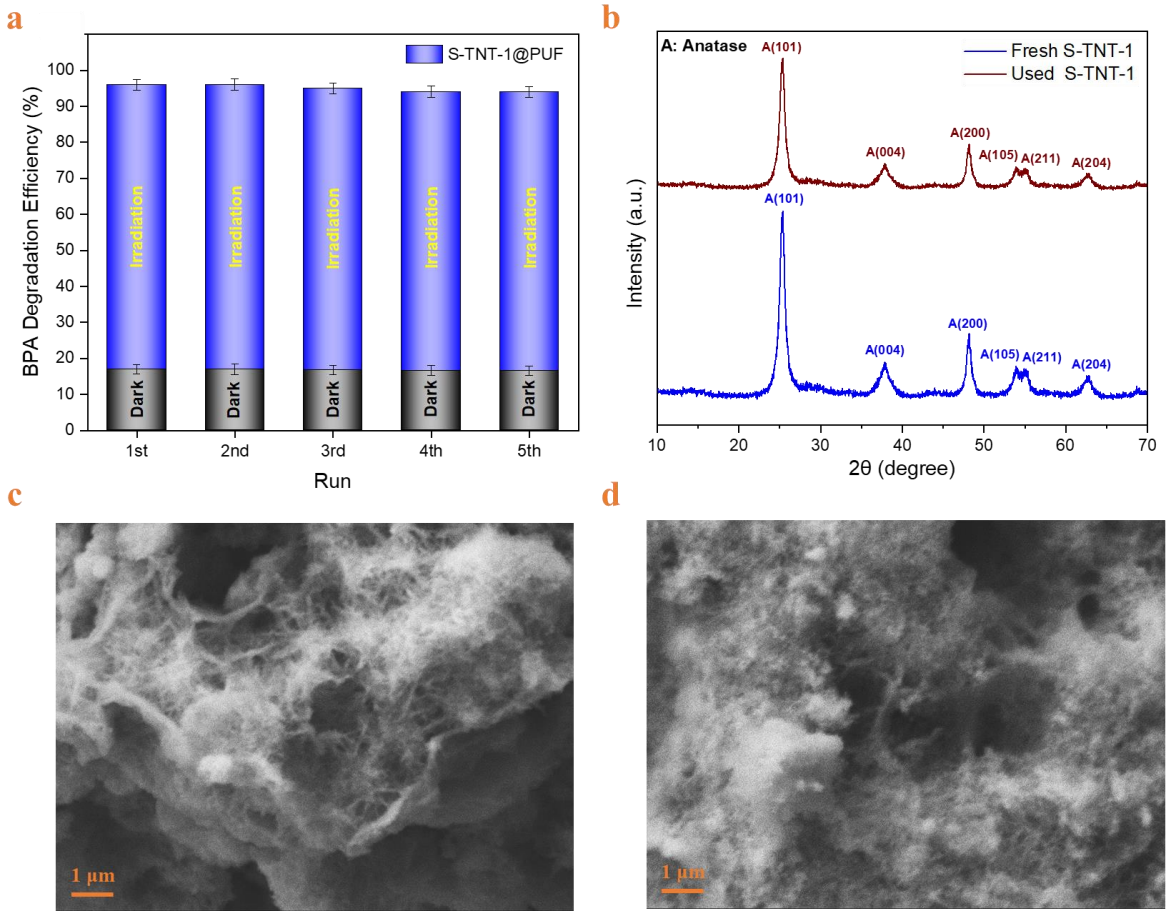

Figure 5.8 (a) Reusability of S-TNT-1@PUF for BPA degradation under optimal treatment conditions; (b) XRD patterns of fresh and used S-TNT-1@PUF; (c, d) SEM images of fresh and used S-TNT-1@PUF after five reuse cycles (Error bars represent the standard deviation of three replicates)

5.4.4 Possible mechanism of BPA degradation

To identify the main reactive species contributing to the degradation of BPA, free radical scavenging experiments were performed using AO (h^+ scavenger), t-BuOH ($^{\bullet}OH$ scavenger), $AgNO_3$ (e^- scavenger), and BZQ ($^{\bullet}O_2^-$ scavenger) under optimal treatment conditions (S-TNT-1@PUF loading = 0.2 g, initial BPA concentration = 10 mg/L, irradiation time = 75 min, and pH = 8). Figure 5.9(a) shows that adding AO to the floating catalyst photoreactor decreased the BPA degradation from >96% to 30%. To examine the direct and indirect contributions of h^+, t-BuOH was added to the BPA solution, leading to a 36% reduction in the BPA degradation. Therefore, the contributions of h^+ for direct reactions and $^{\bullet}OH$ for indirect reactions were calculated as 25% and 31%, respectively (see Figure 5.9(a)). Also, adding $AgNO_3$ to the system decreased the degradation

by 31%, indicating that e^- had a 26% contribution to degrading BPA. Regarding $^{\bullet}O_2^-$, 16% of BPA was degraded in the presence of BZQ, showing that $^{\bullet}O_2^-$ contributed to the BPA degradation by 14%. Thus, $^{\bullet}OH$ was the main reactive species involved in the BPA degradation with a 31% contribution. According to the results, the effect of $^{\bullet}OH$ in BPA degradation was more than that of $^{\bullet}O_2^-$ (31% vs. 14%), which can be explained by the band structure of S-TNT-1@PUF. The valence band of S-TNT-1@PUF (+2.71 eV vs. normal hydrogen electrode [NHE], calculated by Equation 5.4) is more positive than $^{\bullet}OH/H_2O$ (+2.38 eV vs. NHE [257, 287, 288]), which leads to the generation of more $^{\bullet}OH$. In contrast, the conduction band of S-TNT-1@PUF (-0.14 eV vs. NHE, calculated by Equation 5.3) is close to the potential of $O_2/^{\bullet}O_2^-$ (-0.046 eV vs. NHE [135, 289, 290]), which reduces the production of $^{\bullet}O_2^-$.

The formation of ROS in the photocatalytic reaction of BPA was further investigated by EPR. Figures 5.9(b) and 5.9(c) present signals detected by EPR, corresponding to $^{\bullet}OH$ and $^{\bullet}O_2^-$, respectively [291, 292]. Although several ROS, such as $^{\bullet}OH$, $^{\bullet}O_2^-$, $^{\bullet}OOH$, H_2O_2, and $^1O_2$, may participate in photocatalytic degradation, EPR in the present study showed signals only for $^{\bullet}OH$ and $^{\bullet}O_2^-$. No signals corresponding to $^{\bullet}OOH$ and $^1O_2$ were detected. This absence is likely due to the lack of sacrificial agents (e.g., alcohols) in water and the use of photocatalysis without applying electrochemical biasing. Previous reports [292, 293] suggest that such species are typically favoured under more reductive environments or via specific photocatalyst band alignments and surface pathways.

Based on the results from scavenging experiments and EPR analysis, we propose the possible mechanism for BPA degradation using floating S-TNT-1@PUF under simulated sunlight irradiation (Figure 5.9(d)). Upon exposure of S-TNT-1@PUF to light irradiation, electrons in the valence band of the photocatalyst can be excited and then moved to the conduction band. This creates positively charged electron holes in the valence band (h^+_{VB}) and negatively charged electrons in the conduction band (e^-_{CB}) of the photocatalyst (Reaction 5.1). The mechanism of BPA degradation includes direct and indirect photocatalytic reactions. In the valence band of the photocatalyst, h^+_{VB} directly reacts with BPA, degrading the pollutant into its TPs that can be ultimately converted to CO_2 and H_2O (Reaction 5.2). In the indirect reactions, h^+_{VB} has a more positive band energy (+2.71 eV vs. NHE) than $^{\bullet}OH/H_2O$ (+2.38 eV vs. NHE [257, 287, 288]). This allows h^+_{VB} to participate in an oxidation reaction**,** converting water into $^{\bullet}OH$ (Reaction 5.3), which further degrades BPA (Reaction 5.4). In the conduction band of the photocatalyst, e^-_{CB} has a more

negative band energy (-0.14 eV vs. NHE) than $O_2/^{\bullet}O_2^-$ (-0.046 eV vs. NHE [135, 289, 290]), converting dissolved oxygen to $^{\bullet}O_2^-$ through a reduction reaction (Reaction 5.5). The generated $^{\bullet}O_2^-$ reacts with BPA in two mechanisms. First, $^{\bullet}O_2^-$ can degrade BPA into its TPs, resulting in CO_2 and H_2O (Reaction 5.6). Second, $^{\bullet}O_2^-$ can undergo a reaction with hydrogen ions (H^+) to produce hydroperoxyl radicals ($^{\bullet}OOH$) and hydrogen peroxide (H_2O_2) (Reactions 5.7 and 5.8) [52, 53, 294]. The produced H_2O_2 then continues to react with e^-_{CB} to generate $^{\bullet}OH$ (Reaction 5.9), which further contributes to BPA degradation (Reaction 5.10).

$$S-TNT-1@PUF+h\vartheta \rightarrow h^+_{VB}+e^-_{CB} \quad \text{(Reaction 5.1)}$$

$$h^+_{VB}+BPA \rightarrow BPA\ TPs \rightarrow CO_2+H_2O \quad \text{(Reaction 5.2)}$$

$$h^+_{VB}+H_2O \rightarrow \bullet OH + H^+ \quad \text{(Reaction 5.3)}$$

$$\bullet OH+BPA \rightarrow BPA\ TPs \rightarrow CO_2+H_2O \quad \text{(Reaction 5.4)}$$

$$e^-_{CB}+O_2 \rightarrow \bullet O_2^- \quad \text{(Reaction 5.5)}$$

$$\bullet O_2^-+BPA \rightarrow BPA\ TPs \rightarrow CO_2+H_2O \quad \text{(Reaction 5.6)}$$

$$\bullet O_2^-+H^+ \rightarrow \bullet OOH \quad \text{(Reaction 5.7)}$$

$$\bullet OOH+\bullet OOH \rightarrow H_2O_2+O_2 \quad \text{(Reaction 5.8)}$$

$$H_2O_2+e^-_{CB} \rightarrow \bullet OH + OH^- \quad \text{(Reaction 5.9)}$$

$$\bullet OH+BPA \rightarrow BPA\ TPs \rightarrow CO_2+H_2O \quad \text{(Reaction 5.10)}$$

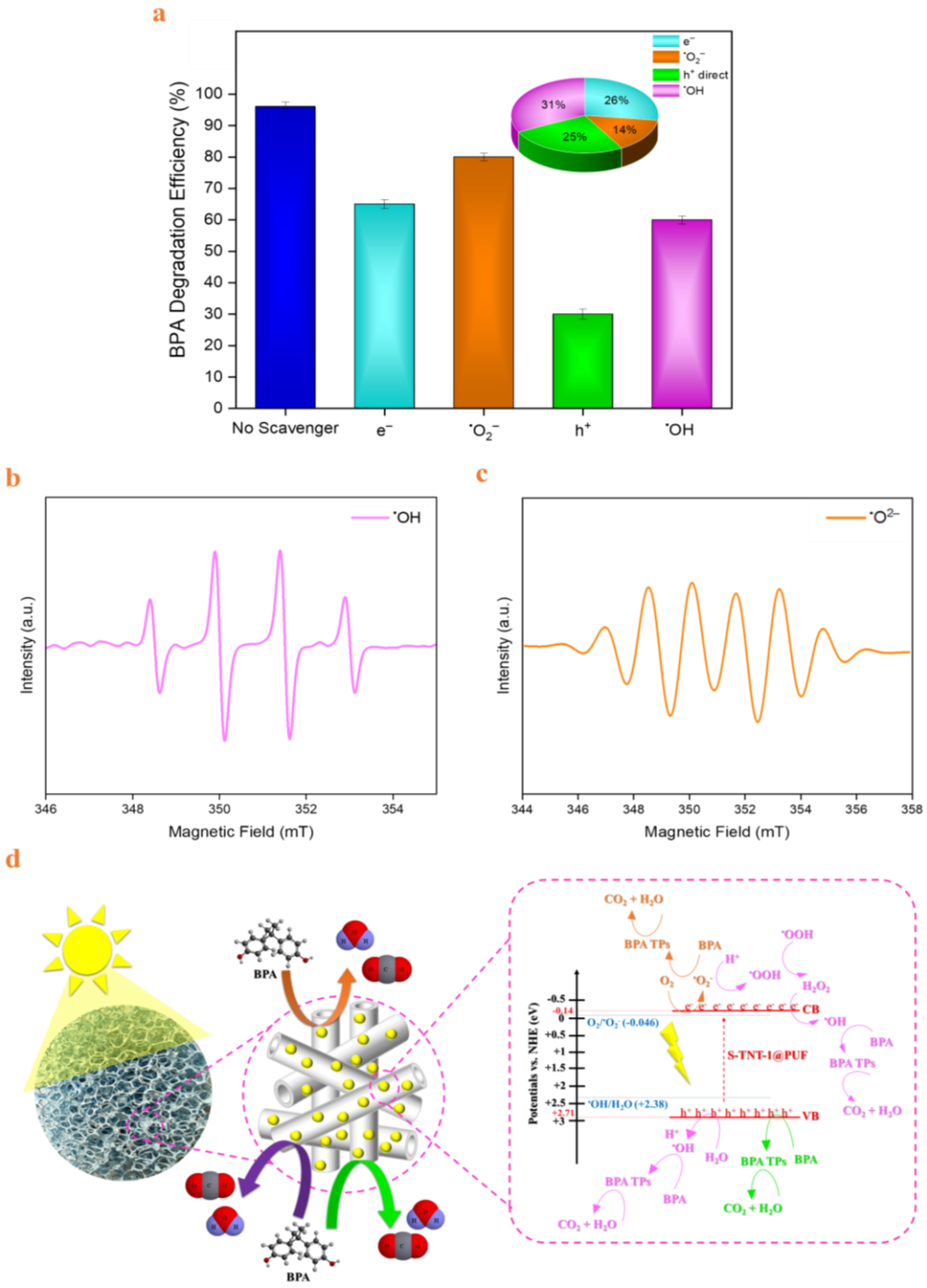

Figure 5.9 (a) Free radical scavenging experiments for BPA degradation under optimal treatment conditions (Insert: Reactive species contribution on BPA degradation); (b, c) EPR spectra of $^{\bullet}OH$ and $^{\bullet}O_2^-$ generated during BPA degradation under optimal treatment conditions; (d) Schematic of the possible mechanism for BPA degradation with S-TNT-1@PUF under simulated sunlight irradiation (Error bars represent the standard deviation of three replicates)

5.4.5 BPA degradation pathways

Figure 5.10 shows the degradation products of BPA detected by HPLC-MS under optimal photocatalytic conditions (S-TNT-1@PUF loading = 0.2 g, initial BPA concentration = 10 mg/L, irradiation time = 75 min, and pH = 8). Based on the TPs, two possible pathways of BPA degradation can be proposed: oxidation and β-scission reactions. In the first pathway, BPA (m/z = 227.1043, $[M-H]^-$) was oxidized to $C_{15}H_{16}O_4$ (m/z = 261.1095, $[M+H]^+$) through an oxidation reaction [181]. In the second pathway, $C_9H_{10}O$ (m/z = 135.0790, $[M+H]^+$), $C_6H_4O_2$ (m/z = 107.0106, $[M-H]^-$), and $C_9H_{12}O$ (m/z = 137.0583, $[M+H]^+$) were generated due to the β-scission of BPA [182, 295]. More progress in the photocatalytic degradation of BPA can result in mineralizing these TPs, thus, the production of CO_2 and H_2O [181, 182]. The corresponding mass spectrometry chromatograms of the BPA TPs are shown in Figure 5.14.

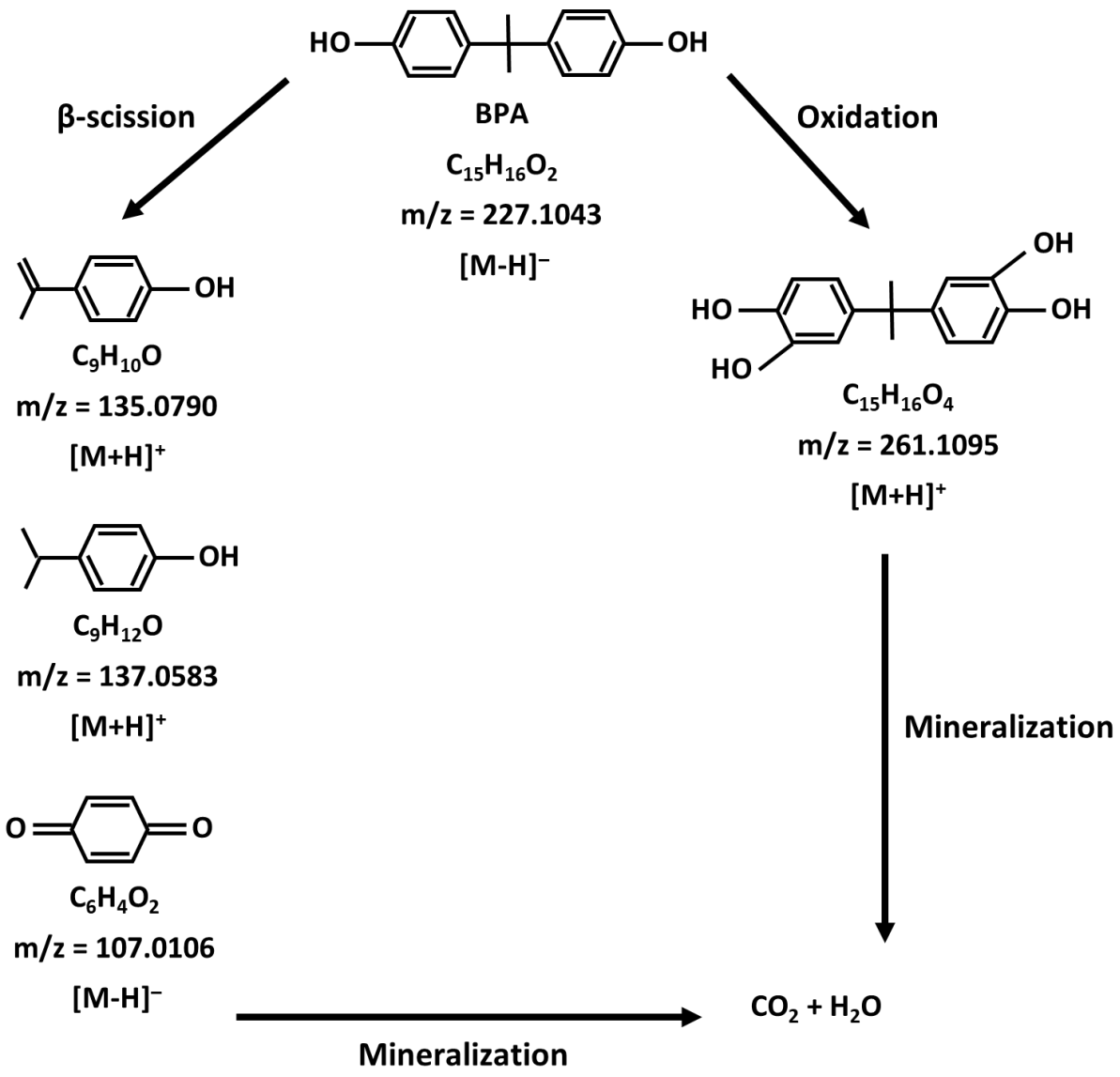

Figure 5.10 Proposed pathways for BPA degradation with S-TNT-1@PUF under optimal treatment conditions (S-TNT-1@PUF loading = 0.2 g, BPA concentration = 10 mg/L, irradiation time = 75 min, and pH = 8)

5.4.6 Comparison of floating S-TNT-1@PUF with previous work

A recent literature review on the photocatalytic degradation of BPA is summarized in Table 5.2. Notably, no work has been reported to degrade BPA using a floating photocatalyst. For the first time, we propose a floating photocatalytic system for BPA degradation under simulated sunlight irradiation. Additionally, some suspended photocatalytic systems showed unsatisfactory activity in degrading BPA. For example, Krishnan et al. [106] reported nearly 43% degradation for 10 mg/L BPA using a co-doped Cu-N/TiO_2 photocatalyst exposed to 120 min of visible light. In another

study, N-doped carbon/TiO_2 composites fabricated by Rajput et al. [107] degraded only 30% of BPA (20 mg/L) under UV light after 210 min. In contrast, our floating system degraded over 96% of BPA (10 mg/L) with S-TNT-1@PUF under simulated sunlight irradiation (75 min). Moreover, the proposed S-TNT-1@PUF photocatalyst exhibited reusability after five consecutive cycles under optimal treatment conditions, contrary to previous reports. For instance, commercial TiO_2 P25 nanoparticles based on natural zeolite clinoptilolite [110] were 30% less photoactive in BPA degradation after four reuse cycles. Similarly, the BPA degradation decreased to 20% after three recovery cycles of co-doped Cu-N/TiO_2 photocatalysts [106]. The kinetics study indicated that BPA degradation in most previous work followed pseudo first-order kinetics, and their apparent rate constants were much lower than 0.05 min^{-1} obtained by floating S-TNT-1@PUF (reported as 4.86×10^{-3} min^{-1}, 3.7×10^{-3} min^{-1}, 0.031 min^{-1}, 0.018 min^{-1}) [106, 110, 112, 117]. Furthermore, the photoelectrochemical properties of photocatalysts remained underexplored in many studies (see Table 5.2) [106, 107, 110, 112]. In the present study, we performed voltammetry analyses, showing that S-TNT-1 had a higher photocurrent density, i.e. 0.6 mA/cm^2, compared to 0.22 $\mu A/cm^2$, which was previously reported [117].

Table 5.2 A recent literature review on the photocatalytic degradation of BPA

Photocatalyst (dosage)	Pollutant (concentration)	Photocatalytic system	Light and irradiation time	Photocurrent density	1st run photocatalytic degradation	Kinetics	Efficiency after recovery (Number of cycles)	Ref.
C-doped TiO_2 nanorods/C-doped α-Fe_2O_3 (0.5 g/L)	BPA (10 mg/L)	Suspension	Simulated solar irradiation (270 min)	0.22 $\mu A/cm^2$	79%	Pseudo first-order $k = 4.86\times10^{-3}$ min^{-1}	~76% (4)	[117]
Co-doped Cu-N/TiO_2 (0.5 g/L)	BPA (10 mg/L)	Suspension	Visible light (120 min)	-	~43%	Pseudo first-order $k = 3.7\times10^{-3}$ min^{-1}	~20% (3)	[106]
TiO_2/graphene oxide (0.75 g/L)	BPA (50 mg/L)	Suspension	UV radiation (60 min)	-	~89%	Pseudo first-order $k = 0.031$ min^{-1}	~80% (5)	[112]
TiO_2 P25/natural zeolite clinoptilolite (2 g/L)	BPA (5 mg/L)	Suspension	Simulated solar light (180 min)	-	100%	Pseudo first-order $k = 0.018$ min^{-1}	70% (4)	[110]
N-doped carbon/TiO_2 (1 g/L)	BPA (20 mg/L)	Suspension	UV light (210 min)	-	30%	-	-	[107]
S-TNT-1@PUF (0.2 g)	BPA (10 mg/L)	Immobilized on a floating Polyurethane foam	Simulated sunlight (75 min)	0.6 mA/cm^2	>96%	First-order $k_{app} = 0.05$ min^{-1}	94% (2)	This work

5.5 Conclusion

We presented an innovative floating photocatalytic system composed of sulfur-doped TNT@PUF, designed for the degradation of BPA under simulated sunlight irradiation. The doping of sulfur on TNT improved its photocatalytic activity, attributed to sulfur-induced modifications in its structural and electronic properties. Among the synthesized floating photocatalysts, S-TNT-1@PUF was the most photoactive, achieving over 96% BPA degradation under optimal treatment conditions: a photocatalyst loading of 0.2 g, an initial BPA concentration of 10 mg/L, pH = 8, and an irradiation time of 75 min using a 300 W commercial solar lamp with a 35 W/m^2 intensity. The kinetic study indicated that the degradation of BPA by S-TNT-1@PUF followed first-order kinetics, with an apparent rate constant of 0.05 min^{-1} under optimal photocatalytic conditions. S-TNT-1@PUF exhibited excellent stability, maintaining its photocatalytic activity after five reuse cycles. Mechanistic investigations identified $^{\bullet}OH$ as the primary reactive species, contributing 31% to BPA degradation under optimum conditions. Our findings underscore the potential of floating S-TNT-1@PUF as an innovative, reusable, and scalable approach for wastewater treatment, overcoming key issues with photocatalyst recovery and performance in real-world conditions.

5.6 Acknowledgments

The authors thank the Velux Stiftung Foundation for the financial support through project 1381, “SUNFLOAT - Water decontamination by sunlight-driven floating photocatalytic systems”, and through the Natural Sciences and Engineering Research Council of Canada (NSERC). We also appreciate the support of Bourse d'excellence Neil R. Mitchell et Danièle Dumais from Polytechnique Montréal, Canada. The authors are grateful to Giulio Cerullo and Franco Valduga de Almeida Camargo for optical investigations.

5.7 Supplementary Material

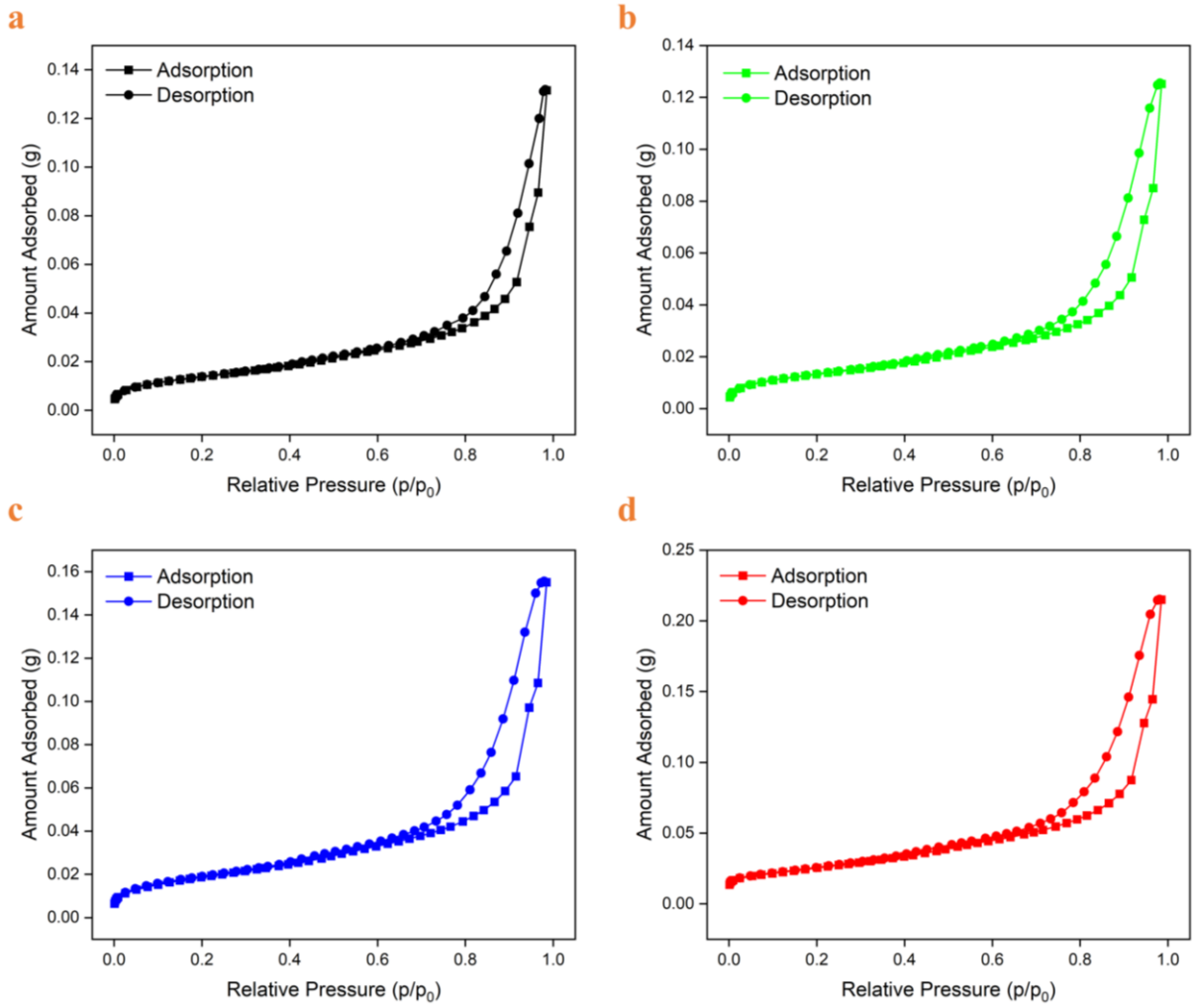

Figure 5.11 Adsorption-desorption isotherms of (a) TNT, (b) S-TNT-0.5, (c) S-TNT-1, and (d) S-TNT-2

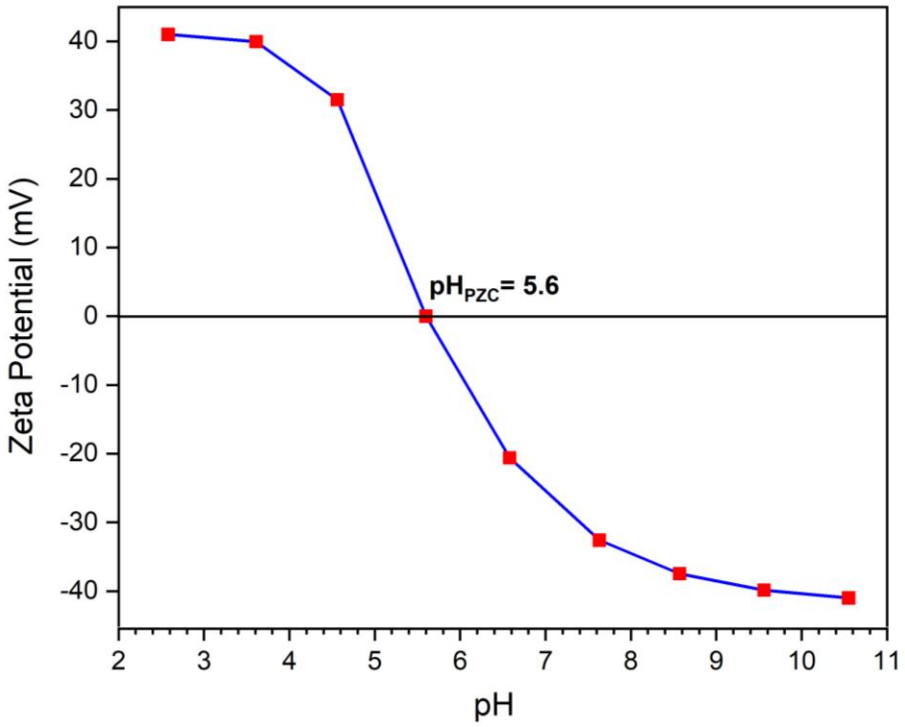

Figure 5.12 Zeta potential of S-TNT-1

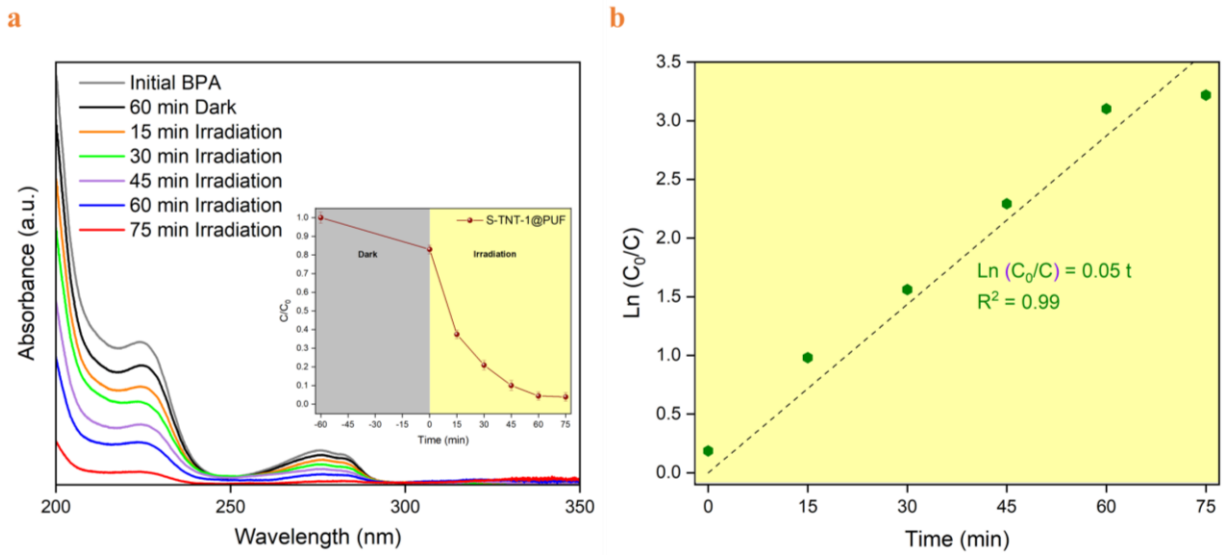

Figure 5.13 Photocatalytic degradation of BPA with S-TNT-1@PUF under optimal conditions (a) UV-Vis absorption spectra and (b) First-order kinetics model

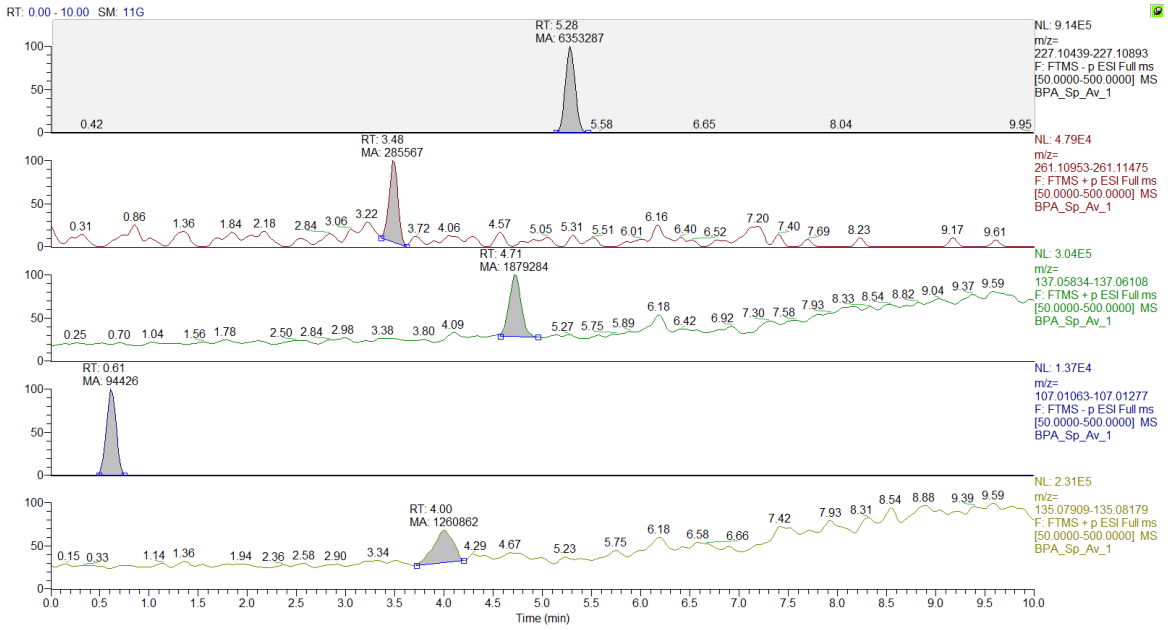

Figure 5.14 Mass spectrometry chromatograms of BPA transformation products under optimal conditions

For zero-order kinetics (n = 0), Equation 5.11 is simplified to Equation 5.12.

$$C = -k_{app}t + C_0 \tag{5.12}$$

Equations 5.13 and 5.14 present the first-order kinetics (n = 1) and the second-order kinetics (n = 2), respectively.

$$Ln\frac{C}{C_0} = -k_{app}t \tag{5.13}$$

$$\frac{1}{C} = k_{app}t + \frac{1}{C_0} \tag{5.14}$$

Where C_0 is the initial concentration of BPA.

Table 5.3 Correlation coefficients and apparent rate constants for kinetics models of BPA degradation under optimal conditions

Kinetics model	R^2	k_{app}
Zero-order (n = 0)	0.81	0.10 (mg L^{-1} min^{-1})
First-order (n = 1)	0.99	0.05 (min^{-1})
Second-order (n = 2)	0.65	0.11 (mg^{-1} L min^{-1})

CHAPTER 6 ARTICLE 4: SOLAR-LIGHT-DRIVEN PHOTOCATALYTIC DEGRADATION OF BISPHENOL A BY ENERGY-STORING FLOATING WS2-TIO2 Z-SCHEME HETEROJUNCTIONS

Nila Davari[1], Javad Vahabzadeh Pasikhani[2], Ermelinda Falletta[3,4], Claudia L. Bianchi[3,4], Viviane Yargeau[5], Daria C. Boffito[1,6*]

[1] Department of Chemical Engineering, Polytechnique Montréal, Montréal, Canada

[2] Process Engineering Advanced Research Lab (PEARL), Department of Chemical Engineering, Polytechnique Montréal, Université de Montréal, PO Box 6079, Stn Centre-Ville, Montréal, QC, H3C 3A7, Canada

[3] Department of Chemistry, University of Milan, via C. Golgi, 19, 20133, Milan, Italy

[4] Consorzio Interuniversitario Nazionale per la Scienza e Tecnologia dei Materiali (INSTM), via Giusti 9, 50121, Florence, Italy

[5] Department of Chemical Engineering, McGill University, Montréal, Canada

[6] Canada Research Chair in Engineering Process Intensification and Catalysis, Montréal, Canada

The article was submitted to Chemical Engineering Journal, 18 March 2026.

Author contributions

Nila Davari: Writing – original draft, Visualization, Validation, Methodology, Investigation, Conceptualization. Javad Vahabzadeh Pasikhani: Writing – review & editing, Visualization, Methodology, Investigation. Ermelinda Falletta: Writing – review & editing, Methodology. Claudia L. Bianchi: Writing – review & editing, Project administration, Methodology, Funding acquisition. Viviane Yargeau: Writing – review & editing, Supervision, Project administration, Methodology. Daria C. Boffito: Writing – review & editing, Supervision, Resources, Project administration, Methodology, Funding acquisition.

6.1 Abstract

Conventional photocatalytic wastewater treatment is inherently constrained by its dependence on continuous irradiation, limiting its effectiveness under realistic day-night cycles. Herein, we present a multifunctional floating Z-scheme heterostructure that integrates interfacial charge engineering with electron storage capacity to achieve round-the-clock photocatalytic degradation of bisphenol A (BPA). A heterostructure composed of TiO_2 nanotubes (TNT) and WS_2 nanospheres was engineered to promote directional charge transfer via a Z-scheme pathway, while WS_2 chalcogenide acts as an electron reservoir that enables reversible redox reactions in the dark. Immobilization onto a porous polyurethane scaffold (PUF) creates a floating triphase interface, enhancing photon capture and oxygen diffusion at the air-water boundary. The optimized WS_2-TNT-1@PUF (1:1 weight ratio of photocatalysts) exhibited a high surface area (192 m^2/g) and improved visible-light response (narrowed bandgap to 2.8 eV), achieving >97% BPA degradation (initial concentration of 10 mg/L) within 60 min under simulated sunlight, following first-order kinetics (apparent rate constant of 0.069 min^{-1}). Importantly, the system demonstrated electron storage capacity (1-1.8 μmol/h), sustaining around 89% degradation in the absence of light via delayed electron release. Photoelectrochemical analysis, EPR spectroscopy, and scavenger experiments confirmed a Z-scheme-mediated mechanism dominated by $^{\bullet}O_2^-$ radicals, arising from electron accumulation in WS_2 and subsequent discharge. The floating configuration further enabled photocatalyst recovery and stable activity over five cycles. This work represents the next generation of photocatalyst design that integrates Z-scheme heterostructures, electron storage, and floating triphase systems, providing a viable strategy to overcome solar intermittency and enabling energy-autonomous photocatalytic wastewater treatment.

Keywords: Buoyant photocatalyst, Round-the-clock Degradation, Reductive electron-storage, Z-scheme heterojunction, Organic pollutant

6.2 Introduction

Floating photocatalysts offer several advantages over powder-suspended photocatalysts in wastewater treatment. The formation of an air/solid/water triphase interface in floating photocatalysts enables direct exposure of the photocatalyst surface to light, thereby improving photon energy capture and photoinduced charge carrier generation [10, 11, 104]. Additionally, the

triphase interface improves oxygen availability from the air, thereby enhancing photocatalytic activity by increasing the generation of reactive oxygen species [10, 12]. Moreover, floating systems facilitate the easy recovery of the photocatalyst and minimize material loss after wastewater treatment [9-11, 103, 105].

Floating photocatalysts typically have a density of 0.1–0.5 g/cm^3, which is lower than that of water (1 g/cm^3) [100], leading to their flotation at the water surface. In floating photocatalytic systems, photocatalysts operate either as inherently buoyant materials or are immobilized on floating carriers [9, 36]. Using a small quantity of photocatalysts [101], avoiding advanced and costly synthesis techniques [102], and allowing the immobilization of various photocatalysts onto a common floating carrier [100] make immobilized floating photocatalysts more practical than self-floating photocatalysts. Numerous floating materials, such as graphite, silica, cork, glass beads, vermiculite, perlite, light-expanded clay aggregate, palm trunk, autoclaved cellular concrete, canvas [9, 103], alginate beads [246, 247], aerogel [8], and polymers [99, 137, 190], have been explored as carriers for floating photocatalysts. To deposit photoactive materials onto these floating carriers, different methods have been reported, including sol-gel, dip coating, spin coating, spray coating, suspension coating, hydrothermal, solvothermal, solvent casting, strewing solvent casting, impregnating solvent casting, chemical vapor deposition, surface modification using strong acid or strong alkali treatment, liquid-phase deposition, direct hydrolysis precipitation, and three-dimensional printing [11, 100, 103].

While floating titanium dioxide (TiO_2) photocatalyst has recently drawn research interest in wastewater treatment, its photocatalytic activity is hindered by a high bandgap energy (3.0–3.2 eV) [133, 296]. This limits the electron-hole pair generation of TiO_2 to UV light ($\lambda \leq 400$ nm), which only accounts for 5-8% of solar radiation [297, 298]. Additionally, the rapid recombination of photoinduced charge carriers in TiO_2 decreases its photocatalytic activity [41, 299]. To tackle these restrictions, floating TiO_2 photocatalysts have been modified by metal doping (e.g., Ag, Bi, Au, Fe) [109, 134, 190, 249, 300-303], non-metal doping (e.g., S, C, B, N, GO/rGO) [104, 109, 134, 253, 304-308], and coupling with secondary semiconductors (e.g., W_xO_y, SiO_2, Ag_2O, g-C_3N_4, Ag_3PO_4, WO_v, polyaniline) [99, 104, 133, 137, 178, 309, 310].

Coupling TiO_2 with a secondary semiconductor forms a heterojunction that alters the interfacial band bending due to differences in their energy band structures. This band alignment generates an

internal driving force for separating photogenerated charge carriers [41, 297] and prolonging their lifetimes [41, 89]. The resulting heterostructure leads to the accumulation of reductive electrons in the conduction band of one semiconductor and oxidative holes in the valence band of the other, establishing two separate sites for reduction and oxidation reactions [41, 89, 311-313]. This suppresses the rapid recombination of photoinduced charge carriers, thereby enhancing photocatalytic activity. TiO_2-based heterojunction photocatalysts are classified according to the secondary semiconductor type involved, namely n-n and p-n configurations. Electrons are the major charge carriers in n-type semiconductors, while p-type semiconductors have holes as the major charge carriers [41]. Additionally, TiO_2-based heterojunctions are categorized by their charge transfer mechanisms, including type I, type II, type III, Z-scheme, and S-scheme heterojunctions [41, 311, 312].

Although heterojunction engineering improves the photocatalytic activity of TiO_2, its dependence on continuous light irradiation remains a critical limitation for photocatalytic wastewater treatment, especially during periods without light, such as overnight. In the absence of illumination, the photocatalytic activity of TiO_2 stops entirely, thereby restricting practical applications [42]. Integrating TiO_2 with a secondary semiconductor possessing energy storage capacity addresses this challenge. Photocatalysts with energy storage capacity store a portion of photon energy during light exposure and subsequently maintain their photocatalytic activity in the absence of light, thereby enabling round-the-clock wastewater treatment [47]. These materials are categorized as either oxidative or reductive storage photocatalysts. Oxidative photocatalysts (e.g., $TiO_2/Ni(OH)_2$, $TiO_2/SiO_2/MnO_x$) store photogenerated holes, while reductive photocatalysts (e.g., WO_3, MoO_3, Cu_2O) store photogenerated electrons [84]. Consequently, designing and constructing photocatalysts capable of operating in the dark is essential for achieving uninterrupted wastewater treatment [314].

Transition metal dichalcogenides (TMDs), particularly sulfide-based materials such as tungsten disulfide (WS_2), are of interest in photocatalysis due to their optical and electrical properties [297, 315]. Most interestingly, WS_2 has energy storage capacity [316-318]. In addition, this photocatalyst is characterized by low bandgap energy (1.4-2 eV), which makes it suitable for visible light-driven photocatalysis [313, 317]. WS_2 also shows nontoxicity, chemical stability, and high charge carrier mobility [89, 313, 319].

The morphology of TiO_2 plays a critical role in its photocatalytic activity [86]. Among various TiO_2 morphologies, one-dimensional (1D) nanostructures have gained attention for their radial directional confinement and high aspect ratio. These features result in a high specific surface area, which improves light absorption and facilitates charge carrier transfer [89]. Our previous work demonstrated that converting TiO_2 nanoparticles into 1D TiO_2 nanotubes (TNT) increases photocatalytic activity for the removal of Bisphenol A (BPA) [191]. Notably, floating TNT photocatalysts supported on polyurethane foam (PUF) achieved over 96% BPA degradation after 180 min under simulated sunlight.

No study has reported the round-the-clock degradation of BPA using an energy-storage floating photocatalyst. The potential of Z-scheme WS_2-TNT@PUF photocatalysts for round-the-clock BPA degradation remains underexplored, especially in floating photocatalytic systems. Constructing a Z-scheme WS_2-TNT@PUF heterostructure can enhance the photocatalytic efficiency of the floating photocatalytic system, and, more importantly, allow for the round-the-clock degradation of BPA without the need for light irradiation. Herein, floating WS_2-TNT@PUF photocatalysts were synthesized by a three-step hydrothermal method and deposited onto PUF using a wet chemical deposition process. The morphology, elemental composition, crystalline phase, chemical structure, valence state, textural and optical properties, and photoelectrochemical performance of the synthesized photocatalysts were characterized. The present study is the first to examine the electron storage capacity of floating WS_2-TNT@PUF using the methylene blue titration method. For the first time, we explored the photocatalytic activity of floating Z-scheme WS_2-TNT@PUF heterostructures for the degradation of BPA, both under simulated sunlight and in its absence. Interestingly, we studied the energy storage mechanism of floating WS_2-TNT@PUF in the absence of light. Key operating parameters for BPA degradation, including photocatalyst loading, BPA concentration, and pH, were optimized. In addition, the reusability of photocatalysts, the kinetics of photocatalytic reaction, the contribution of reactive species to BPA degradation, and the possible mechanism of BPA degradation within the Z-scheme structure were investigated under optimal photocatalytic conditions. Moreover, BPA degradation intermediates were identified, and possible degradation pathways were proposed under optimal treatment conditions.

6.3 Materials and Methods

6.3.1 Chemicals and materials

The reagents employed for TNT synthesis were ethanol (C_2H_6O, 95%, Commercial Alcohols), titanium(IV) butoxide ($C_{16}H_{36}O_4Ti$, 97%, Sigma-Aldrich), hydrochloric acid (HCl, 37% w/w, Fisher Scientific), and sodium hydroxide (NaOH, 98%, Thermo Scientific). For WS_2 synthesis, tungsten(VI) chloride (WCl_6, ≥ 99.9%, Sigma-Aldrich) and thioacetamide (C_2H_5NS, ≥ 99%, Sigma-Aldrich) served as precursors. Additional reagents included polyvinyl alcohol (low molecular weight, 98-99% hydrolyzed, Thermo Scientific Chemicals), methylene blue hydrate (≥ 97%, Sigma-Aldrich), and bisphenol A (≥ 99%, Sigma-Aldrich). Scavenging reactive species tests were conducted using benzoquinone ($C_6H_4O_2$, ≥ 98%, Sigma-Aldrich), tert-butanol ($C_4H_{10}O$, ≥ 99.5%, Sigma-Aldrich), silver nitrate ($AgNO_3$, ≥ 99.9%, Sigma-Aldrich), ammonium oxalate ($(NH_4)_2C_2O_4$, ≥ 99%, Sigma-Aldrich), and DMPO (5,5-Dimethyl-1-pyrroline N-oxide, for ESR-spectroscopy, Sigma-Aldrich). We purchased commercial polyurethane foam (medium porosity, 20 pores per inch) from Amtra and prepared all solutions using deionized water.

6.3.2 Synthesis of photocatalysts

6.3.2.1 TNT

TNT photocatalyst was synthesized by an ultrasound-assisted hydrothermal method, as reported in our previous work [191, 304].

6.3.2.2 WS_2

WS_2 was synthesized by a hydrothermal method [320]. First, C_2H_5NS (3.8 g) was dissolved in deionized water (60 mL). Subsequently, WCl_6 (2 g) was added to the solution, and the mixture was stirred for 1 h at room temperature. The solution was then transferred into a Teflon-lined autoclave (100 mL) and heated in an oven (220 °C, 24 h). After cooling to room temperature, the black precipitate was collected by filtration, rinsed with deionized water, and dried in the oven (80 °C).

6.3.2.3 WS_2-TNT

WS_2-TNT heterojunctions were fabricated by a hydrothermal method. The synthesized TNT and WS_2 with different amounts (0.5 g, 0.67 g, 0.33 g) were mixed with deionized water (60 mL) and

stirred for 1 h at room temperature. Afterward, the mixture was filled into a Teflon-lined autoclave and subjected to an oven (150 °C, 12 h). Once cooled to room temperature, the gray sample was filtered, washed with deionized water, and finally dried at 80 °C. We named the fabricated WS_2-TNT heterojunctions as WS_2-TNT-1, WS_2-TNT-2, and WS_2-TNT-3, corresponding to WS_2-TNT weight ratios of 1:1, 1:2, and 2:1, respectively.

6.3.2.4 WS_2-TNT@PUF

Floating photocatalysts, including TNT@PUF, WS_2@PUF, and WS_2-TNT@PUF heterojunctions (WS_2-TNT-1@PUF, WS_2-TNT-2@PUF, WS_2-TNT-3@PUF), were fabricated via a wet chemical deposition method, in which powder photocatalysts were immobilized onto a PUF substrate. The PUF, serving as a floating carrier, exhibited a diameter of 4 cm, a thickness of 1 cm, and a porosity of 85%. Polyvinyl alcohol (PVA) was employed as a binder [140]. To prepare the mixture, 1 wt.% PVA was dissolved in deionized water (30 mL) and heated at 95 °C for 3 h in a three-neck flask (100 mL). Different amounts of photocatalysts (0.5 g, 0.7 g, 1 g) were added to the solution, which was then heated to 95 °C for an additional 2 h under continuous stirring. The solution was then cooled to 80 °C, after which the PUF carrier was immersed and subsequently dried in an oven at 80 °C. Figure 6.1 presents the synthesis procedures for TNT, WS_2, WS_2-TNT, and floating WS_2-TNT@PUF.

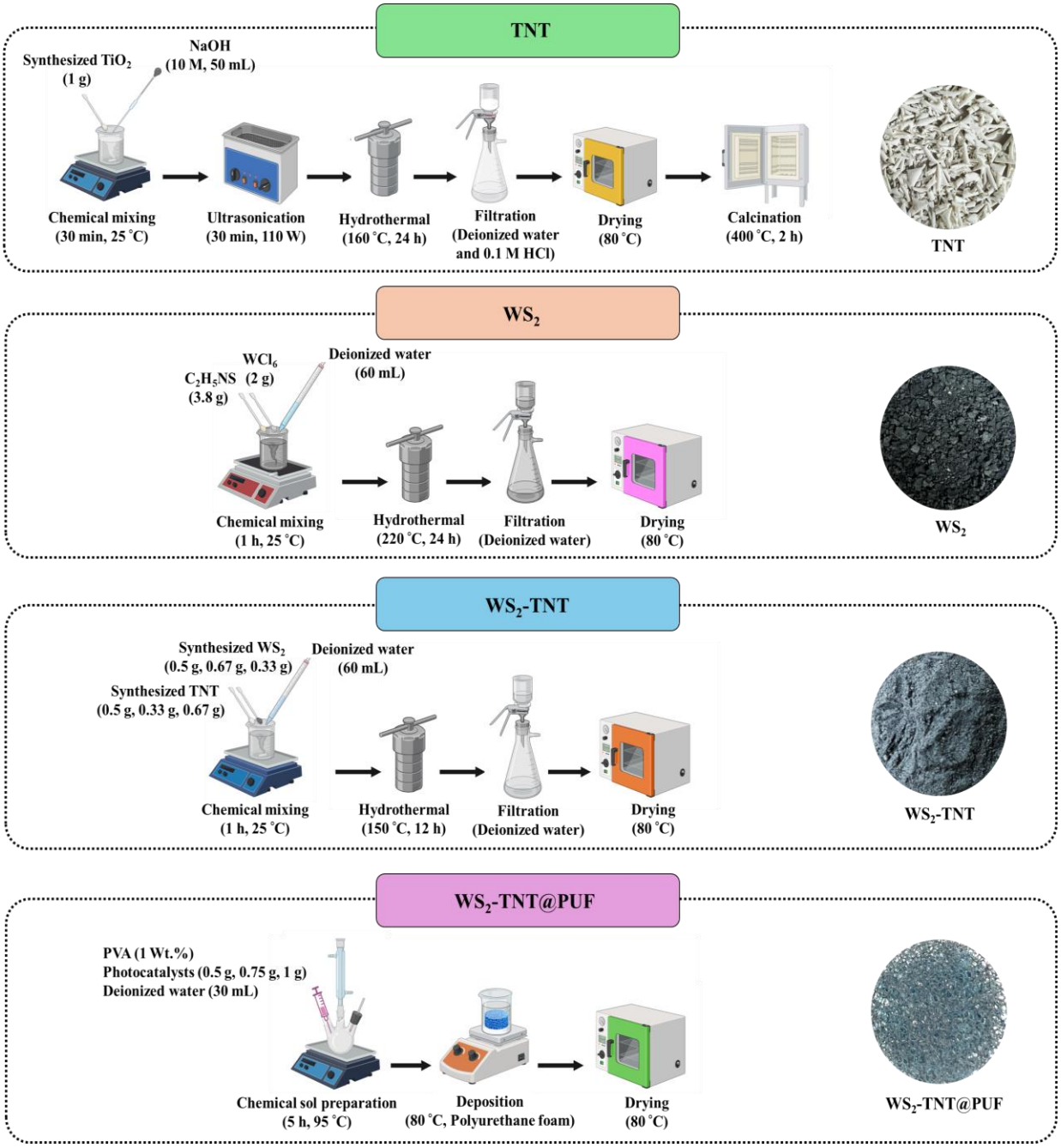

Figure 6.1 Schematic illustration of the synthesis procedures for TNT, WS_2, WS_2-TNT, and WS_2-TNT@PUF.

6.3.3 Characterizations

The morphology and elemental composition of the photocatalysts were characterized using field-emission scanning electron microscopy (FESEM, JSM-7600TFE, JEOL) coupled with energy-dispersive X-ray spectroscopy (EDS). Transmission electron microscopy (TEM) and high-

resolution transmission electron microscopy (HR-TEM) analyses (JEM-2100F, JEOL) were employed to further examine the morphology of the photocatalysts. The particle size of the photocatalysts was determined using Digimizer software (version 6.4.5).

The crystalline phases of the photocatalysts were identified by X-ray diffraction (XRD) using a D8 Advance diffractometer (Bruker). The chemical compositions and valence states of the photocatalysts were analyzed by X-ray photoelectron spectroscopy (XPS) with a VG ESCALAB 250Xi spectrometer (Thermo Scientific).

Nitrogen adsorption-desorption isotherms at 77 K were obtained using the Brunauer-Emmett-Teller (BET) method. The textural properties of the photocatalysts, such as specific surface area, total pore volume, and average pore size, were derived from measurements conducted on an Autosorb analyzer (6100 FKM MP - MP, Anton Paar).

The bandgap energy (E_g) of the photocatalysts was determined by diffuse reflectance spectroscopy (DRS) using a UV-Vis spectrophotometer (Evolution™ 220, Thermo Fisher Scientific). The E_g values were obtained from plots of $[F(R) \times h\vartheta]^{0.5}$ versus $h\vartheta$ as follows [142, 143]:

$$F(R) = \frac{(1-R)^2}{2R} \tag{6.1}$$

In Equation 6.1, *F(R)* is the Kubelka-Munk function, and *R* is reflectance.

$$h\vartheta = \frac{1240}{\lambda} \tag{6.2}$$

In Equation 6.2, $h\vartheta$ corresponds to the photon energy and λ represents the wavelength (nm).

The conduction band (CB) and valence band (VB) edge potentials of the photocatalysts were determined using Mulliken's electronegativity theory as follows [72, 304]:

$$E_{CB} = X - E^e - (0.5\, E_g) \tag{6.3}$$

$$E_{VB} = E_{CB} + E_g \tag{6.4}$$

In Equations 6.3 and 6.4, E_{CB} is the conduction band edge potential, E^e represents the energy of free electrons on the hydrogen scale (~ 4.5 eV), E_{VB} corresponds to the valence band edge potential, and X is the electronegativity of the photocatalysts, calculated as follows:

$$X = (\prod_{i}^{n} x_i^{v_i})^{\frac{1}{\sum_i^n v_i}} \quad (6.5)$$

$$x_i = \frac{E_a + E_{ion}}{2} \quad (6.6)$$

In Equations 6.5 and 6.6, x_i refers to the Mulliken electronegativity of element i, v_i represents the number of elements, E_{ion} is the first ionization energy, and E_a corresponds to the electron affinity.

6.3.4 Photoelectrochemical characterizations

We conducted photoelectrochemical tests to assess the electron storage capacity of the synthesized photocatalysts. The photocatalyst powders were deposited onto a fluorine-doped tin oxide (FTO) glass substrate via the doctor-blade technique. The immobilized photocatalysts were employed as the working electrode, with platinum foil and an Ag/AgCl electrode serving as the counter and reference electrodes, respectively. A 0.01 M sodium sulfate (Na_2SO_4) solution was used as the electrolyte, and voltammetry analysis was performed using a potentiostat/galvanostat (VersaSTAT3, AMETEK Scientific, USA). The working electrode was illuminated with a 300 W commercial solar lamp (Ultra-Vitalux, Osram) at an intensity of 35 W/m^2. Chronoamperometry tests were carried out at a constant potential of 0 V (vs. Ag/AgCl), with two cycles of solar lamp on-off pulses at equal duration. Additionally, electrochemical impedance spectroscopy (EIS) was conducted to examine the charge transfer behavior of the photocatalysts over a 0.1 Hz to 100 kHz frequency range with a 10 mV amplitude.

6.3.5 Determination of the point of zero charge

The pH at the point of zero charge (pH_{pzc}) of the photocatalyst was determined via the pH drift method [321]. A set of 100 mL 0.1 M NaCl solutions with varying initial pH values was prepared by adjusting the pH with 0.1 M HCl and 0.1 M NaOH. Subsequently, 25 mg of photocatalyst was introduced into each solution and stirred for 24 h. The final pH of the solutions was then measured and plotted as a function of the initial pH. The pH_{pzc} was determined at the intersection of the initial-final pH curve and the line y = x.

6.3.6 Floating photocatalytic experiments

The photocatalytic activity of floating WS_2-TNT heterojunctions, including WS_2-TNT-1@PUF, WS_2-TNT-2@PUF, and WS_2-TNT-3@PUF, as well as TNT@PUF and WS_2@PUF, was evaluated for the degradation of BPA in a batch photoreactor under simulated sunlight. We investigated the impact of operational parameters on BPA degradation, including BPA concentration (10-40 mg/L), photocatalyst loading (0.1-0.4 g), and pH (4-10). The photocatalyst loading corresponds to the quantities immobilized on the PUF support. The BPA solution was prepared with an initial volume of 200 mL. The pH of the solution was adjusted with 0.1 M HCl or 0.1 M NaOH, with an initial pH of 5.7. Illumination was provided by a 300 W commercial solar lamp (Ultra-Vitalux, Osram) with a light intensity of 35 W/m^2, positioned 20 cm above the photoreactor. Prior to irradiation, photocatalysts were kept in the dark for 60 min to reach adsorption-desorption equilibrium. Additionally, control experiments (photolysis) were performed under simulated sunlight irradiation without the presence of photocatalysts. All photocatalytic experiments were repeated three times.

6.3.7 Reusability experiments

We evaluated the reusability of floating photocatalysts for the degradation of BPA over five consecutive cycles under optimal treatment conditions. Following each cycle, the photocatalyst was washed with deionized water, dried at 80 $^{\circ}C$, and subsequently reused. The structural stability of the fresh and used photocatalysts after five cycles was further analyzed using XRD.

6.3.8 Scavenging reactive species experiments

The reactive species contributing to BPA degradation were investigated using scavenger experiments conducted under optimal treatment conditions. Specifically, ammonium oxalate (AO, 1 mM) as a scavenger for photogenerated holes (h^+), silver nitrate ($AgNO_3$, 1 mM) for electrons (e^-), tert-butanol (t-BuOH, 1 mM) for hydroxyl radicals ($^{\bullet}OH$), and benzoquinone (BZQ, 1 mM) for superoxide anions ($^{\bullet}O_2^-$) were added to the floating system. In addition, reactive species generated during BPA degradation under optimal treatment conditions were detected using an electron paramagnetic resonance spectrometer (EPR, Magnettech ESR5000, Bruker) with a spin-trapping technique employing 50 mM DMPO.

6.3.9 Electron titration experiments

We investigated the electron storage capacity of photocatalysts using the methylene blue (MB) titration method [322, 323]. Briefly, 0.04 g of each photocatalyst was dispersed in 100 mL of deionized water and irradiated with a solar lamp (Ultra-Vitalux, Osram, 300 W) for 60 min. After stopping light irradiation, 100 µL of MB (1 µmol/mL) was gradually added to the solution, which was stirred in the dark for 10 min. The solution concentration was determined using a UV-Vis spectrophotometer (Evolution™ 220, Thermo Fisher Scientific) at 655 nm.

Reactions 6.1 and 6.2 show the reaction scheme of the MB titration method, which is used to measure the electron storage capacity of photocatalysts [323]. During the simulated sunlight irradiation, some electrons can be stored in the photocatalyst. Then, in the absence of irradiation, the stored electrons are released to an appropriate electron acceptor, such as MB. The MB can accept one electron from the photocatalyst to form $MB^{-\bullet}$, which undergoes rapid transformation into a colourless dye, MB^{2-}. As the MB titration continues, the trapped electrons in the photocatalyst are gradually consumed. Once all the stored electrons are consumed, adding more MB results in an increase in absorption at 655 nm.

$$Photocatalyst\ (e^-) + MB \rightarrow Photocatalyst + MB^{-\bullet} \qquad \text{(Reaction 6.1)}$$

$$MB^{-\bullet} + MB^{-\bullet} \rightarrow MB^{2-} + MB \qquad \text{(Reaction 6.2)}$$

Based on Reactions 6.1 and 6.2, consuming 2 mol of electrons corresponds to using 1 mol of MB.

6.3.10 BPA detection methods

At regular intervals, 1 mL aliquots of the BPA solution were collected from the photoreactor. The concentration of BPA was measured by LC-UV-MS using an LC-TOF 6224 mass spectrometer coupled to an Infinity 1260 HPLC system (Agilent Technologies Inc.), operated with MassHunter Workstation 10.1 software. The mobile phase consisted of (A) water with 0.1% formic acid and (B) acetonitrile. The chromatographic column was a Varian Pursuit XRs 3 Diphenyl (75 mm × 4.6 mm) maintained at a constant temperature of 40 °C and operated at a flow rate of 0.5 mL/min. Aliquots of 1 µL were injected, and elution was performed under the following gradient: 0-0.2 min, 20% B; 0.2-5 min, 20-90% B; 5-6 min, 90% B; 6-6.2 min, 90-20% B, followed by an equilibration step up to 10 min total time. Eluted species were detected sequentially by a UV detector at 280 nm and subsequently analyzed by mass spectrometry in negative electrospray ionization mode over an

m/z range of 100-3000. The MS signal was used to confirm the identity of BPA. Peak areas at 280 nm yielded a linear calibration curve over 50-50,000 ppb (R^2 = 0.9998). The limit of detection (LOD) and quantification (LOQ) were determined to be 0.1 mg/L and 0.3 mg/L, respectively.

The degradation efficiency of BPA (η) was determined as follows:

$$\eta = \left(1 - \frac{C}{C_0}\right) \times 100\% \tag{6.7}$$

In Equation 6.7, C_0 represents the initial BPA concentration, and C is the BPA concentration at time t.

Intermediates generated during the photocatalytic degradation of BPA under optimal treatment conditions were identified by LC-UV-MS. Chromatographic separation was performed on an XBridge Phenyl column (4.6 mm × 100 mm, 3.5 µm) maintained at 50 °C and 0.4 mL/min. For each analysis, a 1 µL aliquot was injected. Elution followed a gradient program: 0-3 min, 10% B; 3-17 min, 10-65% B; 17-17.5 min, 65-98% B; 17.5-19 min, 98% B; 19-19.1 min, 98-10% B, with equilibration to a total time of 25 min. Detection was performed sequentially by a UV detector at 254 nm, followed by mass spectrometry in negative electrospray ionization mode. Mass spectra were recorded from m/z 100 to m/z 3000. Elemental compositions of the detected species were assigned based on accurate mass measurements. Carbon, hydrogen, and up to 20 oxygen atoms were permitted in the molecular formula generation. A mass tolerance of 5 mDa was applied between experimental and theoretical m/z values.

6.4 Results and Discussion

6.4.1 Morphologies and elemental compositions of photocatalysts

Figures 6.2(a–c) present the morphology of TNT, WS_2, and WS_2-TNT-1. The SEM images show that TNT exhibited a nanotubular structure, while WS_2 had a spherical morphology (Figures 6.2(a) and 6.2(b)). In WS_2-TNT-1, the morphological features of both TNT and WS_2 were observed (Figure 6.2(c)), confirming their coexistence within the heterojunction photocatalyst. Notably, WS_2-TNT-1 exhibited the highest photocatalytic efficiency for BPA degradation, as detailed in Section 6.4.6. Additionally, TEM and HR-TEM images show that TNT exhibited a hollow nanotubular morphology, with an outer diameter of 8.2 nm, an inner diameter of 5.8 nm, and a wall thickness of 1.2 nm (Figure 6.2(a)). Also, the size of spherical WS_2 was 100 nm (Figure 6.2(b)).

These values represent average measurements obtained using Digimizer. Moreover, the corresponding EDX spectra of TNT and WS_2 show that TNT was composed of 68% Ti and 32% O, and the elemental composition of WS_2 was 75% W and 25% S (Figures 6.2(d) and 6.2(e)). Figure 6.2(f) indicates the presence of Ti, O, W, and S elements in WS_2-TNT-1 heterojunction, with respective compositions of 25%, 19.5%, 41.5%, and 14%. Furthermore, Figures 6.2(g–i) show a uniform distribution of these elements on the photocatalysts. The SEM images, EDS spectra, and EDS mappings of WS_2-TNT-2 and WS_2-TNT-3 heterojunctions are presented in Figure 6.12.

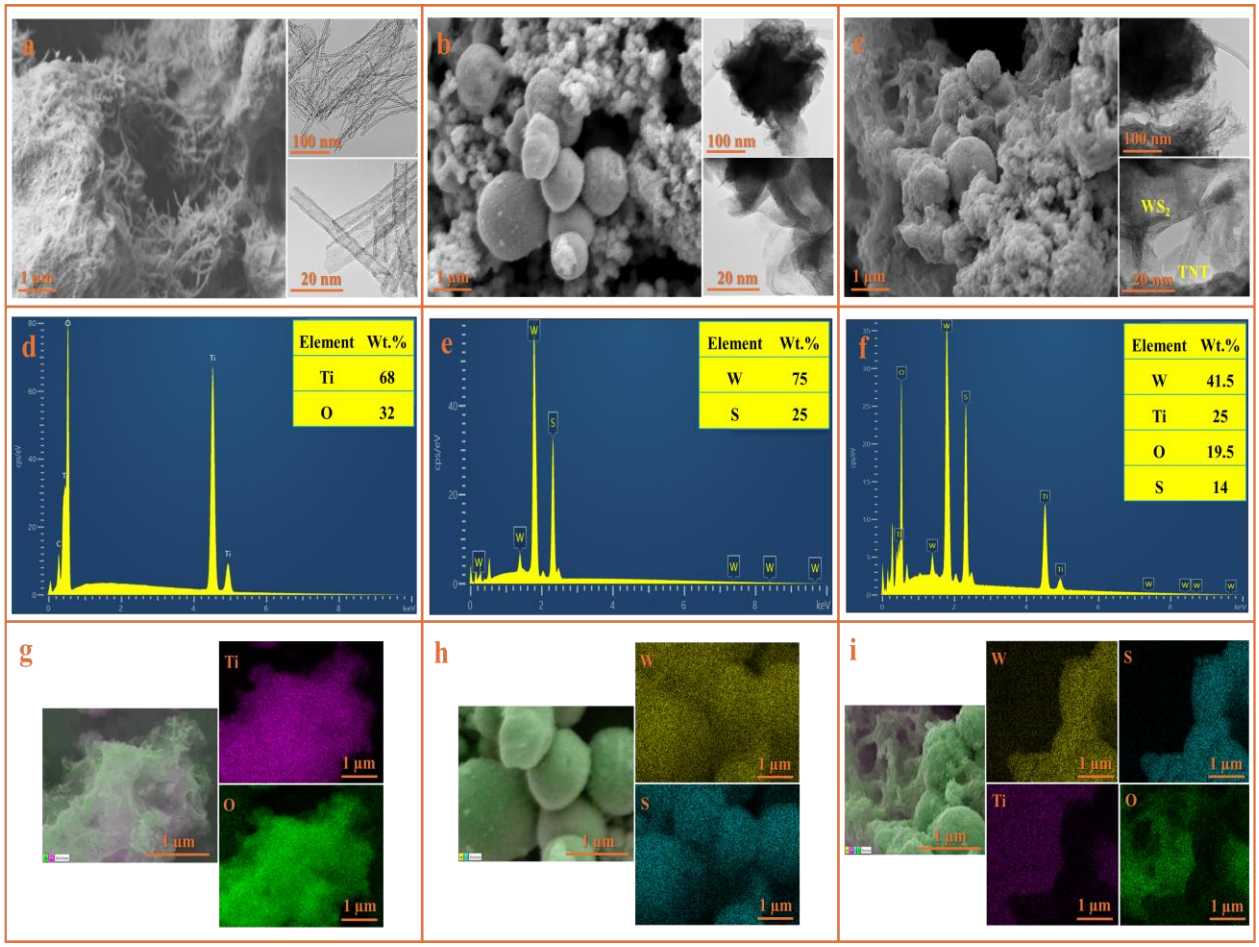

Figure 6.2 SEM, TEM, and HR-TEM images of (a) TNT, (b) WS_2, and (c) WS_2-TNT-1; EDS spectra of (d) TNT, (e) WS_2, and (f) WS_2-TNT-1; EDS mappings of (g) TNT, (h) WS_2, and (i) WS_2-TNT-1

Figure 6.3(a) shows the SEM of pristine PUF before the photocatalyst deposition. This exhibits the open-cell structure of the PUF, along with a relatively smooth surface that retains its inherent roughness. Figure 6.3(b) confirms the successful deposition of WS_2-TNT-1 onto the PUF, leading to the formation of a floating WS_2-TNT-1@PUF photocatalyst. EDS mapping of PUF indicates that the carrier was composed of C, N, and O elements (Figure 6.3(c)). As shown in Figure 6.3(d), Ti, O, W, and S elements were uniformly distributed in WS_2-TNT-1@PUF.

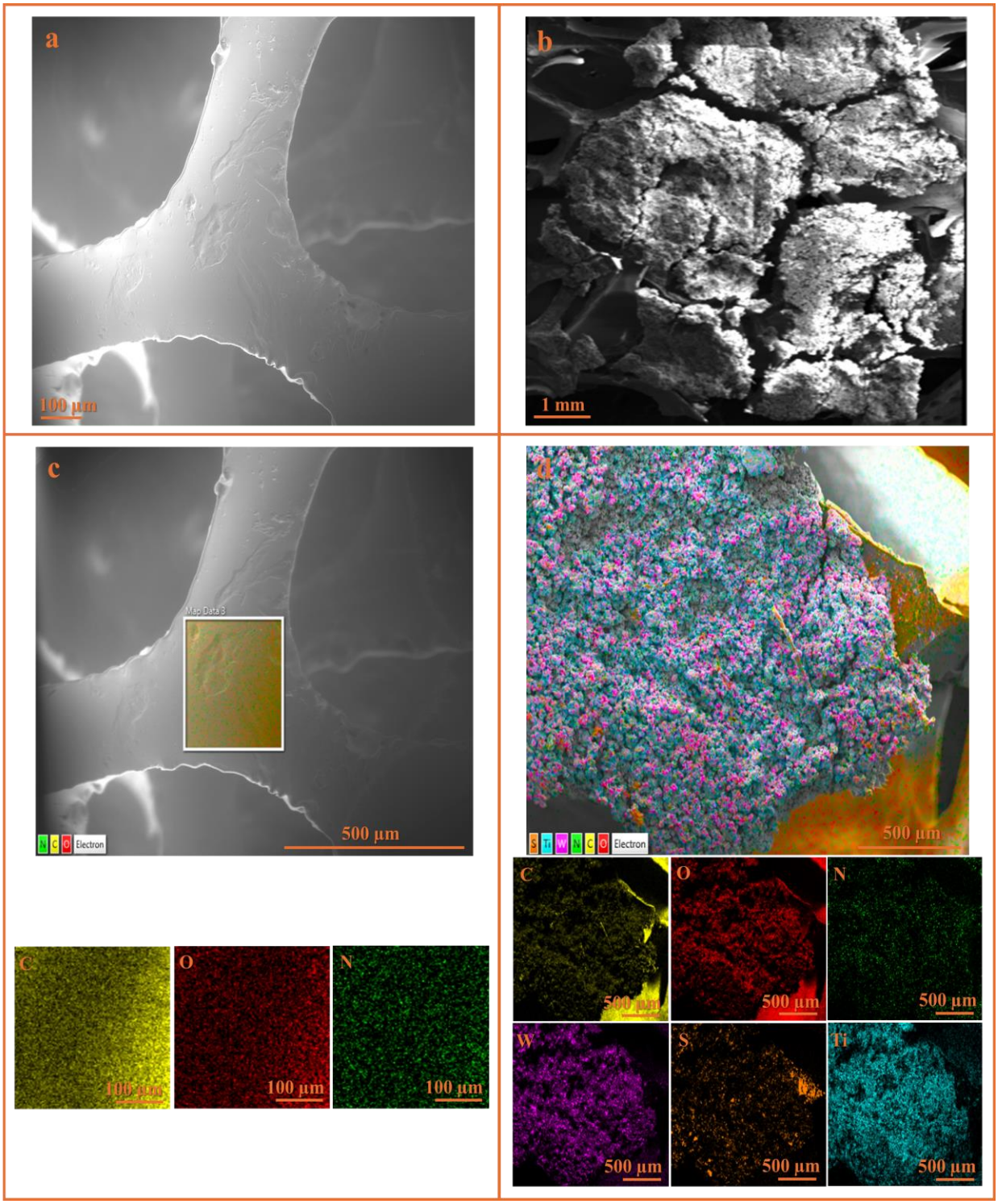

Figure 6.3 SEM images of (a) PUF and (b) WS_2-TNT-1@PUF; EDS mappings of (c) PUF and (d) WS_2-TNT-1@PUF

6.4.2 Chemical compositions and valence states of photocatalysts

Figures 6.4(a–e) show the XPS spectrum of WS_2-TNT-1. The presence of Ti, O, W, and S elements confirmed the existence of both TNT and WS_2 in WS_2-TNT-1 heterojunction (Figure 6.4(a)). WS_2-TNT-1 showed two distinct peaks at binding energies of 464.9 eV (Ti $2p_{1/2}$) and 459.2 eV (Ti $2p_{3/2}$), with a spin-orbit splitting of 5.7 eV, characteristic of Ti^{4+} in TNT (Figure 6.4(b)) [324, 325]. In addition, Figure 6.4(c) shows a peak at 530.6 eV, attributed to lattice oxygen in TNT [325, 326]. The XPS spectra of pristine TNT are presented in Figures 6.13(a) and 6.13(b). Compared to pristine TNT, the spectra of Ti 2p and O 1s in WS_2-TNT-1 exhibited a blueshift of 0.2 eV and 0.1 eV, respectively. Moreover, the spectrum of W 4f showed two peaks at 34.8 eV (W $4f_{5/2}$) and 32.7 eV (W $4f_{7/2}$) (Figure 6.4(d)). The observed peak separation of 2.1 eV refers to W^{4+} in WS_2 [89, 325]. Based on Figure 6.4(e), two peaks of 162.9 eV and 161.8 eV correspond to S $2p_{1/2}$ and S $2p_{3/2}$, respectively, suggesting S^{2-} in WS_2 with a spin-orbit splitting of 1.1 eV [89, 324]. Figures 6.13(c) and 6.13(d) show the XPS spectra of pristine WS_2. The peaks of WS_2 in WS_2-TNT-1 had 0.1 eV redshifts for W 4f and S 2p relative to pristine WS_2. The shifts in peaks of both TNT and WS_2 in WS_2-TNT-1 confirm the formation of a heterojunction between TNT and WS_2 [89, 206, 316, 326].

6.4.3 Crystalline phases of photocatalysts

Figure 6.4(f) presents the XRD patterns of TNT, WS_2, WS_2-TNT-1, WS_2-TNT-2, and WS_2-TNT-3. Pure TNT exhibited characteristic diffraction peaks at 25.3°, 37.9°, 48.1°, 53.9°, 55.2°, and 62.8° assigned to the Miller indices of (101), (004), (200), (105), (211), and (204) planes of the anatase phase, respectively (JCPDS file 21-1272) [191, 304]. In addition, WS_2 showed peaks at 14.3°, 32.6°, 43.8°, 49.5°, 58.2°, and 69.7° corresponding to the Miller indices of (002), (100), (006), (105), (110), and (108) planes of the hexagonal phase, respectively (JCPDS file 08-0237) [326, 327]. In the XRD patterns of WS_2-TNT heterojunctions, the characteristic peaks of both TNT and WS_2 were observed. This indicates the coexistence of WS_2 and TNT crystalline structures within WS_2-TNT heterostructures, confirming the formation of a heterojunction between the two photocatalysts [206, 315, 325]. As shown in Figure 6.4(f), the peak intensities for TNT and WS_2 varied depending on their relative contents in WS_2-TNT heterostructures. In WS_2-TNT-3 heterojunction, the peak intensity of WS_2 increased with an increase in the WS_2 amount, while the peak intensity of TNT decreased. Conversely, in WS_2-TNT-2 heterojunction, where the amount of TNT exceeded that of WS_2, the peaks for TNT became more prominent. Notably, WS_2-TNT-1 heterojunction displayed

intense peaks for both TNT and WS_2. Moreover, no peaks related to impurities were detected in WS_2-TNT heterojunctions, indicating their purity.

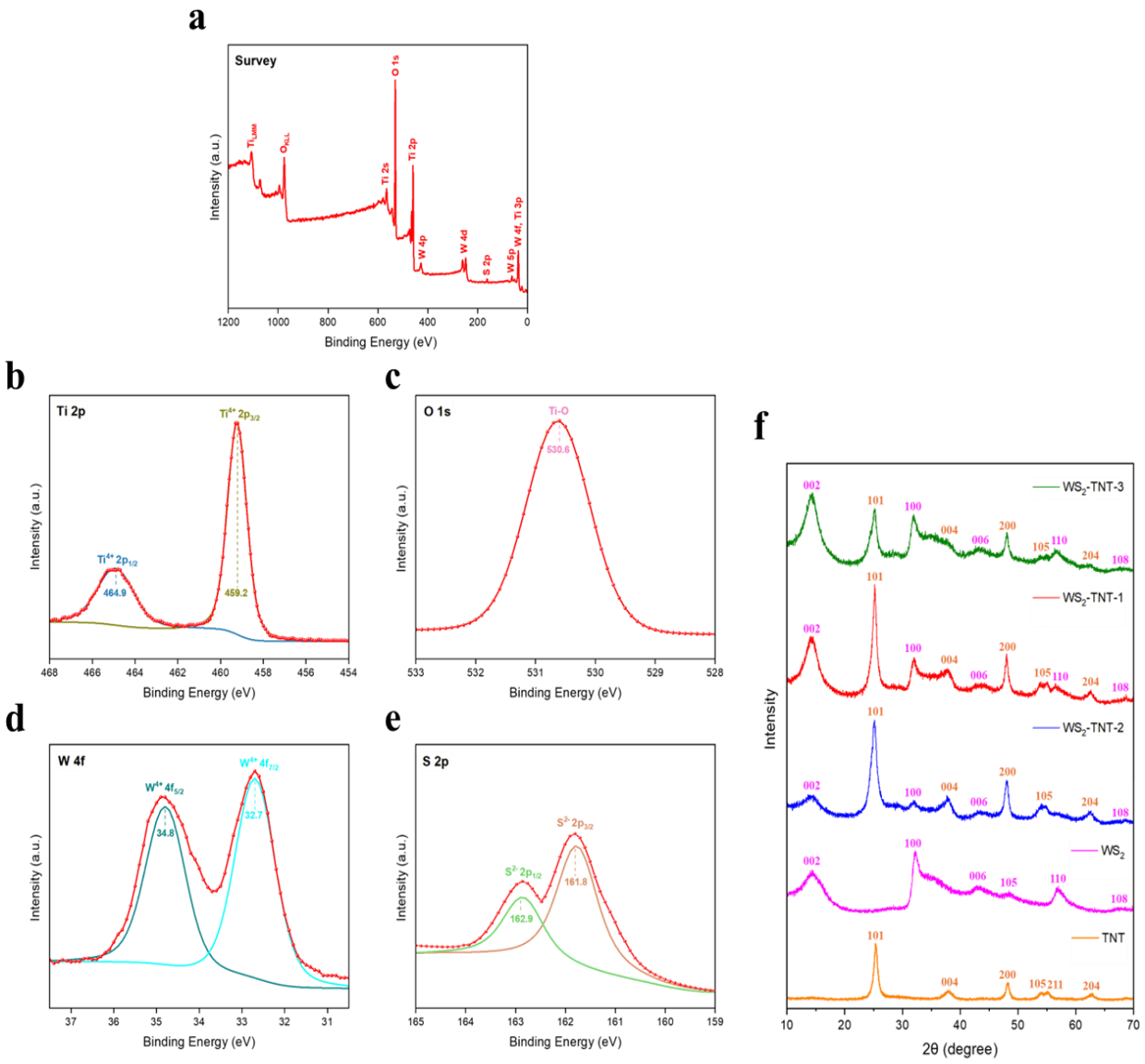

Figure 6.4 XPS spectrum of WS2-TNT-1 (a) Survey spectrum, (b-e) High-resolution spectra of Ti 2p, O 1s, W 4f, and S 2p, respectively; (f) XRD patterns of TNT, WS_2, WS_2-TNT-1, WS_2-TNT-2, and WS_2-TNT-3

6.4.4 Optical features of photocatalysts

Figures 6.5(a) and 6.5(b) show the DRS analyses of TNT, WS_2, WS_2-TNT-1, WS_2-TNT-2, and WS_2-TNT-3. Bare TNT had an intense absorption peak in the UV region, with an absorption edge observed at approximately 415 nm, and WS_2 exhibited strong absorption from the UV region to

the visible light region (Figure 6.5(a)). In addition, the bandgap energies of TNT and WS_2 calculated by Equation 6.2 were 3.0 eV and 1.8 eV, respectively (Figure 6.5(b)). Compared with TNT and WS_2, the absorption edges of WS_2-TNT heterojunctions had a redshift, with values of about 445 nm for WS_2-TNT-1, 430 nm for WS_2-TNT-2, and 460 nm for WS_2-TNT-3 (Figure 6.5(a)). This redshift can be due to the formation of a WS_2-TNT heterojunction that improves the visible light absorption of the photocatalysts [297, 325]. Moreover, the bandgap energies of WS_2-TNT heterojunctions were lower than that of TNT (3 eV), which was 2.9 eV, 2.8 eV, and 2.7 eV for WS_2-TNT-2, WS_2-TNT-1, and WS_2-TNT-3, respectively (Figure 6.5(b)). The bandgap energy of WS_2-TNT heterojunctions was reduced by increasing the ratio of WS_2, leading to improved photocatalytic activity for visible light-driven processes.

6.4.5 Textural properties of photocatalysts

Figure 6.5(c) presents the adsorption-desorption isotherms of TNT, WS_2, WS_2-TNT-1, WS_2-TNT-2, and WS_2-TNT-3. Based on the IUPAC classification of physisorption isotherms and hysteresis loops [175], all photocatalysts exhibited type IV isotherms characterized by H3 hysteresis loops, indicating a slit-like mesoporous structure in the photocatalysts [139].

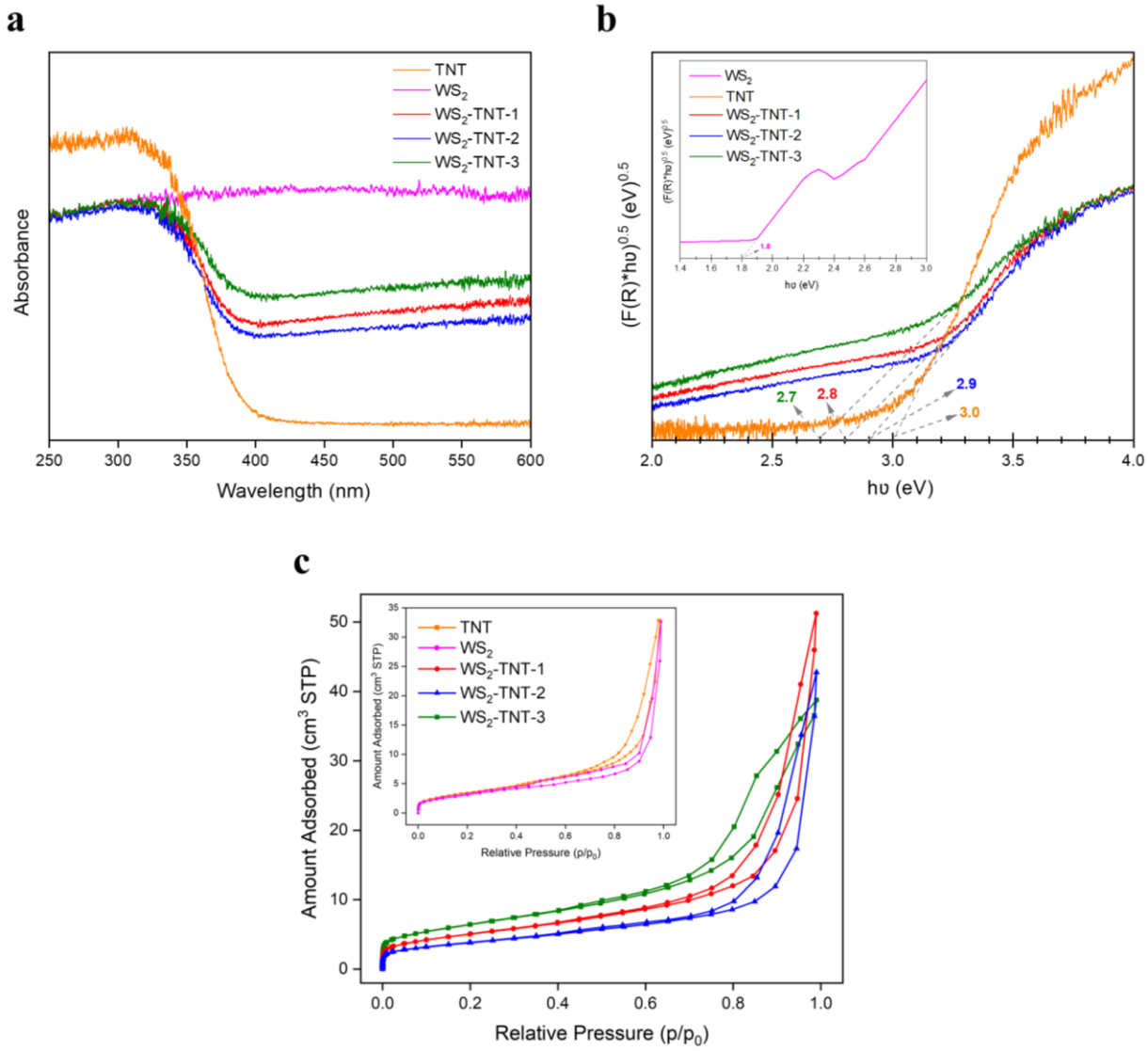

Figure 6.5 (a) Absorption spectra, (b) Bandgap energies, and (c) Adsorption-desorption isotherms of TNT, WS_2, WS_2-TNT-1, WS_2-TNT-2, and WS_2-TNT-3

Table 6.1 lists the BET surface area, total pore volume, and average pore size of TNT, WS_2, WS_2-TNT-1, WS_2-TNT-2, and WS_2-TNT-3. The BET surface areas for TNT and WS_2 were measured at 110 m^2/g and 45 m^2/g, respectively. Notably, the BET surface areas of WS_2-TNT heterojunctions were higher than those of TNT and WS_2, with values of 192 m^2/g for WS_2-TNT-1, 146 m^2/g for WS_2-TNT-2, and 125 m^2/g for WS_2-TNT-3. Additionally, WS_2-TNT heterojunctions exhibited a smaller mean pore size, ranging from 14 nm to 16 nm, compared to TNT (31 nm) and WS_2 (25 nm). The improved textural properties of WS_2-TNT photocatalysts indicate the successful

formation of a TNT-WS_2 heterojunction, which increases the availability of active sites for photocatalytic reactions [297, 325, 326].

Table 6.1 BET results of TNT, WS_2, WS_2-TNT-1, WS_2-TNT-2, and WS_2-TNT-3

Photocatalyst	Specific surface area (m^2/g)	Total pore volume (cm^3/g)	Mean pore size (nm)
TNT	110	0.57	31
WS_2	45	0.43	25
WS_2-TNT-1	192	0.75	14
WS_2-TNT-2	146	0.60	15
WS_2-TNT-3	125	0.58	16

6.4.6 Impact of operational parameters on BPA degradation

Figure 6.6(a) shows the photocatalytic activity of the synthesized floating photocatalysts, including TNT@PUF, WS_2@PUF, WS_2-TNT-1@PUF, WS_2-TNT-2@PUF, and WS_2-TNT-3@PUF, to degrade BPA under simulated sunlight. The experiments were initiated with a BPA concentration of 20 mg/L and a photocatalyst loading of 0.1 g at the spontaneous pH (5.7) for 180 min of irradiation. In photolysis, no BPA degradation was observed. Additionally, during 60 min of darkness in the presence of the photocatalysts, variations in BPA concentration were observed, related to the adsorption-desorption equilibrium between BPA and the photocatalyst surface. WS_2-TNT-1@PUF exhibited the highest BPA adsorption among the photocatalysts (15%). In addition, the adsorption was 13% for WS_2-TNT-2@PUF, 12% for WS_2-TNT-3@PUF, 10% for TNT@PUF, and 9% for WS_2@PUF.

TNT@PUF degraded 75% of BPA, while WS_2@PUF degraded 45%. In comparison, floating WS_2-TNT heterojunctions presented higher photocatalytic activity for BPA degradation than both TNT@PUF and WS_2@PUF. The BPA degradation increased to 81% and 86% for WS_2-TNT-3@PUF and WS_2-TNT-2@PUF, respectively. Among the evaluated floating photocatalysts, WS_2-TNT-1@PUF demonstrated the highest photocatalytic activity, achieving 90% BPA degradation after 180 min of irradiation. The superior photoactivity of WS_2-TNT-1@PUF can be attributed to its physicochemical properties. As shown in Table 6.1, WS_2-TNT-1 has the highest BET surface

area (192 m^2/g) and total pore volume (0.75 cm^3/g), thereby providing more active sites for BPA photocatalytic degradation. In addition, the bandgap energy of WS_2-TNT-1 (2.8 eV; Figure 6.5(b)) enhances visible-light absorption, thus improving its photocatalytic efficiency. Therefore, we selected WS_2-TNT-1@PUF as the most effective floating photocatalyst for the degradation of BPA in the following experiments.

Figure 6.6(b) shows the effect of different loadings of WS_2-TNT-1@PUF, evaluated at 0.1 g, 0.2 g, and 0.4 g, on BPA degradation under constant conditions (20 mg/L BPA, pH 5.7). By increasing WS_2-TNT-1@PUF loading from 0.1 g to 0.2 g, BPA degradation increased from 90% to 96% after 180 min. However, a further increase to 0.4 g led to a decline in degradation efficiency, with BPA removal decreasing to 93%. The enhancement observed at lower dosage is attributed to the presence of more active photocatalytic sites in the PUF that are available for interaction with light irradiation, thereby enhancing the photocatalytic reaction [134, 190, 304]. Conversely, the decline in BPA degradation at higher loading is likely due to pore blockage in the PUF caused by photocatalyst agglomeration during synthesis, which limits light penetration and reduces photocatalytic degradation efficiency [111, 134, 190, 282, 283, 304]. As a result, the loading of WS_2-TNT-1@PUF was optimized to 0.2 g.

Figure 6.6(c) presents the degradation of BPA at different concentrations (10 mg/L, 20 mg/L, 40 mg/L) using 0.2 g of WS_2-TNT-1@PUF at pH 5.7. 20 mg/L BPA resulted in a 96% degradation after 180 min of irradiation. An increase in BPA concentration from 20 mg/L to 40 mg/L resulted in a decrease in BPA degradation to 85%. In contrast, reducing the BPA concentration to 10 mg/L increased the degradation to over 97% after 120 min of irradiation. The results indicate that lower BPA concentrations are associated with greater BPA degradation. With increasing BPA concentration, the accumulation of BPA and its degradation products on the photocatalyst surface reduces the number of available active sites, thereby hindering photocatalytic reactions and lowering degradation efficiency [139, 284, 285, 304]. Based on the results, the optimal BPA concentration for degradation was determined to be 10 mg/L.

Figure 6.6(d) depicts the effect of pH levels, tested at pH 4, 5.7, 8, and 10, on BPA degradation using WS_2-TNT-1@PUF loading of 0.2 g and BPA concentration of 10 mg/L. At pH 10, BPA degradation reached its minimum value of 70% after 120 min. Under the same irradiation time, BPA degradation increased to 80% at pH 4. Conversely, the maximum BPA degradation was

observed at pH 8, where degradation exceeded 97% within 60 min. At pH 5.7, BPA degradation reached more than 97% after 120 min. These observations can be attributed to the surface charge characteristics of WS_2-TNT-1@PUF. The point of zero charge of WS_2-TNT-1@PUF is 4.7 (pH_{PZC} = 4.7; Figure 6.14). The pk_a of BPA is 9.6 [286]. At pH 4, both BPA and the surface of WS_2-TNT-1@PUF have positive charges, leading to electrostatic repulsion that limits BPA adsorption onto the photocatalyst surface and reduces degradation efficiency. Similarly, at pH 10, electrostatic repulsion between the negatively charged BPA and the negatively charged WS_2-TNT-1@PUF surface suppresses BPA degradation. In comparison, at pH 5.7, the surface of WS_2-TNT-1@PUF is negatively charged, while BPA is positively charged. This electrostatic attraction enhances BPA degradation by improving its adsorption onto the WS_2-TNT-1@PUF surface. At pH 8, the surface of WS_2-TNT-1@PUF is more negatively charged, facilitating greater adsorption of the positively charged BPA and thereby improving degradation efficiency (>97% after 60 min).

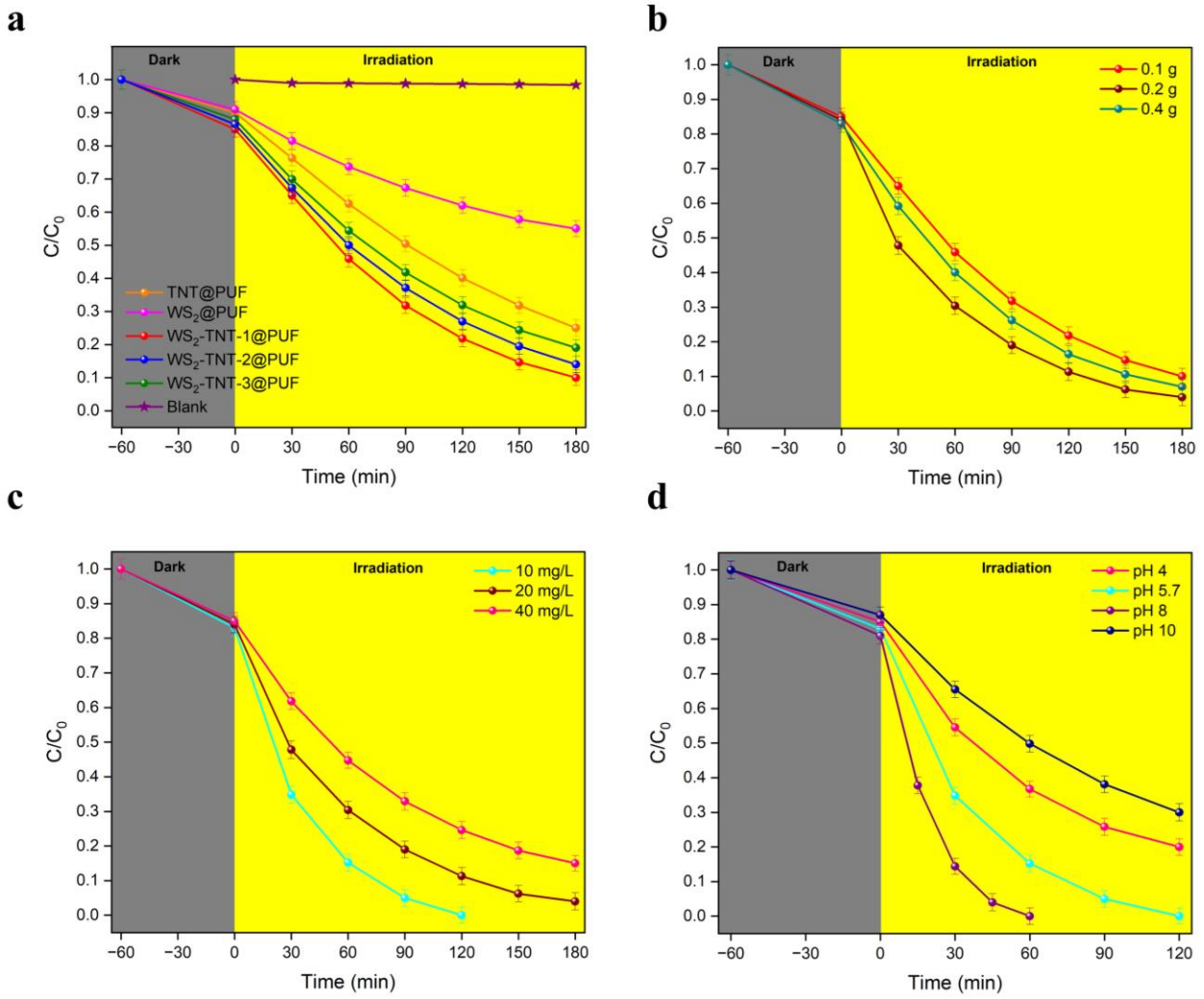

Figure 6.6 Effect of (a) type of photocatalysts, (b) photocatalyst loading, (c) BPA concentration, and (d) pH on BPA degradation (Error bars correspond to the standard deviation derived from three replicates)

The optimal treatment conditions for BPA degradation under simulated sunlight were determined to be 0.2 g of WS_2-TNT-1@PUF, an initial BPA concentration of 10 mg/L, pH 8, and 60 min of irradiation. The LC-MS chromatograms of BPA degradation under optimized conditions are presented in Figure 6.15. After 60 min of the photocatalytic reaction, the BPA peak was not detected, indicating >97% degradation based on the LOQ of 0.3 mg/L.

6.4.7 Kinetics models for BPA degradation

Under optimal treatment conditions (0.2 g WS_2-TNT-1@PUF, 10 mg/L BPA, pH 8, 60 min irradiation), the kinetics of BPA degradation were investigated. Equation 6.8 presents the degradation rate of BPA [72, 170]:

$$r = -\frac{dC}{dt} = k_{app}C^n \tag{6.8}$$

Where k_{app} is the apparent rate constant, C is BPA concentration, n is the reaction order, and t is irradiation time.

Equations 6(9–11) show zero-order kinetics (n = 0), first-order kinetics (n = 1), and second-order kinetics (n = 2), respectively.

$$C = -k_{app}t + C_0 \tag{6.9}$$

$$Ln\frac{C}{C_0} = -k_{app}t \tag{6.10}$$

$$\frac{1}{C} = k_{app}t + \frac{1}{C_0} \tag{6.11}$$

C_0 represents the initial BPA concentration.

Correlation coefficients (R^2) and apparent rate constants (k_{app}) obtained from the kinetics models (Equations 6(9–11)) are presented in Table 6.2. The degradation of BPA followed a first-order kinetic model, yielding a k_{app} of 0.069 min^{-1} (R^2 = 0.99).

Table 6.2 R^2 and k_{app} for BPA degradation kinetic models under optimized conditions

Kinetics models	R^2	k_{app}
n = 0	0.86	0.130 (mg L^{-1} min^{-1})
n = 1	0.99	0.069 (min^{-1})
n = 2	0.79	0.050 (mg^{-1} L min^{-1})

6.4.8 Reusability of photocatalysts

Figure 6.7(a) shows the reusability of WS_2-TNT-1@PUF for the degradation of BPA under optimal treatment conditions (0.2 g WS_2-TNT-1@PUF, 10 mg/L BPA, pH 8, 60 min irradiation). The floating photocatalyst retained consistent activity over five successive cycles. Moreover, the XRD patterns of the fresh and reused WS_2-TNT-1@PUF showed no changes (Figure 6.7(b)). This indicates that the floating photocatalyst maintained its structural stability during repeated BPA degradation cycles.

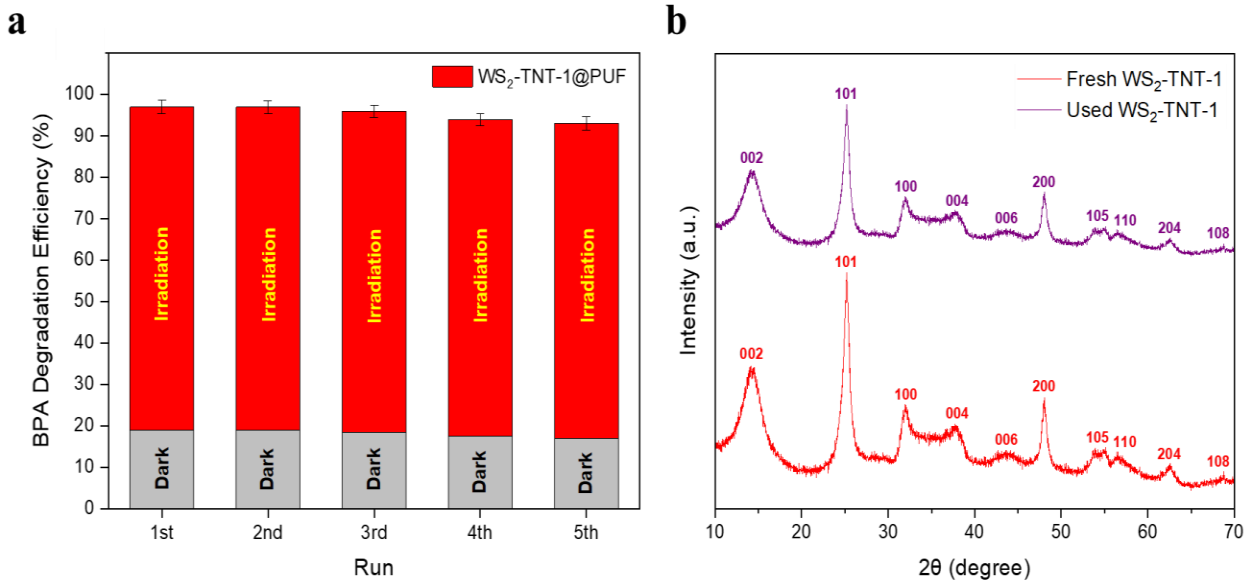

Figure 6.7 (a) Reusability of floating WS_2-TNT-1@PUF for BPA degradation under optimized conditions; (b) XRD patterns of fresh and reused floating WS_2-TNT-1@PUF after five cycles (Error bars correspond to the standard deviation derived from three replicates)

6.4.9 Possible mechanism of BPA degradation

Figure 6.8(a) shows that TNT has higher positive VB and CB energies than WS_2, according to the DRS results (Equations 6.3 and 6.4). With the conjunction of WS_2 in TNT, two structures of n-n heterojunctions can be formed based on the separation pathway of electron-hole pairs, as shown in Figures 6.8(b) and 6.8(c). In the first pathway, a typical type-II heterojunction (Figure 6.8(b)), e^- in the CB of WS_2 migrate to the CB of TNT, while h^+ in the VB of TNT move to the VB of WS_2. Therefore, TNT serves as an electron center in reduction reactions, while WS_2 acts as a hole center in oxidation reactions. In the second pathway, a Z-scheme structure (Figure 6.8(c)), e^- in the CB of TNT combines with h^+ in the VB of WS_2, forming an electron donor-acceptor center. Meanwhile,

the e^- in the CB of WS_2 participates in reductive reactions, while h^+ in the VB of TNT are involved in oxidative reactions. Notably, the more negative CB and more positive VB energies of the Z-scheme structure strengthen the redox potential of WS_2-TNT heterojunction compared to the type-II heterojunction.

The more negative potential of the CB of TNT (-0.29 eV vs. NHE) and WS_2 (-0.82 eV vs. NHE) than the $O_2/^{\bullet}O_2^-$ redox potential (-0.046 eV vs. NHE [135, 289, 290]) allows the formation of $^{\bullet}O_2^-$ in both heterojunction configurations (Figures 6.8(d) and 6.8(e)). However, the VB potential of WS_2 (+0.98 eV vs. NHE) is less positive than the $^{\bullet}OH/H_2O$ redox potential (+2.38 eV vs. NHE [257, 287, 288]), as shown in Figure 6.8(d). Thus, the h^+ in the CB of WS_2 cannot oxidize water into $^{\bullet}OH$. Conversely, the VB potential of TNT (+2.71 eV vs. NHE) is more positive than the $^{\bullet}OH/H_2O$ redox potential, indicating that $^{\bullet}OH$ formation is favorable in the Z-scheme structure (Figure 6.8(e)). Consequently, the electron migration pathway in floating WS_2-TNT-1@PUF follows the Z-scheme structure during BPA degradation.

Figure 6.8(f) shows that $^{\bullet}OH$ and $^{\bullet}O_2^-$ are generated during the degradation of BPA under optimized conditions, as evidenced by the detection of their respective signals [291, 292]. According to the EPR results, $^{\bullet}O_2^-$ and $^{\bullet}OH$ were two reactive species arising from the electron-hole pairs of floating WS_2-TNT-1@PUF.

To assess the contribution of e^-, h^+, $^{\bullet}OH$, and $^{\bullet}O_2^-$ in the degradation of BPA by Z-scheme heterojunction WS_2-TNT-1@PUF, scavenger experiments were performed under optimal treatment conditions (0.2 g WS_2-TNT-1@PUF, 10 mg/L BPA, pH 8, 60 min irradiation), as shown in Figure 6.8(g). The addition of BZQ to the floating system reduced BPA degradation to 35%. This indicates that $^{\bullet}O_2^-$ played a dominant role in BPA degradation, accounting for 41.2%. In the presence of $AgNO_3$, 50% of BPA was degraded, suggesting that e^- contributed 31.2% to BPA degradation. Upon adding AO to the BPA solution, degradation decreased to 60%. Regarding the direct and indirect contributions of h^+, using t-BuOH reduced BPA degradation to 80%. Therefore, h^+ accounted for 13.3% of the direct reactions, while $^{\bullet}OH$ contributed 11.3% to the indirect reactions.

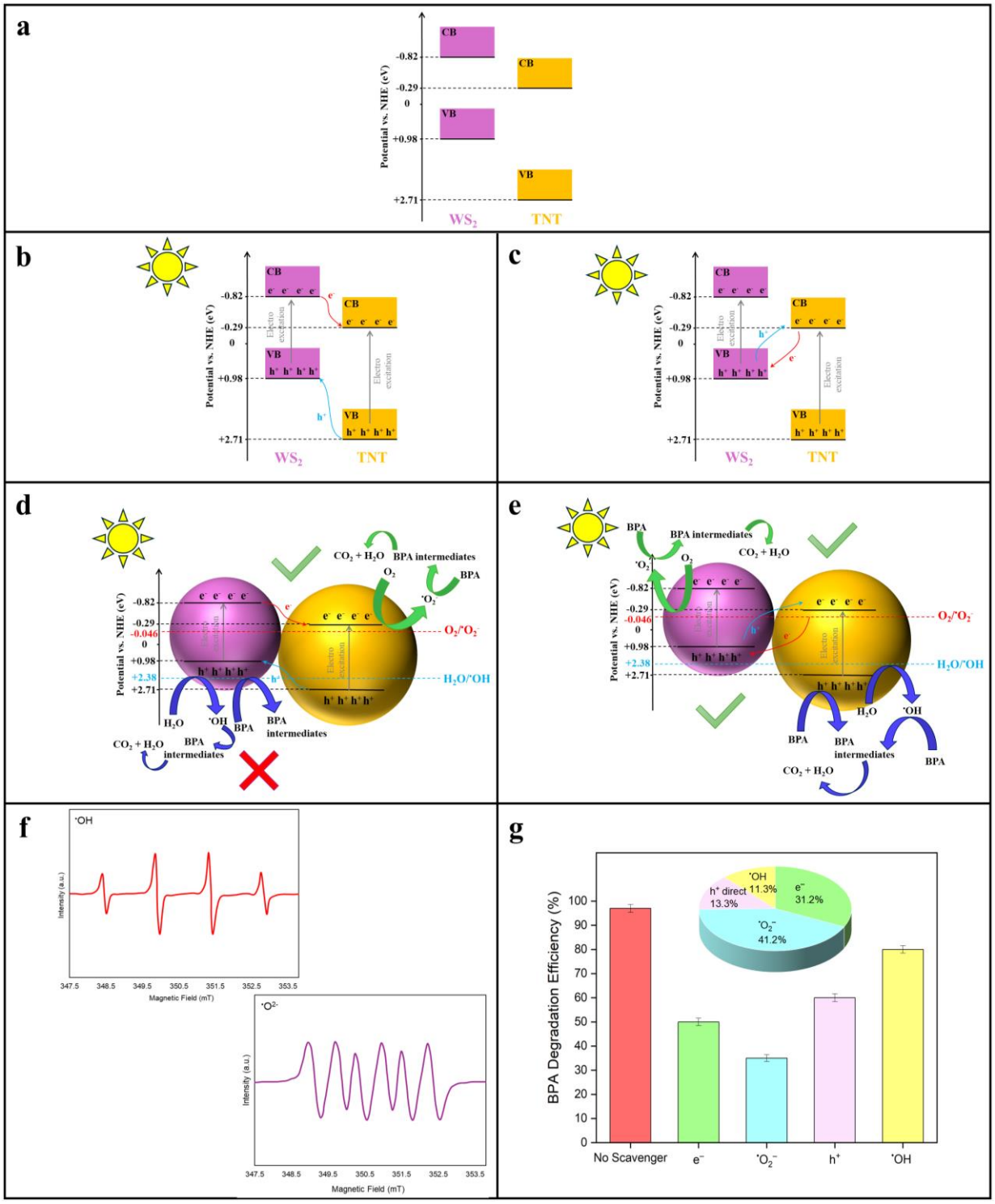

Figure 6.8 Schematic illustration of (a) TNT and WS_2 before contact, (b) type-II heterojunction structure after contact and illumination, (c) Z-scheme structure after contact and illumination; Photocatalytic degradation of BPA in (d) type-II heterojunction structure, (e) Z-scheme structure; (f) EPR spectra showing the generation of $^{\bullet}OH$ and $^{\bullet}O_2^-$ during BPA degradation and (g)

Scavenging reactive species tests for BPA degradation under optimal conditions (Insert: relative contributions of reactive species)

6.4.10 BPA degradation pathway

Figure 6.9(a) shows the LC-MS chromatograms for BPA degradation under optimized treatment conditions (0.2 g WS_2-TNT-1@PUF, 10 mg/L BPA, pH 8, 60 min irradiation). Before starting the photocatalytic degradation, a strong peak was detected at *m/z* = 227.1043 ($[M-H]^-$), which corresponds to BPA. After 20 min and 40 min of degradation, the BPA peak gradually reduced. In contrast, several new peaks were observed, indicating the formation of the BPA degradation products. The BPA intermediates identified by LC-MS included $C_9H_{10}O$ (*m/z* = 135.0790, $[M+H]^+$), $C_8H_8O_2$ (*m/z* = 135.0432, $[M-H]^-$), $C_9H_{10}O_2$ (*m/z* = 149.0608, $[M-H]^-$), and $C_6H_6O_2$ (*m/z* = 111.0441, $[M+H]^+$). Finally, all peaks disappeared after 60 min of BPA degradation (Figure 6.9(a)). The corresponding LC-MS chromatograms of the BPA intermediates are shown in Figures 6(16–19).

Figure 6.9(b) presents a possible degradation pathway for BPA under optimized treatment conditions (0.2 g WS_2-TNT-1@PUF, 10 mg/L BPA, pH 8, 60 min irradiation). Based on the LC-MS results, the BPA intermediates are generated as a result of the β-scission reaction of BPA. As the photocatalytic degradation of BPA continues, these intermediates can be mineralized, ultimately leading to the production of CO_2 and H_2O [181, 328, 329].

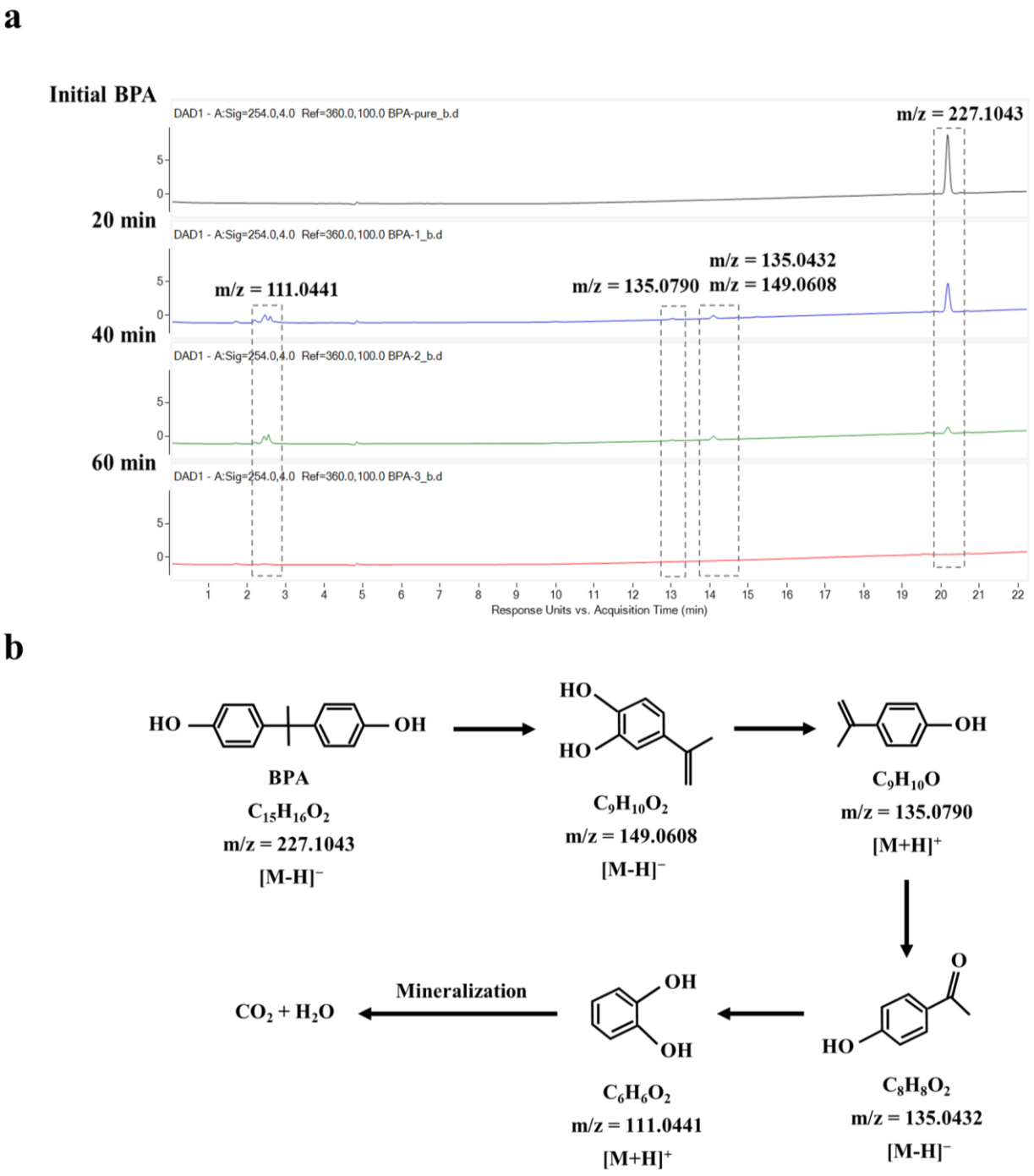

Figure 6.9 LC-MS chromatograms of BPA intermediates after 0 min, 20 min, 40 min, and 60 min of degradation under optimal treatment conditions; (b) Proposed degradation pathway of BPA under optimal treatment conditions (WS_2-TNT-1@PUF: 0.2 g, BPA: 10 mg/L, pH: 8, irradiation: 60 min)

6.4.11 Electron storage capacity

Figure 6.10(a) shows the photocatalytic activity of floating WS_2-TNT-1@PUF under optimal treatment conditions. After 60 min of simulated sunlight, over 97% of BPA was degraded by WS_2-TNT-1@PUF. Under the same conditions, TNT@PUF and WS_2@PUF degraded 60% and 45% of BPA, respectively.

We also evaluated the continuous photocatalytic activity of WS_2-TNT-1@PUF in the cyclic on-off illumination, as depicted in Figure 6.10(b). In this case, the photocatalytic degradation was initiated by 15 min of simulated sunlight, followed by a period in the absence of light. Based on the results, floating WS_2-TNT-1@PUF degraded 89% of BPA in a round-the-clock system, in which 62% of the degradation occurred under light irradiation, and the rest (27%) was achieved when the light was off. This indicates that the floating WS_2-TNT-1@PUF possesses an electron storage capacity and retains its photocatalytic activity even in the absence of light. As shown in Figure 6.10(b), BPA was not degraded by floating TNT@PUF when the light was off. This is because the photocatalyst lacks the capacity to store electrons and continue photocatalytic degradation without light irradiation. Conversely, floating WS_2@PUF degraded about 8% of BPA in the absence of light, suggesting its capacity to store electrons.

Figure 6.10(c) presents the quantity of stored electrons in floating TNT@PUF, WS_2@PUF, WS_2-TNT-1@PUF, as measured by MB titration. The total amount of MB consumed by floating WS_2-TNT-1@PUF was 500 μL. According to Reactions 6.1 and 6.2, the number of stored electrons in WS_2-TNT-1@PUF was calculated to be 1 μmol/h. In addition, WS_2@PUF stored 1.8 μmol/h electrons, while TNT@PUF did not store any electrons.

Figure 6.10(d) presents the reductive mechanism of electron storage in WS_2-TNT-1@PUF under light and dark conditions. Upon light irradiation, charge carriers are generated in TNT (Reaction 6.3). The photogenerated electrons are then transferred to the conduction band of WS_2, where they are stored during illumination (Reaction 6.4). Meanwhile, photogenerated holes oxidize water, producing H^+ (Reaction 6.5). Some photogenerated electrons in the conduction band of WS_2 are captured by H^+ and stored as H_xWS_2 (Reaction 6.6, charging). When the light is turned off, the stored electrons are released from H_xWS_2 (Reaction 6.7, discharging). These long-lived electrons subsequently react with oxygen to drive ongoing reduction reactions in the absence of light

(Reaction 6.8). Similar electron storage mechanisms in tungsten compounds have been previously reported [330, 331].

$$TNT + h\vartheta \rightarrow TNT^*(e^-) + TNT^*(h^+) \quad \text{(Reaction 6.3)}$$

$$TNT^*(e^-) \rightarrow WS_2(e^-) \quad \text{(Reaction 6.4)}$$

$$h^+ + H_2O \rightarrow \bullet OH + H^+ \quad \text{(Reaction 6.5)}$$

$$WS_2 + xe^- + xH^+ \rightarrow H_xWS_2 \text{ (charging)} \quad \text{(Reaction 6.6)}$$

$$H_xWS_2 \rightarrow WS_2 + xe^- + xH^+ \text{ (discharging)} \quad \text{(Reaction 6.7)}$$

$$e^- + O_2 \rightarrow \bullet O_2^- \quad \text{(Reaction 6.8)}$$

Figure 6.10(e) shows the EPR spectrum corresponding to the formation of $^{\bullet}O_2^-$ during BPA degradation under optimal treatment conditions when the light source was turned off. Under 15 min of simulated sunlight, the characteristic peaks of $^{\bullet}O_2^-$ were observed. These signals remained detectable after switching off the light for 15 min, indicating that $^{\bullet}O_2^-$ was still produced by WS_2-TNT-1@PUF during the dark discharge process. Therefore, in the absence of light, the photocatalytic degradation of BPA was still ongoing through driving reduction reactions, which is due to the electron storage capacity of WS_2 in floating WS_2-TNT-1@PUF.

As shown in Figure 6.10(f), WS_2-TNT-1 had a photocurrent density of approximately 0.8 mA/cm^2, which is four and five times higher than those of TNT (0.2 mA/cm^2) and WS_2 (0.16 mA/cm^2), respectively. A higher current density indicates improved light absorption and stronger photoinduced charge carrier generation and separation. This is aligned with the results of DRS and BPA degradation discussed in Figures 6.5(b) and 6.6(a). In the dark, the current density of TNT was nearly zero, whereas WS_2 and WS_2-TNT-1 had current densities of 0.05 mA/cm^2 and 0.23 mA/cm^2, respectively. Upon re-illumination, all photocatalysts exhibited an increase in photocurrent density, indicating effective charge transfer and participation of photogenerated carriers in the photocatalytic reactions.

Regarding the transient photocurrent responses (TPR) shown in Figure 6.10(g), when the light was turned off, the photocurrent of TNT quickly returned to zero, while WS_2 and WS_2-TNT-1 maintained their electron density for specific lifetimes (t_1 and t_2) before gradually returning to their initial levels. The findings indicate that WS_2 and WS_2-TNT-1 have an electron storage capacity and can sustain photocatalytic reactions even in the dark. Compared to WS_2, WS_2-TNT-1 exhibited

longer lifetimes and higher current densities, likely due to a Z-scheme heterojunction formed between TNT and WS_2, which improves photocatalytic activity.

Figure 6.10(h) shows the EIS plots of TNT, WS_2, and WS_2-TNT-1. In the Nyquist plots, a smaller semicircle radius corresponds to lower charge transfer resistance, indicating more efficient separation of photogenerated charge carriers and faster charge transfer at the electrode/electrolyte interface. WS_2-TNT-1 had a smaller arc radius than TNT and WS_2, likely due to the presence of a Z-scheme heterojunction in WS_2-TNT-1. This structure promotes charge carrier mobility, lowers electron transfer resistance, and consequently enhances photocatalytic activity.

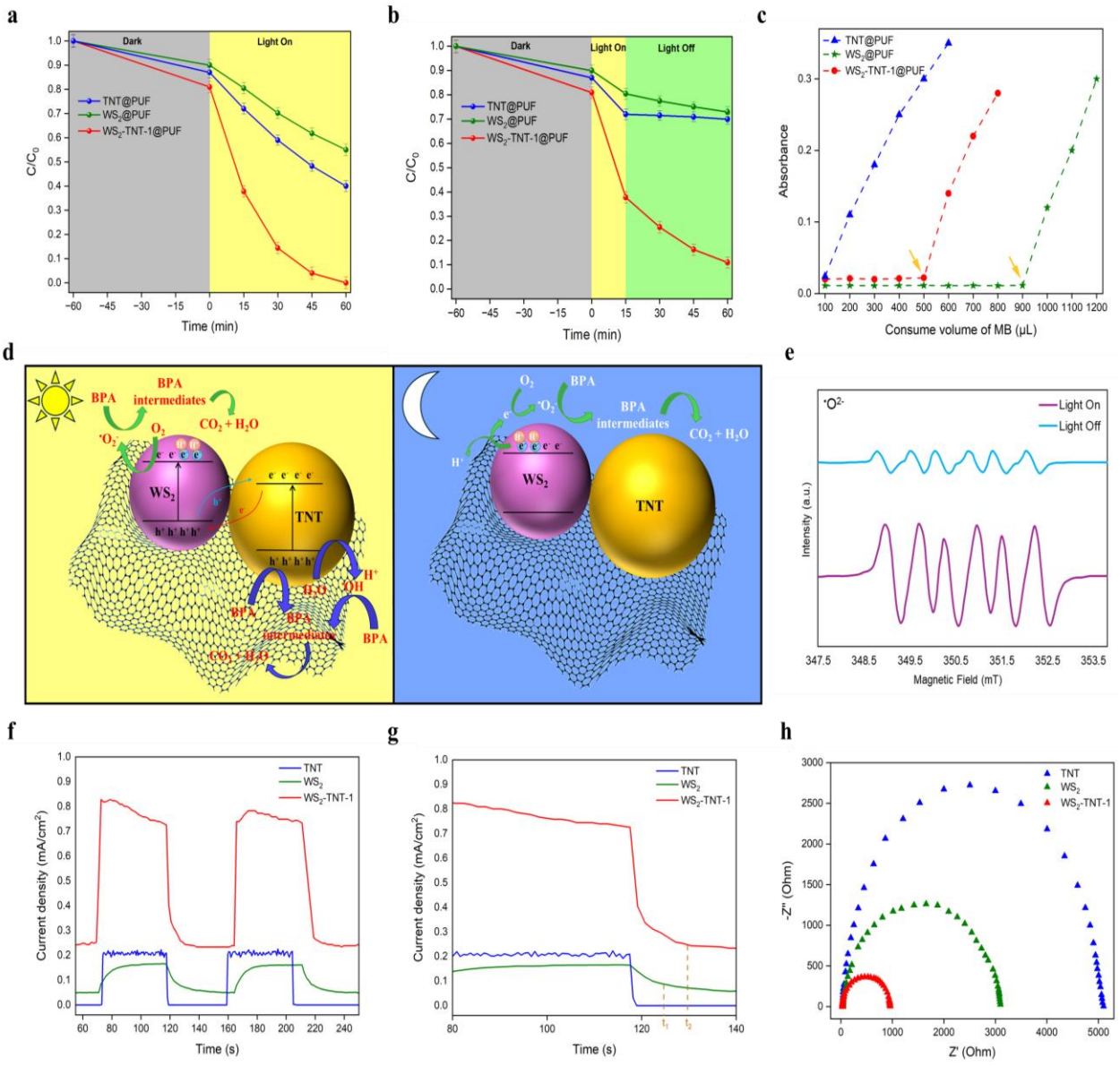

Figure 6.10 BPA degradation (a) under simulated sunlight and (b) in the absence of simulated sunlight after pre-irradiation using floating TNT@PUF, WS_2@PUF, WS_2-TNT-1@PUF under optimal treatment conditions; (c) Stored electrons of floating TNT@PUF, WS_2@PUF, WS_2-TNT-1@PUF measured by MB titration; (d) Reductive energy storage mechanism in WS_2-TNT-1@PUF; (e) EPR spectrum of generated $^{\bullet}O_2^-$ during BPA degradation under optimal treatment conditions in the absence of light; (f) Chronoamperometry plots of TNT, WS_2, WS_2-TNT-1; (g) TPR plots of TNT, WS_2, WS_2-TNT-1; (h) EIS plots of TNT, WS_2, WS_2-TNT-1

6.4.12 Comparison of floating WS_2-TNT-1@PUF for BPA degradation with previous research

Figure 6.11 compares BPA degradation using TiO_2- and WS_2-based photocatalysts reported in recent studies, with the corresponding photocatalytic conditions detailed in Table 6.3. To date, no research has reported the degradation of BPA employing a floating photocatalyst reactor under simulated sunlight. Our results indicate that floating WS_2-TNT-1@PUF achieved more than 97% BPA degradation within 60 min of irradiation. Notably, due to the electron storage capacity of WS_2-TNT-1@PUF, this floating heterojunction photocatalyst exhibited round-the-clock activity for BPA degradation, achieving 85% degradation in the absence of light.

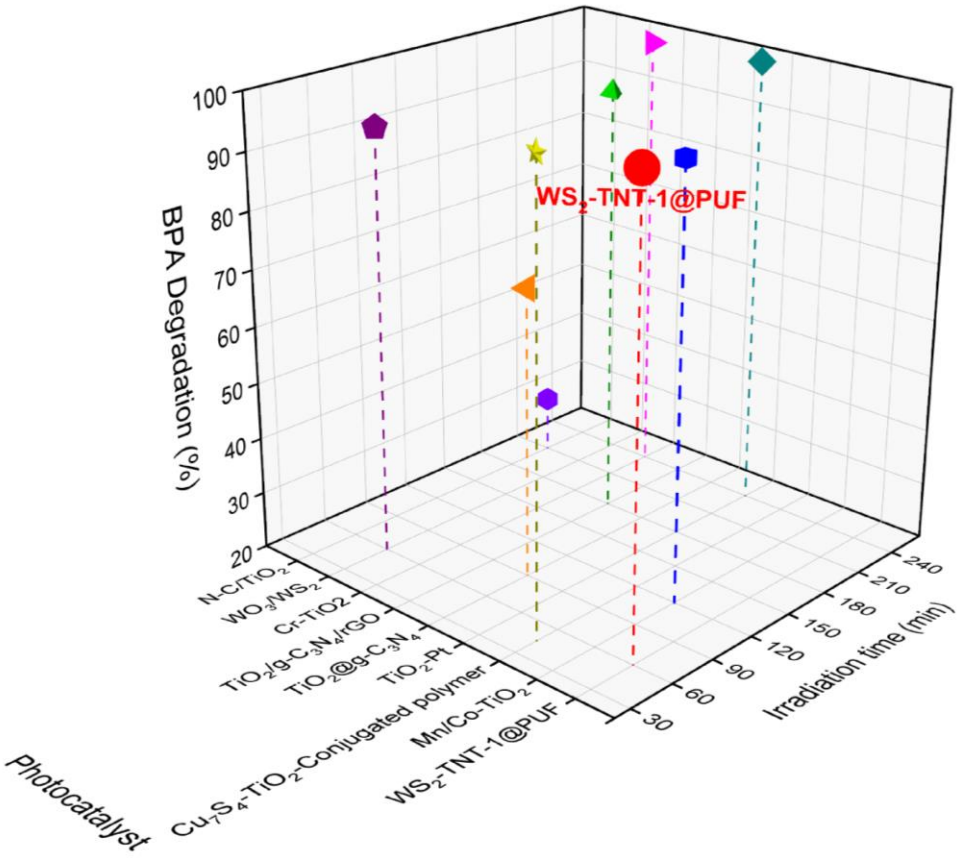

Figure 6.11 Recent studies on TiO_2-based and WS_2-based photocatalysts for BPA degradation

6.5 Conclusion

This study introduced a novel floating photocatalytic system consisting of WS_2-TNT@PUF Z-scheme heterostructures for round-the-clock BPA degradation under simulated sunlight. The successful formation of a heterojunction between TNT and WS_2 not only enhanced the photocatalytic activity of WS_2-TNT@PUF but also provided the floating photocatalyst with electron storage capacity, offering a key advantage over conventional photocatalysts that are limited to operating under illumination. Among all the floating photocatalysts fabricated, WS_2-TNT-1@PUF showed the highest efficiency in degrading BPA, resulting in >97% BPA degradation under optimized treatment conditions: 0.2 g photocatalyst, 10 mg/L BPA, pH 8, and 60 min irradiation (commercial solar lamp, 300 W, 35 W/m^2). Notably, WS_2-TNT-1@PUF exhibited an electron storage capacity of 1 μmol/h, as determined by the MB titration method, which degraded 89% of BPA in round-the-clock floating photocatalysis. In addition, floating WS_2-TNT-1@PUF exhibited stable photocatalytic activity for BPA degradation after five consecutive reuse cycles under optimal conditions. Our findings suggest that floating WS_2-TNT-1@PUF presents a promising approach for round-the-clock photocatalytic wastewater treatment, highlighting its potential for real-world applications.

6.6 Acknowledgments

The authors gratefully acknowledge financial support from the Velux Stiftung Foundation through Project 1381, “SUNFLOAT - Water decontamination by sunlight-driven floating photocatalytic systems,” and from the Natural Sciences and Engineering Research Council of Canada (NSERC). Additional support from the Bourse d'excellence Neil R. Mitchell et Danièle Dumais at Polytechnique Montréal is also gratefully acknowledged.

6.7 Supplementary Material

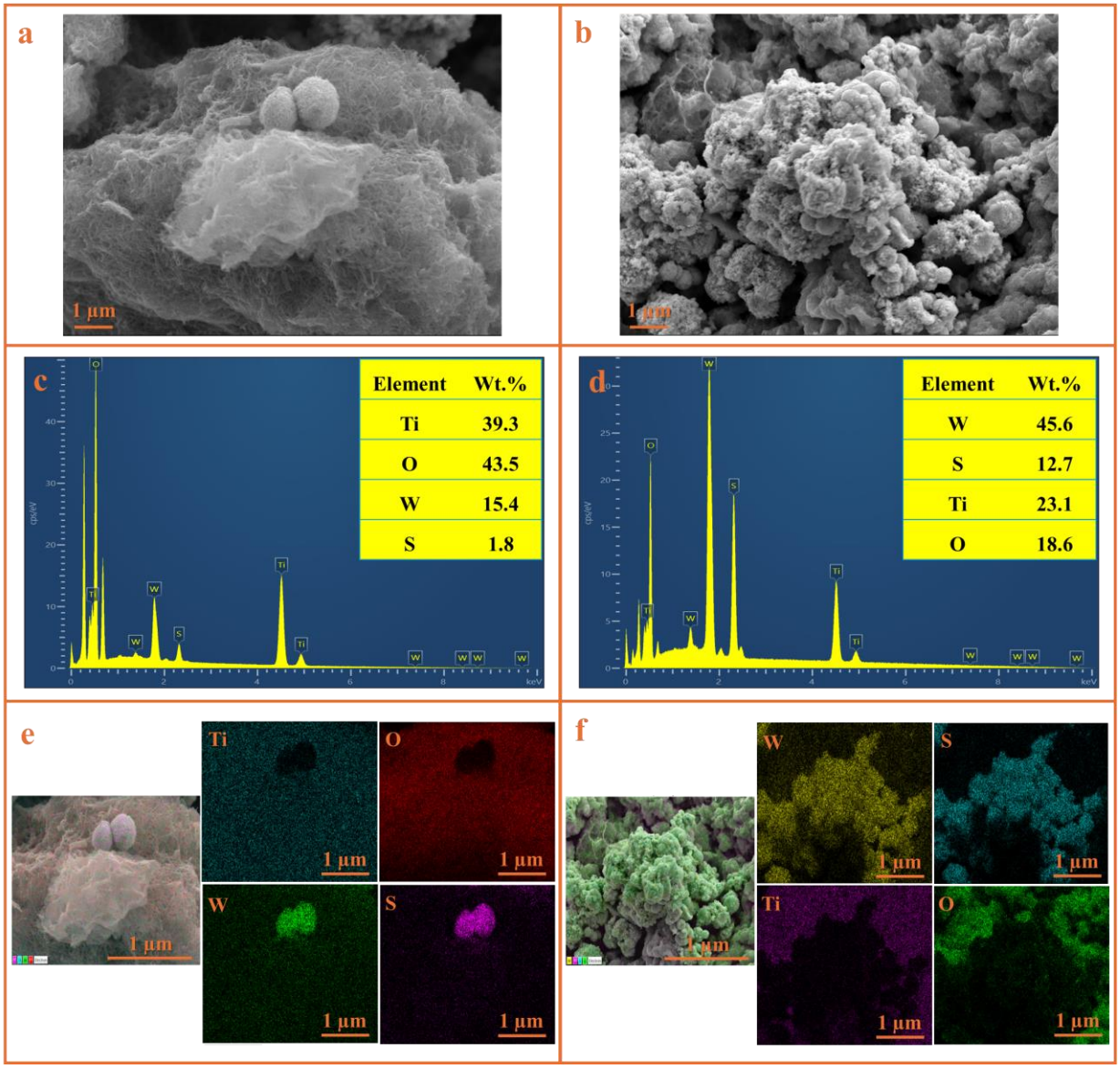

Figure 6.12 SEM images of (a) WS_2-TNT-2 and (b) WS_2-TNT-3; EDS spectra of (c) WS_2-TNT-2 and (d) WS_2-TNT-3; EDS mappings of (e) WS_2-TNT-2 and (f) WS_2-TNT-3

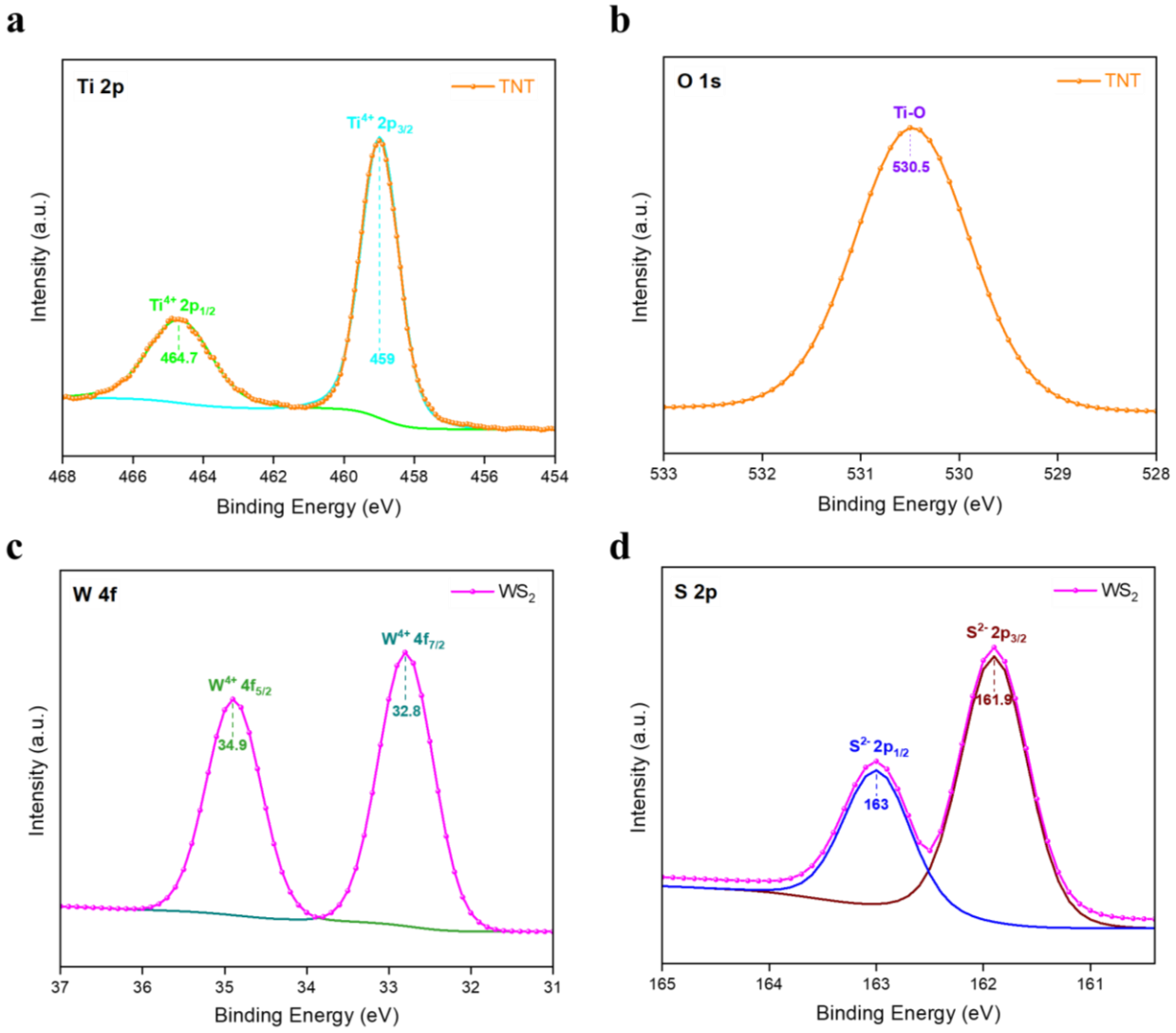

Figure 6.13 XPS spectra of TNT and WS_2 (a, b) High-resolution spectra of Ti 2p and O 1s, (c, d) High-resolution spectra of W 4f and S 2p

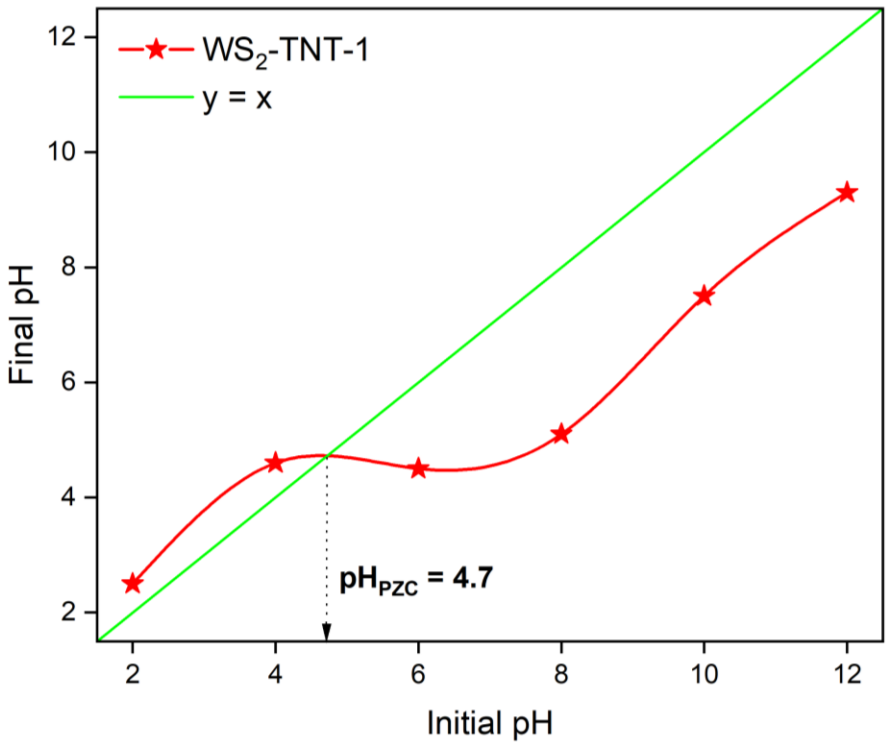

Figure 6.14 Determination of pH_{pzc} for WS_2-TNT-1 via pH drift method

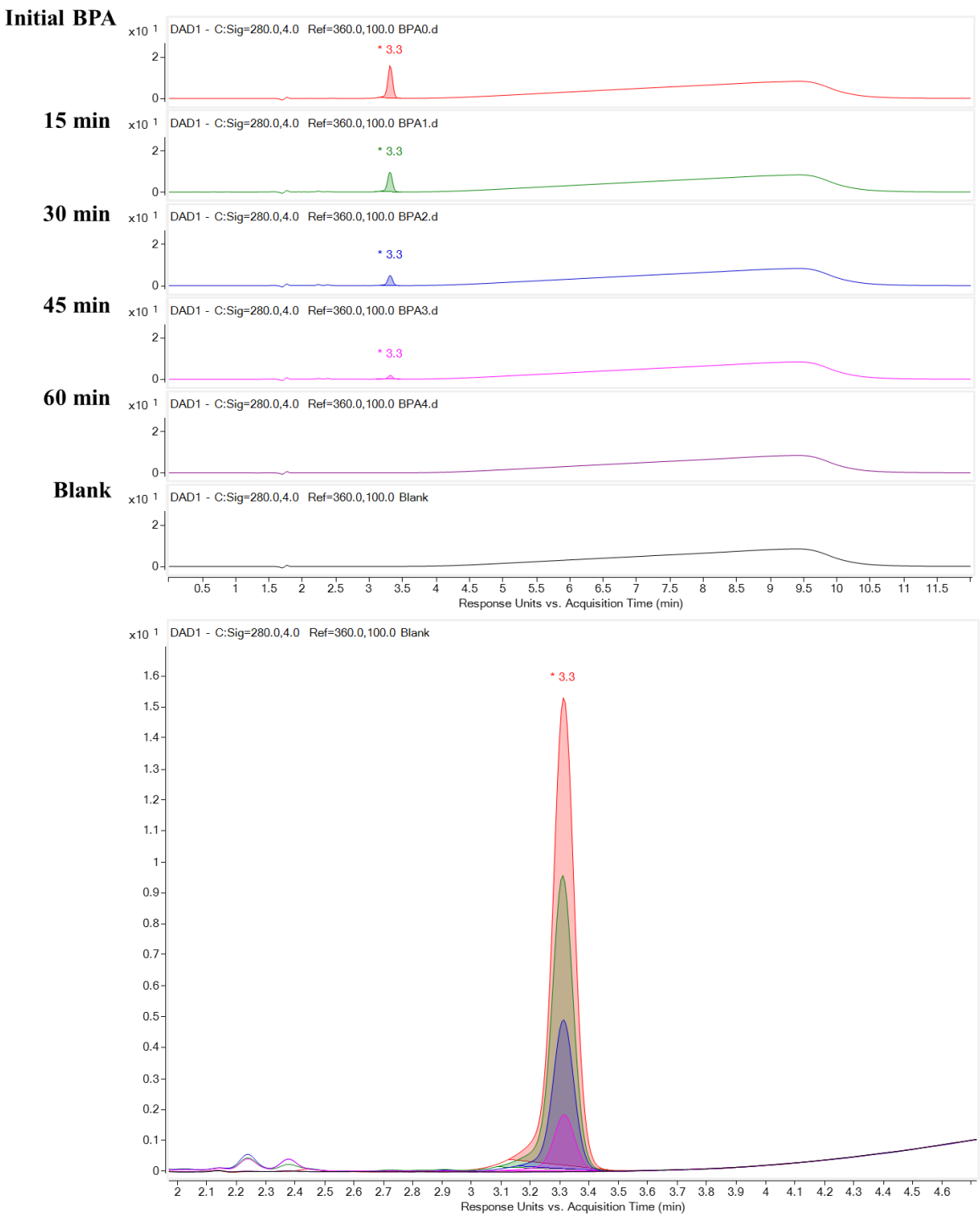

Figure 6.15 LC-MS chromatograms of BPA ($C_{15}H_{16}O_2$) after 0 min, 15 min, 30 min, 45 min, and 60 min of degradation under optimal treatment conditions (WS_2-TNT-1@PUF loading = 0.2 g, BPA concentration = 10 mg/L, pH = 8, and irradiation time = 60 min)

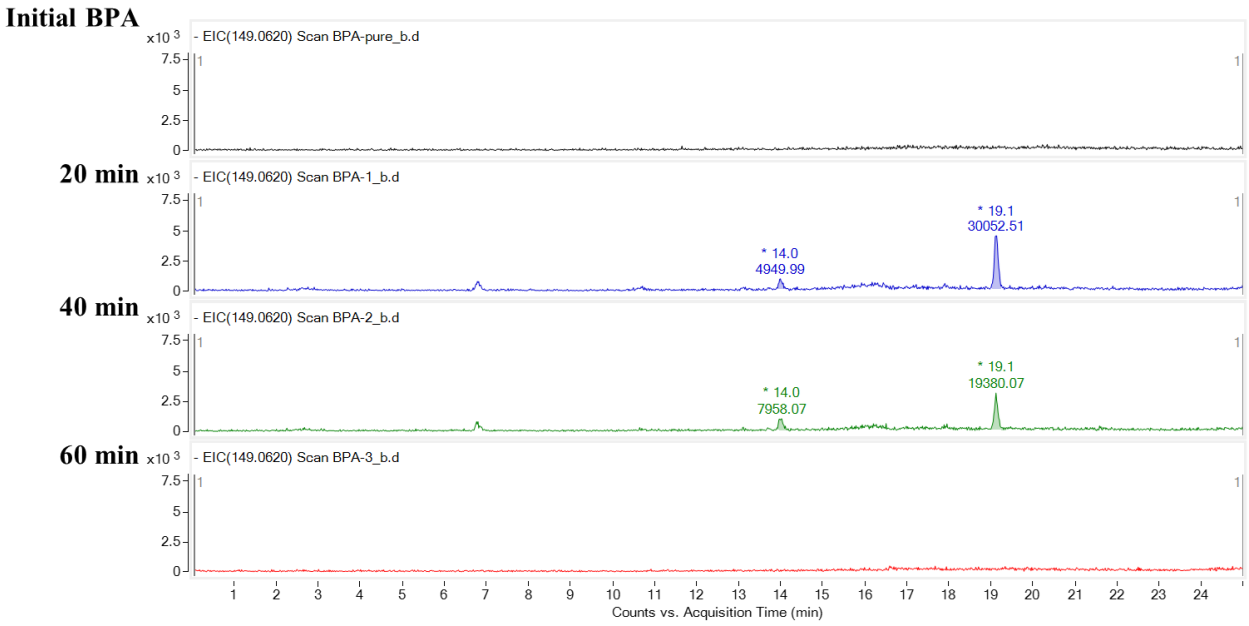

Figure 6.16 LC-MS chromatograms of BPA intermediates ($C_9H_{10}O_2$) after 0 min, 20 min, 40 min, and 60 min of degradation under optimal treatment conditions (WS_2-TNT-1@PUF loading = 0.2 g, BPA concentration = 10 mg/L, pH = 8, and irradiation time = 60 min)

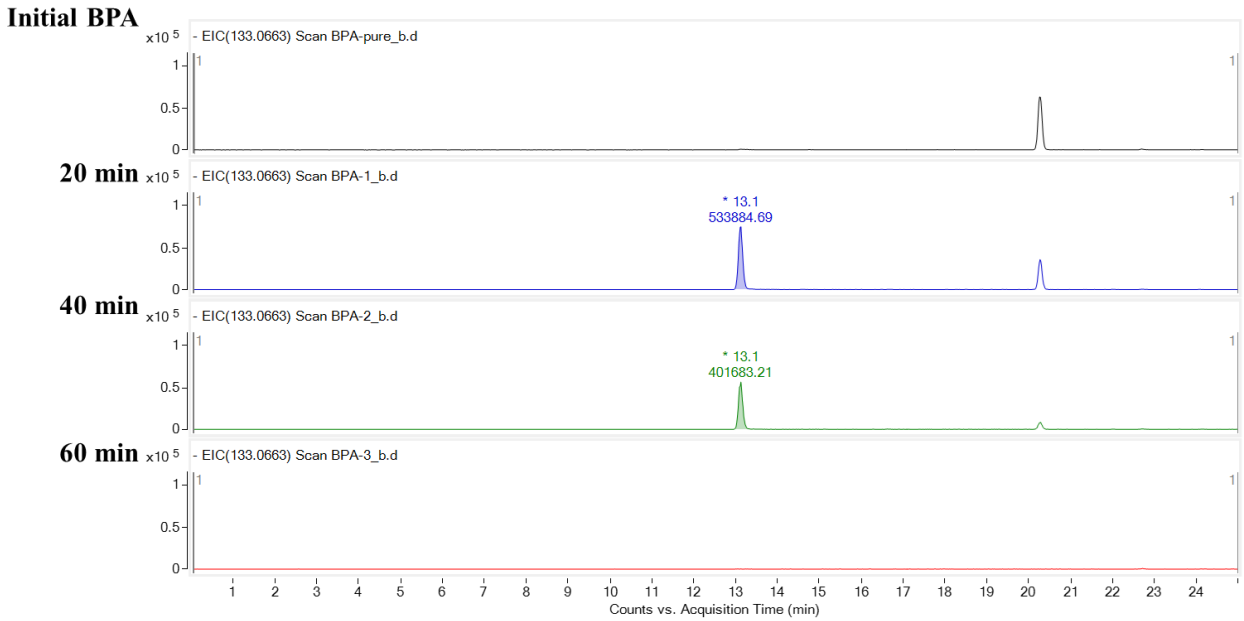

Figure 6.17 LC-MS chromatograms of BPA intermediates ($C_9H_{10}O$) after 0 min, 20 min, 40 min, and 60 min of degradation under optimal treatment conditions (WS_2-TNT-1@PUF loading = 0.2 g, BPA concentration = 10 mg/L, pH = 8, and irradiation time = 60 min)

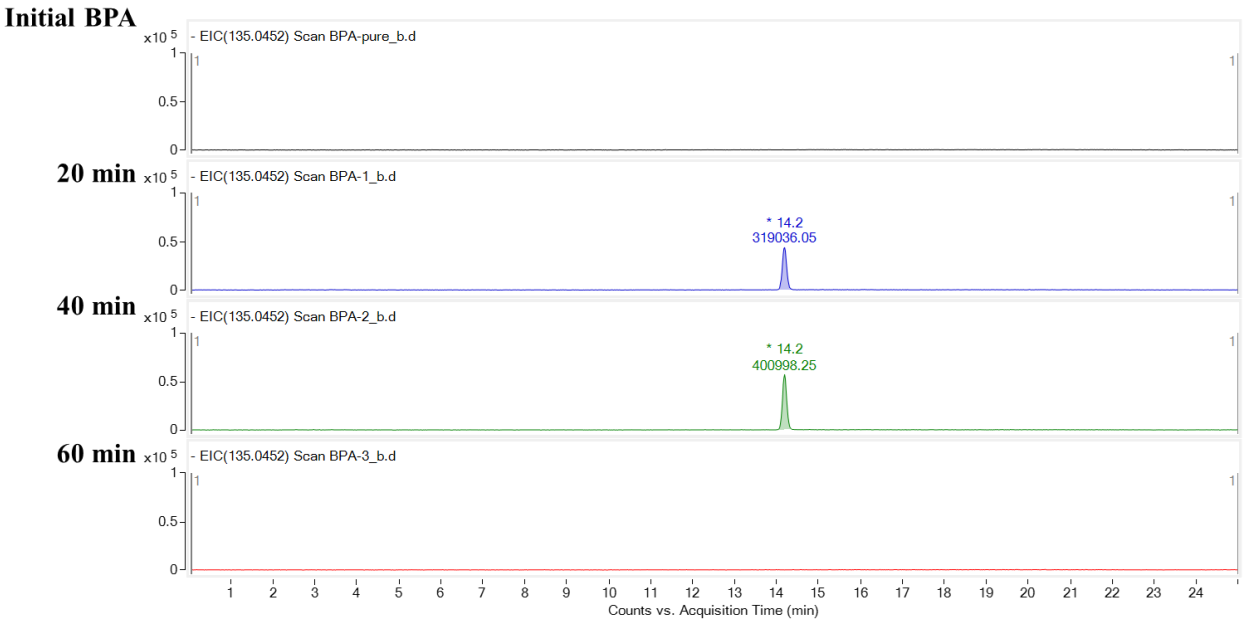

Figure 6.18 LC-MS chromatograms of BPA intermediates ($C_8H_8O_2$) after 0 min, 20 min, 40 min, and 60 min of degradation under optimal treatment conditions (WS_2-TNT-1@PUF loading = 0.2 g, BPA concentration = 10 mg/L, pH = 8, and irradiation time = 60 min

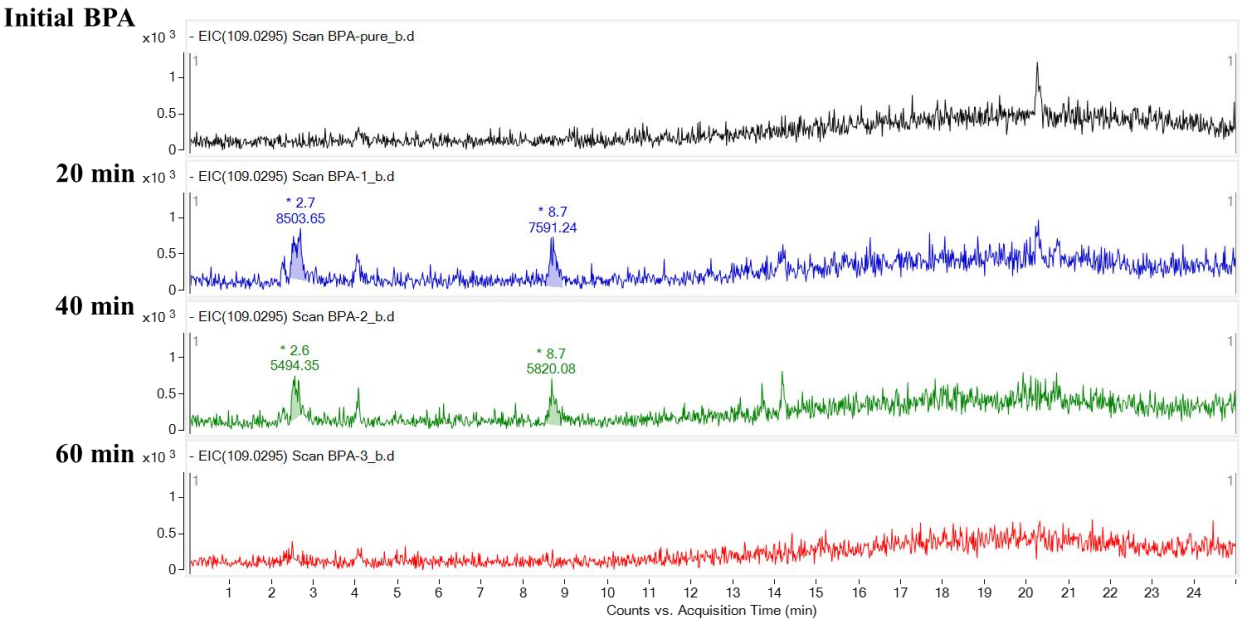

Figure 6.19 LC-MS chromatograms of BPA intermediates ($C_6H_6O_2$) after 0 min, 20 min, 40 min, and 60 min of degradation under optimal treatment conditions (WS_2-TNT-1@PUF loading = 0.2 g, BPA concentration = 10 mg/L, pH = 8, and irradiation time = 60 min)

Table 6.3 Recent studies on TiO_2-based and WS_2-based photocatalysts for BPA degradation

Photocatalyst (Amount)	Morphology (Structure)	BPA concentration (Photocatalytic system)	Light source (Irradiation time)	Degradation efficiency	Ref.
N-C/TiO_2 (50 mg)	TiO_2 microsphere with NC nanoparticles (Non-metals doping)	20 mg/L (50 mL, Suspension)	Ultraviolet (210 min)	30%	[107]
WO_3/WS_2 (150 mg)	Nanorods (Z-scheme heterojunction)	20 mg/L (100 mL, Suspension)	Visible (60 min)	94.5%	[332]
Cr-TiO_2 (100 mg)	Nanoparticles (Metal doping)	10 mg/L (200 mL, Suspension)	Visible (240 min)	99%	[113]
TiO_2/g-C_3N_4/rGO (100 mg)	TiO_2 nanoparticles with g-C_3N_4 and rGO layers (Ternary composite)	10 mg/L (100 mL, Suspension)	Visible (180 min)	95.6%	[120]
TiO_2@g-C_3N_4 (100 mg)	Spherical TiO_2 with g-C_3N_4 layers (Z-scheme heterostructure)	20 mg/L (250 mL, Suspension)	Ultraviolet (90 min)	71%	[118]
TiO_2-Pt (31.25 mg)	TiO_2 nanorods with spherical metals (Plasmonic metals)	10 mg/L (250 mL, Suspension)	Visible (240 min)	100%	[32]
Cu_7S_4-TiO_2-Conjugated polymer (20 mg)	Cu_7S_4 nanosheets with TiO_2 nanosheets (S-scheme heterojunction)	20 mg/L (50 mL, Suspension)	Visible (45 min)	100%	[119]
Mn/Co-TiO_2 (300 mg)	Nanoparticles (Co-doped metal doping)	10 mg/L (100 mL, Suspension)	Simulated sunlight (120 min)	95.4%	[116]
WS_2-TNT-1@PUF (0.2 g)	Nanotubular TiO_2 with spherical WS_2 (Z-scheme heterojunction)	10 mg/L (200 mL, Floating)	Simulated sunlight (60 min)	>97%	Present work

CHAPTER 7 GENERAL DISCUSSION

This dissertation investigated the development of floating photocatalytic systems for the removal of contaminants of emerging concern (CECs) from water under simulated sunlight irradiation. We focused on designing nanostructured TiO_2-based photocatalysts immobilized on floating supports, improving photocatalytic efficiency through structural engineering and chemical modification, and introducing energy storage capacity to enable round-the-clock pollutant degradation. The findings address key limitations of conventional photocatalytic wastewater treatment and provide insights into the design of scalable photocatalytic systems for water remediation.

A key focus of this dissertation is the development of floating photocatalysts immobilized on polyurethane foam via a wet chemical deposition method. As a three-dimensional macroporous polymer, polyurethane foam provides advantages for photocatalyst immobilization, including low density, an open-cell structure, high porosity, and a large surface-to-volume ratio. Conventional photocatalytic systems using suspended photocatalysts face challenges, including the need for vigorous stirring to prevent particle agglomeration, difficulties with photocatalyst recovery and reuse, and the potential release of nanoparticles into treated water. The immobilization approach implemented in this work addresses these challenges by depositing photocatalysts onto a floating substrate positioned at the air-water interface. This configuration creates an air-solid-water triphase interface, improving oxygen transfer from the air and ensuring direct exposure of the photocatalyst to light. This approach addresses both operational and environmental concerns while maintaining high photocatalytic efficiency. Although previous studies have reported that immobilized systems often exhibit reduced photocatalytic activity due to mass-transfer limitations or decreased exposed surface area, we demonstrate that an optimized structural design of the floating configuration can mitigate these limitations.

Another key aspect of this dissertation is the engineering of TiO_2 nanostructures as the primary photocatalyst for the degradation of bisphenol A (BPA) as CECs. TiO_2 is considered one of the most promising photocatalysts for wastewater treatment due to its chemical and thermal stability, optical properties, and strong oxidative potential. However, its wide bandgap energy and rapid electron-hole recombination limit its photocatalytic activity under solar irradiation. We addressed these limitations through nanostructure engineering, particularly by synthesizing one-dimensional

TiO_2 nanotubes using an ultrasound-assisted hydrothermal method. Compared with TiO_2 nanoparticles, nanotubular structures provide several advantages, including a higher specific surface area, greater charge mobility, and enhanced light absorption.

In addition to morphological engineering, we investigated modification methods to improve the photocatalytic activity of TiO_2 nanotubes for the degradation of BPA. Non-metal doping has been reported as an effective method to enhance visible-light absorption by introducing a new energy level within the bandgap energy of TiO_2 nanotubes. In this dissertation, sulfur doping was utilized via an ultrasound-assisted solvothermal method to modify TiO_2 nanotubes, resulting in enhanced light absorption, increased photo-induced charge generation, and more effective electron-hole pair separation. The improved photocatalytic activity observed in sulfur-doped TiO_2 nanotubes highlights the significance of combining morphological control with structural and electronic modifications to optimize floating photocatalytic efficiency under solar irradiation.

Another innovation presented in this dissertation is the integration of energy storage into the floating photocatalytic system by constructing a WS_2-TiO_2 nanotube heterojunction for round-the-clock degradation of BPA. Conventional photocatalytic processes depend on continuous light irradiation, which limits their efficiency under real environmental conditions when solar radiation is absent. To address this limitation, we developed a smart Z-scheme heterojunction by enabling efficient charge separation between two semiconductors with complementary electronic structures. The incorporation of WS_2 into TiO_2 nanotubes not only improves photocatalytic activity but also provides storage for photogenerated electrons. These stored electrons subsequently participate in reduction reactions, enabling ongoing photocatalytic activity in the dark. This approach represents an emerging strategy in photocatalysis that integrates energy storage with photocatalytic activity, enabling treatment to continue beyond the duration of light exposure.

Another important aspect of this work is the evaluation of photocatalytic efficiency under conditions closer to those in a real water environment. While many laboratory studies evaluate photocatalysts using a single contaminant in simplified matrices, natural waters and wastewater streams typically contain complex mixtures of organic compounds and dissolved ions. We investigated the effects of water matrix components, such as natural organic matter and inorganic anions, on photocatalytic activity for removing a wide range of pollutants, including endocrine-disrupting chemicals, dyes, pesticides, and pharmaceuticals. These species affect photocatalytic

activity by competing for reactive radicals or scavenging reactive oxygen species, thereby reducing photocatalytic efficiency. These experiments provide methodological insights into the efficiency of the floating photocatalytic system under more realistic environmental conditions.

The findings of this dissertation underscore the need to integrate materials engineering, photoreactor design, and environmental chemistry to develop effective photocatalytic systems for the removal of CECs. We developed a solar-driven floating photocatalytic system as a promising approach to address several limitations of conventional photocatalytic systems. Immobilizing photocatalysts on a buoyant carrier at the air-water interface enhances light exposure without water attenuation and facilitates oxygen transfer from the air. Moreover, the floating configuration reduces the need for post-treatment photocatalyst recovery and the risk of nanoparticle release into treated water. These advantages indicate that floating photocatalysts may offer a scalable solution for solar-driven wastewater treatment, particularly for large-scale systems operating under natural sunlight.

CHAPTER 8 CONCLUSION AND RECOMMENDATIONS

8.1 Summary of Works

This doctoral work demonstrated that integrating nanostructured TiO_2 photocatalysts with floating reactor configurations is a promising strategy for the solar-driven removal of contaminants of emerging concern (CECs) from water systems. Through systematic material design, photocatalyst modification, and methodological development, this dissertation advances current knowledge in several key areas: (i) the influence of photocatalyst morphology on floating photocatalytic efficiency, particularly using one-dimensional TiO_2 nanotube structures; (ii) the applicability of floating TiO_2 nanotube systems for the degradation of different CECs under complex water matrix conditions; (iii) the enhancement of floating photocatalytic efficiency through controlled non-metal doping; and (iv) the development of energy-storing heterojunction photocatalysts capable of enabling round-the-clock floating degradation of CECs. The findings were obtained under simulated sunlight irradiation using a 300 W commercial solar lamp with an intensity of 35 W/m^2.

In the first part of this work, we explored the effect of TiO_2 morphology on the degradation of bisphenol A (BPA) in floating photocatalytic systems. The results indicate that floating TiO_2 nanotube photocatalyst supported on polyurethane foam (TNTs@PUF) represents a promising approach to removing BPA from contaminated water. The main conclusions are as follows.

1) A floating TiO_2 photocatalyst with nanotubular morphology was successfully fabricated using an ultrasound-assisted hydrothermal synthesis method, followed by wet chemical deposition.

2) The nanotubular TiO_2 structure displayed a biphasic anatase/TiO_2(B) structure, a crystallite size of 26 nm, a bandgap energy of 3.0 eV, a specific surface area of 110 m^2/g, and a photocurrent density of 0.2 mA/cm^2.

3) Floating TNTs@PUF (0.1 g) achieved complete removal of BPA (10 mg/L) after 180 min, while floating TiO_2-NPs@PUF removed 45% under the same conditions.

4) BPA photocatalytic degradation using floating TNTs@PUF followed first-order kinetics, with an apparent rate constant (k_{app}) of 0.016 min^{-1}.

5) Floating TNTs@PUF remained stable after five consecutive photocatalytic cycles.

6) Photogenerated hole (h^+) was identified as the dominant free radical scavenger during BPA degradation with floating TNTs@PUF.

In the second part of this work, we evaluated the photocatalytic activity of floating TNTs@PUF for the removal of various organic contaminants. The findings demonstrate that floating TNTs@PUF photocatalyst is effective for removing a wide range of pollutants, including endocrine-disrupting chemicals (EDCs), dyes, pesticides, and pharmaceuticals. Furthermore, the developed floating photocatalyst showed the ability to remove BPA from different water matrices and a CECs mixture, highlighting its potential for real-world wastewater treatment. The main conclusions are summarized as follows.

1) After 4 h of irradiation, removal efficiencies achieved by floating TNTs@PUF were 98% for BPA, 98% for methyl orange (MO), 85% for methylene blue (MB), 98% for bentazon (BZ), 98% for isoproturon (IPU), 98% for sulfamethoxazole (SMZ), and 97% for carbamazepine (CBZ).

2) The photocatalytic removal of BPA, MO, MB, BZ, IPU, SMZ, and CBZ followed first-order kinetics, with a k_{app} of 0.0156 min^{-1}, 0.0149 min^{-1}, 0.0078 min^{-1}, 0.0162 min^{-1}, 0.0152 min^{-1}, 0.015 min^{-1}, and 0.0137 min^{-1}, respectively.

3) The presence of natural organic matter in the BPA solution reduced removal efficiencies to 80% with humic acid, 86% with citric acid, and 30% with oxalic acid.

4) The k_{app} of BPA decreased to 0.0065 min^{-1} in the presence of humic acid, 0.0078 min^{-1} with citric acid, and 0.0015 min^{-1} with oxalic acid.

5) Inorganic anions reduced BPA removal to 80% with bicarbonate (HCO_3^-), 86% with chloride (Cl^-), and 90% with sulfate (SO_4^{2-}).

6) The addition of HCO_3^-, Cl^-, and SO_4^{2-} to the BPA solution decreased the k_{app} of BPA from 0.0156 min^{-1} to 0.0063 min^{-1}, 0.0081 min^{-1}, and 0.0089 min^{-1}, respectively.

7) Floating TNTs@PUF removed 80% of BPA from a mixture of CECs, including SMZ, CBZ, fluconazole (FLZ), atrazine (ATZ), ibuprofen (IBP), and gemfibrozil (GFZ).

8) The k_{app} of BPA was 0.0062 min^{-1} in the CECs mixture, compared with 0.0156 min^{-1} when BPA was treated as a single pollutant.

In the third part of this work, we introduced a novel floating photocatalyst, sulfur-doped TiO_2 nanotubes supported on polyurethane foam (S-TNT@PUF), for the degradation of BPA. Incorporating sulfur into TiO_2 nanotubes enhanced photocatalytic activity by improving charge separation and visible-light absorption. The results highlight the potential of the optimized floating S-TNT-1@PUF photocatalyst as a promising and reusable system for wastewater treatment, addressing critical challenges in photocatalyst recovery. The key findings are summarized below.

1) The optimal floating S-TNT-1@PUF (1 wt.% sulfur dopant) exhibited a specific surface area of 267 m^2/g, a bandgap energy of 2.48 eV, and a photocurrent density of 0.6 mA/cm^2.

2) Among all synthesized photocatalysts, floating S-TNT-1@PUF was the most effective photocatalyst for BPA degradation.

3) Floating S-TNT-1@PUF degraded over 96% BPA under optimal treatment conditions.

4) Optimal treatment conditions were achieved by a photocatalyst loading of 0.2 g, an initial BPA concentration of 10 mg/L, pH 8, and an irradiation time of 75 min.

5) BPA degradation by floating S-TNT-1@PUF followed first-order kinetics, with a k_{app} of 0.05 min^{-1}.

6) Floating S-TNT-1@PUF exhibited excellent stability after five reuse cycles.

7) The main reactive species involved in BPA degradation was hydroxyl radicals ($^{\bullet}OH$) with a contribution of 31%.

In the fourth part of this work, we developed a novel floating photocatalytic system, WS_2-TiO_2 nanotube Z-scheme heterostructure supported on polyurethane foam (WS_2-TNT@PUF), for the round-the-clock degradation of BPA. The construction of a heterojunction between TiO_2 nanotubes and WS_2 chalcogenides not only enhanced photocatalytic activity but also enabled electron storage within the floating photocatalyst. The results indicate that the optimized floating WS_2-TNT-1@PUF offers a key advantage over conventional photocatalysts, which typically operate only under illumination. The findings underscore the strong potential of this floating photocatalytic system for real-world wastewater treatment applications. The key conclusions are listed below.

1) The optimized floating WS_2-TNT-1@PUF (1:1 WS_2-TNT weight ratio) exhibited a specific surface area of 192 m^2/g and a bandgap energy of 2.8 eV.

2) Floating WS_2-TNT-1@PUF demonstrated the highest efficiency in degrading BPA among all fabricated photocatalysts.

3) Floating WS_2-TNT-1@PUF degraded over 97% BPA under optimal treatment conditions.

4) Optimal treatment conditions were 0.2 g photocatalyst loading, 10 mg/L BPA concentration, pH 8, and 60 min irradiation time.

5) Photocatalytic degradation of BPA by floating WS_2-TNT-1@PUF followed first-order kinetics, with a k_{app} of 0.069 min^{-1}.

6) Floating WS_2-TNT-1@PUF maintained its photocatalytic activity after five reuse cycles.

7) Superoxide anion ($^{\bullet}O_2^-$) was the dominant reactive species, contributing 41.2% to BPA degradation.

8) Floating WS_2-TNT-1@PUF had an electron storage capacity of 1 μmol, determined using the MB titration method.

9) Floating WS_2-TNT-1@PUF photocatalyst achieved 89% degradation of BPA under round-the-clock photocatalytic operation.

8.2 Limitations and Future Research

Despite the promising efficiency of the proposed floating photocatalytic system for the degradation of CECs, several limitations remain that should be addressed in future research.

1) The present work was conducted at a laboratory scale using simulated sunlight irradiation in controlled conditions. Future work should investigate the efficiency of the floating photocatalytic system under real outdoor conditions, with natural sunlight irradiation.

2) Further research is required to address the scalability of the floating photocatalytic system and develop an optimized photoreactor configuration suitable for large-scale applications. This includes evaluating light penetration, photocatalyst distribution, and reactor geometry.

3) Future work should incorporate techno-economic analysis and life-cycle assessment of the floating photocatalytic system to support practical implementation. Assessing material costs, synthesis methods, and operational requirements will clarify the feasibility of large-scale application in wastewater treatment.

4) Although floating photocatalysts in this work demonstrated stability over multiple reuse cycles, the mechanical and chemical stability of the floating photocatalytic system under long-term operational conditions should be assessed for real-world applications.

5) The present work was performed in a batch floating catalyst photoreactor. However, real wastewater treatment systems usually operate under continuous flow conditions. Future research should focus on developing continuous photocatalytic reactors incorporating floating catalysts by redesigning the photoreactor and optimizing operating parameters.

6) The mineralization of pollutants during floating photocatalysis was not investigated in this work. Future research should apply total organic carbon (TOC) analysis to assess contaminant mineralization and verify complete conversion to CO_2 and H_2O.

7) Although transformation products formed during floating photocatalytic degradation were identified using HPLC-MS analysis, their potential toxicity was not examined. Future work should study toxicity assessments to evaluate the potential formation of toxic by-products during degradation.

8) All photocatalytic experiments in this work were conducted using model solutions containing individual pollutants or synthetic mixtures. Future research should investigate the efficiency of floating photocatalysts in real water matrices, including river and lake water and wastewater treatment plant effluents.

REFERENCES

[1] A. Das, M. K. Adak, N. Mahata, and B. Biswas, "Wastewater treatment with the advent of TiO2 endowed photocatalysts and their reaction kinetics with scavenger effect," *Journal of Molecular Liquids,* vol. 338, p. 116479, 2021/09/15/ 2021.

[2] W. Hayouni, S. Pistre, N. Chkir, and K. Zouari, "Contaminants of emerging concern (CECs) as indicators of pollution and hydrological processes in an anthropized mediterranean water basin: Case of the Kasserine Basin (Central Tunisia)," *Science of The Total Environment,* vol. 984, p. 179744, 2025/07/01/ 2025.

[3] W. Feng, Y. Deng, F. Yang, Q. Miao, and S. K. Ngien, "Systematic Review of Contaminants of Emerging Concern (CECs): Distribution, Risks, and Implications for Water Quality and Health," vol. 15, no. 22, p. 3922, 2023.

[4] A. Roy, N. Jk, G. Italiya, and S. Subramanian, "Emerging contaminants jeopardizing groundwater integrity: environmental implications," *Environmental Pollutants and Bioavailability,* vol. 37, no. 1, p. 2572634, 2025/12/31 2025.

[5] M. B. Ahmed, J. L. Zhou, H. H. Ngo, W. Guo, N. S. Thomaidis, and J. Xu, "Progress in the biological and chemical treatment technologies for emerging contaminant removal from wastewater: A critical review," *Journal of Hazardous Materials,* vol. 323, pp. 274-298, 2017/02/05/ 2017.

[6] S. Kato, Y. Sakai, G. Guan, and Y. Kansha, "Illumination conditions of photocatalyst-containing mist on the degradation of organic compounds," *Chemical Engineering and Processing - Process Intensification,* vol. 208, p. 110106, 2025/02/01/ 2025.

[7] T. M. Pham *et al.*, "Visible Light-Driven N–F-Codoped TiO2 for Photocatalysts as Potential Application to Wastewater Treatment," vol. 46, no. 5, pp. 865-872, 2023.

[8] R. Djellabi, X. Zhao, M. F. Ordonez, E. Falletta, and C. L. Bianchi, "Comparison of the photoactivity of several semiconductor oxides in floating aerogel and suspension systems towards the reduction of Cr(VI) under visible light," *Chemosphere,* vol. 281, p. 130839, 2021/10/01/ 2021.

[9] Z. Xing *et al.*, "Recent advances in floating TiO2-based photocatalysts for environmental application," *Applied Catalysis B: Environmental,* vol. 225, pp. 452-467, 2018/06/05/ 2018.

[10] J. Sun *et al.*, "Floating BiOBr/Ti3C2 aerogel spheres for efficient degradation of quinolone antibiotics: Rapid oxygen transfer via triphase interface and effective charges separation by internal electric field," *Journal of Colloid and Interface Science,* 2025/01/23/ 2025.

[11] X. Liu *et al.*, "The advanced development of floatable photocatalysts: Preparation, advantages, and application," *Chemical Engineering Journal,* vol. 476, p. 146868, 2023/11/15/ 2023.

[12] R. Djellabi, L. Zhang, B. Yang, M. R. Haider, and X. Zhao, "Sustainable self-floating lignocellulosic biomass-TiO2@Aerogel for outdoor solar photocatalytic Cr(VI) reduction," *Separation and Purification Technology,* vol. 229, p. 115830, 2019/12/15/ 2019.

[13] M. A. Suara, S. O. Ganiyu, and M. Gamal El-Din, "Harnessing sunlight for effective passive photocatalytic treatment of oil sands process water using a sustainable floating

composite catalyst," *Journal of Environmental Chemical Engineering,* vol. 13, no. 6, p. 120097, 2025/12/01/ 2025.

[14] P. S. Nishmitha, K. A. Akhilghosh, V. P. Aiswriya, A. Ramesh, M. Muthuchamy, and A. Muthukumar, "Understanding emerging contaminants in water and wastewater: A comprehensive review on detection, impacts, and solutions," *Journal of Hazardous Materials Advances,* vol. 18, p. 100755, 2025/05/01/ 2025.

[15] S. Das, V. K. Parida, C. S. Tiwary, A. K. Gupta, and S. Chowdhury, "Emerging Contaminants in the Aquatic Environment: Fate, Occurrence, Impacts, and Toxicity," in *Bioremediation of Emerging Contaminants in Water. Volume 1*, vol. 1475(ACS Symposium Series, no. 1475): American Chemical Society, 2024, pp. 1-32.

[16] R. Kumar *et al.*, "A review on emerging water contaminants and the application of sustainable removal technologies," *Case Studies in Chemical and Environmental Engineering,* vol. 6, p. 100219, 2022/12/01/ 2022.

[17] A. Biswas *et al.*, "Water scarcity: A global hindrance to sustainable development and agricultural production – A critical review of the impacts and adaptation strategies," *Cambridge Prisms: Water,* vol. 3, p. e4, 2025, Art. no. e4.

[18] D. Aversa, N. Adamashvili, M. Fiore, and A. Spada, "Scoping Review (SR) via Text Data Mining on Water Scarcity and Climate Change," vol. 15, no. 1, p. 70, 2023.

[19] N. R. Maddela, B. Ramakrishnan, D. Kakarla, K. Venkateswarlu, and M. Megharaj, "Major contaminants of emerging concern in soils: a perspective on potential health risks," *RSC Advances,* 10.1039/D1RA09072K vol. 12, no. 20, pp. 12396-12415, 2022.

[20] C. B. Anucha, I. Altin, E. Bacaksiz, and V. N. Stathopoulos, "Titanium dioxide (TiO_2)-based photocatalyst materials activity enhancement for contaminants of emerging concern (CECs) degradation: In the light of modification strategies," *Chemical Engineering Journal Advances,* vol. 10, p. 100262, 2022/05/15/ 2022.

[21] X. Li, X. Shen, W. Jiang, Y. Xi, and S. Li, "Comprehensive review of emerging contaminants: Detection technologies, environmental impact, and management strategies," *Ecotoxicology and Environmental Safety,* vol. 278, p. 116420, 2024/06/15/ 2024.

[22] E. Boahen, L. Owusu, and S. O. Adjei-Anim, "A comprehensive review of emerging environmental contaminants of global concern," *Discover Environment,* vol. 3, no. 1, p. 144, 2025/09/16 2025.

[23] Z. Ma *et al.*, "Monodispersed Ag nanoparticles deposited on Ni-based coordination polymer composite with enhanced photocatalytic degradation for bisphenol A," *Colloids and Surfaces A: Physicochemical and Engineering Aspects,* vol. 681, p. 132821, 2024/01/20/ 2024.

[24] Z. You, Z. Wang, K. Tian, and X. Yao, "Activation of persulfate by MIL-100(Fe) coated with perylene diimide heterojunction photocatalyst for efficient removal of Bisphenol A in visible light," *Journal of Environmental Chemical Engineering,* vol. 11, no. 3, p. 110159, 2023/06/01/ 2023.

[25] C. Roledo *et al.*, "A comprehensive study on bisphenol A and estrogenic activity in the Paraíba do Sul River, São Paulo, Brazil," *Journal of Water and Health,* vol. 22, no. 11, pp. 2060-2075, 2024.

[26] C. B. Godiya and B. J. Park, "Removal of bisphenol A from wastewater by physical, chemical and biological remediation techniques. A review," *Environmental Chemistry Letters,* vol. 20, no. 3, pp. 1801-1837, 2022/06/01 2022.

[27] "Risk Management for Bisphenol A (BPA)," United States Environmental Protection Agency March 6, 2025, Available: https://www.epa.gov/assessing-and-managing-chemicals-under-tsca/risk-management-bisphenol-bpa.

[28] Z. Wang, Y. Ma, H. Lin, L. Luo, and H. Zhang, "Zn-Mn bimetallic oxide derived from waste battery to activate peroxymonosulfate for bisphenol A removal under visible light irradiation," *Journal of Environmental Chemical Engineering,* vol. 12, no. 5, p. 113351, 2024/10/01/ 2024.

[29] H. Wu *et al.*, "Novel discrete architecture for quantum dots modified ultrathin hollow nanotube Bi2Sn2O7/Bi4O5I2 S-scheme heterojunction for ultra-efficient photocatalytic degradation of bisphenol A," *Applied Catalysis B: Environment and Energy,* vol. 360, p. 124517, 2025/01/01/ 2025.

[30] Q. Su, D. Yuan, S. Wan, and L. Sun, "A novel visible light-driven oxygen doped C3N4/Bi12O17Cl2/ferrate(VI) system for Bisphenol A degradation: Radical and nonradical pathways," *Chemosphere,* vol. 364, p. 143227, 2024/09/01/ 2024.

[31] T. Vasiljevic and T. Harner, "Bisphenol A and its analogues in outdoor and indoor air: Properties, sources and global levels," *Science of The Total Environment,* vol. 789, p. 148013, 2021/10/01/ 2021.

[32] Š. Slapničar, G. Žerjav, M. Németh, J. Zavašnik, and A. Pintar, "Design and evaluation of plasmonic metal-TiO2 nanostructures for photocatalytic degradation of BPA as a model pollutant," *Journal of Colloid and Interface Science,* vol. 700, p. 138361, 2025/12/15/ 2025.

[33] B. Guan, L. Guo, M. Gibson, and Z. Li, "The derivation of water quality criteria for bisphenol A for the protection of marine species in China," *Water Quality Research Journal,* vol. 53, no. 3, pp. 156-165, 2018.

[34] B. Petrie, L. Lopardo, K. Proctor, J. Youdan, R. Barden, and B. Kasprzyk-Hordern, "Assessment of bisphenol-A in the urban water cycle," *Science of The Total Environment,* vol. 650, pp. 900-907, 2019/02/10/ 2019.

[35] A. Mishra, D. Goel, and S. Shankar, "Bisphenol A contamination in aquatic environments: a review of sources, environmental concerns, and microbial remediation," *Environmental Monitoring and Assessment,* vol. 195, no. 11, p. 1352, 2023/10/20 2023.

[36] J. Y. Son, Y. Jo, H. Lee, Y. J. Jang, and H. Kim, "Water hyacinth-inspired self-floating photocatalytic system for efficient and sustainable water purification," *npj Clean Water,* vol. 8, no. 1, p. 51, 2025/06/10 2025.

[37] M. Huang *et al.*, "BiOIO3/Bi12SiO20 core-shell S-type heterojunction for efficient photocatalytic removal of bisphenol A: Performance and mechanism study," *Journal of Environmental Chemical Engineering,* vol. 12, no. 5, p. 113455, 2024/10/01/ 2024.

[38] W. H. Glaze, J.-W. Kang, and D. H. Chapin, "The Chemistry of Water Treatment Processes Involving Ozone, Hydrogen Peroxide and Ultraviolet Radiation," *Ozone: Science & Engineering,* vol. 9, no. 4, pp. 335-352, 1987/09/01 1987.

[39] L. Rizzo, "Addressing main challenges in the tertiary treatment of urban wastewater: are homogeneous photodriven AOPs the answer?," *Environmental Science: Water Research & Technology,* 10.1039/D2EW00146B vol. 8, no. 10, pp. 2145-2169, 2022.

[40] I. O. Daramola, M. O. Ojemaye, A. I. Okoh, and O. O. Okoh, "Occurrence of herbicides in the aquatic environment and their removal using advanced oxidation processes: a critical review," *Environmental Geochemistry and Health,* vol. 45, no. 5, pp. 1231-1260, 2023/05/01 2023.

[41] K. Qi, C. Imparato, O. Almjasheva, A. Khataee, and W. Zheng, "TiO2-based photocatalysts from type-II to S-scheme heterojunction and their applications," *Journal of Colloid and Interface Science,* vol. 675, pp. 150-191, 2024/12/01/ 2024.

[42] M. Derakhshankhah, N. Gilani, and J. V. Pasikhani, "Synergizing S-scheme charge transfer and fenton reactions via FeS2-anchored Ti3C2Tx MXene heterojunction for efficient round-the-clock photocatalytic wastewater treatment," *Journal of Alloys and Compounds,* vol. 1039, p. 183325, 2025/09/10/ 2025.

[43] R. Djellabi, R. Giannantonio, E. Falletta, and C. L. Bianchi, "SWOT analysis of photocatalytic materials towards large scale environmental remediation," *Current Opinion in Chemical Engineering,* vol. 33, p. 100696, 2021/09/01/ 2021.

[44] B. Davide, B. Claudia, and D. Ridha, "FLOATING PHOTOCATALYSTS FOR WATER PURIFICATION," Dipartimento di Chimica - Lab ISMER (Innovative Smart Materials for Environmental Remediation)2020-2021.

[45] N. Ndiege *et al.*, "Synthesis, Characterization, and Photoactivity of Ta2O5-Grafted SiO2 Nanoparticles," vol. 17, no. 27, pp. 7685-7693, 2011.

[46] A. Samal and N. Das, "Mini-review on remediation of plastic pollution through photoreforming: progress, possibilities, and challenges," *Environmental Science and Pollution Research,* vol. 30, no. 35, pp. 83138-83152, 2023/07/01 2023.

[47] N. Davari, J. V. Pasikhani, C. L. Bianchi, V. Yargeau, and D. C. Boffito, "Recent progress on Ti-based piezo-photocatalysts for wastewater treatment," *Current Opinion in Chemical Engineering,* vol. 47, p. 101090, 2025/03/01/ 2025.

[48] A. Fujishima and K. Honda, "Electrochemical Photolysis of Water at a Semiconductor Electrode," *Nature,* vol. 238, no. 5358, pp. 37-38, 1972/07/01 1972.

[49] S. N. Frank and A. J. Bard, "Heterogeneous photocatalytic oxidation of cyanide ion in aqueous solutions at titanium dioxide powder," *Journal of the American Chemical Society,* vol. 99, no. 1, pp. 303-304, 1977/01/01 1977.

[50] J. A. Rengifo-Herrera and C. Pulgarin, "Why five decades of massive research on heterogeneous photocatalysis, especially on TiO2, has not yet driven to water disinfection and detoxification applications? Critical review of drawbacks and challenges," *Chemical Engineering Journal,* vol. 477, p. 146875, 2023/12/01/ 2023.

[51] A. Chakravorty and S. Roy, "A review of photocatalysis, basic principles, processes, and materials," *Sustainable Chemistry for the Environment,* vol. 8, p. 100155, 2024/12/01/ 2024.

[52] J. Nath, V. P. Singh, R. Sehgal, S. Kumar, V. Kumar, and R. Sehgal, "14 - Utilization of magnetic nanoferrite-based photocatalysts for elimination of organic pollutants from wastewater," in *Magnetic Nanoferrites and their Composites*, S. Kalia, R. Jasrotia, and V. Pratap Singh, Eds.: Woodhead Publishing, 2023, pp. 317-350.

[53] B. T. Son, N. V. Long, and N. T. Nhat Hang, "Fly ash-, foundry sand-, clay-, and pumice-based metal oxide nanocomposites as green photocatalysts," *RSC Advances,* 10.1039/D1RA05647F vol. 11, no. 49, pp. 30805-30826, 2021.

[54] D. R. Eddy *et al.*, "Heterophase Polymorph of TiO2 (Anatase, Rutile, Brookite, TiO2 (B)) for Efficient Photocatalyst: Fabrication and Activity," vol. 13, no. 4, p. 704, 2023.

[55] S. Reghunath, D. Pinheiro, and S. D. Kr, "A review of hierarchical nanostructures of TiO2: Advances and applications," *Applied Surface Science Advances,* vol. 3, p. 100063, 2021/03/01/ 2021.

[56] Z. Chen, J. Xiong, and G. Cheng, "Recent advances in brookite phase TiO2-based photocatalysts toward CO2 reduction," *Fuel,* vol. 357, p. 129806, 2024/02/01/ 2024.

[57] T. T. Nguyen and K. Edalati, "Brookite TiO2 as an active photocatalyst for photoconversion of plastic wastes to acetic acid and simultaneous hydrogen production: Comparison with anatase and rutile," *Chemosphere,* vol. 355, p. 141785, 2024/05/01/ 2024.

[58] Q. Tay, X. Liu, Y. Tang, Z. Jiang, T. C. Sum, and Z. Chen, "Enhanced Photocatalytic Hydrogen Production with Synergistic Two-Phase Anatase/Brookite TiO2 Nanostructures," *The Journal of Physical Chemistry C,* vol. 117, no. 29, pp. 14973-14982, 2013/07/25 2013.

[59] G. W. C. Kumarage *et al.*, "Synthesis of TiO2-(B) Nanobelts for Acetone Sensing," vol. 23, no. 19, p. 8322, 2023.

[60] S. Z. Alsheheri, "Nanocomposites containing titanium dioxide for environmental remediation," *Designed Monomers and Polymers,* vol. 24, no. 1, pp. 22-45, 2021/01/01 2021.

[61] J. A. Rengifo-Herrera, P. Osorio-Vargas, and C. Pulgarin, "A critical review on N-modified TiO2 limits to treat chemical and biological contaminants in water. Evidence that enhanced visible light absorption does not lead to higher degradation rates under whole solar light," *Journal of Hazardous Materials,* vol. 425, p. 127979, 2022/03/05/ 2022.

[62] F. Tanos, A. Razzouk, G. Lesage, M. Cretin, and M. Bechelany, "A Comprehensive Review on Modification of Titanium Dioxide-Based Catalysts in Advanced Oxidation Processes for Water Treatment," vol. 17, no. 6, p. e202301139, 2024.

[63] A. Sabir, T. A. Sherazi, and Q. Xu, "Porous polymer supported Ag-TiO2 as green photocatalyst for degradation of methyl orange," *Surfaces and Interfaces,* vol. 26, p. 101318, 2021/10/01/ 2021.

[64] D. Jiang *et al.*, "A Review on Metal Ions Modified TiO2 for Photocatalytic Degradation of Organic Pollutants," vol. 11, no. 9, p. 1039, 2021.

[65] W. Choi, A. Termin, and M. R. Hoffmann, "The Role of Metal Ion Dopants in Quantum-Sized TiO2: Correlation between Photoreactivity and Charge Carrier Recombination Dynamics," *The Journal of Physical Chemistry,* vol. 98, no. 51, pp. 13669-13679, 1994/12/01 1994.

[66] L. G. Devi, N. Kottam, B. N. Murthy, and S. G. Kumar, "Enhanced photocatalytic activity of transition metal ions Mn2+, Ni2+ and Zn2+ doped polycrystalline titania for the degradation of Aniline Blue under UV/solar light," *Journal of Molecular Catalysis A: Chemical,* vol. 328, no. 1, pp. 44-52, 2010/08/03/ 2010.

[67] C. B. Anucha *et al.*, "Synthesis and Characterization of B/NaF and Silicon Phthalocyanine-Modified TiO2 and an Evaluation of Their Photocatalytic Removal of Carbamazepine," vol. 7, no. 4, p. 71, 2020.

[68] J. Ge, Y. Zhang, Y.-J. Heo, and S.-J. Park, "Advanced Design and Synthesis of Composite Photocatalysts for the Remediation of Wastewater: A Review," vol. 9, no. 2, p. 122, 2019.

[69] R. Sharma and J. Prakash, "TiO2 Nanomaterials: Synthesis, Properties, Modifications, and Applications," in *Titanium Dioxide-Based Multifunctional Hybrid Nanomaterials: Application on Health, Energy and Environment*, J. Prakash, J. Cho, O. Ruzimuradov, and D. Fang, Eds. Cham: Springer Nature Switzerland, 2025, pp. 1-25.

[70] R. S. Pedanekar, S. K. Shaikh, and K. Y. Rajpure, "Thin film photocatalysis for environmental remediation: A status review," *Current Applied Physics,* vol. 20, no. 8, pp. 931-952, 2020/08/01/ 2020.

[71] S. Impemba *et al.*, "Engineering the heterojunction between TiO2 and In2O3 for improving the solar-driven hydrogen production," *International Journal of Hydrogen Energy,* vol. 63, pp. 896-904, 2024/04/18/ 2024.

[72] M. Riyaheini, N. Gilani, and J. V. Pasikhani, "Engineering the photo-induced charge generation between TiO2 and FeS2 heterojunction for enhanced photocatalytic wastewater purification," *Ceramics International,* vol. 49, no. 22, Part A, pp. 34682-34696, 2023/11/15/ 2023.

[73] S. Xu, Q. Gao, Z. Hu, Y. Lu, Y. Qin, and Y. Li, "CdS–SH/TiO2 Heterojunction Photocatalyst Significantly Improves Selectivity for C–O Bond Breaking in Lignin Models," *ACS Catalysis,* vol. 13, no. 21, pp. 13941-13954, 2023/11/03 2023.

[74] P. Dhiman, J. Sharma, A. Kumar, G. Sharma, G. Rana, and G. T. Mola, "Recent advances in piezo-photocatalytic heterojunctions for energy and environmental applications," *Materials Today Sustainability,* vol. 28, p. 100973, 2024/12/01/ 2024.

[75] I. Ahmad *et al.*, "Recent advances and challenges in 2D/2D heterojunction photocatalysts for solar fuels applications," *Advances in Colloid and Interface Science,* vol. 304, p. 102661, 2022/06/01/ 2022.

[76] Z. Wang, Z. Lin, S. Shen, W. Zhong, and S. Cao, "Advances in designing heterojunction photocatalytic materials," *Chinese Journal of Catalysis,* vol. 42, no. 5, pp. 710-730, 2021/05/01/ 2021.

[77] H. Wang *et al.*, "Semiconductor heterojunction photocatalysts: design, construction, and photocatalytic performances," *Chemical Society Reviews,* 10.1039/C4CS00126E vol. 43, no. 15, pp. 5234-5244, 2014.

[78] Z. Liao *et al.*, "Advances in Z-scheme photocatalysts for efficient photocatalytic H2O2 production: A comprehensive review," *Journal of Alloys and Compounds,* vol. 976, p. 173322, 2024/03/05/ 2024.

[79] X. Liu, Q. Zhang, and D. Ma, "Advances in 2D/2D Z-Scheme Heterojunctions for Photocatalytic Applications," vol. 5, no. 2, p. 2000397, 2021.

[80] H. Yang *et al.*, "Engineering the S-scheme heterojunction between NiO microrods and MgAl-LDH nanoplates for efficient and selective photoreduction of CO2 to CH4," *Chemical Engineering Journal,* vol. 474, p. 145813, 2023/10/15/ 2023.

[81] L. Wang, B. Zhu, J. Zhang, J. B. Ghasemi, M. Mousavi, and J. Yu, "S-scheme heterojunction photocatalysts for CO2 reduction," *Matter,* vol. 5, no. 12, pp. 4187-4211, 2022/12/07/ 2022.

[82] R. Mishra *et al.*, "A review on Z/S – scheme heterojunction for photocatalytic applications based on metal halide perovskite materials," *Applied Surface Science Advances,* vol. 9, p. 100241, 2022/06/01/ 2022.

[83] Y. Lu *et al.*, "Cu2O nanocrystals/TiO2 microspheres film on a rotating disk containing long-afterglow phosphor for enhanced round-the-clock photocatalysis," *Applied Catalysis B: Environmental,* vol. 224, pp. 239-248, 2018/05/01/ 2018.

[84] T. Cai, Y. Liu, L. Wang, W. Dong, and G. Zeng, "Recent advances in round-the-clock photocatalytic system: Mechanisms, characterization techniques and applications," *Journal of Photochemistry and Photobiology C: Photochemistry Reviews,* vol. 39, pp. 58-75, 2019/06/01/ 2019.

[85] B. Li, X.-j. Liu, H.-w. Zhu, H.-p. Guan, and R.-t. Guo, "Recent Progress of Round-the-Clock Photocatalytic System in Environmental and Energy Applications: A Review," vol. 26, no. 9, p. e202401144, 2025.

[86] Y. Yu *et al.*, "The Design of TiO2 Nanostructures (Nanoparticle, Nanotube, and Nanosheet) and Their Photocatalytic Activity," *The Journal of Physical Chemistry C,* vol. 118, no. 24, pp. 12727-12733, 2014/06/19 2014.

[87] M. A. S. Alothoum, "A Review of the Synthesis, Structural, and Optical Properties of TiO2 Nanoparticles: Current State of the Art and Potential Applications," vol. 15, no. 11, p. 944, 2025.

[88] G. Centi and S. Perathoner, "Nano-architecture and reactivity of Titania catalytic materials. Quasi-1D nanostructures," in *Catalysis*, vol. 20, J. J. Spivey and K. M. Dooley, Eds.: Royal Society of Chemistry, 2007, p. 0.

[89] S. Ladhane *et al.*, "Direct growth of WS2 nanosheets using RF-magnetron sputtering on hydrothermally grown TiO2 nanorods for enhancing photoelectrochemical water splitting," *Materials Chemistry and Physics,* vol. 334, p. 130440, 2025/04/01/ 2025.

[90] H.-Y. Yang, W.-Y. Rho, S. K. Lee, S. H. Kim, and Y.-B. Hahn, "TiO2 Nanoparticles/Nanotubes for Efficient Light Harvesting in Perovskite Solar Cells," vol. 9, no. 3, p. 326, 2019.

[91] J. M. Macak, M. Zlamal, J. Krysa, and P. Schmuki, "Self-Organized TiO2 Nanotube Layers as Highly Efficient Photocatalysts," vol. 3, no. 2, pp. 300-304, 2007.

[92] S. Ananthakumar, J. Ramkumar, and S. M. Babu, "Semiconductor nanoparticles sensitized TiO2 nanotubes for high efficiency solar cell devices," *Renewable and Sustainable Energy Reviews,* vol. 57, pp. 1307-1321, 2016/05/01/ 2016.

[93] O. Zakir *et al.*, "A review on TiO2 nanotubes: synthesis strategies, modifications, and applications," *Journal of Solid State Electrochemistry,* vol. 27, no. 9, pp. 2289-2307, 2023/09/01 2023.

[94] N. Liu, X. Chen, J. Zhang, and J. W. Schwank, "A review on TiO2-based nanotubes synthesized via hydrothermal method: Formation mechanism, structure modification, and photocatalytic applications," *Catalysis Today,* vol. 225, pp. 34-51, 2014/04/15/ 2014.

[95] D. L. Morgan, H.-W. Liu, R. L. Frost, and E. R. Waclawik, "Implications of Precursor Chemistry on the Alkaline Hydrothermal Synthesis of Titania/Titanate Nanostructures," *The Journal of Physical Chemistry C,* vol. 114, no. 1, pp. 101-110, 2010/01/14 2010.

[96] D. V. Bavykin, V. N. Parmon, A. A. Lapkin, and F. C. Walsh, "The effect of hydrothermal conditions on the mesoporous structure of TiO2 nanotubes," *Journal of Materials Chemistry,* 10.1039/B406378C vol. 14, no. 22, pp. 3370-3377, 2004.

[97] M. Zlamal, J. M. Macak, P. Schmuki, and J. Krýsa, "Electrochemically assisted photocatalysis on self-organized TiO2 nanotubes," *Electrochemistry Communications,* vol. 9, no. 12, pp. 2822-2826, 2007/12/01/ 2007.

[98] H. Qiao *et al.*, "Novel Mixed-Dimensional Photocatalysts Based on 3D Graphene Aerogel Embedded with TiO2/MoS2 Hybrid," *The Journal of Physical Chemistry C,* vol. 123, no. 17, pp. 10949-10955, 2019/05/02 2019.

[99] E. Falletta *et al.*, "Solar Light Photoactive Floating Polyaniline/TiO2 Composites for Water Remediation," vol. 11, no. 11, p. 3071, 2021.

[100] F. Seifikar and A. Habibi-Yangjeh, "Floating photocatalysts as promising materials for environmental detoxification and energy production: A review," *Chemosphere,* vol. 355, p. 141686, 2024/05/01/ 2024.

[101] S. Nouacer and R. Djellabi, "Easy-handling semi-floating TiO2-based aerogel for solar photocatalytic water depollution," *Environmental Science and Pollution Research,* vol. 30, no. 9, pp. 22388-22395, 2023/02/01 2023.

[102] L. Dai, B. Li, Z. Li, and C. Yu, "Floatable photocatalysts: Design principles and application advances," *Journal of Environmental Chemical Engineering,* vol. 12, no. 4, p. 113029, 2024/08/01/ 2024.

[103] A. M. Nasir *et al.*, "A review on floating nanocomposite photocatalyst: Fabrication and applications for wastewater treatment," *Journal of Water Process Engineering,* vol. 36, p. 101300, 2020/08/01/ 2020.

[104] Z. Zhang *et al.*, "“Floating Catalytic Foam” with prominent heat-induced convection for the effective photocatalytic removal of antibiotics," *Journal of Hazardous Materials,* vol. 463, p. 132879, 2024/02/05/ 2024.

[105] J. Yoo, J. Lee, and J. Kim, "A floating photocatalytic fabric integrated with a AgI/UiO-66-NH2 heterojunction as a facile strategy for wastewater treatment," *RSC Advances,* 10.1039/D3RA07534F vol. 14, no. 3, pp. 1794-1802, 2024.

[106] S. Krishnan, A. V. Karim, and A. Shriwastav, "Visible light responsive Cu-N/TiO2 nanoparticles for the photocatalytic degradation of bisphenol A," *Water Science and Technology,* vol. 86, no. 6, pp. 1527-1539, 2022.

[107] R. B. Rajput, R. S. Mane, S. N. Jamble, N. Jha, and R. B. Kale, "N-doped carbon/TiO2 composites with enhanced photocatalytic performance for the removal of organic pollutants," *Journal of Physics and Chemistry of Solids,* vol. 184, p. 111677, 2024/01/01/ 2024.

[108] R.-a. Doong and C.-w. Tsai, "Synergistic effect of Cu adsorption on the enhanced photocatalytic degradation of bisphenol A by TiO2/titanate nanotubes composites," *Journal of the Taiwan Institute of Chemical Engineers,* vol. 57, pp. 69-76, 2015/12/01/ 2015.

[109] Y. Cai *et al.*, "Co-doped magnetic N-TiO2-x/rGO heterojunction@cellulose nanofibrous flakelet for enhanced photocatalytic oxidation and facile separation: Efficient charge separation and self-floatability," *Chemical Engineering Journal,* vol. 425, p. 131462, 2021/12/01/ 2021.

[110] S. Stojanović, V. Rac, K. Mojsilović, R. Vasilić, S. Marković, and L. Damjanović-Vasilić, "Photocatalytic degradation of bisphenol A in aqueous solution using TiO2/clinoptilolite hybrid photocatalyst," *Environmental Science and Pollution Research,* vol. 30, no. 35, pp. 84046-84060, 2023/07/01 2023.

[111] L. Li, Y. Li, H. Xu, and W. Zhang, "Novel Floating TiO2 Photocatalysts for Polluted Water Decontamination Based on Polyurethane Composite Foam," *Separation Science and Technology,* vol. 50, no. 2, pp. 164-173, 2015/01/22 2015.

[112] R. A. Dianati, N. Mengelizadeh, M. A. Zazouli, J. Yazdani Cherati, D. Balarak, and S. Ashrafi, "Photocatalytic degradation of bisphenol A by GO-TiO2 nanocomposite under ultraviolet light: synthesis, effect of parameters and mineralisation," *International Journal of Environmental Analytical Chemistry,* pp. 1-18, 2022.

[113] A. Mantilla *et al.*, "Enhanced photocatalytic degradation of Bisphenol A under visible light by Cr-TiO2 nanoparticles," *Journal of Photochemistry and Photobiology A: Chemistry,* vol. 459, p. 116079, 2025/02/01/ 2025.

[114] Y. Jari *et al.*, "Enhanced visible-light degradation and mineralization of bisphenol A using Cu-doped TiO2 photocatalysts: characterization, effectiveness, mechanism and DFT insights," *Water Resources and Industry,* vol. 35, p. 100335, 2026/06/01/ 2026.

[115] C.-Y. Kuo, H.-K. Jheng, and S.-E. Syu, "Effect of non-metal doping on the photocatalytic activity of titanium dioxide on the photodegradation of aqueous bisphenol A," *Environmental Technology,* vol. 42, no. 10, pp. 1603-1611, 2021/04/29 2021.

[116] H. Shi *et al.*, "Synergistic manganese-cobalt co-doped TiO2 for enhanced photocatalytic degradation of bisphenol A: Mechanism, DFT calculations, and toxicity assessment," *Journal of Alloys and Compounds,* vol. 1036, p. 182032, 2025/07/20/ 2025.

[117] M. A. Mohamed *et al.*, "Hematite microcube decorated TiO2 nanorods as heterojunction photocatalyst with in-situ carbon doping derived from polysaccharides bio-templates hydrothermal carbonization," *Journal of Alloys and Compounds,* vol. 820, p. 153143, 2020/04/15/ 2020.

[118] S. S. Abdallah, M. C. Maridevaru, F. A. Marzouqi, and R. Selvaraj, "Green synthesis of TiO2@g-C3N4 nanocomposites for the photocatalytic degradation of pesticides and toxic organics present in water and wastewater," *Journal of Photochemistry and Photobiology A: Chemistry,* vol. 459, p. 116015, 2025/02/01/ 2025.

[119] W. Xu *et al.*, "TiO2–Cu7S4 modified with a carbazole-based conjugated porous polymer for adsorption and photocatalytic degradation of bisphenol A," *Green Energy & Environment,* vol. 10, no. 3, pp. 598-608, 2025/03/01/ 2025.

[120] M. Sain and S. Chowdhury, "Sustainable degradation of bisphenol A using a pH-responsive TiO2/g-C3N4/rGO photocatalyst with easy recovery," *Environmental Research,* vol. 282, p. 122004, 2025/10/01/ 2025.

[121] Y. Wei, Q. Wu, H. Meng, Y. Zhang, and C. Cao, "Recent advances in photocatalytic self-cleaning performances of TiO2-based building materials," *RSC Advances,* 10.1039/D2RA07839B vol. 13, no. 30, pp. 20584-20597, 2023.

[122] A. Tabet *et al.*, "Photo-electrochemical properties of nanostructured metal-semiconductorAl/TiO2 thin film. Application to Rhodamine B oxidation under sunlight," *Optik,* vol. 249, p. 168288, 2022/01/01/ 2022.

[123] M. Riyaheini, N. Gilani, and J. V. Pasikhani, "Engineering the photo-induced charge generation between TiO2 and FeS2 heterojunction for enhanced photocatalytic wastewater purification," *Ceramics International,* 2023/08/15/ 2023.

[124] Q. Kang, S. Ning, D. Jiang, Y. Wang, and F. Zhou, "Chapter 16 - Semiconductor-based artificial photosynthesis for water-splitting and CO2 reduction," in *Photosynthesis*, H. J. M. Hou and S. I. Allakhverdiev, Eds.: Academic Press, 2023, pp. 377-405.

[125] Z. Huang and H. Liu, "Insights into the pathways, intermediates, influence factors and toxicological properties in the degradation of tetracycline by TiO2-based photocatalysts," *Journal of Environmental Chemical Engineering,* vol. 11, no. 5, p. 110587, 2023/10/01/ 2023.

[126] S. N. Sadikin *et al.*, "Photocatalytic activity and stability properties of porous TiO2 film as photocatalyst for methylene blue and methylene orange degradation," *International Journal of Electrochemical Science,* vol. 18, no. 9, p. 100246, 2023/09/01/ 2023.

[127] D. Beketova *et al.*, "One-Step Decoration of TiO2 Nanotubes with Fe3O4 Nanoparticles: Synthesis and Photocatalytic and Magnetic Properties," *ACS Applied Nano Materials,* vol. 3, no. 2, pp. 1553-1563, 2020/02/28 2020.

[128] N. K. Shrestha *et al.*, "Magnetically Guided Titania Nanotubes for Site-Selective Photocatalysis and Drug Release," vol. 48, no. 5, pp. 969-972, 2009.

[129] D. Kanakaraju, F. D. anak Kutiang, Y. C. Lim, and P. S. Goh, "Recent progress of Ag/TiO2 photocatalyst for wastewater treatment: Doping, co-doping, and green materials functionalization," *Applied Materials Today,* vol. 27, p. 101500, 2022/06/01/ 2022.

[130] H. H. Nguyen, G. Gyawali, A. Martinez-Oviedo, Y. K. Kshetri, and S. W. Lee, "Physicochemical properties of Cr-doped TiO2 nanotubes and their application in dye-sensitized solar cells," *Journal of Photochemistry and Photobiology A: Chemistry,* vol. 397, p. 112514, 2020/06/15/ 2020.

[131] A. Bjelajac *et al.*, "Enhanced absorption of TiO2 nanotubes by N-doping and CdS quantum dots sensitization: insight into the structure," *RSC Advances,* 10.1039/C8RA06341A vol. 8, no. 61, pp. 35073-35082, 2018.

[132] N. H. Mohamad Idris, K. Y. Cheong, S. M. Smith, and H. L. Lee, "C,N-Codoped TiO2 Nanoparticles Immobilized on Floating Alginate Beads for Diazinon Removal under Solar Light Irradiation," *ACS Applied Nano Materials,* 2023/11/13 2023.

[133] C. T. Mehmood, Z. Zhong, H. Zhou, C. Zhang, and Y. Xiao, "Immobilizing a visible light-responsive photocatalyst on a recyclable polymeric composite for floating and suspended applications in water treatment," *RSC Advances,* 10.1039/D0RA06864K vol. 10, no. 60, pp. 36349-36362, 2020.

[134] L. Ni, Y. Li, C. Zhang, L. Li, W. Zhang, and D. Wang, "Novel floating photocatalysts based on polyurethane composite foams modified with silver/titanium dioxide/graphene ternary nanoparticles for the visible-light-mediated remediation of diesel-polluted surface water," vol. 133, no. 19, 2016.

[135] Y. Fu, T. Huang, L. Zhang, J. Zhu, and X. Wang, "Ag/g-C3N4 catalyst with superior catalytic performance for the degradation of dyes: a borohydride-generated superoxide radical approach," *Nanoscale,* 10.1039/C5NR03260A vol. 7, no. 32, pp. 13723-13733, 2015.

[136] L. S. Mendieta-Rodríguez, L. M. González-Rodríguez, J. J. Alcaraz-Espinoza, A. E. Chávez-Guajardo, and J. C. Medina-Llamas, "Synthesis and characterization of a polyurethane-polyaniline macroporous foam material for methyl orange removal in aqueous media," *Materials Today Communications,* vol. 26, p. 102155, 2021/03/01/ 2021.

[137] L. Zhang *et al.*, "High thermostable ordered mesoporous SiO2–TiO2 coated circulating-bed biofilm reactor for unpredictable photocatalytic and biocatalytic performance," *Applied Catalysis B: Environmental,* vol. 180, pp. 521-529, 2016/01/01/ 2016.

[138] Z. Khani, D. Schieppati, C. L. Bianchi, and D. C. Boffito, "The Sonophotocatalytic Degradation of Pharmaceuticals in Water by MnOx-TiO2 Systems with Tuned Band-Gaps," vol. 9, no. 11, p. 949, 2019.

[139] S. G. Hosseini and J. V. Pasikhani, "Enhanced optical properties and photocatalytic activity of TiO2 nanotubes by using magnetic activated carbon: evaluating photocatalytic reduction of Cr(VI)," *Environmental Technology,* vol. 42, no. 6, pp. 914-931, 2021/03/08 2021.

[140] H. Taghvaei, E. Pirzadeh, M. Jahanbakhsh, O. Khalifeh, and M. R. Rahimpour, "Polyurethane foam: A novel support for metal oxide packing used in the non-thermal plasma decomposition of CO2," *Journal of CO2 Utilization,* vol. 44, p. 101398, 2021/02/01/ 2021.

[141] S. Aflaki, M. Farhadian, A. R. Solaimany Nazar, S. Tangestaninejad, and N. Davari, "Investigation of copper plates as anode and TiO2/glycine/ZnFe2O4 stabilized on graphite as cathode for textile dyes degradation from aqueous solution under visible light," *Journal of Applied Electrochemistry,* vol. 51, no. 10, pp. 1387-1405, 2021/10/01 2021.

[142] N. Davari, M. Farhadian, A. R. S. Nazar, and M. Homayoonfal, "Degradation of diphenhydramine by the photocatalysts of ZnO/Fe2O3 and TiO2/Fe2O3 based on clinoptilolite: Structural and operational comparison," *Journal of Environmental Chemical Engineering,* vol. 5, no. 6, pp. 5707-5720, 2017/12/01/ 2017.

[143] N. Davari, M. Farhadian, and A. R. Solaimany Nazar, "Synthesis and characterization of Fe2O3 doped ZnO supported on clinoptilolite for photocatalytic degradation of metronidazole," *Environmental Technology,* vol. 42, no. 11, pp. 1734-1746, 2021/05/12 2021.

[144] Y. Kameya and H. Yabe, "Optical and Superhydrophilic Characteristics of TiO2 Coating with Subwavelength Surface Structure Consisting of Spherical Nanoparticle Aggregates," vol. 9, no. 9, p. 547, 2019.

[145] Y. Q. Wang, G. Q. Hu, X. F. Duan, H. L. Sun, and Q. K. Xue, "Microstructure and formation mechanism of titanium dioxide nanotubes," *Chemical Physics Letters,* vol. 365, no. 5, pp. 427-431, 2002/11/13/ 2002.

[146] X. Sun and Y. Li, "Synthesis and Characterization of Ion-Exchangeable Titanate Nanotubes," vol. 9, no. 10, pp. 2229-2238, 2003.

[147] L. Niu *et al.*, "Difference in performance and mechanism for methylene blue when TiO2 nanoparticles are converted to nanotubes," *Journal of Cleaner Production,* vol. 297, p. 126498, 2021/05/15/ 2021.

[148] J. Yang *et al.*, "Highly Hydrophilic TiO2 Nanotubes Network by Alkaline Hydrothermal Method for Photocatalysis Degradation of Methyl Orange," vol. 9, no. 4, p. 526, 2019.

[149] T. Kubo and A. Nakahira, "Local Structure of TiO2-Derived Nanotubes Prepared by the Hydrothermal Process," *The Journal of Physical Chemistry C,* vol. 112, no. 5, pp. 1658-1662, 2008/02/01 2008.

[150] K. Alkanad *et al.*, "One-Step Hydrothermal Synthesis of Anatase TiO2 Nanotubes for Efficient Photocatalytic CO2 Reduction," *ACS Omega,* vol. 7, no. 43, pp. 38686-38699, 2022/11/01 2022.

[151] N. Gilani, J. Vahabzadeh Pasikhani, P. Tafazoli Motie, M. Akbari, "Fabrication of quantum Cu(II) nanodot decorated TiO2 nanotubes by the photochemical deposition-assisted hydrothermal method: study catalytic activity in hydrogen generation," *Desalination and Water Treatment,* vol. 139, pp. 145–155, 2019.

[152] L. Jiao, H. Xiao, Q. Wang, and J. Sun, "Thermal degradation characteristics of rigid polyurethane foam and the volatile products analysis with TG-FTIR-MS," *Polymer Degradation and Stability,* vol. 98, no. 12, pp. 2687-2696, 2013/12/01/ 2013.

[153] N. Rastegarfar, R. Behrooz, and M. Barikani, "Characterization of polyurethane foams prepared from liquefied sawdust by crude glycerol and polyethylene glycol," *Journal of Polymer Research,* vol. 25, no. 7, p. 154, 2018/06/20 2018.

[154] P. M. A. Ebrahimian Pirbazari, B. Fakhari Kisomi, "Co/TiO2 nanoparticles: preparation, characterization and its application for photocatalytic degradation of methylene blue," *Desalination and Water Treatment,* vol. 63, pp. 283–292, 2017.

[155] Y. Ding, C. Zhang, W. Liao, and J. Peng, "Mechanical and electrochemical properties of TiO2 modified polyurethane nanofibers," *Applied Physics A,* vol. 129, no. 2, p. 162, 2023/02/02 2023.

[156] E. Hajialilou, H. Asgharzadeh, and S. Khameneh Asl, "TiO2/rGO/Cu2O ternary hybrid for high-performance photoelectrochemical applications," *Applied Surface Science,* vol. 544, p. 148832, 2021/04/01/ 2021.

[157] W. Gao *et al.*, "Photocatalytic Degradation of Methylene Blue from Aqueous Solutions by rGO/TiO2 Nanocomposites," *Water, Air, & Soil Pollution,* vol. 234, no. 7, p. 437, 2023/06/29 2023.

[158] J. Rashid *et al.*, "Stabilized fabrication of anatase-TiO2/FeS2 (pyrite) semiconductor composite nanocrystals for enhanced solar light-mediated photocatalytic degradation of methylene blue," *RSC Advances,* 10.1039/C8RA02077A vol. 8, no. 22, pp. 11935-11945, 2018.

[159] Z. Cui *et al.*, "Thermoplastic polyurethane/titania/polydopamine(TPU/TiO2/PDA) 3-D porous composite foam with outstanding oil/water separation performance and photocatalytic dye degradation," *Advanced Composites and Hybrid Materials,* vol. 5, no. 4, pp. 2801-2816, 2022/12/01 2022.

[160] Y. Wang *et al.*, "Fabrication of ultra-high working range strain sensor using carboxyl CNTs coated electrospun TPU assisted with dopamine," *Applied Surface Science,* vol. 566, p. 150705, 2021/11/15/ 2021.

[161] M. Smith, L. Scudiero, J. Espinal, J.-S. McEwen, and M. Garcia-Perez, "Improving the deconvolution and interpretation of XPS spectra from chars by ab initio calculations," *Carbon,* vol. 110, pp. 155-171, 2016/12/01/ 2016.

[162] S. D. Delekar *et al.*, "Structural and Optical Properties of Nanocrystalline TiO2 with Multiwalled Carbon Nanotubes and Its Photovoltaic Studies Using Ru(II) Sensitizers," *ACS Omega,* vol. 3, no. 3, pp. 2743-2756, 2018/03/31 2018.

[163] R. Jonathan *et al.*, "Low-cost and large-scale preparation of ultrafine TiO2@C hybrids for high-performance degradation of methyl orange and formaldehyde under visible light," vol. 12, no. 1, 2023.

[164] M. Xing, F. Shen, B. Qiu, and J. Zhang, "Highly-dispersed Boron-doped Graphene Nanosheets Loaded with TiO2 Nanoparticles for Enhancing CO2 Photoreduction," *Scientific Reports,* vol. 4, no. 1, p. 6341, 2014/09/11 2014.

[165] E. Carrasco, M. Oujja, M. Sanz, J. F. Marco, and M. Castillejo, "X-ray and ion irradiation effects on azurite, malachite and alizarin pictorial models," *Microchemical Journal,* vol. 137, pp. 381-391, 2018/03/01/ 2018.

[166] X. Qin, L. Ji, and A. Zhu, "Construction of rutile/anatase Ohmic heterojunction of TiO2/Ti3C2 with robust built-in electric field for boosting photocatalytic organic pollutant and hydrogen evolution," *Applied Surface Science,* vol. 652, p. 159338, 2024/04/15/ 2024.

[167] Y. Yang, S.-H. Liao, W. Shi, Y. Wu, R. Zhang, and S. J. R. A. Leng, "Nitrogen-doped TiO2(B) nanorods as high-performance anode materials for rechargeable sodium-ion batteries," vol. 7, pp. 10885-10890, 2017.

[168] N. Li, D. Geng, and J. Zhou, "Ag and Cu Nanoparticles Synergistically Enhance Photocatalytic CO2 Reduction Activity of B Phase TiO2," *Catalysis Letters,* vol. 152, no. 1, pp. 124-138, 2022/01/01 2022.

[169] D. Li *et al.*, "Effects of Particle Size on the Structure and Photocatalytic Performance by Alkali-Treated TiO2," vol. 10, no. 3, p. 546, 2020.

[170] J. V. Pasikhani, B. G. Aliabadi, N. Gilani, and A. E. Pirbazari, "Construction of NiO and Ti3+ self-doped TNTs thin film as a high quantum yield p-n type heterojunction via a novel photoelectrodeposition-assisted anodization method," *Journal of Photochemistry and Photobiology A: Chemistry,* vol. 418, p. 113433, 2021/09/01/ 2021.

[171] X. Deng *et al.*, "Fabrication of p-NiO/n-TiO2 nano-tube arrays photoelectrode and its enhanced photocatalytic performance for degradation of 4-chlorphenol," *Separation and Purification Technology,* vol. 186, pp. 1-9, 2017/10/02/ 2017.

[172] M. Zulfiqar, S. Chowdhury, and A. A. Omar, "Hydrothermal synthesis of multiwalled TiO2 nanotubes and its photocatalytic activities for Orange II removal," *Separation Science and Technology,* vol. 53, no. 9, pp. 1412-1422, 2018/06/13 2018.

[173] Z. Liu, Q. Zhang, and L.-C. Qin, "Reduction in the electronic band gap of titanium oxide nanotubes," *Solid State Communications,* vol. 141, no. 3, pp. 168-171, 2007/01/01/ 2007.

[174] T. Peng, S. Ray, S. S. Veeravalli, J. A. Lalman, and F. Arefi-Khonsari, "The role of hydrothermal conditions in determining 1D TiO2 nanomaterials bandgap energies and crystal phases," *Materials Research Bulletin,* vol. 105, pp. 104-113, 2018/09/01/ 2018.

[175] M. Thommes *et al.*, "Physisorption of gases, with special reference to the evaluation of surface area and pore size distribution (IUPAC Technical Report)," vol. 87, no. 9-10, pp. 1051-1069, 2015.

[176] A. H. Zaki, S. Adel, M. M. Abd El-hafiez, and A. A. Abdel-Khalek, "Improved production of titanate nanotubes by hydrothermal method for adsorption of organic dyes," *Beni-Suef University Journal of Basic and Applied Sciences,* vol. 10, no. 1, p. 86, 2021/12/04 2021.

[177] S. Rashad, A. H. Zaki, and A. A. Farghali, "Morphological effect of titanate nanostructures on the photocatalytic degradation of crystal violet," *Nanomaterials and Nanotechnology,* vol. 9, p. 1847980418821778, 2019/01/01 2019.

[178] S. Zhang *et al.*, "Aeration-Free In Situ Fenton-like Reaction: Specific Adsorption and Activation of Oxygen on Heterophase Oxygen Vacancies," *Environmental Science & Technology,* vol. 58, no. 4, pp. 1921-1933, 2024/01/30 2024.

[179] L. Ren *et al.*, "All-in-one self-floating porous foams as robust heat-blocking layers for efficient photothermal conversion and solar desalination," *Science Bulletin,* vol. 68, no. 22, pp. 2760-2768, 2023/11/30/ 2023.

[180] A. Gordanshekan, S. Arabian, A. R. Solaimany Nazar, M. Farhadian, and S. Tangestaninejad, "A comprehensive comparison of green Bi2WO6/g-C3N4 and Bi2WO6/TiO2 S-scheme heterojunctions for photocatalytic adsorption/degradation of

Cefixime: Artificial neural network, degradation pathway, and toxicity estimation," *Chemical Engineering Journal,* vol. 451, p. 139067, 2023/01/01/ 2023.

[181] R. Ji, Z. Zhang, L. Tian, L. Jin, Q. Xu, and J. Lu, "Z- scheme heterojunction of BiOI nanosheets grown in situ on NH2-UiO-66 crystals with rapid degradation of BPA in real water," *Chemical Engineering Journal,* vol. 453, p. 139897, 2023/02/01/ 2023.

[182] Q. Zhou *et al.*, "Persulfate enhanced removal of bisphenol A by copper oxide/reduced graphene oxide foam: Influencing factors, mechanism and degradation pathway," *Chemosphere,* vol. 340, p. 139786, 2023/11/01/ 2023.

[183] K. Nelson, A. C. Mecha, H. M. Samuel, and Z. A. Suliman, "Recent Trends in the Application of Photocatalytic Membranes in Removal of Emerging Organic Contaminants in Wastewater," vol. 13, no. 1, p. 163, 2025.

[184] A. Intisar *et al.*, "Adsorptive and photocatalytic degradation potential of porous polymeric materials for removal of pesticides, pharmaceuticals, and dyes-based emerging contaminants from water," *Chemosphere,* vol. 336, p. 139203, 2023/09/01/ 2023.

[185] R. B. González-González, R. Parra-Saldívar, W. F. Alsanie, and H. M. N. Iqbal, "Nanohybrid catalysts with porous structures for environmental remediation through photocatalytic degradation of emerging pollutants," *Environmental Research,* vol. 214, p. 113955, 2022/11/01/ 2022.

[186] V. N. Panchenko, M. A. Matsko, D. S. Selishchev, and D. V. Kozlov, "Polymeric Floating Photocatalysts Based on PE/TiO2 Composites for the Removal of Organic Pollutants in Water," vol. 7, no. 8, p. 318, 2023.

[187] M. Ahtasham Iqbal *et al.*, "Advanced photocatalysis as a viable and sustainable wastewater treatment process: A comprehensive review," *Environmental Research,* vol. 253, p. 118947, 2024/07/15/ 2024.

[188] R. Habibi, N. Gilani, J. V. Pasikhani, and A. E. Pirbazari, "Improved photoelectrocatalytic activity of anodic TiO2 nanotubes by boron in situ doping coupled with geometrical optimization: Application of a potent photoanode in the purification of dye wastewater," *Journal of Solid State Electrochemistry,* vol. 25, no. 2, pp. 545-560, 2021/02/01 2021.

[189] M. Rahman, S. Shaheen, and T. Ahmad, "Photocatalytic transformation of organic pollutants and remediation strategies of carbon emissions and nitrogen fixation in inland water," *Materials Today Catalysis,* vol. 9, p. 100103, 2025/06/01/ 2025.

[190] N. Davari, E. Falletta, C. L. Bianchi, V. Yargeau, C. Rodriguez-Seco, and D. C. Boffito, "Comparing the photocatalytic activity of suspended and floating Ag-decorated TiO2 for dye removal," *Tetrahedron Green Chem,* vol. 5, p. 100059, 2025/06/01/ 2025.

[191] N. Davari, E. Falletta, C. L. Bianchi, V. Yargeau, and D. C. Boffito, "TiO2 nanotubes immobilized on polyurethane foam as a floating photocatalyst for water treatment," *Catalysis Today,* vol. 436, p. 114725, 2024/06/15/ 2024.

[192] N. Davari *et al.*, "Enhanced photo-induced charge generation of floating sulfur-doped TiO2 double-walled nanotubes for efficient sunlight-driven photocatalytic degradation of bisphenol A," *Ceramics International,* vol. 51, no. 27, Part B, pp. 53519-53534, 2025/11/01/ 2025.

[193] J. Du, X. Dang, and H. Zhao, "Photo-enzyme cascade catalysis treatment of bisphenol A in water: Synergistic hydroxylation pathway for mineralization and detoxification," *Journal of Hazardous Materials,* vol. 489, p. 137454, 2025/06/05/ 2025.

[194] L. Hu, G. Zhang, M. Liu, Q. Wang, and P. Wang, "Enhanced degradation of Bisphenol A (BPA) by peroxymonosulfate with Co3O4-Bi2O3 catalyst activation: Effects of pH, inorganic anions, and water matrix," *Chemical Engineering Journal,* vol. 338, pp. 300-310, 2018/04/15/ 2018.

[195] L. Abdul, X. Si, K. Sun, and Y. Si, "Degradation of bisphenol A in aqueous environment using peroxymonosulfate activated with carbonate: Performance, possible pathway, and mechanism," *Journal of Environmental Chemical Engineering,* vol. 9, no. 4, p. 105419, 2021/08/01/ 2021.

[196] B.-M. Jun *et al.*, "Photocatalytic and electrocatalytic degradation of bisphenol A in the presence of graphene/graphene oxide-based nanocatalysts: A review," *Chemosphere,* vol. 356, p. 141941, 2024/05/01/ 2024.

[197] L. Zhang, J. Hao, Z. Jia, and C. Wang, "Visible light responding β-SiC/BiOBr S-scheme heterojunction photocatalyst with improved photodegradation efficiency of bisphenol A," *Journal of Solid State Chemistry,* vol. 325, p. 124167, 2023/09/01/ 2023.

[198] L. Chao *et al.*, "Three-dimensional ordered microporous silica supported p-lanthanum ferrite and n-ceria as heterojunction photocatalyst to activate peroxymonosulfate for bisphenol a degradation," *International Journal of Hydrogen Energy,* vol. 48, no. 41, pp. 15433-15446, 2023/05/12/ 2023.

[199] Z. Katančić *et al.*, "Solar-active photocatalysts based on TiO2 and conductive polymer PEDOT for the removal of bisphenol A," *Journal of Photochemistry and Photobiology A: Chemistry,* vol. 396, p. 112546, 2020/06/01/ 2020.

[200] J. Ma *et al.*, "Highly Efficient Degradation of Bisphenol A by Peroxymonosulfate Activation Using Bamboo Kraft Lignin Single-Atom Catalyst," *Small,* vol. 21, no. 8, p. 2409803, 2025.

[201] Y. Zeng *et al.*, "Degradation of bisphenol a using peroxymonosulfate activated by WO3@MoS2/Ag hollow nanotubes photocatalyst," *Chemosphere,* vol. 227, pp. 589-597, 2019/07/01/ 2019.

[202] R. A. Dianati, N. Mengelizadeh, M. A. Zazouli, J. Yazdani Cherati, D. Balarak, and S. Ashrafi, "Photocatalytic degradation of bisphenol A by GO-TiO2 nanocomposite under ultraviolet light: synthesis, effect of parameters and mineralisation," *International Journal of Environmental Analytical Chemistry,* vol. 104, no. 17, pp. 5065-5082, 2024/12/20 2024.

[203] A. Latif, S. Kai, and Y. Si, "Catalytic degradation of organic pollutants in Fe(III)/peroxymonosulfate (PMS) system: performance, influencing factors, and pathway," *Environmental Science and Pollution Research,* vol. 26, no. 36, pp. 36410-36422, 2019/12/01 2019.

[204] Z.-H. Diao, Q. Wei, P.-R. Guo, L.-J. Kong, and S.-Y. Pu, "Photo-assisted degradation of bisphenol A by a novel FeS2@SiO2 microspheres activated persulphate process: Synergistic effect, pathway and mechanism," *Chemical Engineering Journal,* vol. 349, pp. 683-693, 2018/10/01/ 2018.

[205] A. Hassani, P. Eghbali, F. Mahdipour, S. Wacławek, K.-Y. A. Lin, and F. Ghanbari, "Insights into the synergistic role of photocatalytic activation of peroxymonosulfate by UVA-LED irradiation over CoFe2O4-rGO nanocomposite towards effective Bisphenol A degradation: Performance, mineralization, and activation mechanism," *Chemical Engineering Journal,* vol. 453, p. 139556, 2023/02/01/ 2023.

[206] L.-M. Lyu, K.-Y. Hsiao, C.-Y. Lin, Y.-H. Tseng, Y.-C. Chang, and M.-Y. Lu, "WS2–TiO2 hetero-photocatalysts for efficient hydrogen evolution via plasmon-induced resonance energy transfer," *International Journal of Hydrogen Energy,* vol. 48, no. 76, pp. 29604-29614, 2023/09/05/ 2023.

[207] J. Jia, D. Liu, J. Tian, W. Wang, J. Ni, and X. Wang, "Visible-light-excited humic acid for peroxymonosulfate activation to degrade bisphenol A," *Chemical Engineering Journal,* vol. 400, p. 125853, 2020/11/15/ 2020.

[208] M. Zhang *et al.*, "Rational fabrication of Z-scheme heterojunction ZnFe2O4-seed@TpTt-COF for the visible-light-driven photocatalytic degradation of bisphenol A in food waste leachate boosted by primitive humic acid," *Chemical Engineering Journal,* vol. 487, p. 150684, 2024/05/01/ 2024.

[209] K. Hughes, M. Pineda, S. Omanovic, and V. Yargeau, "Study on the importance of the reductive degradation of GenX in its overall electrochemical degradation process on different cathode materials," *Science of The Total Environment,* vol. 908, p. 168415, 2024/01/15/ 2024.

[210] T. Lei, Y. Xie, X. Wang, S. Miao, J. Xiong, and C. Yan, "TiO2 Feather Duster as Effective Polysulfides Restrictor for Enhanced Electrochemical Kinetics in Lithium–Sulfur Batteries," vol. 13, no. 37, p. 1701013, 2017.

[211] M. Li, L. Wang, F. Li, and L. Xu, "Construction of Co3O4 nanopolyhedra with rich oxygen vacancies from ZIF-67 for efficient photocatalytic nitrogen fixation," *Photochemical & Photobiological Sciences,* vol. 22, no. 6, pp. 1233-1243, 2023/06/01 2023.

[212] G. Wang, Z. Jin, and T. Zhao, "Oxygen-vacancy-rich hydrated bimetallic chloride for supercapacitor cathode with remarkable enhanced performance," vol. 45, no. 2, pp. 2899-2911, 2021.

[213] X. Sun, Y. Zhu, G. An, G. Chen, and Y. Yang, "Enhancing Photocatalytic Hydrogen Evolution with Oxygen Vacancy-Modified P/Ag/Ag2O/Ag3PO4/TiO2 by Using Optimized NaBH4 Reduction Strategy," vol. 15, no. 2, p. 167, 2025.

[214] Y. Wang, M. Zhang, S. Lv, X. Li, D. Wang, and C. Song, "Photogenerated Oxygen Vacancies in Hierarchical Ag/TiO2 Nanoflowers for Enhanced Photocatalytic Reactions," *ACS Omega,* vol. 5, no. 23, pp. 13994-14005, 2020/06/16 2020.

[215] S. Rajendran and R. Vijayaraghavan, "Oxygen vacancies mediated enhanced photocatalytic activity of band gap engineered BaSn1−xCuxO3 towards methylene blue degradation under visible and sunlight," *RSC Advances,* 10.1039/D5RA02900G vol. 15, no. 30, pp. 24802-24814, 2025.

[216] Z. Mu *et al.*, "Oxygen vacancy assisted the enhancement of photocatalytic activities in ultrathin Bi7Fe2Ti2O17Cl nanosheets," *International Journal of Hydrogen Energy,* vol. 59, pp. 1156-1165, 2024/03/15/ 2024.

[217] T. Zhang *et al.*, "Performance-enhanced oxygen vacancy-rich C-TiO2 nanofiber membranes for dual photocatalytic/bactericidal water treatment," *Separation and Purification Technology,* vol. 377, p. 134169, 2025/12/19/ 2025.

[218] L. Zhang, W. Zheng, H. Jiu, W. Zhu, and G. Qi, "Preparation of the anatase/TiO2(B) TiO2 by self-assembly process and the high photodegradable performance on RhB," *Ceramics International,* vol. 42, no. 11, pp. 12726-12734, 2016/08/15/ 2016.

[219] C. Sun, Q. Xu, Y. Xie, Y. Ling, and Y. Hou, "Designed synthesis of anatase–TiO2 (B) biphase nanowire/ZnO nanoparticle heterojunction for enhanced photocatalysis," *Journal of Materials Chemistry A,* 10.1039/C7TA10274G vol. 6, no. 18, pp. 8289-8298, 2018.

[220] R. Mu, Y. Ao, T. Wu, C. Wang, and P. Wang, "Synthesis of novel ternary heterogeneous anatase-TiO2 (B) biphase nanowires/Bi4O5I2 composite photocatalysts for the highly efficient degradation of acetaminophen under visible light irradiation," *Journal of Hazardous Materials,* vol. 382, p. 121083, 2020/01/15/ 2020.

[221] D. Yang *et al.*, "An Efficient Photocatalyst Structure: TiO2(B) Nanofibers with a Shell of Anatase Nanocrystals," *Journal of the American Chemical Society,* vol. 131, no. 49, pp. 17885-17893, 2009/12/16 2009.

[222] P. Mikrut, M. Kobielusz, P. Indyka, and W. Macyk, "Photocatalytic activity of TiO2 polymorph B revisited: physical, redox, spectroscopic, and photochemical properties of TiO2(B)/anatase series of titanium dioxide materials," *Materials Today Sustainability,* vol. 10, p. 100052, 2020/12/01/ 2020.

[223] D. Nanda Gopala Krishna, R. P. George, and J. Philip, "Role of Oxygen Vacancy Formation Energy and Insulating Behavior in Darkening of White Amorphous TiO2," *The Journal of Physical Chemistry C,* vol. 125, no. 29, pp. 16136-16146, 2021/07/29 2021.

[224] L. Dai, P. Fu, J. Chen, and F. Sun, "Nitrogen doping mediated oxygen vacancy and Ti valence regulation to enhance photocatalytic H2 generation," *International Journal of Hydrogen Energy,* vol. 48, no. 67, pp. 26187-26199, 2023/08/05/ 2023.

[225] J. Cabrera, H. Alarcón, A. López, R. Candal, D. Acosta, and J. Rodriguez, "Synthesis, characterization and photocatalytic activity of 1D TiO2 nanostructures," *Water Science and Technology,* vol. 70, no. 6, pp. 972-979, 2014.

[226] N. T. Nguyen, S. Ozkan, I. Hwang, A. Mazare, and P. Schmuki, "TiO2 nanotubes with laterally spaced ordering enable optimized hierarchical structures with significantly enhanced photocatalytic H2 generation," *Nanoscale,* 10.1039/C6NR06329B vol. 8, no. 38, pp. 16868-16873, 2016.

[227] S. Sassi, A. Bouich, B. Bessais, L. Khezami, B. M. Soucase, and A. Hajjaji, "Comparative Analysis of Anodized TiO2 Nanotubes and Hydrothermally Synthesized TiO2 Nanotubes: Morphological, Structural, and Photoelectrochemical Properties," vol. 17, no. 21, p. 5182, 2024.

[228] Z.-R. Tang, Y. Zhang, and Y.-J. Xu, "Tuning the Optical Property and Photocatalytic Performance of Titanate Nanotube toward Selective Oxidation of Alcohols under Ambient Conditions," *ACS Applied Materials & Interfaces,* vol. 4, no. 3, pp. 1512-1520, 2012/03/28 2012.

[229] L. Rekeb, L. Hamadou, A. Kadri, N. Benbrahim, and E. Chainet, "Highly broadband plasmonic Cu film modified Cu2O/TiO2 nanotube arrays for efficient photocatalytic performance," *International Journal of Hydrogen Energy,* vol. 44, no. 21, pp. 10541-10553, 2019/04/23/ 2019.

[230] M. Wtulich, M. Szkoda, G. Gajowiec, K. Jurak, G. Trykowski, and A. Lisowska-Oleksiak, "Hydrothermal modification of TiO2 nanotubes in water and alkali metal electrolytes (LiNO3, NaNO3, KNO3) – Direct evidence for photocatalytic activity enhancement," *Electrochimica Acta,* vol. 426, p. 140802, 2022/09/10/ 2022.

[231] A. Hajjaji *et al.*, "Enhancement of photocatalytic and photoelectrochemical properties of TiO2 nanotubes sensitized by SILAR - Deposited PbS nanoparticles," *Journal of Materiomics,* vol. 6, no. 1, pp. 62-69, 2020/03/01/ 2020.

[232] P. Wang, F. Dong, D. He, S. Liu, N. Chen, and T. Huo, "Organic acid mediated photoelectrochemical reduction of U(vi) to U(iv) in waste water: electrochemical parameters and spectroscopy," *RSC Advances,* 10.1039/D1RA02505H vol. 11, no. 38, pp. 23241-23248, 2021.

[233] B.-j. Yang *et al.*, "Photogenerated-hole scavenger for enhancing photocatalytic chalcopyrite bioleaching," *Transactions of Nonferrous Metals Society of China,* vol. 30, no. 1, pp. 200-211, 2020/01/01/ 2020.

[234] D.-D. Chen, X.-H. Yi, L. Ling, C.-C. Wang, and P. Wang, "Photocatalytic Cr(VI) sequestration and photo-Fenton bisphenol A decomposition over white light responsive PANI/MIL-88A(Fe)," vol. 34, no. 9, p. e5795, 2020.

[235] C. Wang *et al.*, "A novel iron sulfide phase with remarkable hydroxyl radical generation capability for contaminants degradation," *Water Research,* vol. 251, p. 121166, 2024/03/01/ 2024.

[236] J. Saha and S. Kumar Gupta, "The production and quantification of hydroxyl radicals at economically feasible tin-chloride modified graphite electrodes," *Journal of Environmental Chemical Engineering,* vol. 6, no. 4, pp. 3991-3998, 2018/08/01/ 2018.

[237] V. Repousi *et al.*, "Photocatalytic degradation of bisphenol A over Rh/TiO2 suspensions in different water matrices," *Catalysis Today,* vol. 284, pp. 59-66, 2017/04/15/ 2017.

[238] R. Xiao *et al.*, "The overlooked carbonate radical in micropollutant degradation: An insight into hydration interaction," *Chemical Engineering Journal,* vol. 474, p. 145245, 2023/10/15/ 2023.

[239] Z. Hu, H. Du, W.-L. Man, C.-F. Leung, H. Liang, and T.-C. Lau, "Catalytic reactions of chlorite with a polypyridylruthenium(ii) complex: disproportionation, chlorine dioxide formation and alcohol oxidation," *Chemical Communications,* 10.1039/C1CC15860K vol. 48, no. 8, pp. 1102-1104, 2012.

[240] J. Ma, F. Wang, and M. Mostafavi, "Ultrafast Chemistry of Water Radical Cation, H2O•+, in Aqueous Solutions," vol. 23, no. 2, p. 244, 2018.

[241] Y. Abdelkrim *et al.*, "Cobalt germanium hydroxides with asymmetric electron distribution and surface hydroxyl groups for superb catalytic degradation performances," *Journal of Colloid and Interface Science,* vol. 677, pp. 282-293, 2025/01/01/ 2025.

[242] B. Rabeie and N. M. Mahmoodi, "Heterogeneous MIL-88A on MIL-88B hybrid: A promising eco-friendly hybrid from green synthesis to dual application (Adsorption and photocatalysis) in tetracycline and dyes removal," *Journal of Colloid and Interface Science,* vol. 654, pp. 495-522, 2024/01/15/ 2024.

[243] H.-i. Kim *et al.*, "Anodic TiO2 nanotube layer directly formed on the inner surface of Ti pipe for a tubular photocatalytic reactor," *Applied Catalysis A: General,* vol. 521, pp. 174-181, 2016/07/05/ 2016.

[244] A. Miyawaki, S. Taira, and F. Shiraishi, "Performance of continuous stirred-tank reactors connected in series as a photocatalytic reactor system," *Chemical Engineering Journal,* vol. 286, pp. 594-601, 2016/02/15/ 2016.

[245] U. Bellè *et al.*, "A novel nanotubular TiO2-based Plug-Flow reactor for gas phase photocatalytic degradation of toluene," *Chemical Engineering Journal,* vol. 437, p. 135323, 2022/06/01/ 2022.

[246] E. Falletta, M. Longhi, A. Di Michele, D. C. Boffito, and C. L. Bianchi, "Floatable graphitic carbon nitride/alginate beads for the photodegradation of organic pollutants under solar light irradiation," *Journal of Cleaner Production,* vol. 371, p. 133641, 2022/10/15/ 2022.

[247] M. G. Galloni *et al.*, "Novel eco-friendly and easily recoverable bismuth-based materials for capturing and removing polyphenols from water," *Journal of Environmental Management,* vol. 369, p. 122365, 2024/10/01/ 2024.

[248] M. Larrieu, G. Agusti, K. Rekab, D. Blaha, and D. Edouard, "Photoreactor based on original catalytic foam-filter for wastewater treatment," *Chemical Engineering Journal,* vol. 500, p. 157166, 2024/11/15/ 2024.

[249] D. Chi *et al.*, "Bifunctional nest-like self-floating microreactor for enhanced photothermal catalysis and biocatalysis," *Environmental Science: Nano,* 10.1039/C9EN00968J vol. 6, no. 12, pp. 3551-3559, 2019.

[250] M. Rico-Santacruz *et al.*, "Coating-free TiO2@β-SiC alveolar foams as a ready-to-use composite photocatalyst with tunable adsorption properties for water treatment," *RSC Advances,* 10.1039/C9RA09553E vol. 10, no. 7, pp. 3817-3825, 2020.

[251] T. Yildiz, H. C. Yatmaz, and K. Öztürk, "Anatase TiO2 powder immobilized on reticulated Al2O3 ceramics as a photocatalyst for degradation of RO16 azo dye," *Ceramics International,* vol. 46, no. 7, pp. 8651-8657, 2020/05/01/ 2020.

[252] A. M. Pedroza, R. Mosqueda, N. Alonso-Vante, and R. Rodríguez-Vázquez, "Sequential treatment via Trametes versicolor and UV/TiO2/RuxSey to reduce contaminants in waste water resulting from the bleaching process during paper production," *Chemosphere,* vol. 67, no. 4, pp. 793-801, 2007/03/01/ 2007.

[253] D. S. Pattanayak, J. Mishra, J. Nanda, P. K. Sahoo, R. Kumar, and N. K. Sahoo, "Photocatalytic degradation of cyanide using polyurethane foam immobilized Fe-TCPP-S-TiO2-rGO nano-composite," *Journal of Environmental Management,* vol. 297, p. 113312, 2021/11/01/ 2021.

[254] L. G. Devi and R. Kavitha, "Enhanced photocatalytic activity of sulfur doped TiO2 for the decomposition of phenol: A new insight into the bulk and surface modification," *Materials Chemistry and Physics,* vol. 143, no. 3, pp. 1300-1308, 2014/02/14/ 2014.

[255] S. A. Bakar and C. Ribeiro, "A comparative run for visible-light-driven photocatalytic activity of anionic and cationic S-doped TiO2 photocatalysts: A case study of possible sulfur doping through chemical protocol," *Journal of Molecular Catalysis A: Chemical,* vol. 421, pp. 1-15, 2016/09/01/ 2016.

[256] T. Kasuga, M. Hiramatsu, A. Hoson, T. Sekino, and K. Niihara, "Formation of Titanium Oxide Nanotube," *Langmuir,* vol. 14, no. 12, pp. 3160-3163, 1998/06/01 1998.

[257] Y. Cheng, L. He, G. Xia, C. Ren, and Z. Wang, "Nanostructured g-C3N4/AgI composites assembled by AgI nanoparticles-decorated g-C3N4 nanosheets for effective and mild photooxidation reaction," *New Journal of Chemistry,* 10.1039/C9NJ02725D vol. 43, no. 37, pp. 14841-14852, 2019.

[258] F. Zhang, S. Chen, Y. Yin, C. Lin, and C. Xue, "Anodic formation of ordered and bamboo-type TiO2 anotubes arrays with different electrolytes," *Journal of Alloys and Compounds,* vol. 490, no. 1, pp. 247-252, 2010/02/04/ 2010.

[259] R. Li *et al.*, "Preparation of Gd-Doped TiO2 Nanotube Arrays by Anodization Method and Its Photocatalytic Activity for Methyl Orange Degradation," vol. 10, no. 3, p. 298, 2020.

[260] T. Li, A. Abdelhaleem, W. Chu, S. Pu, F. Qi, and J. Zou, "S-doped TiO2 photocatalyst for visible LED mediated oxone activation: Kinetics and mechanism study for the photocatalytic degradation of pyrimethanil fungicide," *Chemical Engineering Journal,* vol. 411, p. 128450, 2021/05/01/ 2021.

[261] E. Zhang, Y. Pan, T. Lu, Y. a. Zhu, and W. Dai, "Novel synthesis of S-doped anatase TiO2 via hydrothermal reaction of Cu–Ti amorphous alloy," *Applied Physics A,* vol. 126, no. 8, p. 606, 2020/07/12 2020.

[262] N. Jiménez-Arévalo *et al.*, "Protecting TiS3 Photoanodes for Water Splitting in Alkaline Media by TiO2 Coatings," *ACS Applied Materials & Interfaces,* vol. 16, no. 26, pp. 33696-33709, 2024/07/03 2024.

[263] C. Yang, S. Shang, and X.-y. Li, "Fabrication of sulfur-doped TiO2 nanotube array as a conductive interlayer of PbO2 anode for efficient electrochemical oxidation of organic pollutants," *Separation and Purification Technology,* vol. 258, p. 118035, 2021/03/01/ 2021.

[264] C. McManamon, J. O'Connell, P. Delaney, S. Rasappa, J. D. Holmes, and M. A. Morris, "A facile route to synthesis of S-doped TiO2 nanoparticles for photocatalytic activity," *Journal of Molecular Catalysis A: Chemical,* vol. 406, pp. 51-57, 2015/09/01/ 2015.

[265] S. Arunmetha, N. R. Dhineshbabu, A. Kumar, and R. Jayavel, "Preparation of sulfur doped TiO2 nanoparticles from rutile sand and their performance testing in hybrid solar cells," *Journal of Materials Science: Materials in Electronics,* vol. 32, no. 24, pp. 28382-28393, 2021/12/01 2021.

[266] N. Li *et al.*, "High quality sulfur-doped titanium dioxide nanocatalysts with visible light photocatalytic activity from non-hydrolytic thermolysis synthesis," *Inorganic Chemistry Frontiers,* 10.1039/C4QI00027G vol. 1, no. 7, pp. 521-525, 2014.

[267] G. Yan, M. Zhang, J. Hou, and J. Yang, "Photoelectrochemical and photocatalytic properties of N+S co-doped TiO2 nanotube array films under visible light irradiation," *Materials Chemistry and Physics,* vol. 129, no. 1, pp. 553-557, 2011/09/15/ 2011.

[268] S. Das, C. Agarkoti, and P. R. Gogate, "A novel method for the remediation of wastewater containing acid red 131 dye using acoustic cavitation combined with sulphur-doped TiO2 and oxidants," *Environmental Monitoring and Assessment,* vol. 195, no. 8, p. 972, 2023/07/20 2023.

[269] M. M. Momeni, M. Akbarnia, M. Atapour, and M. Khalaghi, "Preparation of chromium and sulfur single and co-doped TiO2 nanostructures for efficient photoelectrochemical water splitting: effect of aliphatic alcohols on their activity," *Journal of Solid State Electrochemistry,* vol. 26, no. 1, pp. 281-291, 2022/01/01 2022.

[270] V. V. Pillai, S. P. Lonkar, and S. M. Alhassan, "Template-Free, Solid-State Synthesis of Hierarchically Macroporous S-Doped TiO2 Nano-Photocatalysts for Efficient Water Remediation," *ACS Omega,* vol. 5, no. 14, pp. 7969-7978, 2020/04/14 2020.

[271] S. Cravanzola, F. Cesano, F. Gaziano, and D. Scarano, "Sulfur-Doped TiO2: Structure and Surface Properties," vol. 7, no. 7, p. 214, 2017.

[272] J. Wang, G. Wang, B. Cheng, J. Yu, and J. Fan, "Sulfur-doped g-C3N4/TiO2 S-scheme heterojunction photocatalyst for Congo Red photodegradation," *Chinese Journal of Catalysis,* vol. 42, no. 1, pp. 56-68, 2021/01/01/ 2021.

[273] Y.-Q. Li, S.-Y. Fu, G. Yang, and M. Li, "Preparation and characterization of a novel solid titania precursor," *Journal of Non-Crystalline Solids,* vol. 352, no. 30, pp. 3339-3342, 2006/09/01/ 2006.

[274] V. Kale, C. Chavan, C. Bhongale, K. G. Girija, and S. N. Kale, "Resonance-based detection of perilous sulphur dioxide using TiO2 nanoparticles and unit-cell ring resonator," *Sensors and Actuators A: Physical,* vol. 331, p. 112898, 2021/11/01/ 2021.

[275] A. Bansal *et al.*, "Visible light-induced surface initiated atom transfer radical polymerization of methyl methacrylate on titania/reduced graphene oxide nanocomposite," *RSC Advances,* 10.1039/C4RA15615C vol. 5, no. 27, pp. 21189-21196, 2015.

[276] B. Anitha *et al.*, "Self assembled sulfur induced interconnected nanostructure TiO2 electrode for visible light photoresponse and photocatalytic application," *Physica E: Low-dimensional Systems and Nanostructures,* vol. 91, pp. 148-160, 2017/07/01/ 2017.

[277] S. Abu Bakar and C. Ribeiro, "An insight toward the photocatalytic activity of S doped 1-D TiO2 nanorods prepared via novel route: As promising platform for environmental leap," *Journal of Molecular Catalysis A: Chemical,* vol. 412, pp. 78-92, 2016/02/01/ 2016.

[278] P. G. Chavan, S. V. Shende, D. S. Joag, and M. A. More, "Photo-enhanced field emission study of TiO2 nanotubes array," *Ultramicroscopy,* vol. 111, no. 6, pp. 415-420, 2011/05/01/ 2011.

[279] D. Bala *et al.*, "Luminescence, Paramagnetic, and Electrochemical Properties of Copper Oxides-Decorated TiO2/Graphene Oxide Nanocomposites," vol. 23, no. 23, p. 14703, 2022.

[280] D. John, A. S. Rajalakshmi, R. M. Lopez, and V. S. Achari, "TiO2-reduced graphene oxide nanocomposites for the trace removal of diclofenac," *SN Applied Sciences,* vol. 2, no. 5, p. 840, 2020/04/07 2020.

[281] H. Wang *et al.*, "Nitrogen-doped TiO2 nanoparticles better TiO2 nanotube array photo-anodes for dye sensitized solar cells," *Electrochimica Acta,* vol. 137, pp. 744-750, 2014/08/10/ 2014.

[282] D. Cao *et al.*, "Rational Design of Monolithic g-C3N4 with Floating Network Porous-like Sponge Monolithic Structure for Boosting Photocatalytic Degradation of Tetracycline under Simulated and Natural Sunlight Illumination," vol. 28, no. 10, p. 3989, 2023.

[283] G. Fan *et al.*, "Recyclable self-floating A-GUN-coated foam as effective visible-light-driven photocatalyst for inactivation of Microcystis aeruginosa," *Journal of Hazardous Materials,* vol. 419, p. 126407, 2021/10/05/ 2021.

[284] M. A. Al-Nuaim, A. A. Alwasiti, and Z. Y. Shnain, "The photocatalytic process in the treatment of polluted water," *Chemical Papers,* vol. 77, no. 2, pp. 677-701, 2023/02/01 2023.

[285] M. F. Hanafi and N. Sapawe, "Effect of initial concentration on the photocatalytic degradation of remazol brilliant blue dye using nickel catalyst," *Materials Today: Proceedings,* vol. 31, pp. 318-320, 2020/01/01/ 2020.

[286] C. Oussalah, F. Kaouah, S. Boumaza, and M. Trari, "Highly efficient removal of the bisphenol A from aqueous solution by activated carbon derived from cores of nuts of Sapindus mukorossi," *Biomass Conversion and Biorefinery,* vol. 14, no. 16, pp. 18869-18885, 2024/08/01 2024.

[287] L. Yang *et al.*, "Ultrasonication-Assisted Synthesis of ZnxCd1−xS for Enhanced Visible-Light Photocatalytic Activity," vol. 10, no. 3, p. 276, 2020.

[288] P. Kumar, E. Vahidzadeh, K. M. Alam, D. Laishram, K. Cui, and K. Shankar, "Radial Nano-Heterojunctions Consisting of CdS Nanorods Wrapped by 2D CN:PDI Polymer with Deep HOMO for Photo-Oxidative Water Splitting, Dye Degradation and Alcohol Oxidation," vol. 13, no. 9, p. 1481, 2023.

[289] C. Yang *et al.*, "Roles of photo-generated holes and oxygen vacancies in enhancing photocatalytic performance over CeO2 prepared by molten salt method," *Advanced Powder Technology,* vol. 31, no. 9, pp. 4072-4081, 2020/09/01/ 2020.

[290] L. Li, J. Cai, Y. Yan, F. Zhao, and J. Zhou, "Flower-like direct Z-scheme WS2/Bi2O2CO3 photocatalyst with enhanced photocatalytic activity," *Journal of Alloys and Compounds,* vol. 810, p. 151872, 2019/11/25/ 2019.

[291] H. Wang *et al.*, "Preparing a photocatalytic Fe doped TiO2/rGO for enhanced bisphenol A and its analogues degradation in water sample," *Applied Surface Science,* vol. 505, p. 144640, 2020/03/01/ 2020.

[292] B. Liu, C. Bie, Y. Zhang, L. Wang, Y. Li, and J. Yu, "Hierarchically Porous ZnO/g-C3N4 S-Scheme Heterojunction Photocatalyst for Efficient H2O2 Production," *Langmuir,* vol. 37, no. 48, pp. 14114-14124, 2021/12/07 2021.

[293] N. Watanabe, S. Horikoshi, H. Kawabe, Y. Sugie, J. Zhao, and H. Hidaka, "Photodegradation mechanism for bisphenol A at the TiO2/H2O interfaces," *Chemosphere,* vol. 52, no. 5, pp. 851-859, 2003/08/01/ 2003.

[294] C. Awungacha Lekelefac, N. Busse, M. Herrenbauer, and P. Czermak, "Photocatalytic Based Degradation Processes of Lignin Derivatives," vol. 2015, no. 1, p. 137634, 2015.

[295] J. Wang, B. Li, S. Xie, and B. Ji, "Degradation of Bisphenol A Using Self-Excited Oscillating Jets in Synergy with Fenton and Periodate Oxidation: Experimental and Artificial Neural Network Modeling Study," vol. 16, no. 16, p. 2326, 2024.

[296] V. Muelas-Ramos, M. Peñas-Garzón, J. J. Rodriguez, J. Bedia, and C. Belver, "Solar photocatalytic degradation of emerging contaminants using NH2-MIL-125 grafted by heterocycles," *Separation and Purification Technology,* vol. 297, p. 121442, 2022/09/15/ 2022.

[297] Y. Wu, Z. Liu, Y. Li, J. Chen, X. Zhu, and P. Na, "Construction of 2D-2D TiO2 nanosheet/layered WS2 heterojunctions with enhanced visible-light-responsive photocatalytic activity," *Chinese Journal of Catalysis,* vol. 40, no. 1, pp. 60-69, 2019/01/01/ 2019.

[298] N. Abd Rahman *et al.*, "Recent advances in the TiO2 based photoreactors for removing contaminants of emerging concern in water," *Separation and Purification Technology,* vol. 304, p. 122294, 2023/01/01/ 2023.

[299] V. Muelas-Ramos, C. Belver, J. J. Rodriguez, and J. Bedia, "Synthesis of noble metal-decorated NH2-MIL-125 titanium MOF for the photocatalytic degradation of acetaminophen under solar irradiation," *Separation and Purification Technology,* vol. 272, p. 118896, 2021/10/01/ 2021.

[300] P. C. Hernández-Del Castillo, J. Oliva, B. P. Núñez-Luna, and V. Rodríguez-González, "Novel polypropylene-TiO2:Bi spherical floater for the efficient photocatalytic degradation of the recalcitrant 2,4,6-TCP herbicide," *Journal of Environmental Management,* vol. 329, p. 117057, 2023/03/01/ 2023.

[301] B. Yaou Balarabe and P. Maity, "A polymer-Au/TiO2 nano-composite based floating catalyst for photocatalytic dye degradation under natural sunlight," *Journal of Photochemistry and Photobiology A: Chemistry,* vol. 449, p. 115405, 2024/04/01/ 2024.

[302] S. Singh, P. K. Singh, and H. Mahalingam, "Novel Floating Ag+-Doped TiO2/Polystyrene Photocatalysts for the Treatment of Dye Wastewater," *Industrial & Engineering Chemistry Research,* vol. 53, no. 42, pp. 16332-16340, 2014/10/22 2014.

[303] M. Piispanen and L. Hupa, "Comparison of self-cleaning properties of three titania coatings on float glass," *Applied Surface Science,* vol. 258, no. 3, pp. 1126-1131, 2011/11/15/ 2011.

[304] N. Davari *et al.*, "Enhanced photo-induced charge generation of floating sulfur-doped TiO2 double-walled nanotubes for efficient sunlight-driven photocatalytic degradation of bisphenol A," *Ceramics International,* 2025/09/06/ 2025.

[305] S. Varnagiris, M. Urbonavicius, S. Sakalauskaite, E. Demikyte, S. Tuckute, and M. Lelis, "Photocatalytic Inactivation of Salmonella typhimurium by Floating Carbon-Doped TiO2 Photocatalyst," vol. 14, no. 19, p. 5681, 2021.

[306] H. Xue *et al.*, "Floating photocatalyst of B–N–TiO2/expanded perlite: a sol–gel synthesis with optimized mesoporous and high photocatalytic activity," *Scientific Reports,* vol. 6, no. 1, p. 29902, 2016/07/19 2016.

[307] N. H. Mohamad Idris, K. Y. Cheong, S. M. Smith, and H. L. Lee, "C,N-Codoped TiO2 Nanoparticles Immobilized on Floating Alginate Beads for Diazinon Removal under Solar Light Irradiation," *ACS Applied Nano Materials,* vol. 7, no. 16, pp. 18273-18286, 2024/08/23 2024.

[308] X. Yang *et al.*, "Hierarchical porous N-TiO2/carbon foam composite for enhancement of photodegradation activity under simulated sunlight," *Diamond and Related Materials,* vol. 128, p. 109234, 2022/10/01/ 2022.

[309] M. Sboui *et al.*, "TiO2/Ag2O immobilized on cellulose paper: A new floating system for enhanced photocatalytic and antibacterial activities," *Environmental Research,* vol. 198, p. 111257, 2021/07/01/ 2021.

[310] M. Sboui, M. F. Nsib, A. Rayes, M. Swaminathan, and A. Houas, "TiO2–PANI/Cork composite: A new floating photocatalyst for the treatment of organic pollutants under sunlight irradiation," *Journal of Environmental Sciences,* vol. 60, pp. 3-13, 2017/10/01/ 2017.

[311] S. N. Kulkarni, R. Ragesh Nath, K. Alkanad, A. Amasegowda, S.-C. Ke, and N. K. Lokanath, "Recent trends in TiO2 focused S-scheme heterojunctions for photocatalytic innovations: A comprehensive analysis," *Journal of Alloys and Compounds,* vol. 1016, p. 178876, 2025/02/15/ 2025.

[312] W. Wang, S. Mei, H. Jiang, L. Wang, H. Tang, and Q. Liu, "Recent advances in TiO2-based S-scheme heterojunction photocatalysts," *Chinese Journal of Catalysis,* vol. 55, pp. 137-158, 2023/12/01/ 2023.

[313] D. Aswal *et al.*, "Enhanced Photocatalytic Activity in 2D-1D WS2/TiO2 and 2D-2D MoS2/WS2 Heterosystems," vol. 8, no. 34, p. e202204998, 2023.

[314] F. He *et al.*, "Persistent Luminescent Nanoparticle-Coated Metal–Organic Frameworks for Round-the-Clock Photocatalytic Degradation of Pollutants," *ACS Applied Nano Materials,* vol. 6, no. 14, pp. 12871-12881, 2023/07/28 2023.

[315] E.-C. Cho *et al.*, "Microwave-assisted synthesis of TiO2/WS2 heterojunctions with enhanced photocatalytic activity," *Journal of the Taiwan Institute of Chemical Engineers,* vol. 91, pp. 489-498, 2018/10/01/ 2018.

[316] S. Dangwal *et al.*, "Interfacial Engineering of Z-Scheme-Based 2D/1D -WS2/TiO2 Heterostructures: Enhanced Hydrogen Evolution Reaction and Fabrication of Facile Photoelectrochemical Device," *ACS Applied Energy Materials,* vol. 8, no. 9, pp. 5911-5924, 2025/05/12 2025.

[317] N. J. Ismail *et al.*, "Improved visible light-responsive bisphenol A photodegradation utilizing TiO2/WS2 photocatalytic membranes with energy storage ability," *Journal of Materials Science,* vol. 59, no. 27, pp. 12361-12383, 2024/07/01 2024.

[318] R. Jha and P. K. Guha, "An effective liquid-phase exfoliation approach to fabricate tungsten disulfide into ultrathin two-dimensional semiconducting nanosheets," *Journal of Materials Science,* vol. 52, no. 12, pp. 7256-7268, 2017/06/01 2017.

[319] Z. A. Thiehmed and T. M. Altahtamouni, "Morphology Control of WS2 Nanoflakes Using Chemical Vapor Deposition for Improving the Photocatalytic Activity of the WS2/TiO2 Heterostructure," *The Journal of Physical Chemistry C,* vol. 127, no. 24, pp. 11600-11608, 2023/06/22 2023.

[320] C. Yang, J. Qin, S. Rajendran, X. Zhang, and R. Liu, "WS2 and C-TiO2 Nanorods Acting as Effective Charge Separators on g-C3N4 to Boost Visible-Light Activated Hydrogen Production from Seawater," vol. 11, no. 23, pp. 4077-4085, 2018.

[321] T. S. Hui and M. A. A. Zaini, "Textile sludge–sawdust chemically produced activated carbon: equilibrium and dynamics studies of malachite green adsorption," *Biomass Conversion and Biorefinery,* vol. 12, no. 7, pp. 2847-2859, 2022/07/01 2022.

[322] T. Cai *et al.*, "“Dark Deposition” of Ag Nanoparticles on TiO2: Improvement of Electron Storage Capacity To Boost “Memory Catalysis” Activity," *ACS Applied Materials & Interfaces,* vol. 10, no. 30, pp. 25350-25359, 2018/08/01 2018.

[323] X. Fu, Y. Kong, M. Wang, T. Cai, and Q. Zeng, "MXene derived Ti3C2/TiO2/Ag persistent photocatalyst with enhanced electron storage capacity for round-the-clock degradation of organic pollutant," *Journal of Colloid and Interface Science,* vol. 656, pp. 233-240, 2024/02/15/ 2024.

[324] Y. Wu, Z. Liu, Y. Li, J. Chen, X. Zhu, and P. Na, "WS2 nanodots-modified TiO2 nanotubes to enhance visible-light photocatalytic activity," *Materials Letters,* vol. 240, pp. 47-50, 2019/04/01/ 2019.

[325] L. Chen, Y. Chuang, C.-W. Chen, and C.-D. Dong, "Outstanding photocatalytic activity of WS2/TiO2 quantum dots for ciprofloxacin removal," *Optical Materials,* vol. 131, p. 112654, 2022/09/01/ 2022.

[326] S. Dangwal *et al.*, "Direct Z-scheme based WS2/TiO2 heterostructures for hydrogen evolution reactions," *International Journal of Hydrogen Energy,* vol. 137, pp. 1148-1160, 2025/06/12/ 2025.

[327] X. Ren *et al.*, "Investigating the photocurrent generation and optoelectronic responsivity of WS2-TiO2 heterostructure," *Optics Communications,* vol. 406, pp. 118-123, 2018/01/01/ 2018.

[328] S. An *et al.*, "Oxidative degradation of bisphenol A by Bio-Fenton reaction equipped with glucose oxidase and ferric citrate: Degradation kinetics and pathway," *Journal of Environmental Chemical Engineering,* vol. 11, no. 2, p. 109349, 2023/04/01/ 2023.

[329] X. He, X. Yang, C. Zhang, Y. Xiao, and Y. Tang, "Catalytic degradation of bisphenol A by heterogeneous bimetal composite carbon in the PMS and H2O2 systems: Performance and mechanism," *Journal of Cleaner Production,* vol. 414, p. 137571, 2023/08/15/ 2023.

[330] T. Tatsuma, S. Saitoh, P. Ngaotrakanwiwat, Y. Ohko, and A. Fujishima, "Energy Storage of TiO2−WO3 Photocatalysis Systems in the Gas Phase," *Langmuir,* vol. 18, no. 21, pp. 7777-7779, 2002/10/01 2002.

[331] C. Ng, Y. H. Ng, A. Iwase, and R. Amal, "Visible light-induced charge storage, on-demand release and self-photorechargeability of WO3 film," *Physical Chemistry Chemical Physics,* 10.1039/C1CP20412B vol. 13, no. 29, pp. 13421-13426, 2011.

[332] H. B. Truong *et al.*, "Tungsten-based nanocatalysts with different structures for visible light responsive photocatalytic degradation of bisphenol A," *Journal of Environmental Sciences,* vol. 139, pp. 569-588, 2024/05/01/ 2024.

[333] N. Gilani, J. Vahabzadeh Pasikhani, M. Akbari, and P. Tafazoli Motie, "Hydrogen evolution from catalytic hydrolysis of NaBH4: Comparative study between the catalytic activity of TiO2 nanotubes with various arrangements %J Journal of Nanostructures," vol. 9, no. 3, pp. 587-599, 2019.

[334] F. D. Ali, S. H. Ammar, N. D. Ali, Y. R. Abdulmajeed, and Z. H. Jabbar, "Synthesis of AgCl/ZIF-8/C–TiO2 heterojunction photocatalysts for enhanced degradation of levofloxacin under visible-light," *Materials Science in Semiconductor Processing,* vol. 172, p. 108100, 2024/03/15/ 2024.

[335] M. Hajiali, M. Farhadian, S. Aflaki, and N. Davari, "Application of TiO2/ZnFe2O4/glycine nanocatalyst to the treatment of methyl orange dye from aqueous solution: Impacts of dissolved mineral salts on dye removal efficiency %J Scientia Iranica," *Scientia Iranica,* vol. 28, no. 3, pp. 1464-1477, 2021.

[336] Q. Zhang, D. Thrithamarassery Gangadharan, Y. Liu, Z. Xu, M. Chaker, and D. Ma, "Recent advancements in plasmon-enhanced visible light-driven water splitting," *Journal of Materiomics,* vol. 3, no. 1, pp. 33-50, 2017/03/01/ 2017.

[337] Q. Zhang, J. Deng, Z. Xu, M. Chaker, and D. Ma, "High-Efficiency Broadband C3N4 Photocatalysts: Synergistic Effects from Upconversion and Plasmons," *ACS Catalysis,* vol. 7, no. 9, pp. 6225-6234, 2017/09/01 2017.

[338] J. Jia, S. Giannakis, D. Li, B. Yan, and T. Lin, "Efficient and sustainable photocatalytic inactivation of E. coli by an innovative immobilized Ag/TiO2 photocatalyst with peroxymonosulfate (PMS) under visible light," *Science of The Total Environment,* vol. 901, p. 166376, 2023/11/25/ 2023.

[339] M. Rehan and E. Elhaddad, "An efficient multi-functional ternary reusable nanocomposite based on chitosan@TiO2@Ag NP immobilized on cellulosic fiber as a support substrate for wastewater treatment," *Environmental Pollution,* vol. 340, p. 122850, 2024/01/01/ 2024.

[340] T. Z. Liza, M. M. H. Tusher, F. Anwar, M. F. Monika, K. F. Amin, and F. N. U. Asrafuzzaman, "Effect of Ag-doping on morphology, structure, band gap and photocatalytic activity of bio-mediated TiO2 nanoparticles," *Results in Materials,* vol. 22, p. 100559, 2024/06/01/ 2024.

[341] Z. Mohammadi, S. Sharifnia, and Y. Shavisi, "Photocatalytic degradation of aqueous ammonia by using TiO2ZnO/LECA hybrid photocatalyst," *Materials Chemistry and Physics,* vol. 184, pp. 110-117, 2016/12/01/ 2016.

[342] N. H. Mohamad Idris *et al.*, "Titanium Dioxide/Polyvinyl Alcohol/Cork Nanocomposite: A Floating Photocatalyst for the Degradation of Methylene Blue under Irradiation of a Visible Light Source," *ACS Omega,* vol. 6, no. 22, pp. 14493-14503, 2021/06/08 2021.

[343] M. Stucchi *et al.*, "Ultrasound assisted synthesis of Ag-decorated TiO2 active in visible light," *Ultrasonics Sonochemistry,* vol. 40, pp. 282-288, 2018/01/01/ 2018.

[344] M. Stucchi, A. Elfiad, M. Rigamonti, H. Khan, and D. C. Boffito, "Water treatment: Mn-TiO2 synthesized by ultrasound with increased aromatics adsorption," *Ultrasonics Sonochemistry,* vol. 44, pp. 272-279, 2018/06/01/ 2018.

[345] J. S. Jeyaprakash, M. Rajamani, P. Mani, C. Yazhini, S. H. Sonawane, and B. Neppolian, "Highly Efficient Ultrasound-Driven Ti3+-Doped TiO2 with Oxygen Vacancies: A Promising Visible-Light Catalyst for Complete Sonophotocatalytic Degradation of Tetracycline," *Industrial & Engineering Chemistry Research,* vol. 63, no. 12, pp. 5135-5147, 2024/03/27 2024.

[346] X. Xiong *et al.*, "Complete defluorination of perfluorooctanoic acid (PFOA) by ultrasonic pyrolysis towards zero fluoro-pollution," *Water Research,* vol. 235, p. 119829, 2023/05/15/ 2023.

[347] W. L. Ang, P. J. McHugh, and M. D. Symes, "Sonoelectrochemical processes for the degradation of persistent organic pollutants," *Chemical Engineering Journal,* vol. 444, p. 136573, 2022/09/15/ 2022.

[348] S. Manickam *et al.*, "Ultrasonics and sonochemistry: Editors' perspective," *Ultrasonics Sonochemistry,* vol. 99, p. 106540, 2023/10/01/ 2023.

[349] V. K. Landge, S. H. Sonawane, S. Manickam, G. U. Bhaskar Babu, and G. Boczkaj, "Ultrasound-assisted wet-impregnation of Ag–Co nanoparticles on cellulose nanofibers: Enhanced catalytic hydrogenation of 4-nitrophenol," *Journal of Environmental Chemical Engineering,* vol. 9, no. 4, p. 105719, 2021/08/01/ 2021.

[350] H. Khan, M. G. Rigamonti, G. S. Patience, and D. C. Boffito, "Spray dried TiO2/WO3 heterostructure for photocatalytic applications with residual activity in the dark," *Applied Catalysis B: Environmental,* vol. 226, pp. 311-323, 2018/06/15/ 2018.

[351] H. Khan, M. G. Rigamonti, and D. C. Boffito, "Enhanced photocatalytic activity of Pt-TiO2/WO3 hybrid material with energy storage ability," *Applied Catalysis B: Environmental,* vol. 252, pp. 77-85, 2019/09/05/ 2019.

[352] D. Meroni, R. Djellabi, M. Ashokkumar, C. L. Bianchi, and D. C. Boffito, "Sonoprocessing: From Concepts to Large-Scale Reactors," *Chemical Reviews,* vol. 122, no. 3, pp. 3219-3258, 2022/02/09 2022.

[353] M. Mokhtarifar, R. Kaveh, M. Bagherzadeh, A. Lucotti, M. Pedeferri, and M. V. Diamanti, "Heterostructured TiO2/SiO2/γ-Fe2O3/rGO Coating with Highly Efficient Visible-Light-Induced Self-Cleaning Properties for Metallic Artifacts," *ACS Applied Materials & Interfaces,* vol. 12, no. 26, pp. 29671-29683, 2020/07/01 2020.

[354] M. V. Roldán, E. Porta, A. Durán, Y. Castro, and N. Pellegri, "Development of photocatalysts based on TiO2 films with embedded Ag nanoparticles," vol. 13, no. 3, pp. 429-443, 2022.

[355] R. K. Polagani, M. A. Devani, G. U. B. Babu, M. Chinthala, K. N. Dhanavath, and S. H. Sonawane, "Ultrasound assisted impregnation of platinum on carbon for ORR activity in PEM fuel cell," *International Journal of Ambient Energy,* vol. 43, no. 1, pp. 8239-8247, 2022/12/31 2022.

[356] P. Apopei, C. Catrinescu, C. Teodosiu, and S. Royer, "Mixed-phase TiO2 photocatalysts: Crystalline phase isolation and reconstruction, characterization and photocatalytic activity in the oxidation of 4-chlorophenol from aqueous effluents," *Applied Catalysis B: Environmental,* vol. 160-161, pp. 374-382, 2014/11/01/ 2014.

[357] R. Senthil Kumar and B. Gnanavel, "High performance catalytic activity of pure and silver (Ag) doped TiO2 nanoparticles by a novel microwave irradiation technique," *Journal of Materials Science: Materials in Electronics,* vol. 28, no. 5, pp. 4253-4259, 2017/03/01 2017.

[358] A. Sirivallop, T. Areerob, and S. Chiarakorn, "Enhanced Visible Light Photocatalytic Activity of N and Ag Doped and Co-Doped TiO2 Synthesized by Using an In-Situ Solvothermal Method for Gas Phase Ammonia Removal," vol. 10, no. 2, p. 251, 2020.

[359] T. Ali, A. Ahmed, U. Alam, I. Uddin, P. Tripathi, and M. Muneer, "Enhanced photocatalytic and antibacterial activities of Ag-doped TiO2 nanoparticles under visible light," *Materials Chemistry and Physics,* vol. 212, pp. 325-335, 2018/06/15/ 2018.

[360] Y. Zhang, F. Fu, Y. Li, D. Zhang, and Y. Chen, "One-Step Synthesis of Ag@TiO2 Nanoparticles for Enhanced Photocatalytic Performance," vol. 8, no. 12, p. 1032, 2018.

[361] M. Xu, Y. Wang, J. Geng, and D. Jing, "Photodecomposition of NOx on Ag/TiO2 composite catalysts in a gas phase reactor," *Chemical Engineering Journal,* vol. 307, pp. 181-188, 2017/01/01/ 2017.

[362] O. Zakir *et al.*, "Fabrication and characterization of Ag- and Cu-doped TiO2 nanotubes (NTs) by in situ anodization method as an efficient photocatalyst," *Journal of Solid State Electrochemistry,* vol. 26, no. 10, pp. 2247-2260, 2022/10/01 2022.

[363] K. Nanaji, R. K. Siri Kiran Janardhana, T. N. Rao, and S. Anandan, "Energy level matching for efficient charge transfer in Ag doped - Ag modified TiO2 for enhanced visible light photocatalytic activity," *Journal of Alloys and Compounds,* vol. 794, pp. 662-671, 2019/07/25/ 2019.

[364] R. Kumar, J. Rashid, and M. A. Barakat, "Zero valent Ag deposited TiO2 for the efficient photocatalysis of methylene blue under UV-C light irradiation," *Colloids and Interface Science Communications,* vol. 5, pp. 1-4, 2015/03/01/ 2015.

[365] X. H. Yang, H. T. Fu, X. C. Wang, J. L. Yang, X. C. Jiang, and A. B. Yu, "Synthesis of silver-titanium dioxide nanocomposites for antimicrobial applications," *Journal of Nanoparticle Research,* vol. 16, no. 8, p. 2526, 2014/07/25 2014.

[366] Z. Tian *et al.*, "A novel biomass coated Ag–TiO2 composite as a photoanode for enhanced photocurrent in dye-sensitized solar cells," *RSC Advances,* 10.1039/C3RA40195B vol. 3, no. 18, pp. 6369-6376, 2013.

[367] B. Basumatary, R. Basumatary, A. Ramchiary, and D. Konwar, "Evaluation of Ag@TiO2/WO3 heterojunction photocatalyst for enhanced photocatalytic activity towards methylene blue degradation," *Chemosphere,* vol. 286, p. 131848, 2022/01/01/ 2022.

[368] E. Albiter, M. A. Valenzuela, S. Alfaro, G. Valverde-Aguilar, and F. M. Martínez-Pallares, "Photocatalytic deposition of Ag nanoparticles on TiO2: Metal precursor effect on the structural and photoactivity properties," *Journal of Saudi Chemical Society,* vol. 19, no. 5, pp. 563-573, 2015/09/01/ 2015.

[369] L. Da Già, C. Recchi, T. E. Davies, N. Greeves, and J. A. Lopez-Sanchez, "Visible-Light-Controlled Oxidation of Glucose using Titania-Supported Silver Photocatalysts," vol. 8, no. 22, pp. 3475-3483, 2016.

[370] Y. Gu, Y. Jiao, X. Zhou, A. Wu, B. Buhe, and H. Fu, "Strongly coupled Ag/TiO2 heterojunctions for effective and stable photothermal catalytic reduction of 4-nitrophenol," *Nano Research,* vol. 11, no. 1, pp. 126-141, 2018/01/01 2018.

[371] M. Manjunatha and H. Mahalingam, "Upcycling of waste EPS beads to immobilized codoped TiO2 photocatalysts for ciprofloxacin degradation and E. coli disinfection under sunlight," *Scientific Reports,* vol. 13, no. 1, p. 14631, 2023/09/05 2023.

[372] P. M. Martins, R. Miranda, J. Marques, C. J. Tavares, G. Botelho, and S. Lanceros-Mendez, "Comparative efficiency of TiO2 nanoparticles in suspension vs. immobilization into P(VDF–TrFE) porous membranes," *RSC Advances,* 10.1039/C5RA25385C vol. 6, no. 15, pp. 12708-12716, 2016.

[373] M. Ren, F. H. Frimmel, and G. Abbt-Braun, "Multi-cycle photocatalytic degradation of bezafibrate by a cast polyvinyl alcohol/titanium dioxide (PVA/TiO2) hybrid film," *Journal of Molecular Catalysis A: Chemical,* vol. 400, pp. 42-48, 2015/05/01/ 2015.

[374] A. C. Swathi, S. T. Sandhiya, S. B, and M. Chandran, "Precursor dependent - Visible light-driven g-C3N4 coated polyurethane foam for photocatalytic applications," *Chemosphere,* vol. 350, p. 141013, 2024/02/01/ 2024.

[375] Q. Zhang, L. Jiang, J. Wang, Y. Zhu, Y. Pu, and W. Dai, "Photocatalytic degradation of tetracycline antibiotics using three-dimensional network structure perylene diimide supramolecular organic photocatalyst under visible-light irradiation," *Applied Catalysis B: Environmental,* vol. 277, p. 119122, 2020/11/15/ 2020.

[376] W. S. Koe, J. W. Lee, W. C. Chong, Y. L. Pang, and L. C. Sim, "An overview of photocatalytic degradation: photocatalysts, mechanisms, and development of photocatalytic membrane," *Environmental Science and Pollution Research,* vol. 27, no. 3, pp. 2522-2565, 2020/01/01 2020.

[377] F. Loosli, P. Le Coustumer, and S. Stoll, "Impact of alginate concentration on the stability of agglomerates made of TiO2 engineered nanoparticles: Water hardness and pH effects," *Journal of Nanoparticle Research,* vol. 17, no. 1, p. 44, 2015/01/21 2015.

[378] S. H. Mir, B. D. Jennings, G. E. Akinoglu, A. Selkirk, R. Gatensby, and P. Mokarian-Tabari, "Enhanced Dye Degradation through Multi-Particle Confinement in a Porous Silicon Substrate: A Highly Efficient, Low Band Gap Photocatalyst," vol. 9, no. 11, p. 2002238, 2021.

[379] D. Komaraiah, E. Radha, J. Sivakumar, M. V. Ramana Reddy, and R. Sayanna, "Photoluminescence and photocatalytic activity of spin coated Ag+ doped anatase TiO2 thin films," *Optical Materials,* vol. 108, p. 110401, 2020/10/01/ 2020.

[380] D. Gogoi, A. Namdeo, A. K. Golder, and N. R. Peela, "Ag-doped TiO2 photocatalysts with effective charge transfer for highly efficient hydrogen production through water splitting," *International Journal of Hydrogen Energy,* vol. 45, no. 4, pp. 2729-2744, 2020/01/24/ 2020.

[381] M. Humayun, F. Raziq, A. Khan, and W. Luo, "Modification strategies of TiO2 for potential applications in photocatalysis: a critical review," *Green Chemistry Letters and Reviews,* vol. 11, no. 2, pp. 86-102, 2018/04/03 2018.

[382] W. D. Xing, M. S. Lee, and S. H. Choi, "Separation of Ag(I) by Ion Exchange and Cementation from a Raffinate Containing Ag(I), Ni(II) and Zn(II) and Traces of Cu(II) and Sn(II)," vol. 6, no. 8, p. 112, 2018.

[383] T. Chen, Y. Zheng, J.-M. Lin, and G. Chen, "Study on the photocatalytic degradation of methyl orange in water using Ag/ZnO as catalyst by liquid chromatography electrospray ionization ion-trap mass spectrometry," *Journal of the American Society for Mass Spectrometry,* vol. 19, no. 7, pp. 997-1003, 2008/07/01 2008.

[384] J. Zhu, Y. Zhu, Y. Zhou, C. Wu, Z. Chen, and G. Chen, "Synergistic Promotion of Photocatalytic Degradation of Methyl Orange by Fluorine- and Silicon-Doped TiO2/AC Composite Material," vol. 28, no. 13, p. 5170, 2023.

[385] N. Nagar and V. Devra, "A kinetic study on the degradation and biodegradability of silver nanoparticles catalyzed Methyl Orange and textile effluents," *Heliyon,* vol. 5, no. 3, 2019.

[386] R. A. Putri, S. Safni, N. Jamarun, U. Septiani, M.-K. Kim, and K.-d. Zoh, "Kinetics studies on photodegradation of methyl orange in the presence of C-N-codoped TiO2 catalyst %J Egyptian Journal of Chemistry," vol. 62, no. Special Issue (Part 2) Innovation in Chemistry, pp. 563-575, 2019.

[387] C. H. Nguyen, C.-C. Fu, and R.-S. Juang, "Degradation of methylene blue and methyl orange by palladium-doped TiO2 photocatalysis for water reuse: Efficiency and degradation pathways," *Journal of Cleaner Production,* vol. 202, pp. 413-427, 2018/11/20/ 2018.

[388] S. Liang, M. An, S. Xia, B. Zhang, B. Xue, and G. Xu, "Enhanced photocatalytic degradation of methyl orange by TiO2/biochar composites under simulated sunlight irradiation," *Optical Materials,* vol. 142, p. 114105, 2023/08/01/ 2023.

[389] R. Prasetyowati *et al.*, "Degradation of methyl orange dye using Fe3O4/GO photocatalyst with iron derived from coastal Glagah Kulon Progo ore," *Nano-Structures & Nano-Objects,* vol. 38, p. 101153, 2024/05/01/ 2024.

[390] R. Thirugnanam *et al.*, "Radiant synergy: Illuminating methyl orange dye removal with g-C3N4/ZnO heterojunction photocatalyst," *Diamond and Related Materials,* vol. 147, p. 111325, 2024/08/01/ 2024.

[391] L. Predoană *et al.*, "Photocatalytic Performance of Sn–Doped TiO2 Nanopowders for Photocatalytic Degradation of Methyl Orange Dye," vol. 13, no. 3, p. 534, 2023.

[392] B. He, M. Feng, X. Chen, and J. Sun, "Multidimensional (0D-3D) functional nanocarbon: Promising material to strengthen the photocatalytic activity of graphitic carbon nitride," *Green Energy & Environment,* vol. 6, no. 6, pp. 823-845, 2021/12/01/ 2021.

[393] P. Jiménez-Calvo, "Synergy of visible-light responsive photocatalytic materials and device engineering for energy and environment: Minireview on hydrogen production and water decontamination," *Materials Today Catalysis,* vol. 4, p. 100040, 2024/03/01/ 2024.

[394] N. Meng *et al.*, "Fundamentals, advances and perspectives of piezocatalysis: A marriage of solid-state physics and catalytic chemistry," *Progress in Materials Science,* vol. 138, p. 101161, 2023/09/01/ 2023.

[395] P. Jia, J. Li, and H. Huang, "Piezocatalysts and Piezo-Photocatalysts: From Material Design to Diverse Applications," vol. 34, no. 44, p. 2407309, 2024.

[396] L. Jing *et al.*, "Piezo-photocatalysts in the field of energy and environment: Designs, applications, and prospects," *Nano Energy,* vol. 112, p. 108508, 2023/07/01/ 2023.

[397] X. Liu, L. Xiao, Y. Zhang, and H. Sun, "Significantly enhanced piezo-photocatalytic capability in BaTiO3 nanowires for degrading organic dye," *Journal of Materiomics,* vol. 6, no. 2, pp. 256-262, 2020/06/01/ 2020.

[398] X. Zhou, Q. Sun, Z. Xiao, H. Luo, and D. Zhang, "Three-dimensional BNT/PVDF composite foam with a hierarchical pore structure for efficient piezo-photocatalysis," *Journal of Environmental Chemical Engineering,* vol. 10, no. 5, p. 108399, 2022/10/01/ 2022.

[399] R. Djellabi, M. F. Ordonez, F. Conte, E. Falletta, C. L. Bianchi, and I. Rossetti, "A review of advances in multifunctional XTiO3 perovskite-type oxides as piezo-photocatalysts for environmental remediation and energy production," *Journal of Hazardous Materials,* vol. 421, p. 126792, 2022/01/05/ 2022.

[400] M. A. Mahmoud, B. R. Alsehli, M. T. Alotaibi, M. Hosni, and A. Shahat, "A comprehensive review on the application of semiconducting materials in the degradation of effluents and water splitting," *Environmental Science and Pollution Research,* vol. 31, no. 3, pp. 3466-3494, 2024/01/01 2024.

[401] H. Sudrajat, I. Rossetti, I. Carra, and J. C. Colmenares, "Piezocatalytic reduction: an emerging research direction with bright prospects," *Current Opinion in Chemical Engineering,* vol. 45, p. 101043, 2024/09/01/ 2024.

[402] K. Wang, C. Han, J. Li, J. Qiu, J. Sunarso, and S. Liu, "The Mechanism of Piezocatalysis: Energy Band Theory or Screening Charge Effect?," *Angewandte Chemie International Edition,* vol. 61, no. 6, p. e202110429, 2022/02/01 2022.

[403] L. Wang, S. Zhang, Y. Zhang, and Q. An, "Piezodynamic therapy: Mechanisms and biomedical applications," *Nano Energy,* vol. 110, p. 108342, 2023/06/01/ 2023.

[404] H. Xu *et al.*, "Multimodal energy harvesting and catalysis of piezoelectric nanosheets for efficient and round-the-clock wastewater treatment," *Journal of Colloid and Interface Science,* vol. 651, pp. 705-713, 2023/12/01/ 2023.

[405] L. Wan, J. Han, W. Tian, N. Li, D. Chen, and J. Lu, "Barium titanate@covalent organic framework core–shell nanoparticles for adsorption-enhanced piezo-photocatalysis," *Chemical Engineering Journal,* vol. 462, p. 142324, 2023/04/15/ 2023.

[406] H. Yu *et al.*, "Macroscopic polarization enhancement boosting piezo-photocatalytic performance via Nb-doping on B-site of Bi4Ti3O12 nanosheets," *Journal of Advanced Ceramics,* vol. 13, no. 4, pp. 437-446, 2024.

[407] Y. Zhao *et al.*, "Enhanced piezoelectricity and spectral absorption in Nd-doped bismuth titanate hierarchical microspheres for efficient piezo-photocatalytic H2 production and pollutant degradation," *Journal of Materials Chemistry A,* 10.1039/D3TA06341K vol. 12, no. 3, pp. 1753-1763, 2024.

[408] S. Zhong *et al.*, "Improved piezo-photocatalysis for aquatic multi-pollutant removal via BiOBr/BaTiO3 heterojunction construction," *Chemical Engineering Journal,* vol. 488, p. 151002, 2024/05/15/ 2024.

[409] H. Yu *et al.*, "Coupling Enhanced Piezo-Photocatalysis on Robust Intergrowth Ferroelectric SrBi8Ti7O27 Nanosheets," *ACS Sustainable Chemistry & Engineering,* vol. 12, no. 26, pp. 9947-9956, 2024/07/01 2024.

[410] Q. Liu *et al.*, "Piezo-photoelectronic coupling effect of BaTiO3@TiO2 nanowires for highly concentrated dye degradation," *Nano Energy,* vol. 92, p. 106702, 2022/02/01/ 2022.

[411] M. Li, L. Liu, Y. Li, and Y. Li, "Tuning piezoelectric driven photocatalysis by TiO2/ZnS heterojunction for mineral processing wastewater degradation," *Journal of Water Process Engineering,* vol. 64, p. 105727, 2024/07/01/ 2024.

[412] M. Chen, Z. Kang, J. Wu, N. Qin, and D. Bao, "Significantly enhanced piezo-photocatalytic properties of recyclable nanocomposite films by growing ZnO nanorods on inverse opal structured TiO2 framework," *Journal of Alloys and Compounds,* vol. 985, p. 174032, 2024/05/25/ 2024.

[413] H. Bian, D. Li, J. Yan, and S. Liu, "Perovskite – A wonder catalyst for solar hydrogen production," *Journal of Energy Chemistry,* vol. 57, pp. 325-340, 2021/06/01/ 2021.

[414] C. Yu *et al.*, "Ultrahigh piezocatalytic capability in eco-friendly BaTiO3 nanosheets promoted by 2D morphology engineering," *Journal of Colloid and Interface Science,* vol. 596, pp. 288-296, 2021/08/15/ 2021.

[415] T. Cheng *et al.*, "Piezocatalytic degradation of methylene blue, tetrabromobisphenol A and tetracycline hydrochloride using Bi4Ti3O12 with different morphologies," *Materials Research Bulletin,* vol. 141, p. 111350, 2021/09/01/ 2021.

[416] W. Zhu, C. Wang, W. Hui, X. Huang, C. Yang, and Y. Liang, "Intrinsically morphological effect of perovskite BaTiO3 boosting piezocatalytic uranium extraction efficiency and mechanism investigation," *Journal of Hazardous Materials,* vol. 455, p. 131578, 2023/08/05/ 2023.

[417] X. Sun, Z. Zheng, J. Ma, T. Xian, G. Liu, and H. Yang, "Development of ternary Pt/BaTiO3/Bi2O3 heterostructured piezo-photocatalysts for antibiotic degradation," *Applied Surface Science,* vol. 653, p. 159421, 2024/04/30/ 2024.

[418] Y. Wang *et al.*, "Coupled piezo-pyro-photocatalysis of oxygen vacancies and Bi quantum dots co-modified BaTiO3 for highly efficient removal of ciprofloxacin," *Separation and Purification Technology,* vol. 337, p. 126392, 2024/06/13/ 2024.

[419] H. Gao *et al.*, "The Piezo–Fenton synergistic effect of ferroelectric single-crystal BaTiO3 nanoparticles for high-efficiency catalytic pollutant degradation in aqueous solution," *Dalton Transactions,* 10.1039/D2DT01248K vol. 51, no. 31, pp. 11876-11883, 2022.

[420] H. Khan and M. U. H. Shah, "Modification strategies of TiO2 based photocatalysts for enhanced visible light activity and energy storage ability: A review," *Journal of Environmental Chemical Engineering,* vol. 11, no. 6, p. 111532, 2023/12/01/ 2023.

[421] D. Masekela, N. C. Hintsho-Mbita, S. Sam, T. L. Yusuf, and N. Mabuba, "Application of BaTiO3-based catalysts for piezocatalytic, photocatalytic and piezo-photocatalytic degradation of organic pollutants and bacterial disinfection in wastewater: A comprehensive review," *Arabian Journal of Chemistry,* vol. 16, no. 2, p. 104473, 2023/02/01/ 2023.

[422] P. Kumar *et al.*, "Effect of Poling on Photocatalysis, Piezocatalysis, and Photo–Piezo Catalysis Performance of BaBi4Ti4O15 Ceramics," vol. 7, no. 2, p. 2200142, 2023.

[423] H. Wang, X. Zhang, C. Hu, H. Cai, S. Tu, and H. Huang, "Layered perovskite piezoelectric Bi3TiNbO9 as a piezo-photocatalyst: Synergistically enhanced catalytic activity and mechanism," *Applied Surface Science,* vol. 650, p. 159214, 2024/03/30/ 2024.

[424] P. Wang *et al.*, "Signally enhanced piezo-photocatalysis of Bi0.5Na0.5TiO3/MWCNTs composite for degradation of rhodamine B," *Chemosphere,* vol. 308, p. 136596, 2022/12/01/ 2022.

[425] P. Wang *et al.*, "Enhanced piezo-photocatalysis in Bi0.5Na0.5TiO3@Ag composite to efficiently degrade multiple organic pollutants," *Journal of Environmental Management,* vol. 323, p. 116186, 2022/12/01/ 2022.

[426] H. Meng, Z. Chen, Z. Lu, and X. Wang, "Piezoelectric effect enhanced plasmonic photocatalysis in the Pt/BaTiO3 heterojunctions," *Journal of Molecular Liquids,* vol. 369, p. 120846, 2023/01/01/ 2023.

[427] M. Sharma, A. Halder, and R. Vaish, "Effect of Ce on piezo/photocatalytic effects of Ba0.9Ca0.1CexTi1-xO3 ceramics for dye/pharmaceutical waste water treatment," *Materials Research Bulletin,* vol. 122, p. 110647, 2020/02/01/ 2020.

[428] M. Sharma and R. Vaish, "Piezo/pyro/photo-catalysis activities in Ba0.85Ca0.15(Ti0.9Zr0.1)1-xFexO3 ceramics," vol. 104, no. 1, pp. 45-56, 2021.

[429] K. Wang *et al.*, "Remarkably enhanced catalytic performance in CoOx/Bi4Ti3O12 heterostructures for methyl orange degradation via piezocatalysis and piezo-photocatalysis," *Ultrasonics Sonochemistry,* vol. 100, p. 106616, 2023/11/01/ 2023.

[430] P. Jia, Y. Li, Z. Zheng, Y. Wang, T. Liu, and J. Duan, "Piezoelectricity-enhanced photocatalytic degradation performance of SrBi4Ti4O15/Ag2O p-n heterojunction," *Separation and Purification Technology,* vol. 305, p. 122457, 2023/01/15/ 2023.

[431] D. Masekela, N. C. Hintsho-Mbita, and N. Mabuba, "Application of a piezo-photocatalytic thin film (FTO/BaTiO3/SnO2) for enhanced degradation of organic pollutants and

disinfection of wastewater," *Ceramics International,* vol. 49, no. 5, pp. 7566-7579, 2023/03/01/ 2023.

[432] C. Yu *et al.*, "Remarkably enhanced piezo-photocatalytic performance in BaTiO3/CuO heterostructures for organic pollutant degradation," *Journal of Advanced Ceramics,* vol. 11, no. 3, pp. 414-426, 2022/03/01 2022.

[433] Q. Liu, Q. Hu, D. Zhai, Q. Sun, H. Luo, and D. Zhang, "Superior photo-piezoelectric catalytic performance using Bi0.5Na0.5TiO3@BiVO4 based cloth," *Journal of Materials Chemistry A,* 10.1039/D1TA05315A vol. 9, no. 33, pp. 17841-17854, 2021.

[434] X. Xu, X. Lin, F. Yang, S. Huang, and X. Cheng, "Piezo-photocatalytic Activity of Bi0.5Na0.5TiO3@TiO2 Composite Catalyst with Heterojunction for Degradation of Organic Dye Molecule," *The Journal of Physical Chemistry C,* vol. 124, no. 44, pp. 24126-24134, 2020/11/05 2020.

[435] Q. Han *et al.*, "Direct Z-scheme MoSe2/TiO2 heterostructure with improved piezoelectric and piezo-photocatalytic performance," *Journal of Colloid and Interface Science,* vol. 622, pp. 637-651, 2022/09/15/ 2022.

[436] X. Chu *et al.*, "Microstructure Engineering of Al Doped SrTiO3/TiO2 Heterostructure Nanorod Arrays Boosting Piezo-Photocatalytic Performances," vol. 7, no. 12, p. 2200390, 2022.

[437] M. Habib, I. Lantgios, and K. Hornbostel, "A review of ceramic, polymer and composite piezoelectric materials," *Journal of Physics D: Applied Physics,* vol. 55, no. 42, p. 423002, 2022/08/19 2022.

[438] D. Ding *et al.*, "Piezo-photocatalytic flexible PAN/TiO2 composite nanofibers for environmental remediation," *Science of The Total Environment,* vol. 824, p. 153790, 2022/06/10/ 2022.

APPENDIX A ARTICLE 5: COMPARING THE PHOTOCATALYTIC ACTIVITY OF SUSPENDED AND FLOATING AG-DECORATED TiO_2 FOR DYE REMOVAL

Nila Davari[1], Ermelinda Falletta[2,3], Claudia L. Bianchi[2,3], Viviane Yargeau[4], Cristina Rodriguez-Seco[1], Daria C. Boffito[1,5*]

[1] Department of Chemical Engineering, Polytechnique Montréal, Montréal, Canada

[2] Department of Chemistry, University of Milan, Milan, Italy

[3] Consorzio Interuniversitario Nazionale per la Scienza e Tecnologia dei Materiali (INSTM), via Giusti 9, 50121, Florence, Italy

[4] Department of Chemical Engineering, McGill University, Montréal, Canada

[5] Canada Research Chair in Engineering Process Intensification and Catalysis

The article was published in Tetrahedron Green Chem, Volume 5, June 2025, 100059, Available online since December 4, 2024.

Author contributions

Nila Davari: Writing – original draft, Visualization, Validation, Methodology, Investigation, Formal analysis, Data curation, Conceptualization. Ermelinda Falletta: Writing – review & editing, Methodology, Investigation, Data curation. Claudia L. Bianchi: Writing – review & editing, Project administration, Methodology, Investigation, Funding acquisition, Data curation. Viviane Yargeau: Writing – review & editing, Supervision, Project administration, Methodology, Investigation, Data curation. Cristina Rodriguez-Seco: Writing – review & editing. Daria C. Boffito: Writing – review & editing, Supervision, Resources, Project administration, Methodology, Investigation, Funding acquisition, Data curation.

Abstract

We proposed a two-step synthesis process to fabricate floating TiO_2 and Ag-decorated TiO_2 (Ag/TiO_2) photocatalysts. In the first step, an ultrasound-assisted sol-gel method followed by spray drying was adopted to synthesize powder photocatalysts. Next, the powder samples were immobilized onto a floating polyurethane foam (PUF) support with an ultrasound-assisted impregnation method. The photocatalytic activity of TiO_2 and Ag/TiO_2 was evaluated to remove methyl orange (MO) as a dye pollutant in two suspended and floating photocatalytic systems. Ag decoration on TiO_2 improved the optical and textural properties by narrowing the bandgap energy to 2.9 eV and increasing the surface area from 10 m^2/g to 30 m^2/g. Ag/TiO_2 exhibited higher photocatalytic activity compared to TiO_2 for MO removal, which was 98% for suspended and 95% for floating catalysts under simulated sunlight irradiation. In addition, floating photocatalysts exhibited higher photocatalytic activity over five cycles of reuse. Floating Ag/TiO_2@PUF maintained 89% of its initial photoactivity, while suspended Ag/TiO_2 lost 50% after the five cycles. Moreover, we investigated the effect of operating conditions on the photocatalytic performance of floating Ag/TiO_2@PUF. Optimal conditions for the complete removal of MO below detection limits were obtained as follows: Ag/TiO_2@PUF loading = 0.4:200 g/mL, initial MO concentration = 5 mg/L, time = 90 min, and pH = 4 under simulated sunlight irradiation. This study highlights the potential of floating photocatalyst systems as a sustainable, reusable, and scalable approach for wastewater treatment, addressing challenges in catalyst recovery and efficiency under real-world conditions.

Keywords: Ag-Decorated, Floating Photocatalyst, Spray Drying, Suspended Photocatalyst, Ultrasonication

Introduction

TiO_2 as an n-type semiconductor photocatalyst has been investigated for wastewater treatment owing to its super-hydrophilicity, chemical and thermal stability, optical properties, and photocatalytic activity [125, 126, 139, 333]. However, the wide bandgap of TiO_2 (3.0 - 3.2 eV) confines its photoactivity to the UV region ($\lambda \leq 400$ nm). The fast recombination of photogenerated electron-hole pairs in TiO_2 also reduces its photocatalytic efficiency [7, 188, 334, 335].

To cope with the restrictions mentioned above, TiO_2 can be modified by metals, non-metals, and secondary semiconductors [63]. The incorporation of metals into TiO_2 can narrow its bandgap energy and prevent the recombination of electron-hole pairs, thereby improving the photocatalytic activity of TiO_2 for wastewater treatment applications [129]. This modification involves a variety of metals, including transition metals (e.g., Cr, Cu, Ni, Fe, V, W, Mn, Zn, and Ru), noble metals (e.g., Ag, Au, Pt, and Pd), and rare earth metals (e.g., Nd, Tb, Ce, Er, La, and Eu) [64]. Among these, composite Ag/TiO_2 photocatalysts have drawn research interest in wastewater treatment [336, 337]. The presence of Ag in TiO_2 enhances its photocatalytic activity by reducing the recombination of photogenerated electron-hole pairs and improving visible light absorption [338-340].

Immobilizing photocatalysts on supports affects the stability and reusability of photoactive materials [129]. Porous polyurethane foam (PUF) is one of the floating supports, which has a low density (< 1000 kg/m^3) [134, 135]. PUF improves the adsorption of pollutants due to its open-pore structure, which increases porosity and surface area [136]. In addition, photocatalysts deposited onto floating PUF tackle shortcomings such as the recovery and reusability of suspended photocatalysts, which hinder practical applications [136]. Moreover, the floating catalytic foam under sunlight irradiation benefits from access to the water-air interface [191]. This floating system causes a temperature gradient at the water-air interface, called the photothermal effect [104, 178, 179]. This attains the temperature-induced pumping effect and speeds up the mass transfer for photocatalysis [104]. The photothermal effect in the floating catalyst photoreactor also improves the absorption of oxygen from the air, enhancing photocatalytic reactions with increasing reactive oxygen species in the submerged part of floating photocatalysts in water [178].

Floating TiO_2-based photocatalysts have been explored for wastewater treatment. According to the literature, Zhang et al. [137] synthesized mesoporous SiO_2-TiO_2 photocatalysts supported on a floating polyurethane foam. Phenol and 2,4,5-trichlorophenol were completely removed by floating SiO_2-TiO_2/PUF after 3h and 6h under UV irradiation, respectively. TiO_2-ZnO photocatalysts immobilized on a floating light-expanded clay aggregate support (TiO_2-ZnO/LECA) were prepared by Mohammadi et al. [341], achieving 95.2% of ammonia removal under UV light within 3h. Mohamad Idris et al. [342] fabricated floating photocatalysts, which were TiO_2 nanoparticles immobilized on cork as a floating substrate. This resulted in 98.4% of methylene blue degradation after 2h of visible light. Cai et al. [109] described immobilizing co-

doped magnetic N-TiO_{2-x}/rGO photocatalysts on floating cellulose nanofibrous. The floating N-TiO_{2-x} /rGO@cellulose degraded 96.2% of Bisphenol A after 60 min under visible light. In another study, carbon and nitrogen co-doped TiO_2 nanoparticles supported on floating alginate beads were designed to remove diazinon [307]. The floating C, N-TiO_2/alginate bead removed 80.6% of diazinon after 8h of exposure to solar light.

In the synthesis process of photocatalysts, ultrasonication assists in providing a uniform particle size distribution in photocatalysts through acoustic cavitation and macro shear rates [343, 344]. This phenomenon consists of the fast formation, expansion, and intense collapse of bubbles in the liquid, leading to a high temperature (up to 5000 K) and pressure (20 MPa) and quick cooling rate [345-347]. In addition, the ultrasound-assisted impregnation method leads to the uniform distribution of photocatalysts onto their supports [348, 349]. Besides ultrasonication, spray drying during the photocatalyst synthesis process provides a swift, continuous approach whereby lengthy drying steps are avoided. This technique is also advantageous when scaling up during the commercialization process [350, 351]. Therefore, by applying ultrasonication and spray drying in subsequent steps during the synthesis of photoactive materials, we expect to enhance photocatalytic activity.

To the best of our knowledge, no study has been reported for the treatment of dye-containing wastewater using floating Ag/TiO_2 photocatalyst immobilized on porous PUF (Ag/TiO_2@PUF). We proposed a new synthesis process, i.e., an ultrasound-assisted sol-gel method followed by spray drying to manufacture a floating photocatalytic device. We compared the photocatalytic activity of suspended TiO_2 and Ag/TiO_2 with floating TiO_2@PUF and Ag/TiO_2@PUF to remove methyl orange (MO) as a model organic dye pollutant under simulated sunlight irradiation. In addition, we investigated the effects of operating parameters, including photocatalyst amount, MO concentration, and pH, on MO removal efficiency and kinetics study. Moreover, we examined the possible mechanism of MO removal by Ag/TiO_2@PUF and the main reactive species involved in the photocatalytic reaction under optimal conditions.

We hypothesized that floating TiO_2@PUF and Ag/TiO_2@PUF photocatalysts, inspired by photosynthesis, offer key advantages such as enhanced sunlight and oxygen harnessing over conventional suspended systems to remove MO at lower cost.

Materials and Methods

Materials

Ti(IV)-butoxide ($C_{16}H_{36}O_4Ti$, 97%) and methyl orange ($C_{14}H_{14}N_3NaO_3S$, 85%) were analytical grade reagents purchased from Sigma-Aldrich. Ethanol (C_2H_6O, 95%) was provided by Commercial Alcohols, and silver nitrate solution ($AgNO_3$, 0.1 N) was supplied by Merck. A commercial polyurethane foam (PUF, Porosity: Medium, 20 PPI) was obtained from Amtra (Italy). All solutions were prepared with deionized water, and the reagents were used as they were received without further purification.

Synthesis of photocatalysts

We synthesized pure TiO_2 and 2 wt.% Ag-decorated TiO_2 by an ultrasound-assisted sol-gel method followed by spray drying. An ultrasonic processor (VCX500, Sonics and Materials) equipped with a solid probe with a diameter of 13 mm was employed (measured power: 40 W; duty cycle: 2 s on, 2 s off for 1 h; processing volume: 120 mL). The ultrasound power was calibrated through calorimetry [352]. The operating parameters of the spray dryer (TP-S15, TOPTION) included a feeding slurry concentration of 20%, peristaltic pump feed rate of 30 rpm, temperature of 180 $^{\circ}$C, and needle of 6 s. For the synthesis of Ag/TiO_2, we added $AgNO_3$ solution (5 mL) dropwise in deionized water (10 mL) to the mixture of $C_{16}H_{36}O_4Ti$ (25 mL) and ethanol (80 mL) under continuous ultrasonication [63, 138]. After that, the resulting sol was fed to the spray dryer. The powder sample obtained from the spray dryer was then calcined in a furnace at 600 $^{\circ}$C for 2 h at a temperature rate of 2 $^{\circ}$C/min under static air, yielding Ag/TiO_2. TiO_2 was prepared using the same procedure without adding $AgNO_3$ solution.

The next step of the synthesis was to immobilize TiO_2 and Ag/TiO_2 onto a floating PUF by an ultrasound-assisted impregnation method. First, different amounts of TiO_2 and Ag/TiO_2 (0.5 g, 1 g, and 1.5 g) in deionized water were added to the PUF under continuous ultrasonication (40 W, 20 min). After that, ethanol (15 mL) was added to the solution, and the PUF was then immersed in the solution of deionized water and ethanol. Finally, the resulting solutions were dried at 80 °C for 24 h in the oven to obtain floating TiO_2@PUF and Ag/TiO_2@PUF.

Characterization

The crystalline phase of the synthesized photocatalysts was analyzed by a powder X-ray diffractometer (XRD, D8 advance, Bruker). Weight fractions of anatase and rutile phases were calculated by the Spurr Equation (Equation A.1), where I_R and I_A are the intensity of the strongest reflections for rutile and anatase phases [353].

$$f_A\ \% = \frac{1}{(1 + 1.26\ \frac{(I_R)}{(I_A)})} \tag{A.1}$$

The crystallite size of the photocatalysts was calculated using the Scherrer Equation [142].

$$D = \frac{K\lambda}{\beta cos\theta} \tag{A.2}$$

In Equation A.2, D is the crystallite size (nm), K is a constant (shape factor = 0.94), λ is the wavelength of the X-ray radiation source (Cu-Kα = 0.15406 nm), β is the full width at half maximum (FWHM) of the peak (in radian), and θ is half of the Bragg angle (in degrees).

The lattice parameters of the synthesized photocatalysts were determined with Bragg's law by the following equations [170] using XRD diffraction peaks of tetragonal TiO_2.

$$d_{(hkl)} = \frac{\lambda}{2sin\theta} \tag{A.3}$$

$$\frac{1}{(d_{(hkl)})^2} = \frac{h^2}{a^2} + \frac{k^2}{b^2} + \frac{l^2}{c^2} \tag{A.4}$$

In Equations A.3 and A.4, h, k, l are the indices of crystal planes, $d_{(hkl)}$ is the distance between the crystal planes of (hkl), θ is the diffraction angle of the crystal planes of (hkl), and a, b, c are lattice parameters of the photocatalysts ($a = b \neq c$).

Diffuse reflectance spectroscopy (DRS) analysis was performed by a UV-Vis spectrophotometer (Evolution™ 220, Thermo Fisher Scientific) to study the optical properties of the synthesized photocatalysts. The bandgap energy of the photocatalysts was calculated by plotting $[F(R) \times hv]^{0.5}$ vs. hv based on Equation A.5 [142, 143].

$$F(R) = \frac{(1 - R)^2}{2R} \tag{A.5}$$

Where *F(R)* is the Kubelka-Munk function, and *R* is the reflectance.

The infrared photothermal images of floating samples were taken by forward looking infrared camera (FLIR-T621xx). Scanning electron microscopy (SEM) equipped with energy-dispersive X-ray spectroscopy (EDS) was employed to investigate the morphology and elemental compositions of the photocatalysts (JSM-7600TFE, JEOL). Transmission electron microscopy (TEM) (JEM-2100F, JEOL) was operated to further study their morphology. Also, the size of the synthesized samples was measured using Digimizer version 5.3.5 software. For the chemical compositions and valence states of the photoactive materials, X-ray photoelectron spectroscopy (XPS) analysis was performed by an X-ray photoelectron spectrometer microprobe (VG ESCALAB 250Xi, Thermo Scientific). Nitrogen adsorption-desorption isotherms using the Brunauer-Emmett-Teller (BET) method measured the specific surface area, total pore volume, and pore size of the photocatalysts by an Autosorb-1 device (Quantachrome Instruments).

Photocatalytic system

We evaluated the photocatalytic activity of the synthesized materials to remove MO in a batch photoreactor under simulated sunlight irradiation. In addition, the stability of TiO_2, Ag/TiO_2, TiO_2@PUF, and Ag/TiO_2@PUF was assessed for five consecutive cycles. After each cycle, we removed the photocatalysts from the system, washed them with deionized water, and then dried them in the oven at 80 °C before reusing them for the next cycle. Each cycle had the same conditions.

We investigated the effect of operating parameters on MO removal with floating Ag/TiO_2@PUF under simulated sunlight irradiation as follows: Ag/TiO_2@PUF amount (0.2:200 g/mL, 0.4:200 g/mL, 0.8:200 g/mL), MO concentration (5 mg/L, 10 mg/L, 20 mg/L), and pH (4, 5.7, 10). The total irradiation time was 180 min, and the initial MO volume was 200 mL. Note that the values expressed for the photocatalysts as 0.2:200 g/mL, 0.4:200 g/mL, and 0.8:200 g/mL indicate the mass coated on PUF in the 200 mL of MO solution. The pH of MO solutions was adjusted by HCl (0.1 M) and NaOH (0.1 M), and the natural pH of the MO solution was measured at 5.7. In addition, the light source was a 300 W commercial solar lamp (Ultra-Vitalux, Osram) with an intensity of 35 W/m^2, located 20 cm above the reactor. Before being exposed to irradiation, each sample was kept in the dark for 60 min to reach absorption-desorption equilibrium. We repeated photocatalytic experiments three times under simulated sunlight irradiation, and error bars show the standard

deviation of these repetitions. MO concentration was monitored by a UV-Vis spectrophotometer (Evolution™ 220, Thermo Fisher Scientific) at λ_{max} = 464 nm. The photocatalytic efficiency of MO removal (η) was calculated according to Equation A.6:

$$\eta = \left(1 - \frac{C}{C_0}\right) \times 100\% \quad (A.6)$$

Where C_0 is the initial concentration of MO and C is the concentration of MO at time t.

We identified intermediates generated during the photocatalytic degradation of MO with floating Ag/TiO_2@PUF under optimal conditions using liquid chromatography-mass spectrometry (LC-MS). LC-UV-MS analyses were performed on an LC-TOF 6224 instrument from Agilent technologies with negative electrospray ionization.

We quantified the concentration of Ti and Ag elements leaching from Ag/TiO_2@PUF using inductively coupled plasma-optical emission spectroscopy (ICP-OES, Agilent, 5110-SVDV).

Photocatalytic kinetic study

The impact of operating parameters mentioned in the *Photocatalytic system* section was also examined on the kinetic of MO photocatalysis with floating Ag/TiO_2@PUF under simulated sunlight irradiation. We followed the Langmuir-Hinshelwood kinetics model, as shown in Equation A.7 [354].

$$r = \frac{dC}{dt} = \frac{kKC}{1 + KC} \quad (A.7)$$

r is the rate of MO removal (mg/L.min), *C* is MO concentration (mg/L), *t* is irradiation time (min), *k* is reaction rate constant (mg/L.min), and *K* is MO adsorption constant (L/mg).

For low concentrations of MO, Equation A.7 can be simplified to Equation A.8, representing a first-order kinetics.

$$ln\left(\frac{C_0}{C}\right) = kKt = k_{app}t \quad (A.8)$$

In Equation A.8, k_{app} is the apparent first-order rate constant (min^{-1}).

Scavenging experiments

We investigated the main reactive species involved in MO photocatalysis by floating Ag/TiO_2@PUF by adding the scavengers Ethylenediaminetetraacetic acid (EDTA), isopropyl alcohol (IPA), and p-benzoquinone (BQ) for photogenerated holes (h^+), hydroxyl radicals ($^{\bullet}OH$), and superoxide anions ($^{\bullet}O_2^-$), respectively. We added 1 mM of each scavenger to the floating catalyst photoreactor under simulated sunlight irradiation. We performed scavenging experiments for the optimized conditions of the photocatalysts in MO removal.

Results and Discussion

Morphology and elemental compositions of TiO_2@PUF and Ag/TiO_2@PUF

Figure A.1(a) presents the smooth surface of the pristine PUF before immobilizing the photocatalysts. Figures A.1(b) and A.1(c) show the SEM images of TiO_2@PUF and Ag/TiO_2@PUF after the deposition of the photocatalysts, confirming that TiO_2 and Ag/TiO_2 were uniformly immobilized onto the PUF. This is due to ultrasonication in the impregnation synthesis method [349, 355]. In addition, the synthesized TiO_2 and Ag/TiO_2 had spherical morphology, as depicted in Figures A.1(d) and A.1(e).

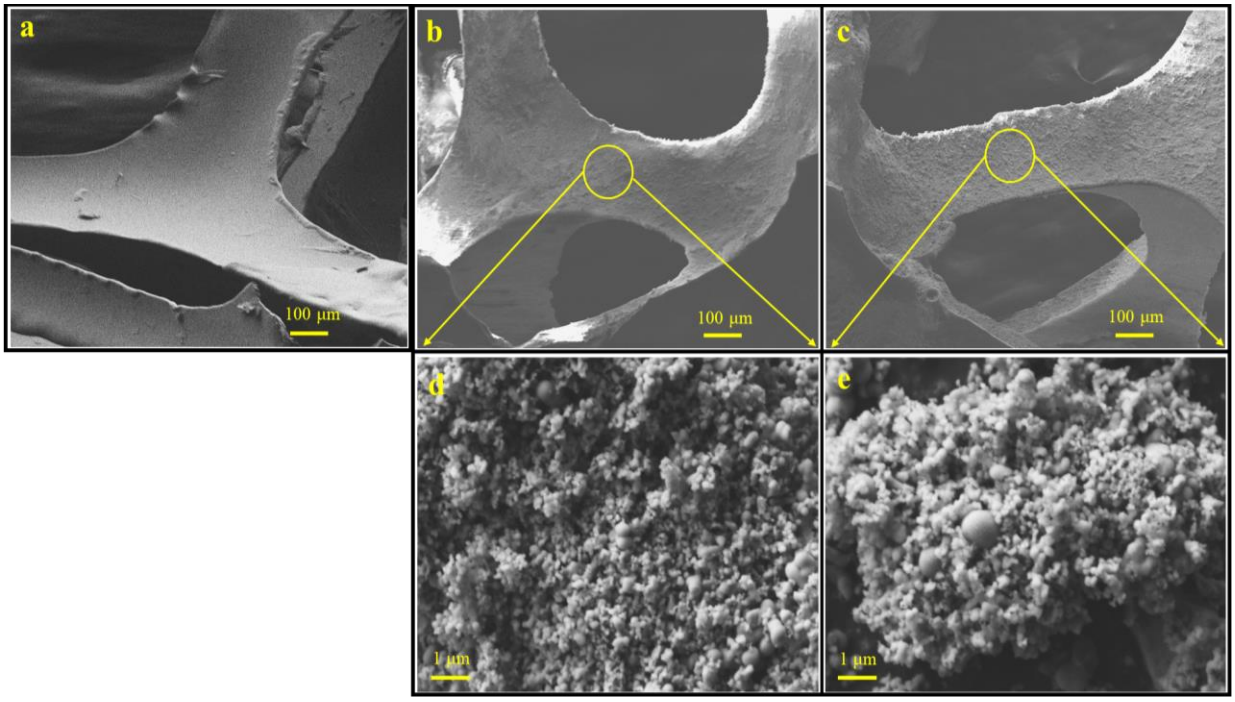

Figure A.1 SEM images of (a) PUF, (b) TiO_2@PUF, (c) Ag/TiO_2@PUF, (d) TiO_2, and (e) Ag/TiO_2

Figure A.2(a) shows the TEM image of Ag/TiO_2. Ag was uniformly loaded onto TiO_2, marked by highlighted circles. The size of spherical Ag was 10 nm, as shown in Figure A.2(b).

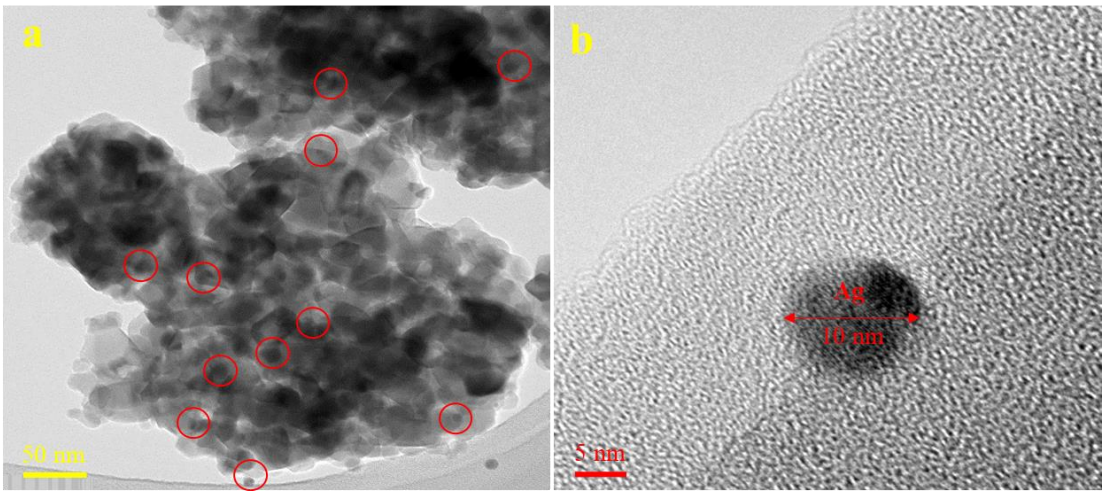

Figure A.2 TEM images of (a) Ag/TiO_2 and (b) Ag

EDS detected Ti (64.5%) and O (35.5%) in TiO_2 (Figure A.3(a)). Also, the presence of 2.1% Ag in Ag/TiO_2 was confirmed, along with 59.7% of Ti and 38.2% of O in the photocatalyst (Figure A.3(b)). Figures A.3(c) and A.3(d) show that the elements were evenly dispersed onto the synthesized photocatalysts.

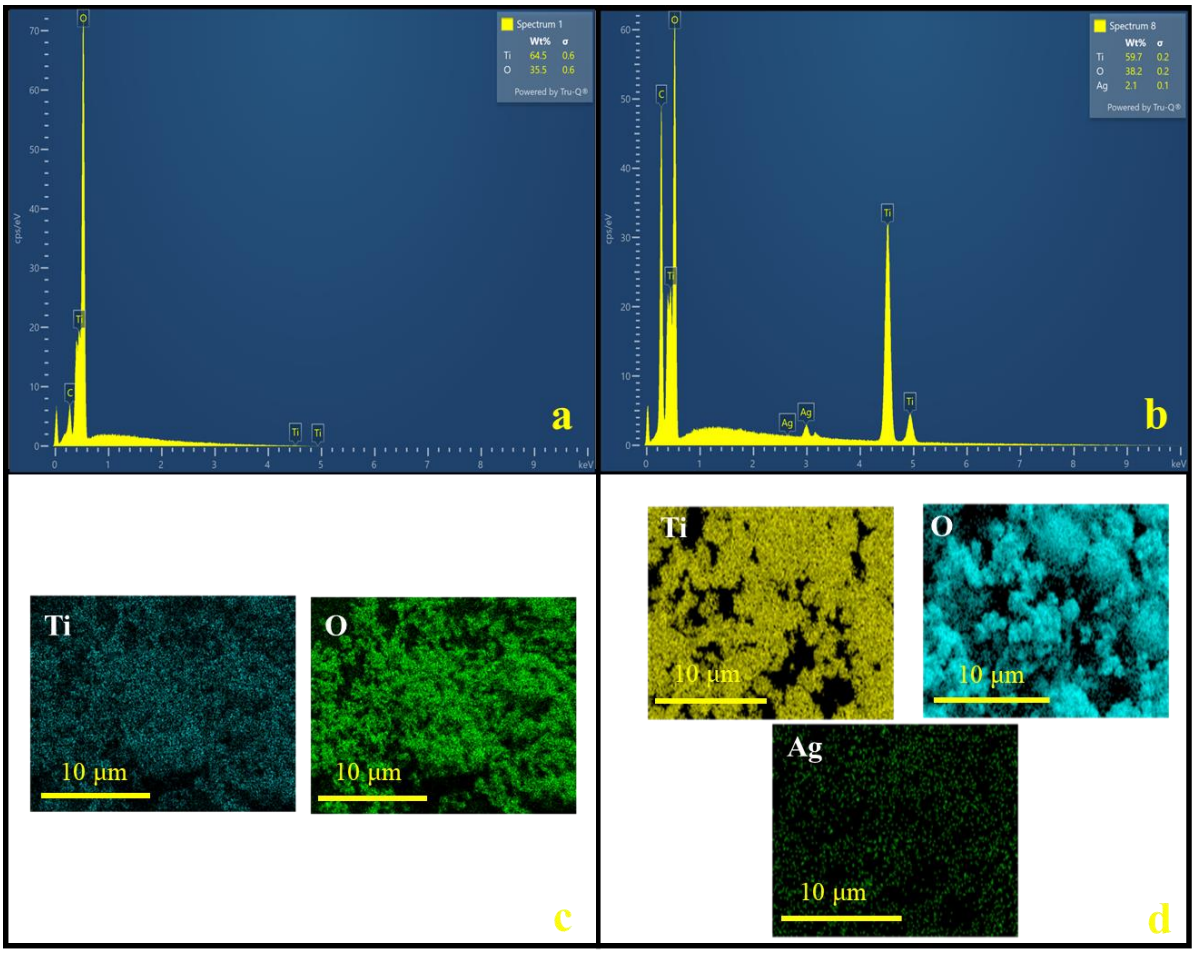

Figure A.3 EDS spectra of (a) TiO_2 and (b) Ag/TiO_2; EDS mappings of (c) TiO_2 and (d) Ag/TiO_2

Crystalline phase of TiO_2 and Ag/TiO_2

Figure A.4 shows the XRD patterns of TiO_2 and Ag/TiO_2. The lattice planes of the anatase phase (101), (103), (004), (112), (200), (105), (211), (204), and (220) were confirmed at 2θ values of 25.47°, 37.15°, 37.97°, 38.78°, 48.21°, 54.04°, 55.22°, 62.87°, and 69.01°, respectively (JCPDS Card Number: 01-071-1166). Moreover, peaks at 2θ values of 27.60°, 36.22°, and 41.44° equivalent to the Miller indexes of (110), (101), and (111) were characteristic of the rutile phase in the synthesized photocatalysts (JCPDS Card Number: 00-001-1292). TiO_2-based photocatalysts

having mixed phases (anatase/rutile) present higher photocatalytic activity compared to single-phase TiO_2 [54, 356].

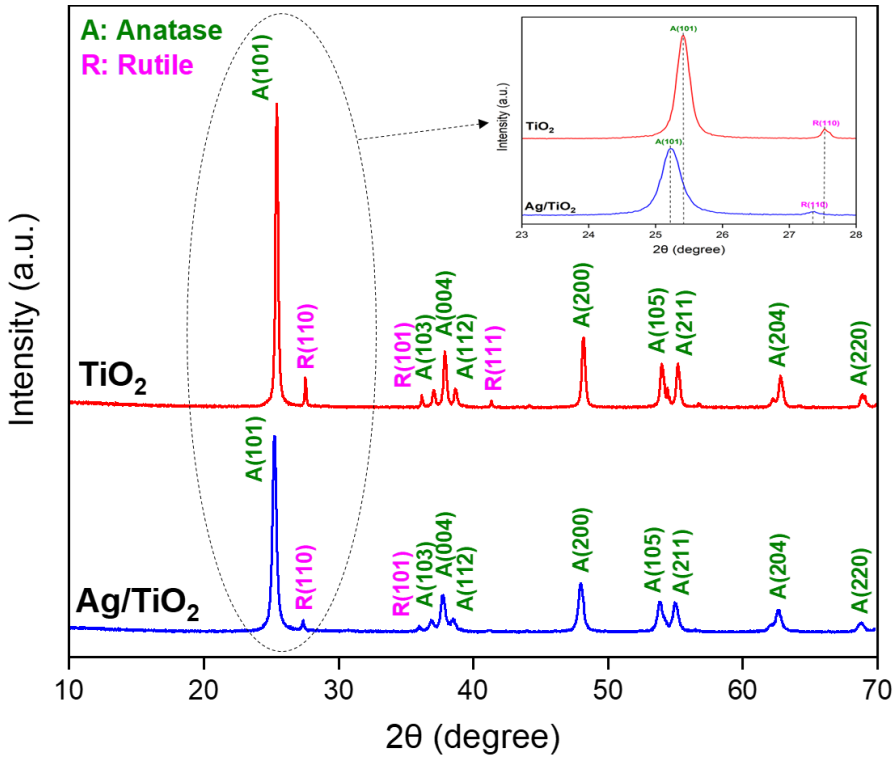

Figure A.4 XRD of TiO_2 and Ag/TiO_2

As shown in Figure A.4, the peak associated with Ag was not detected due to either the highly fine dispersion on TiO_2 or, more likely, the low concentration of Ag in Ag/TiO_2 [63]. However, for Ag/TiO_2, the position of TiO_2 peaks shifted to a lower angle side, and the intensity of peaks decreased, indicating that Ag was decorated on TiO_2 [357]. We calculated the crystalline phase, crystallite size, lattice parameters, and cell volume of TiO_2 and Ag/TiO_2 for both the anatase phase at A (101) and the rutile phase at R (110) (Table A.1). Based on the Spurr Equation, TiO_2 had 88% of the anatase phase compared to 92% for Ag/TiO_2. According to the Scherrer Equation, the average crystallite size of anatase in TiO_2 was 32.8 nm and 26.5 nm for Ag/TiO_2. On the other hand, for the rutile phase, the crystallite size of TiO_2 and Ag/TiO_2 was 74.4 nm and 26.6 nm, respectively. The crystallite size of Ag/TiO_2 was smaller than that of pure TiO_2 due to the higher ionic radius of Ag^+ (126 Å) compared to Ti^{4+} (68 Å). This hinders the growth of TiO_2 crystallites [358]. As reported in Table A.1, the lattice parameters of Ag/TiO_2 were smaller than those of TiO_2 in both anatase and rutile phases. Also, the anatase cell volume of Ag/TiO_2 was 132.16 $Å^3$

compared to 138.98 $Å^3$ for TiO_2. The reduction in lattice parameters and cell volume originates from Ag decoration on TiO_2 [357, 359].

Table A.1 Crystalline parameters of TiO_2 and Ag/TiO_2

Photocatalyst	Crystalline phase	Crystalline phase percentage	Crystallite size (nm)	Lattice parameters (Å)		Cell volume ($Å^3$)
				a = b	c	
TiO_2	Anatase	88	32.8	3.7917	9.6672	138.98
Ag/TiO_2		92	26.5	3.7746	9.2756	132.16
TiO_2	Rutile	12	74.4	4.6113	2.9712	63.18
Ag/TiO_2		8	26.6	4.5695	2.9528	61.65

Chemical compositions and valence states of TiO_2 and Ag/TiO_2

Figure A.5(a) depicts the XPS survey spectra of TiO_2 and Ag/TiO_2, which indicates the presence of Ti and O in TiO_2 and Ti, O, and Ag elements for Ag/TiO_2. Ag/TiO_2 exhibited two peaks at binding energies of 458.8 eV for Ti $2p_{3/2}$ and 464.5 eV for Ti $2p_{1/2}$, indicating the existence of Ti^{4+} in Ag/TiO_2 based on the peak separation of 5.7 eV (Figure A.5(b)) [360-362]. In addition, there was about 0.1 eV shift in the Ti 2p spectrum of Ag/TiO_2 towards higher binding energy compared with TiO_2, which can result from the improved interaction between Ti and Ag [363]. Figure A.5(c) shows a peak at 530 eV attributed to the lattice oxygen in Ag/TiO_2 (Ti-O) [364, 365]. In Figure A.5(d), Ag 3d peaks were present at binding energies of 368.5 eV and 374.5 eV for Ag $3d_{5/2}$ and Ag $3d_{3/2}$, respectively. The binding energy difference between the two spin-orbit components was 6 eV, confirming the presence of metallic silver (Ag^0) in Ag/TiO_2 [360, 362, 366, 367]. Additional binding energy peaks were observed at 367.9 eV for Ag $3d_{5/2}$ and 373.9 eV for Ag $3d_{3/2}$, suggesting the presence of oxidized silver, either as Ag_2O or AgO (Ag^{+1} or Ag^{+2}) in the surface of TiO_2 [343, 362, 364, 366, 368, 369]. The presence of oxidized silver is likely due to the oxidation of Ag during the calcination of Ag/TiO_2 [343]. Our results confirmed that Ag existed in Ag/TiO_2 as a mixture of metallic and oxidized silver.

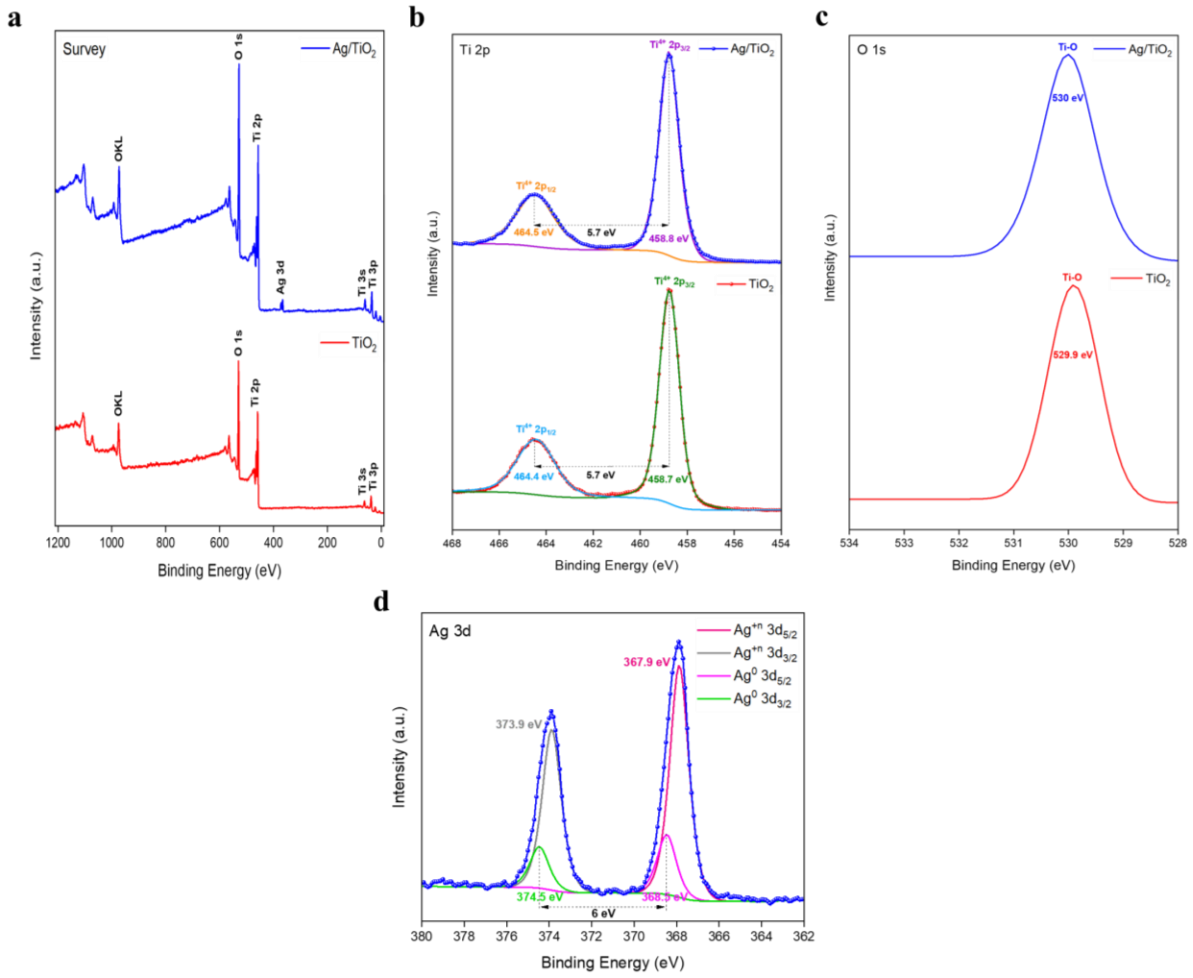

Figure A.5 XPS spectra of TiO_2 and Ag/TiO_2 (a) Full spectrum, (b-d) High-resolution spectra of Ti 2p, O 1s, and Ag 3d, respectively

Optical features and photothermal performance of TiO_2 and Ag/TiO_2

Figure A.6(a) presents the absorption spectra of TiO_2 and Ag/TiO_2. Pure TiO_2 exhibited an intense absorption peak in the UV region below 400 nm, which belongs to the electron excitation from the 2p of O^{2-} to the 3d orbital of Ti^{4+} [170]. According to Figure A.6(a), a redshift towards 470 nm was observed in the spectrum of Ag/TiO_2 compared to bare TiO_2. This redshift can be due to the effect of Ag decoration on TiO_2, which improves the visible light absorption of TiO_2 [249, 338].

Figure A.6(b) shows Tauc plots of TiO_2 and Ag/TiO_2. The bandgap energy of pure TiO_2 was determined as 3 eV. Ag decreased the bandgap energy of TiO_2 to 2.9 eV owing to decorating Ag on TiO_2 [339]. A new energy level can be formed between the conduction band of TiO_2 and the conduction band of Ag that decreases the bandgap energy of TiO_2, reducing the recombination rate

of photogenerated charge carriers and thus enhancing the photocatalytic activity of Ag/TiO_2 [343, 359].

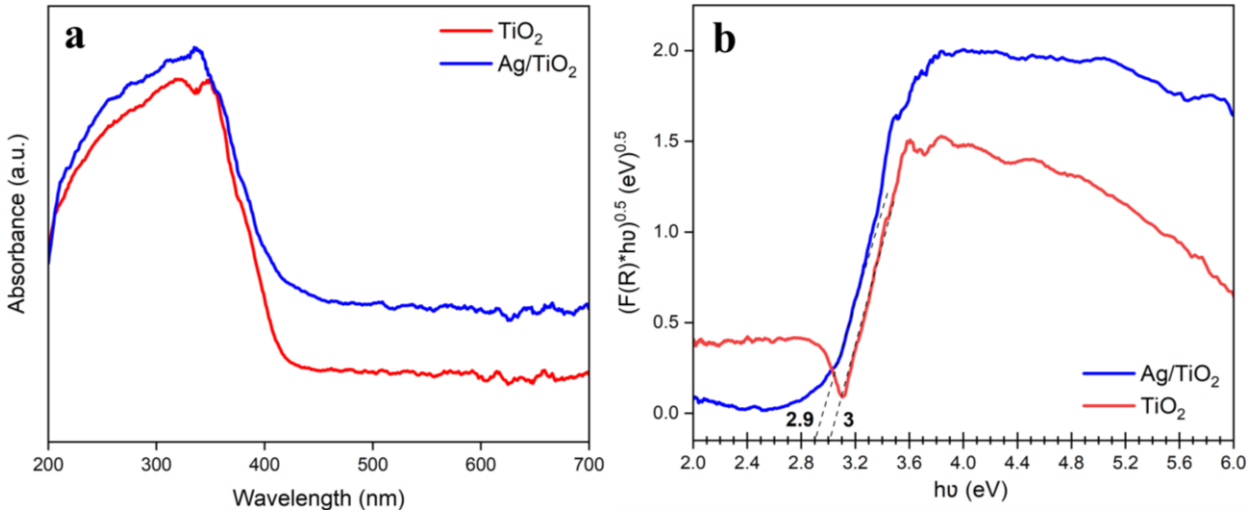

Figure A.6 DRS (a) absorption spectra and (b) Tauc plots of TiO_2 and Ag/TiO_2

Figure A.7 shows the infrared photothermal images of floating samples. The system reached the highest temperature at 26 °C, 32 °C and 40 °C for PUF, TiO_2@PUF and Ag/TiO_2@PUF, respectively, after 5 min of simulated sunlight irradiation. Ag/TiO_2@PUF exhibited the highest temperature of all samples (40 °C), which can be due to the local surface plasmon resonance (LSPR) effect of Ag [179, 249]. Ag can generate high-energy hot electrons, resulting in local heating around the particles under light irradiation [370].

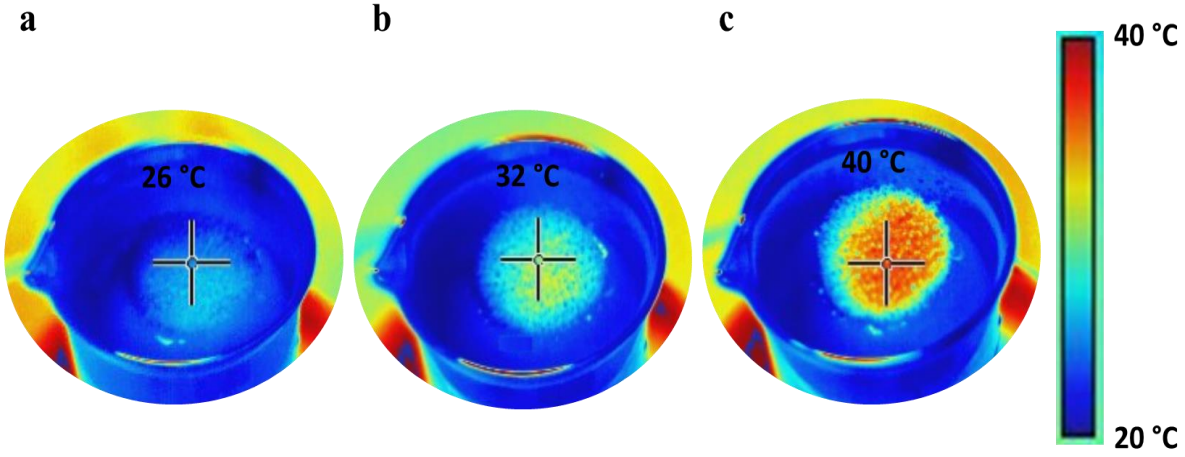

Figure A.7 Top-view infrared photothermal images of (a) PUF, (b) TiO_2@PUF, and (c) Ag/TiO_2@PUF in water under simulated sunlight irradiation

Textural properties of TiO_2 and Ag/TiO_2

Table A.2 presents BET results of TiO_2 and Ag/TiO_2. BET surface area of Ag/TiO_2 (30 m^2/g) was three times higher than that of TiO_2 (10 m^2/g). In addition, Ag/TiO_2 had a total pore volume of 0.12 cm^3/g, four times greater than TiO_2 (0.03 cm^3/g).

Table A.2 BET of TiO_2 and Ag/TiO_2

Photocatalyst	BET surface area (m^2/g)	Pore volume (cm^3/g)	Pore size (nm)
TiO_2	10	0.03	12
Ag/TiO_2	30	0.12	10

Figures A.8(a) and A.8(b) show N_2 adsorption-desorption isotherms of TiO_2 and Ag/TiO_2, respectively. Based on the IUPAC classification [175], TiO_2 presented a type IV(a) isotherm with an H3 hysteresis loop, indicating its mesoporous geometry with a mean pore size of 12 nm (see Table A.2). In addition, Ag/TiO_2 had a type IV(a) isotherm with an H1 hysteresis loop, suggesting a narrow range of uniform mesopores in Ag/TiO_2 and a mean pore size of 10 nm.

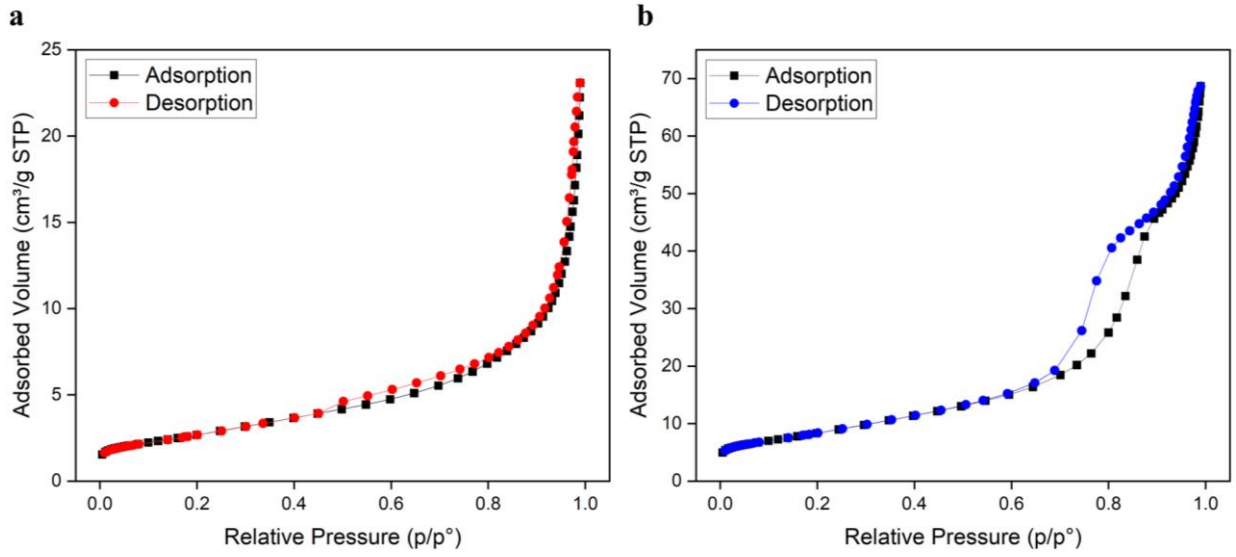

Figure A.8 N_2 adsorption-desorption isotherms of (a) TiO_2 and (b) Ag/TiO_2

Photocatalytic activity of TiO_2 and Ag/TiO_2 in suspended and floating systems for MO removal

We investigated suspended and floating devices based on TiO_2 and Ag/TiO_2 to remove MO under simulated sunlight irradiation for five consecutive cycles. The experimental conditions for MO photocatalysis were 10 mg/L of MO concentration, 0.4 g of photocatalysts, and pH = 5.7 for 180 min irradiation time. In the first cycle, the MO removal was 75% and 70% for TiO_2 and TiO_2@PUF, respectively (Figure A.9(a)). This slightly higher efficiency by suspended TiO_2 (5%) can be attributed to the larger surface in contact with the MO solution, which is typical of suspensions, improving the mass transfer rate between the surface of TiO_2 nanoparticles and pollutant species [371-373]. On the other hand, in the second cycle, floating TiO_2@PUF maintained 70% of MO removal, while it decreased to 67% for suspended TiO_2. This reduction can be due to the loss of TiO_2 in the suspended form during its reuse [371]. In addition, floating TiO_2@PUF showed higher photocatalytic activity than suspended TiO_2 in the fifth cycle, achieving 64% MO removal compared to 39%. Immobilizing powder photocatalysts onto floating supports not only addresses the challenges of reuse of suspended photocatalysts but also enhances solar light harnessing through access to the water-air interface [8, 246].

Figure A.9(b) presents the MO removal with Ag/TiO_2 and Ag/TiO_2@PUF in suspension and floating systems, respectively. Figure A.9(b) followed the same trend as observed in Figure A.9(a). In the first cycle, suspended Ag/TiO_2 removed 98% of MO, while Ag/TiO_2@PUF achieved 95%. In the following cycles, floating Ag/TiO_2@PUF exhibited higher photocatalytic activity than suspended Ag/TiO_2. The MO removal was 89% with floating Ag/TiO_2@PUF and 50% for suspended Ag/TiO_2 in the final cycle. Comparing Figure A.9(b) with Figure A.9(a), Ag in both suspended and floating photocatalysts increased the MO removal with respect to the pure photocatalysts. Our results indicated that floating Ag/TiO_2@PUF was the most effective photocatalyst, with a MO removal efficiency of 89% after five consecutive cycles. Based on the results from Ag/TiO_2@PUF characterizations, Ag decoration on TiO_2 decreased the bandgap energy to 2.9 eV and caused an increase in the visible light absorption of bare TiO_2 [179, 338]. Also, the surface area of Ag/TiO_2 increased to 30 m^2/g, three times higher than that of TiO_2, providing more active sites for the decomposition of MO. In addition, the mixed phase found for Ag/TiO_2 exhibited higher photocatalytic activity than the single-phase one [54, 356].

Floating photocatalysts (TiO_2@PUF and Ag/TiO_2@PUF) were 5-7% more effective than suspended ones (TiO_2 and Ag/TiO_2) in adsorbing MO in dark conditions. This is because the floating photocatalytic systems benefit from the photothermal effect [104, 178, 179, 249] that enhances the diffusion and adsorption of MO molecules on the surface of floating photocatalysts during the photocatalytic process.

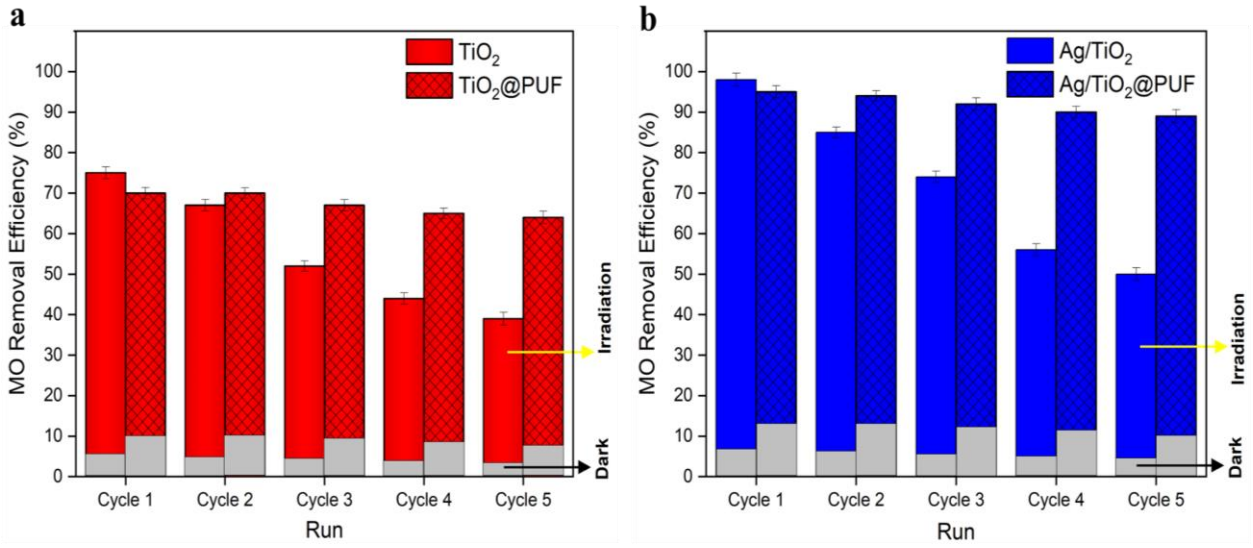

Figure A.9 MO removal efficiency with (a) TiO_2 and TiO_2@PUF, (b) Ag/TiO_2 and Ag/TiO_2@PUF after 180 min of irradiation time

Effects of operating parameters on MO removal by floating Ag/TiO_2@PUF

The effect of Ag/TiO_2@PUF amount on MO removal efficiency under simulated sunlight irradiation was investigated by varying it to 0.2:200 g/mL, 0.4:200 g/mL, and 0.8:200 g/mL. The rest of the experimental conditions were maintained constant (pH = 5.7, 10 mg/L MO, and 180 min irradiation time). Figure A.10(a) shows that when the photocatalyst amount increased from 0.2:200 g/mL to 0.4:200 g/mL, the MO removal rose from 70% to 95%. This increase is because more active photocatalytic sites inside the PUF can be available to harness light irradiation and participate in the photocatalytic reaction [134]. On the other hand, the MO removal decreased by 10% with increasing amount of the photocatalyst from 0.4:200 g/mL to 0.8:200 g/mL due to the agglomeration of Ag/TiO_2 and blockage of PUF pores that hinder light penetration [111, 134, 282, 283]. Our results suggested that the optimal amount of Ag/TiO_2@PUF for MO photocatalysis was 0.4:200 g/mL, achieving 95% removal after 180 min.

Figure A.10(b) presents the effect of Ag/TiO_2@PUF amount on the apparent rate constant. The correlation coefficients (R^2) were higher than 0.98, confirming that the MO photocatalytic removal by Ag/TiO_2@PUF followed first-order kinetics. As shown in Figure A.10(b), by increasing the amount of Ag/TiO_2@PUF from 0.2:200 g/mL to 0.4:200 g/mL, the apparent first-order rate constant (k_{app}) increased from 0.007 min^{-1} to 0.017 min^{-1}. However, as the amount of Ag/TiO_2@PUF further raised to 0.8:200 g/mL, k_{app} diminished to 0.011 min^{-1}.

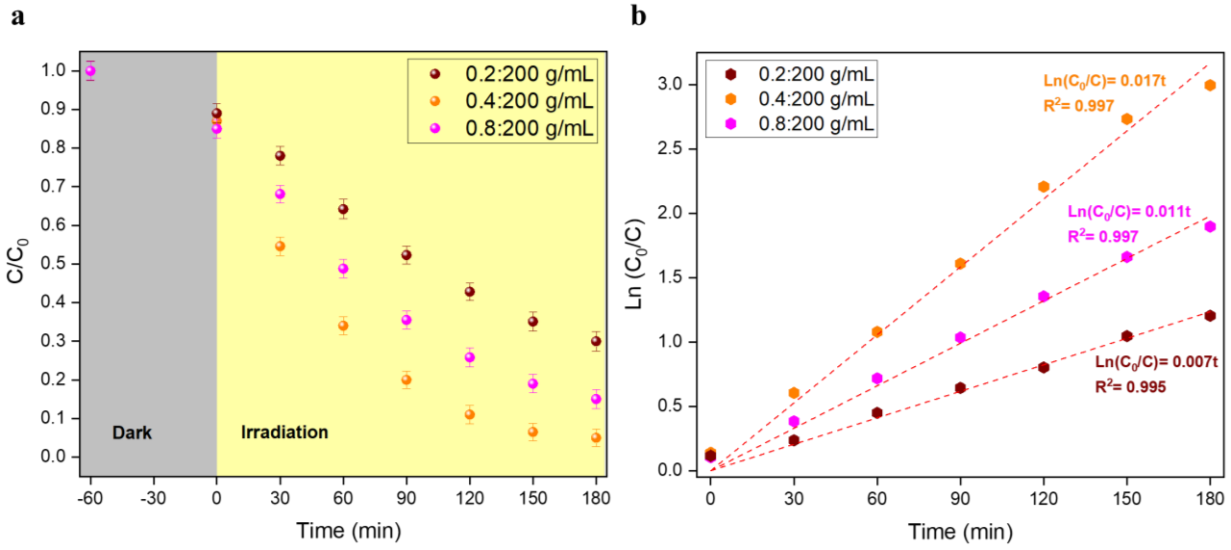

Figure A.10 Effect of Ag/TiO_2@PUF amount (0.2:200 g/mL, 0.4:200 g/mL, 0.8:200 g/mL) on (a) MO removal efficiency and (b) apparent rate constant

The effect of MO concentration (5 mg/L, 10 mg/L, and 20 mg/L) on the MO removal was examined with 0.4:200 g/mL Ag/TiO_2@PUF at pH = 5.7. For Mo concentration of 5 mg/L, we observed a complete removal after 150 min of irradiation time (Figure A.11(a)). However, increasing the MO concentration to 10 mg/L decreased the efficiency to 95% after 180 min, and it was 93% for 150 min. In addition, a further increase in MO concentration to 20 mg/L resulted in a 7% reduction in the MO removal (see Figure A.11(a)). The results showed that the photocatalytic performance of Ag/TiO_2@PUF decreased by increasing the MO concentration. This can be owing to the large adsorption of MO on the photocatalyst surface, decreasing the photodecomposition efficiency [374, 375]. The MO photocatalytic removal was affected by the initial pollutant concentration in which complete elimination was achieved for 5 mg/L MO after 150 min.

Figure A.11(b) shows how the concentration of MO impacts the apparent rate constant in the MO photocatalytic process. When applying Ag/TiO_2@PUF for MO removal, the system obeyed first-

order kinetics, with R^2 exceeding 0.99. Also, rising MO concentration from 5 mg/L to 20 mg/L lowered k_{app} from 0.029 min^{-1} to 0.011 min^{-1}.

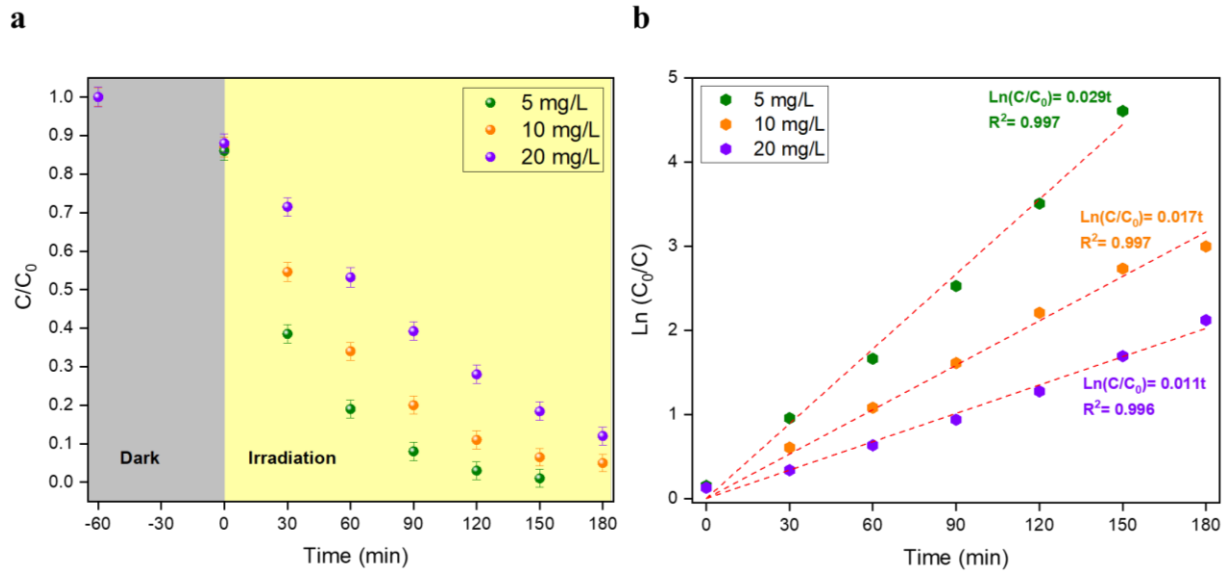

Figure A.11 Effect of MO concentration (5 mg/L, 10 mg/L, 20 mg/L) on (a) MO removal efficiency and (b) apparent rate constant

The effect of pH on MO removal was also evaluated. We tested the pH of MO solution (4, 5.7, and 10) using 5 mg/L MO and 0.4:200 g/mL Ag/TiO_2@PUF. Figure A.12(a) shows that as the pH of the MO solution decreases, the removal efficiency increases. The lowest MO removal rate happened at pH = 10 (40% after 180 min), which can be explained by the surface charge properties of Ag/TiO_2@PUF. The point of zero charge for TiO_2 is 6 (pH_{PZC} = 6) [339, 354, 376]. Thus, the surface of TiO_2 in Ag/TiO_2@PUF is negatively charged at pH = 10, as presented in Equation A.9.

$$TiOH + OH^- \leftrightarrow TiO^- + H_2O \quad (A.9)$$

On the other hand, MO is an anionic dye with a pk_a of 3.4 [354], which is negatively charged at pH = 10. Consequently, electrostatic repulsion between the negatively charged MO and the negatively charged surface of Ag/TiO_2@PUF [339, 354] inhibits the adsorption of MO onto the photocatalyst, decreasing the photocatalytic efficiency. In addition, at pH = 5.7, the surface of TiO_2 in Ag/TiO_2@PUF is positively charged according to Equation A.10, while MO is negatively charged [339, 354].

$$TiOH + H^+ \leftrightarrow TiOH_2^+ \quad (A.10)$$

Therefore, there is an electrostatic attraction between the negatively charged pollutant and the positively charged surface of the photocatalyst [339, 354] that favours the adsorption of MO onto the photocatalyst and thus increases MO removal. MO was completely removed at pH = 5.7 after 150 min of irradiation time. Moreover, MO removal was predominant at pH = 4, achieving complete removal after 90 min of light irradiation (see Figure A.12(a)). The improved photocatalytic activity of Ag/TiO_2@PUF at pH = 4 compared to pH = 5.7 can be attributed to the pH_{PZC} of TiO_2 (pH_{PZC} = 6). At pH = 4, the surface of TiO_2 in Ag/TiO_2@PUF is strongly positively charged with a zeta potential value of around +30 mV [148, 377], while it is about +5 mV at pH = 5.7 [148, 377]. Consequently, the surface of Ag/TiO_2@PUF at pH = 4 is more positively charged to adsorb negatively charged MO and increases the removal efficiency. Our findings indicated that MO (5 mg/L) at pH = 4 was completely removed by Ag/TiO_2@PUF (0.4:200 g/mL) under simulated sunlight irradiation (90 min).

Figure A.12(b) shows the effect of pH on the apparent rate constant, suggesting that MO removal by Ag/TiO_2@PUF followed a first-order kinetics. At pH = 4, k_{app} was 0.050 min^{-1}, which was the highest value obtained for this system.

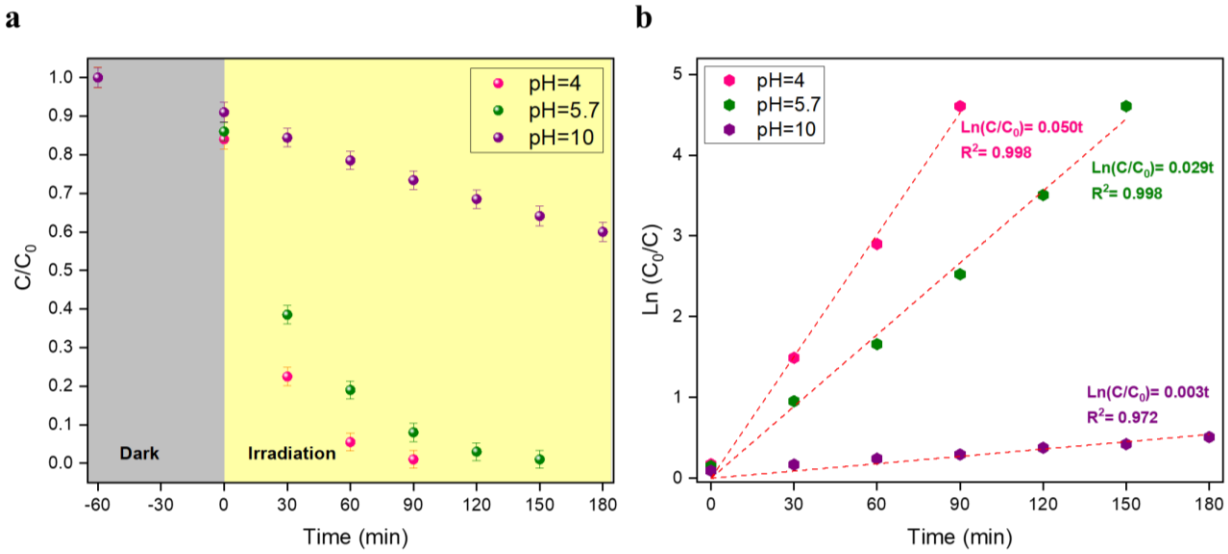

Figure A.12 Effect of pH (4, 5.7, 10) on (a) MO removal efficiency and (b) apparent rate constant

The faster removal rate for MO occurred at the beginning of the photocatalytic reaction due to the high initial concentration of MO. Based on the Langmuir-Hinshelwood kinetics model ($-r_A = k_{app}C_A$), the reaction rate was directly proportional to the concentration of MO. Therefore, at the start of the photocatalytic reaction, MO has its maximum concentration, resulting in a higher

reaction rate. As the reaction proceeds, MO concentration decreases over time, which reduces the reaction rate.

Figure A.13 shows the UV-Vis absorption spectra of MO removal under the optimal conditions: MO concentration = 5 mg/L, Ag/TiO_2@PUF amount = 0.4:200 g/mL, pH = 4, and irradiation time = 90 min. The maximum absorption peak of MO was observed at 464 nm, which decreased to nearly zero during 90 min irradiation time. This suggests the potential cleavage of the azo group (–N=N–) in the MO structure [378], resulting in the complete removal of MO after 90 min. In addition, we investigated ICP-OES analysis for the leaching of Ti and Ag elements from Ag/TiO_2@PUF during MO removal under optimal conditions. According to the results, Ti and Ag were not observed (limit of detection of 0.000028 ppm for Ti and 0.0007 ppm for Ag) in the solution, suggesting that the metals were not released from the photocatalyst.

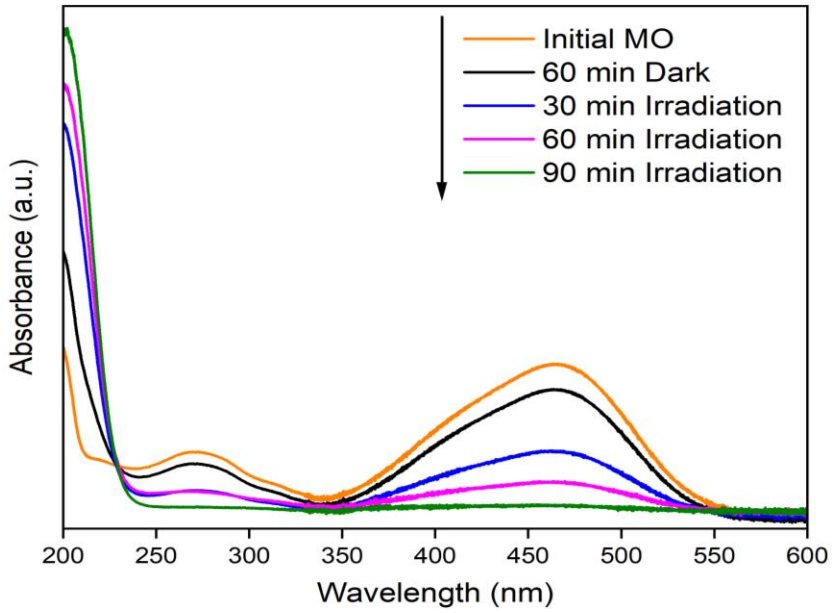

Figure A.13 UV-Vis absorption spectra of MO removal under the optimal conditions (MO concentration = 5 mg/L, Ag/TiO_2@PUF amount = 0.4:200 g/mL, pH = 4, and irradiation time = 90 min)

Possible mechanism of MO removal by Ag/TiO_2@PUF

We proposed the possible mechanism of photocatalytic MO removal using Ag/TiO_2@PUF under simulated sunlight irradiation (Figure A.14). According to Equation A.11, electrons in the valence band (VB) of TiO_2 were excited by simulated solar light and then migrated to the conduction band

(CB) of TiO_2, creating positively charged holes in the VB and negatively charged electrons in the CB of TiO_2. From the XPS results, Ag existed on the surface of TiO_2 as Ag^0. At the same time, the metallic silver absorbed sunlight irradiation and created hot electrons by means of the LSPR effect (Equation A.12) [338, 379, 380]. The creation of hot electrons corresponded to forming Ag^+, which participated in an oxidation reaction to produce $^{\bullet}OH$ (Equation A.13). The hot electrons of Ag^0 had more negative energy than the CB of TiO_2 (-0.5 V vs. NHE [381]), so they migrated to the CB of TiO_2 and reacted with oxygen to form $^{\bullet}O_2^-$ (Equation A.14). In addition, oxidized silver (Ag_2O or AgO) was present in the photocatalyst surface, which can contribute to removing MO. Ag^{+n} (Ag^{+1} or Ag^{+2}) had more positive band energy (0.8 V vs. NHE [382]) than TiO_2. Under sunlight irradiation, excited electrons from the VB of TiO_2 moved to Ag^{+n} by interfacial charge transfer (IFCT) [363, 380]. The IFCT improves the separation of electron-hole pairs and contributes to MO removal by generating reactive oxygen species [363]. The existing electrons in the CB of TiO_2 and Ag^{+n} participated in the reduction reaction and converted O_2 to $^{\bullet}O_2^-$ (Equation A.14). Consequently, the presence of Ag in TiO_2 not only improves the photoinduced charge generation but also suppresses the electron-hole pairs recombination [339, 340, 380]. Simultaneously, the photoinduced holes on the VB of TiO_2 participated in an oxidation reaction and converted H_2O into $^{\bullet}OH$ (Equation A.15). Eventually, the generated reactive species (i.e., $^{\bullet}O_2^-$ and $^{\bullet}OH$) can react with MO and convert it into CO_2 and H_2O (Equations A.16 and A.17). Moreover, as shown in Equation A.18, the photoinduced holes on the VB of TiO_2 can convert MO into CO_2 and H_2O directly.

$$TiO_2 + h\nu \rightarrow h_{VB}^+ + e_{CB}^- \quad \text{(A.11)}$$

$$Ag^0 + h\nu \rightarrow Ag^+ + \boldsymbol{e}^- \quad \text{(A.12)}$$

$$Ag^+ + H_2O \rightarrow {}^{\bullet}OH + H^+ \quad \text{(A.13)}$$

$$e_{CB}^- + O_2 \rightarrow {}^{\bullet}O_2^- \quad \text{(A.14)}$$

$$h_{VB}^+ + H_2O \rightarrow {}^{\bullet}OH + H^+ \quad \text{(A.15)}$$

$$^{\bullet}O_2^- + MO \rightarrow CO_2 + H_2O \quad \text{(A.16)}$$

$$^{\bullet}OH + MO \rightarrow CO_2 + H_2O \quad \text{(A.17)}$$

$$h_{VB}^+ + MO \rightarrow CO_2 + H_2O \quad \text{(A.18)}$$

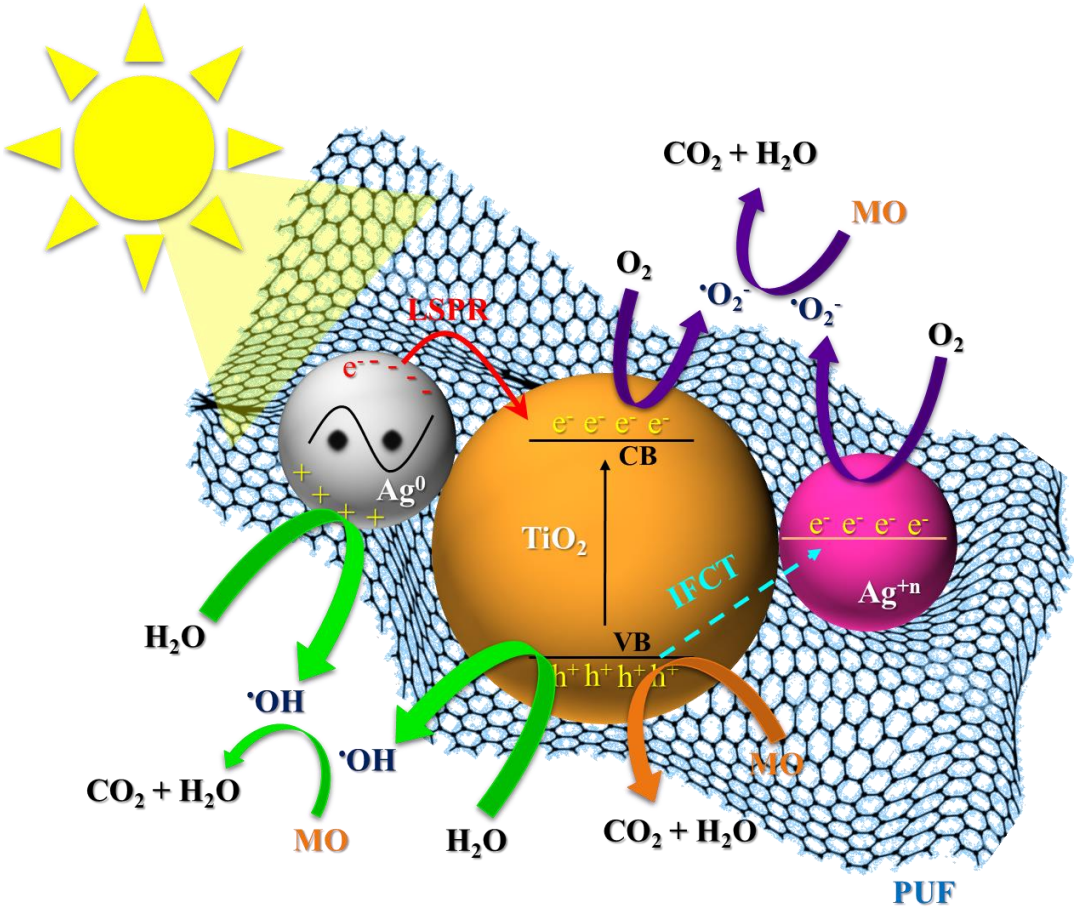

Figure A.14 Schematic of the possible mechanism for MO removal with Ag/TiO_2@PUF under simulated sunlight irradiation

Figure A.15(a) shows free radical scavenging experiments performed under optimal conditions to evaluate the contribution of each reactive species to the photocatalytic MO removal. Figure A.15(a) shows that adding BQ as a $^{\bullet}O_2^-$ scavenger decreased MO removal from 100% to 45%, indicating a 55% reduction in the removal efficiency by $^{\bullet}O_2^-$. In addition, 55% of MO was removed in the presence of EDTA as a h^+ scavenger. To determine the direct and indirect contributions of h^+, IPA as a $^{\bullet}OH$ scavenger was added to the floating system, causing a 26% reduction in the MO removal. Thus, h^+ had a 19% contribution to remove MO directly and the contribution of $^{\bullet}OH$ was 26%. Also, $^{\bullet}O_2^-$ was the main reactive species in MO removal with a 55% contribution, as depicted in Figure A.15(b).

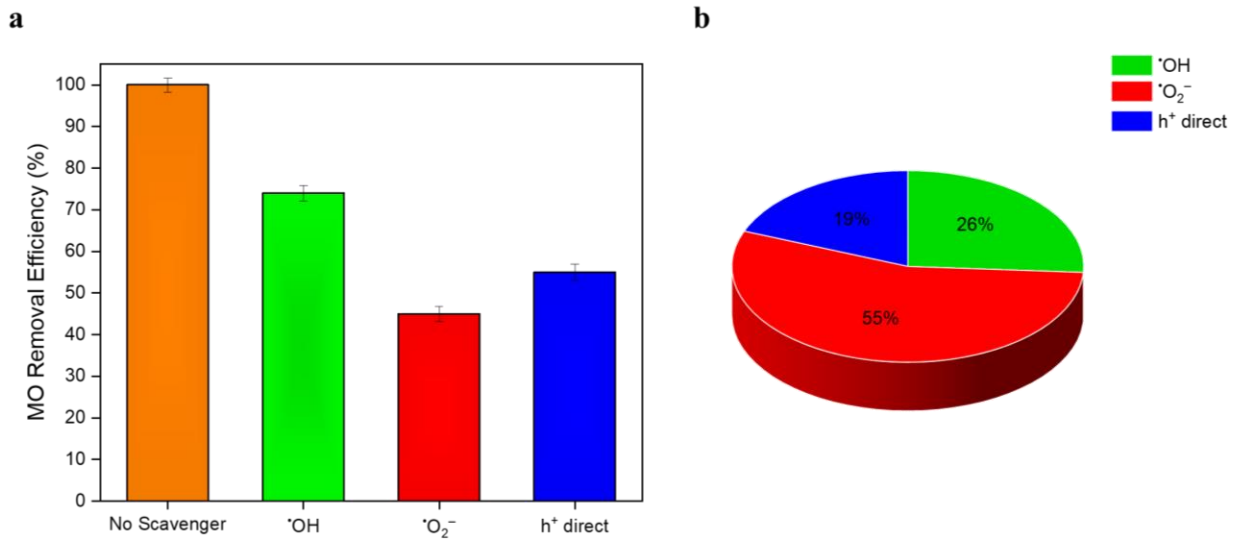

Figure A.15 (a) Free radical scavenging experiments and (b) reactive species contribution on MO removal using Ag/TiO_2@PUF under optimal conditions

Figure A.16(a) shows the LC-MS chromatograms for the photocatalytic degradation of MO under optimal conditions (MO concentration = 5 mg/L, Ag/TiO_2@PUF amount = 0.4:200 g/mL, pH = 4, and irradiation time = 90 min). Initially, a strong peak was observed at m/z = 304, which belongs to MO. After 30 min of degradation, the MO peak decreased, while some new peaks appeared, which were attributed to the degradation products of MO. After 60 min, all the peaks gradually decreased and finally disappeared at 90 min. Figure A.16(b) depicts intermediates generated after 30 min of MO degradation, with identified peaks at m/z = 320, 306, 290 and 276. The intermediate compounds of m/z = 320 and m/z = 306 are related to the monohydroxylated product of MO and the oxidation in the aromatic ring of MO, respectively [383]. Also, the detected compounds with m/z = 290 and m/z = 276 correspond to demethylated products of MO [384, 385]. According to the literature, further photocatalytic degradation of MO can lead to the mineralization of these intermediates, forming CO_2 and H_2O [384-387].

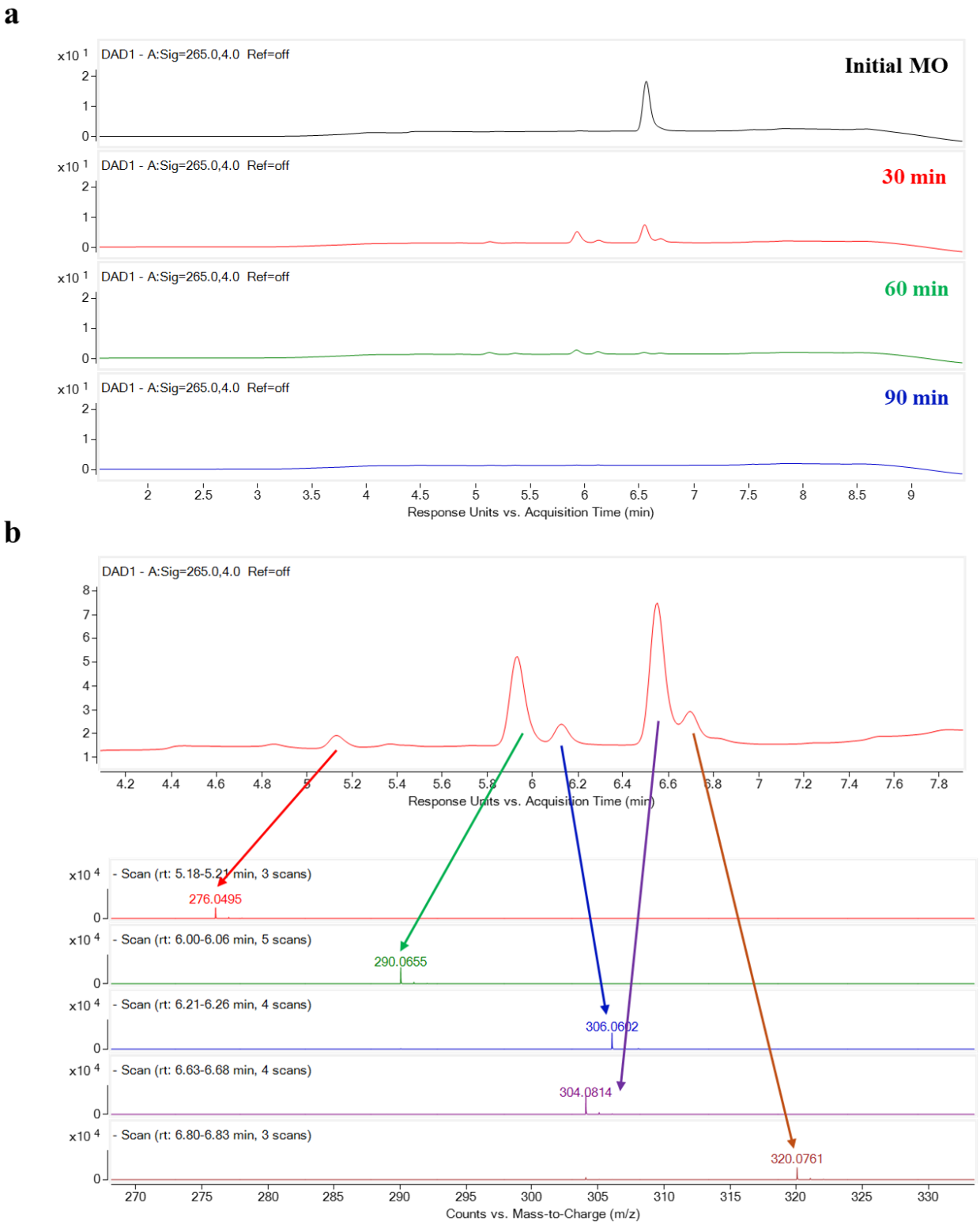

Figure A.16 (a) LC-MS chromatograms of MO degradation for 0 min, 30 min, 60 min, and 90 min under optimal conditions and (b) identified intermediates from MO degradation after 30 min

Comparison of floating Ag/TiO_2@PUF for MO removal with previous work

Table A.3 reports a comparison of the present work with other recent studies for the photocatalytic removal of MO. Based on Table A.3, only one study utilized a floating photocatalytic system for MO removal. Swathi et al. [374] synthesized floating g-C_3N_4 photocatalysts supported on PUF, removing 75.1% of MO after 240 min of irradiation. In another study [388], the removal efficiency of MO was 97.9% by suspended TiO_2/biochar photocatalysts after 270 min based on pseudo first-order kinetics. In this work, our floating Ag/TiO_2@PUF photocatalyst was efficient in eliminating MO after 90 min of simulated sunlight irradiation.

Table A.3 Recent literature review on the photocatalytic removal of MO

Photocatalytic system	Photocatalyst	Synthesis method	Pollutant	Reaction time	Removal efficiency	Kinetics	Ref.
Floating	g-C_3N_4 on PUF (30 mg/L)	Thermal decomposition and dip coating	MO (5 mg/L)	240 min (LED lamp)	75.1%	Pseudo first-order ($k = 0.0032\ min^{-1}$)	[374]
Suspension	Fe_3O_4/GO (0.150 g/40 mL)	Co-precipitation, modified Hummers, and ultrasonication	MO (10 mg/L)	240 min (UV light)	99%	NA	[389]
Suspension	g-C_3N_4/ZnO (2 g/L)	Thermal polycondensation	MO (NA)	120 min (Solar light)	98%	NA	[390]
Suspension	TiO_2/biochar (6 g/L)	High-temperature pyrolysis, sol-gel, and ultrasonic-assisted vacuum impregnation	MO (50 mg/L)	270 min (Xenon lamp)	97.9%	Pseudo first-order ($k = 0.00769\ min^{-1}$)	[388]
Suspension	Sn-doped TiO_2 (0.5 g/L)	Microwave-assisted sol-gel	MO (1×10^{-5} M)	180 min (UV light)	94%	NA	[391]
Floating	Ag/TiO_2@PUF (0.4:200 g/mL)	Ultrasound-assisted sol-gel followed by spray drying and ultrasound-assisted impregnation	MO (5 mg/L)	90 min (Simulated sunlight)	100%	First-order ($k = 0.050\ min^{-1}$)	Present work

Conclusion

We fabricated suspended and floating TiO_2 and Ag/TiO_2 photocatalysts using an ultrasound-assisted sol-gel method, followed by spray drying to remove MO. The results showed the uniform deposition of the photocatalysts onto the floating PUF due to the ultrasonication in the impregnation synthesis method. The decoration of Ag on TiO_2 extends its absorption into the visible-light range. Ag/TiO_2 had a mixed-phase, and its BET surface area increased to 30 m^2/g, which was three times higher than TiO_2. The existence of Ag in TiO_2 for both suspended and floating systems increased MO removal efficiency. Floating Ag/TiO_2@PUF had more photocatalytic activity than suspended Ag/TiO_2, removing 89% of MO after five consecutive cycles. In addition, MO was completely removed with Ag/TiO_2@PUF under optimal conditions as MO concentration = 5 mg/L, photocatalyst amount = 0.4:200 g/mL, pH = 4, and irradiation time = 90 min (300 W commercial solar lamp with an intensity of 35 W/m^2). Moreover, MO removal by Ag/TiO_2@PUF followed first-order kinetics ($k_{app,\ Maximum}$ = 0.050 min^{-1}), and the main reactive species involved in MO removal was $^{\bullet}O_2^-$ (55%). Our results suggest that Ag/TiO_2@PUF constitutes a promising approach to removing coloured organic pollutants from wastewater. Due to the photocatalytic properties of Ag/TiO_2@PUF, we suggest applying this floating photocatalyst to treat other aqueous organic pollutants. Future work can focus on either modifying the elemental composition of the photocatalyst or adding oxidants like H_2O_2 to decrease the activation energy for the MO removal and consequently decrease the degradation process time.

Acknowledgments

The authors thank the Velux Stiftung Foundation for the financial support through project 1381, “SUNFLOAT - Water decontamination by sunlight-driven floating photocatalytic systems”. We also appreciate the support of Bourse d'excellence Neil R. Mitchell et Danièle Dumais.

APPENDIX B ARTICLE 6: RECENT PROGRESS ON TI-BASED PIEZO-PHOTOCATALYSTS FOR WASTEWATER TREATMENT

Nila Davari[1], Javad Vahabzadeh Pasikhani[2], Claudia L. Bianchi[3,4], Viviane Yargeau[5], Daria C. Boffito[1,6*]

[1] Department of Chemical Engineering, Polytechnique Montréal, Montréal, Canada

[2] Process Engineering Advanced Research Lab (PEARL), Department of Chemical Engineering, Polytechnique Montréal, Université de Montréal, PO Box 6079, Stn Centre-Ville, Montréal, QC, H3C 3A7, Canada

[3] Department of Chemistry, University of Milan, Milan, Italy

[4] Consorzio Interuniversitario Nazionale per la Scienza e Tecnologia dei Materiali (INSTM), via Giusti 9, 50121, Florence, Italy

[5] Department of Chemical Engineering, McGill University, Montréal, Canada

[6] Canada Research Chair in Engineering Process Intensification and Catalysis

The article was published in Current Opinion in Chemical Engineering, Volume 47, March 2025, 101090, Available online since January 20, 2025.

Author contributions

Nila Davari: Conceptualization, Methodology, Formal analysis, Investigation, Writing – original draft, Visualization. Javad Vahabzadeh Pasikhani: Conceptualization, Methodology, Software, Formal analysis, Investigation, Writing – original draft, Visualization. Claudia L. Bianchi: Methodology, Investigation, Writing – Review & Editing, Project administration, Funding acquisition. Viviane Yargeau: Methodology, Investigation, Writing – Review & Editing, Supervision, Project administration. Daria C. Boffito: Methodology, Investigation, Resources, Writing – Review & Editing, Supervision, Project administration, Funding acquisition.

Abstract

Piezo-photocatalysis has emerged as a promising hybrid advanced oxidation process to eliminate resistant organic pollutants in wastewater via harnessing light irradiation and mechanical vibration. This process offers a synergistic enhancement of photocatalytic efficiency by coupling piezo-electricity with photocatalytic activity, addressing limitations of conventional photocatalysis, including rapid electron-hole pairs recombination and deactivation in the absence of illumination. We concisely review recent advancements in Ti-based piezo-electric semiconductors for wastewater treatment, focusing on research from 2020 to 2025. The studies included in this review are based on materials categorized into two main groups: integrated Ti-based piezo-photocatalysts and hybrid piezo-electric materials-incorporated TiO_2 photocatalysts. We critically discuss the impact of piezo-potential and corresponding internal electric fields on photoinduced charge separation and reactive oxygen species generation. Methodologies for assessing the piezo-electric and photocatalytic properties are explored. This review highlights piezo-photocatalysis's potential applications and challenges, offering insights into future developments in advanced oxidation processes for wastewater treatment.

Keywords: Advanced Oxidation Processes, Photocatalysts, Piezo-photocatalysts, Ti-based Materials, Ultrasound

Introduction

Inspired by natural photosynthesis, photocatalysis is a sustainable process in which a semiconductor absorbs photon energy from light irradiation and transforms it into various redox reactions [191]. TiO_2 stands out as an n-type semiconductor that drives the generation of reactive oxygen species (ROS) in wastewater treatment. Anatase TiO_2, with a bandgap energy of 3.2 eV, comprising a valence band potential (VB) at 2.59 eV and a conduction band potential (CB) at -0.66 eV versus NHE, exhibits a favourable alignment with the redox potential of various organic compounds, making it a highly suitable photocatalyst to eliminate organic pollutants [392, 393].

A new concept in photocatalytic wastewater treatment that has emerged from 2015 is integrating piezo-electric materials with semiconductors, forming piezo-photocatalysts. Piezo-electric materials generate electric charges in response to mechanical stress, which influences photocatalytic mechanisms by promoting charge separation, enhancing redox potential, and

generating a dynamic piezo-electric field. The mechanical stress induced by ultrasound causes deformation in piezo-electric materials, producing a localized electric field. This field, especially under oscillating mechanical forces, prevents shielding by free carriers, maintaining long-term activity and improving pollutant elimination. The localized electric field generated by piezo-electric materials facilitates the transfer of photogenerated electron-hole pairs to the catalyst surface, where they interact with water and oxygen to generate ROS, leading to the degradation of resistant organic pollutants [394, 395].

Figure B.1(a) depicts research conducted on piezo-photocatalytic wastewater treatment from 2020 to 2025 based on bibliometric keywords. Piezo-electric materials are categorized into single crystals (e.g., quartz, Rochelle salt, tourmaline), ceramics (e.g., $Pb[Zr,Ti]O_2$, $BaTiO_3$, $LiNbO_3$), semiconductors (e.g., ZnS, SnO, g-C_3N_4), polymers (e.g., polyvinylidene fluoride (PVDF), polyacrylonitrile (PAN)), and organic materials (e.g., silk, wood, bone, enamel) [396-398]. Each category exhibits excellent properties utilized for enhanced photocatalytic performance. Perovskite materials, such as $BaTiO_3$, $BiTiO_3$, $MgTiO_3$, $SrTiO_3$, and $CaTiO_3$ [399, 400], are known for their high piezo-electric coefficients and strong electric fields generated under mechanical stress that exhibit excellent candidacy for piezo-photocatalysis. Ti-based piezo-electric materials with a perovskite structure are directly utilized as an integrated piezo-photocatalyst for wastewater treatment. Constructing hybrid piezo-electric materials with TiO_2 is another classification of Ti-based piezo-photocatalyst that efficiently eliminates organic pollutants from wastewater.

Herein, we comprehensively examined the latest advancements in Ti-based piezo-photocatalysts from 2020 to 2025, focusing on their potential for wastewater treatment under illumination combined with ultrasonication. By addressing the fundamental mechanisms, band energy alignment, and ROS generation, we provided insight into how the synergetic effects of piezo-electricity and photocatalysis can overcome the limitations of conventional TiO_2 photocatalysts in wastewater treatment. Given this aim, we divided this short review into five key sections. The *Principles of Photocatalysis and Piezo-photocatalysis* section introduces the fundamental mechanisms driving these processes, emphasizing how piezo-electric potential and internal electric fields enhance charge separation and ROS generation. The *Ti-based Integrated Piezo-photocatalysts* section discusses materials with intrinsic piezo-electric and photocatalytic properties, highlighting their electronic and crystal structures, morphologies, and synthesis methods for pollutant removal. The *Modification of Ti-based Integrated Piezo-photocatalysts*

section explores various strategies, including the incorporation of metals, non-metals, and secondary semiconductors, to improve the piezo-electric and photocatalytic performance of Ti-based integrated piezo-photocatalysts. The *Hybrid Piezo-TiO_2 Photocatalysts* section focuses on composites of piezo-electric materials with TiO_2 photocatalysts, detailing their structures, mechanisms, and applications for wastewater treatment. Finally, the *Conclusions and Prospects* section summarizes the advancements discussed, identifies current challenges, and provides an outlook for future directions.

Principles of Photocatalysis and Piezo-photocatalysis

Upon irradiation of a semiconductor, VB electrons are excited to the CB if the photon energy matches or exceeds the bandgap energy. These electron-hole pairs participate in redox reactions upon reaching the photocatalyst's surface. Directly, photogenerated holes oxidize organic pollutants. Indirectly, the electron-hole pairs oxidize water into $^{\bullet}OH$ and reduce dissolved oxygen into $^{\bullet}O_2^-$. These reactive species degrade pollutants into CO_2 and H_2O (Figure B.1(b)) [72].

The piezo-catalytic process represents a new advanced oxidation method that converts external mechanical energy into electrical energy, subsequently driving chemical reactions. Applying strain on materials with non-centrosymmetric crystals induces surface polarization (Figure B.1(c)). If the piezo-electric potential exceeds 3V, polarized charges separate and drive redox reactions. Two main mechanisms govern piezo-catalysis: the energy band theory and screening charge effect theory [401, 402]. The former applies to semiconductors such as $BaTiO_3$, $BiFeO_3$, ZnO, CdS, g-C_3N_4, MoS_2, and ZnS, while the latter explains catalysis in insulating materials like quartz.

Conventional photocatalytic processes for wastewater treatment are limited by their reliance on light irradiation and the rapid recombination of photogenerated electron-hole pairs. Piezo-catalysis, through mechanical stimulation, offers an alternative but demands continuous strain, risking material integrity. Combining photocatalysis and piezo-catalysis results in piezo-photocatalysis. This approach utilizes the piezo-electric potential generated under mechanical stress in piezo-electric materials as a continuous driving force to enhance the separation of photogenerated charge carriers, thereby boosting photocatalytic efficiency (Figure B.1(d)). It also extends semiconductor activity into visible light. This method benefits from efficiency, stability, low energy demands, strong oxidation potential, and minimal secondary pollution.

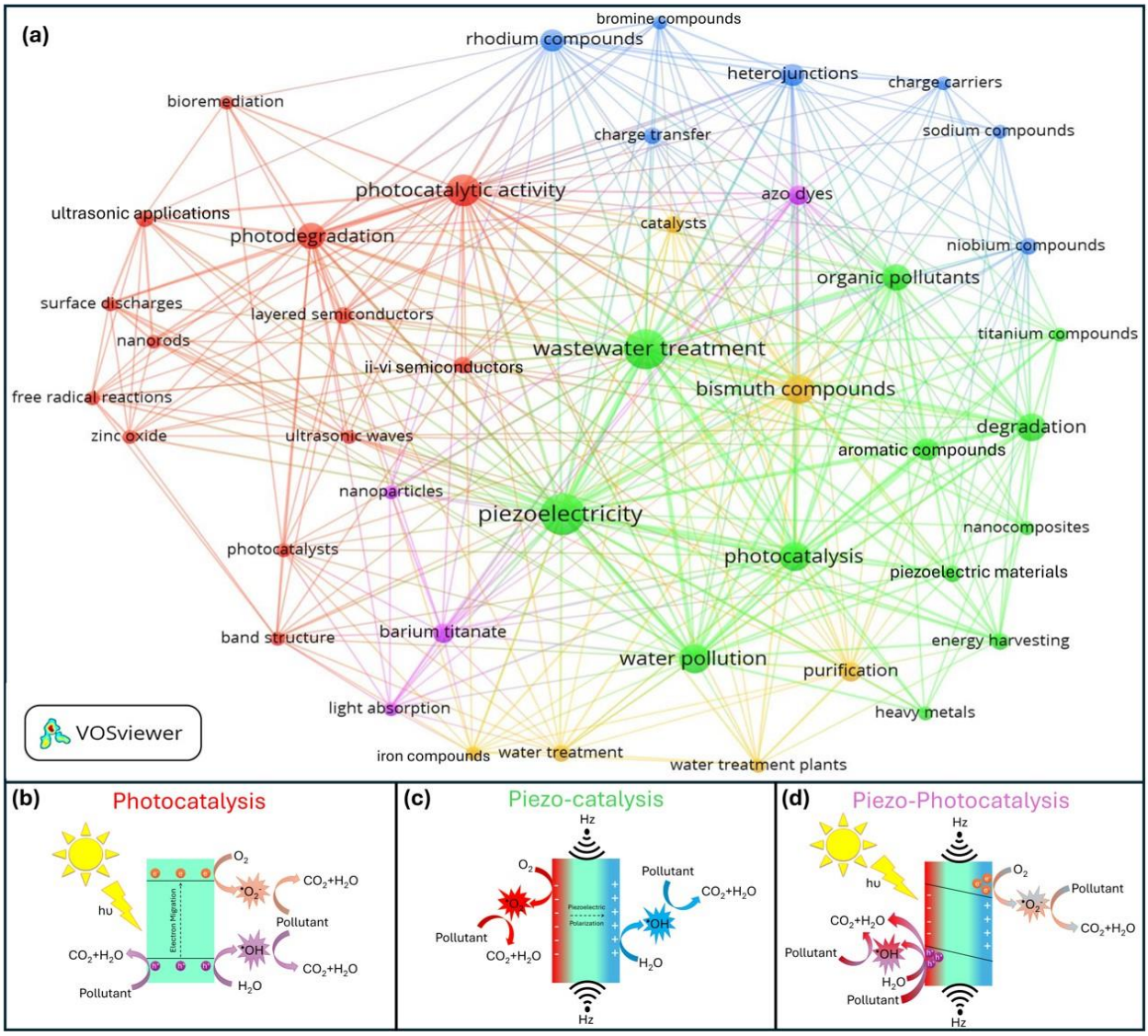

Figure B.1 (a) Bibliometric map of keywords created with VOSviewer software containing 42 frequent keywords on piezo-photocatalytic wastewater treatment classified into 5 clusters. The data were extracted from 111 articles indexed in Engineering Village from 2020 to 2025. The size of labels and circles in the map represent the weight of keywords co-occurrence in the articles. Piezo-electricity and photocatalytic activity are the dominant circles in green and red clusters, with total link strengths of 115 and 62. Bismuth compound (yellow cluster) linked with titanium compound (green cluster) and barium titanate (pink cluster) are the most common Ti-based piezo-photocatalysts reported in the literature. And wastewater treatment based on (b) photocatalysis, (c) piezo-catalysis, and (d) piezo-photocatalysis mechanisms

Ti-based Integrated Piezo-photocatalysts

Ti-based integrated piezo-photocatalysts are semiconductors with both photocatalytic and piezo-electric properties, where a built-in electric field facilitates charge carrier movement and suppresses recombination. Perovskite materials combine high piezo-electric coefficients with strong ferroelectric properties, allowing them to generate piezo-electric potential under strain and maintain stable polarization even without an external field. Such characteristics are necessary for effective piezo-photocatalytic performance, which enhances charge separation and reduces recombination, thus improving pollutant degradation [396, 403]. In addition, Ti-based piezo-photocatalysts offer superior mechanical stability compared to ZnO or polymer systems, ensuring long-term durability under cyclic strain. Unlike Pb-based or metal chalcogenide piezo-photocatalysts, Ti-based variants are environmentally benign, making them ideal for sustainable environmental remediation and green hydrogen production applications. Table B.1 reports a summary of recent advancements (2020-2025) in Ti-based piezo-photocatalysts under combined irradiation and ultrasonication, including integrated, modified integrated piezo-photocatalysts, and hybrid piezo-TiO_2 photocatalysts for wastewater treatment.

Table B.1 Ti-based piezo-photocatalysts for pollutant removal

Category	Catalyst	Synthesis method (morphology)	Conditions	Pollutant	Removal efficiency
Integrated piezo-photocatalyst	$BaTiO_3$ [397]	Hydrothermal (nanowires)	Ultrasound (180 W) UV-LED light (4.2 W)	Methyl Orange	~98.2%
	$Bi_4Ti_3O_{12}$ [404]	Hydrothermal (nanosheets)	Ultrasound (900 W) Simulated solar light (100 mW/cm^2)	Rhodamine B	~99.4%
Modified integrated piezo-photocatalyst	$BaTiO_3$@TD-COF [405]	Polycondensation (core-shell structured spheres)	Ultrasound (180 W) UV-Vis light (200 W)	Bisphenol A	100%
	Nb-$Bi_4Ti_3O_{12}$ [406]	Hydrothermal (nanosheets)	Ultrasound (240 W) UV-Vis light (300 W)	Rhodamine B	94%
	Nd-$Bi_4Ti_3O_{12}$ [407]	Hydrothermal (microspheres)	Ultrasound (200 W) UV-Vis light (300 W)	Rhodamine B	97.5%
	BiOBr/ $BaTiO_3$ [408]	Chemical precipitation (irregular particles adhered to nanosheets)	Ultrasound (40 kHz) UV-Vis light (300 W)	Rhodamine B Mitoxantrone Methyl Orange Ciprofloxacin	100% 96% 97% 82%

Table B.1 Ti-based piezo-photocatalysts for pollutant removal (cont'd)

Category	Catalyst	Synthesis method (morphology)	Conditions	Pollutant	Removal efficiency
Modified integrated piezo-photocatalyst	$Bi_4Ti_3O_{12}$-$SrBi_4Ti_4O_{15}$ [409]	Hydrothermal (nanosheets)	Ultrasound (240 W) UV-Vis light (300 W)	Rhodamine B	100%
	$Bi_{0.5}Na_{0.5}TiO_3$/PVDF [398]	Sol-gel-electrospinning (nanofibers)	Ultrasound (200 W) UV-Vis light (300 W)	Rhodamine B	90.8 %
Hybrid piezo-TiO_2 photocatalyst	$BaTiO_3$-TiO_2 [410]	Chemical bath (core-shell structured nanowires)	Ultrasound (200 W) UV-Vis light (300 W)	Rhodamine B Methylene Blue Indigo Carmine	99.5% 99.8% 99.7%
	TiO_2/ZnS [411]	Solvothermal (nanospheres)	Ultrasound (40 kHz) Visible light (300 W)	Xanthate	98.6%
	ZnO-TiO_2 [412]	Chemical bath method (nanocomposite film)	Ultrasound (80 W) UV light (100 W)	Methylene Blue	99%

Selecting a suitable piezo-photocatalyst requires materials with high piezo-electric coefficients and photocatalytic properties that generate electric potential under mechanical stress and possess an appropriate bandgap for efficient light absorption, electron-hole pairs generation, and coverage of redox potential for reactions of organic pollutants. Piezo-electric properties are analyzed by piezoresponse force microscopy (PFM), Quasi-static d33 meters, the Berlincourt method, laser doppler vibrometry (LDV), and electrochemical impedance spectroscopy (EIS). The photocatalytic activity relies on the optical properties of semiconductors. The bandgap energy, electron excitation from the VB of semiconductors in the UV or visible regions, photoinduced charge separation, electron-hole recombination, photocurrent density, photocurrent response, and photoconversion efficiency can be characterized and quantified by diffuse reflectance spectroscopy (DRS), photoluminescence (PL) spectroscopy, and voltammetry (i.e., linear sweep voltammetry (LSV) and chronoamperometry) analyses.

Ti-based perovskite materials are defined by the chemical structure of $XTiO_3$, which exhibits a cubic crystal structure with a high-symmetry phase. These materials involve titanium as a primary cation located at the center of each octahedron and a central cation (X) surrounded by oxygen. Figure B.2(a) presents $CaTiO_3$ as one of the typical titanate perovskites [413].

The morphology of Ti-based piezo-electric materials plays a critical role in determining their piezo-catalytic activities. Common morphologies that have been reported so far include zero-dimensional (0D: particles), one-dimensional (1D: wires, fibers, rods), two-dimensional (2D: sheets, plates, films), and three-dimensional (3D: spheres) nano/micro structures. These material structures can be synthesized by different methods such as solid-state reactions, hydrothermal, solvothermal, electrospinning, sol-gel, chemical vapour deposition, flame-based synthesis, anodic aluminum oxide template, and molten salt [399]. The influence of morphology on piezo-catalytic performance has been investigated by some researchers. Yu et al. [414] studied the effect of $BaTiO_3$ nanostructures synthesized by hydrothermal methods on Rhodamine B degradation and H_2 production. $BaTiO_3$ nanosheets demonstrated superior piezo-catalytic activity, achieving a degradation rate constant of 0.1279 min^{-1} compared to nanowires and nanoparticles. This enhancement is attributed to the higher piezo-electric potential of 2D nanostructures, which can undergo greater mechanical deformation under ultrasonication, thereby generating stronger piezo-electric effects. Similarly, Cheng et al. [415] explored the impact of different morphologies on the piezo-catalytic performance of $Bi_4Ti_3O_{12}$ synthesized by hydrothermal and molten salt methods.

Among hierarchical microrods, microplates, and hierarchical microspheres, $Bi_4Ti_3O_{12}$ microplates exhibited the highest activity by degrading 94% of Methylene Blue, 82% of Tetracycline Hydrochloride, and 64% of Tetrabromobisphenol A with an apparent rate constant of 0.01735 min^{-1}, 0.01077 min^{-1}, 0.00731 min^{-1}, respectively. The superior performance of the microplates results from their larger active surface area and higher mechanical deformation under external stress, which enhances charge separation and ROS generation.

Among integrated Ti-based piezo-photocatalysts, $BaTiO_3$ with a tetragonal structure (P4mm space group) stands out for its chemical stability, cost, ease of synthesis, high dielectric constant, and high refractive index [416, 417]. $BaTiO_3$ nanostructures, especially with nanotubular morphology, exhibit a d_{33} of 45 pC/N [396]. The structure of $BaTiO_3$ is responsive to external stress that generates a piezo-electric effect. This response results from the strong interaction between the Ti d-orbital and O p-orbital, as well as the presence of ionic/covalent bonds for Ba and O atoms [418]. The colour contrast in 3D amplitude and phase images of $BaTiO_3$ (Figures B.2(b) and B.2(c)) indicate a piezo-electric response by polarized domains [416]. Figure B.2(d) shows a butterfly-like curve in amplitude-voltage response and a 180° phase shift in phase-voltage hysteresis [419], confirming the ferroelectric behaviour of $BaTiO_3$, which drives its piezo-catalytic activity in advanced oxidation processes (AOPs). $BaTiO_3$ exhibits an absorption peak around 395 nm, corresponding to a bandgap energy of 3.22 eV (Figure B.2(e)) [405]. Given this bandgap, its photocatalytic activity is primarily triggered by UV light. However, since only 3-8% of solar radiation falls within the UV spectrum, extending the activity of Ti-based piezo-photocatalysts into the visible light is necessary for solar-driven AOPs.

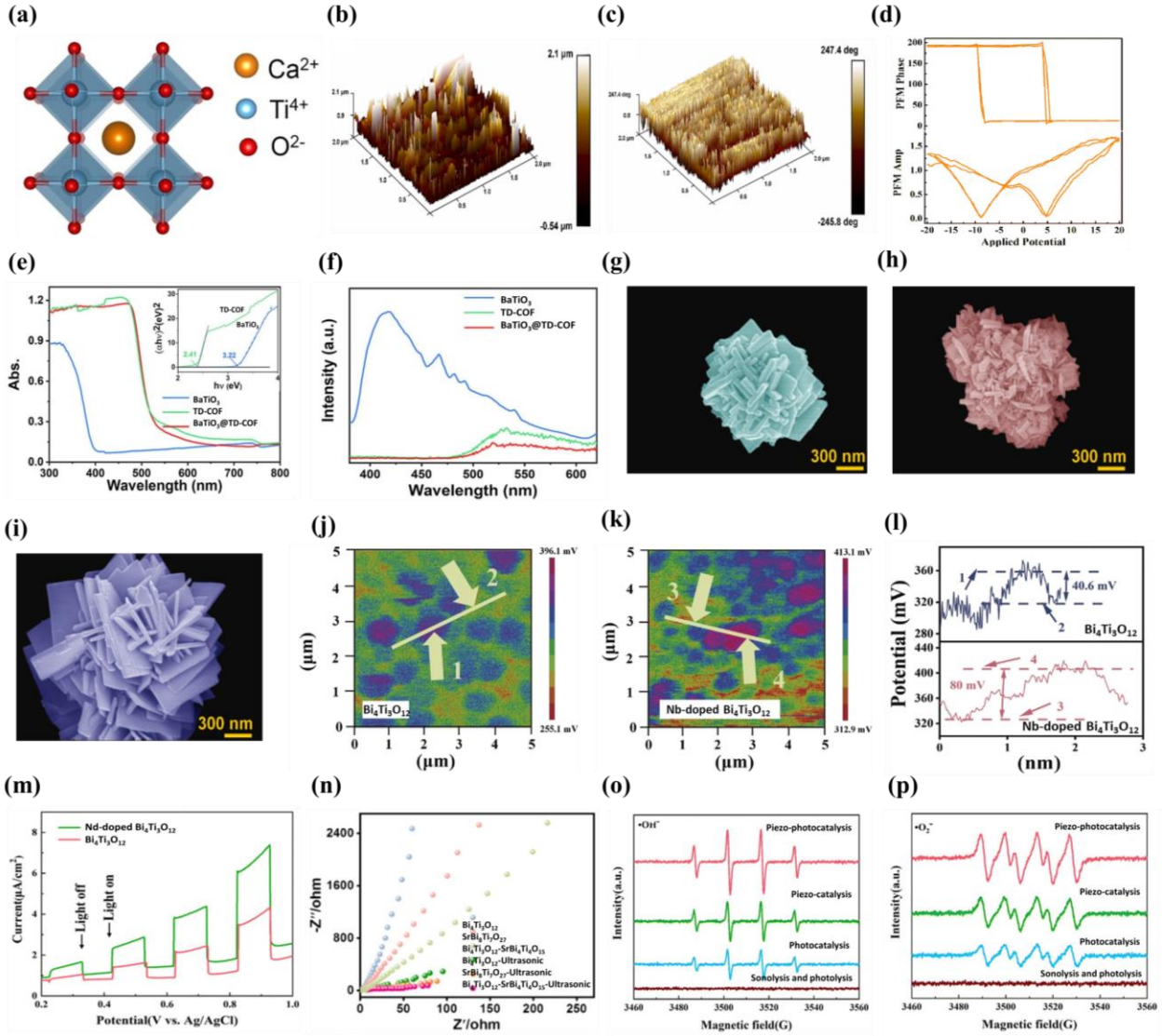

Figure B.2 (a) Crystal structure of $CaTiO_3$ as a typical Ti-based perovskite material; (b) 3D amplitude and (c) phase images of $BaTiO_3$; (d) polarization-electric field and strain-electric field loops of $BaTiO_3$; (e) DRS and (f) PL spectra of $BaTiO_3$, TD-COF, and $BaTiO_3$@TD-COF; (g-i) SEM images of $Bi_4Ti_3O_{12}$, $SrBi_8Ti_7O_{27}$, and $Bi_4Ti_3O_{12}$-$SrBi_4Ti_4O_{15}$; (j-l) Surface charge and charge difference profile of $Bi_4Ti_3O_{12}$ and Nb-doped $Bi_4Ti_3O_{12}$; (m) Transient photocurrent responses of $Bi_4Ti_3O_{12}$ and Nd-doped $Bi_4Ti_3O_{12}$; (n) EIS Nyquist plots of $Bi_4Ti_3O_{12}$, $SrBi_8Ti_7O_{27}$, and $Bi_4Ti_3O_{12}$-$SrBi_4Ti_4O_{15}$ without and with ultrasonic vibration; (o, p) ESR spectra of $^{\bullet}OH$ and $^{\bullet}O_2^-$ generated by Nd-doped $Bi_4Ti_3O_{12}$

Reprinted with permission from (a) [413]. (b, c) [416]. (d) [419]. (e, f) [405]. (g-i) [409]. (j-l) [406]. (m) [407]. (n) [409]. (o, p) [407].

Modification of Ti-based Integrated Piezo-photocatalysts

Over recent decades, the optical properties of TiO_2 have been enhanced for wastewater treatment by doping with non-metals (e.g., C, N, B, F) or metals (e.g., Ag, Au, Cu, Co, Pd) [129] to narrow its bandgap by introducing new energy states near the VB or CB. Another approach involves coupling TiO_2 with secondary semiconductors (e.g., WO_3, Bi_2O_3, Fe_2O_3) to form Z-scheme, S-scheme, or heterojunction structures [420], reducing its bandgap and electron-hole pairs recombination rate. The optical and piezo-electric properties of integrated Ti-based piezo-photocatalysts have been improved through crystal phase transition (e.g., Ba_2TiO_4, $Bi_4Ti_3O_{12}$, $BaBi_4Ti_4O_{15}$) [404, 421, 422], metal cation incorporation (e.g., $SrBi_4Ti_4O_{15}$, $Bi_{0.5}Na_{0.5}TiO_3$, Bi_3TiNbO_9) [409, 423, 424], metal doping (e.g., Nd, Nb, Ce, Ag, Pt, Fe) [406, 407, 425-428], and secondary semiconductor integration (e.g., CoO_x, ZnO, CuO, SnO_2, Ag_2O, BiOBr) [408, 412, 429-432]. Growing covalent organic frameworks (TD-COF) on $BaTiO_3$ [405] resulted in narrower bandgap energy (2.41 eV) than that of $BaTiO_3$ (3.22 eV) and lowered the PL spectrum compared to $BaTiO_3$, indicating improved photoinduced charge separation and enhanced visible light absorption in the composite photocatalyst (Figures B.2(e) and B.2(f)). This incorporation accelerates carrier migration through spontaneous polarization electric field, enhancing piezo-photocatalytic activity.

Among layered Ti-based ferroelectric materials, $Bi_4Ti_3O_{12}$ stands out due to its unique band structure that is hybridized VB of Bi 6s and O 2p orbitals and hybridized CB of Bi 6p and Ti 3d orbitals [415]. $Bi_4Ti_3O_{12}$ also has favourable ferroelectric properties with a spontaneous polarization of ~40 $\mu C/cm^2$ along the a-axis and ~4 $\mu C/cm^2$ along the c-axis [407]. The layered structure of $[Bi_2O_2]^{2+}$ and $[Bi_2Ti_3O_{10}]^{2-}$ along the c-axis allows 2D crystal growth (Figures B.2(g–i)) [409], making it deformable under mechanical vibrations. As shown in Figures B.2(j–l), Nb doping with $Bi_4Ti_3O_{12}$ [406] caused a difference in the surface potential distribution between bright and dark regions, in which Nb-$Bi_4Ti_3O_{12}$ indicated 40 mV higher surface charge potential compared to $Bi_4Ti_3O_{12}$. Nd doping enhanced the photocurrent density of $Bi_4Ti_3O_{12}$ from 4.37 to 7.44 $\mu A/cm^2$ (Figure B.2(m)) [407]. Combining $Bi_4Ti_3O_{12}$ with $SrBi_8Ti_7O_{27}$ [409] resulted in the smallest arc radius under UV-Vis light and ultrasound, implying reduced charge transfer resistance and the fastest charge migration by creating a heterojunction-structured piezo-photocatalyst (Figure B.2(n)).

Piezo-electric properties and photoresponse enhanced by metal doping or semiconductor integration increase ROS generation, improving pollutant decomposition. Figures B.2(o) and B.2(p) show the highest signals of $^{\bullet}OH$ and $^{\bullet}O_2^-$ under both ultrasonication and irradiation [407], confirming that piezo-electric polarization improves the photocatalytic performance of modified $Bi_4Ti_3O_{12}$. Wan et al. [405], Zhao et al. [407], and Yu et al. [409] reported that modified Ti-based piezo-photocatalysts ($BaTiO_3$@TD-COF, Nd-doped $Bi_4Ti_3O_{12}$, and $Bi_4Ti_3O_{12}$-$SrBi_4Ti_4O_{15}$) efficiently removed Bisphenol A and Rhodamine B from wastewater (See Table B.1).

Some layered Ti-based piezo-photocatalysts possess energy storage capabilities, making them suitable for round-the-clock wastewater treatment. In other words, these materials can store a portion of photon energy during light absorption in the form of photogenerated electrons (called reductive energy storage) or holes (called oxidative energy storage) and subsequently utilize them to maintain photocatalytic activity in the absence of light. Therefore, uninterrupted photocatalytic wastewater treatment will continue even under dark conditions. Xu et al. [404] showed that three-layer Aurivillius $Bi_4Ti_3O_{12}$ nanosheets, with photocatalytic, piezo-electric, and pyroelectric properties, degraded Rhodamine B, Methylene Blue, and Methyl Orange using solar, ultrasound, and thermal energy for continuous wastewater treatment.

Hybrid Piezo-TiO_2 Photocatalysts

The orientation of the internal electric field generated by a piezo-electric material influences photocatalytic activity. According to simulations by Liu et al. [433], when the junction between a piezo-electric and photocatalytic material is aligned perpendicularly to the built-in electric field, the charge separation efficiency is maximized, leading to more ROS generation. Current research focuses on constructing heterojunctions between n-type TiO_2 nanostructures and piezo-electric materials. The hybrid piezo-TiO_2 photocatalysts are categorized into ceramic (e.g., ZnS, $BaTiO_3$, ZnO, $Bi_{0.5}Na_{0.5}TiO_3$, $MoSe_2$, Al-doped $SrTiO_3$) [410-412, 434-436] or organic (e.g., PVDF, PAN) [437, 438] piezo-electric materials. Their selection depends on pollutant type, operational conditions, and cost. Ceramic materials excel in high-stress and chemically aggressive environments due to their superior piezo-electric activities and stabilities, though their higher cost and potential metal leaching under acidic conditions pose environmental risks. Piezo-electric polymers offer several advantages, including flexibility, lightweight properties, cost-effectiveness, and environmental safety, making them ideal for low-stress applications. Polymers such as PVDF

can generate considerable strain under minimal stress, enhancing their ease of handling, recovery, and suitability for practical applications. Despite these benefits, organic piezo-electric polymers lack the mechanical strength required for heavy-load applications and tend to deform under stress. They also have lower piezo-electric constants, faster decaying responses due to the absence of stiff grain boundaries, and limited temperature tolerance because of their low Curie temperatures. These limitations reduce energy harvesting efficiency and operational ranges compared to piezo-electric ceramics. However, exceptions like cellular polypropylene (PP), classified as ferroelectric, exhibit unique properties that broaden the applicability of organic piezo-electric polymers [437].

Figure B.3 depicts the piezo-photocatalytic synergy in $BaTiO_3$-TiO_2 [410]. $BaTiO_3$ is electrically neutral without external force (Figure B.3(a)). Under ultrasonication (Figure B.3(b)), cavitation bubbles exert pressure on $BaTiO_3$, which causes lattice deformation and creates asymmetric centers, leading to internal polarization and charge generation. This internal polarization shifts $BaTiO_3$'s CB below the reduction potential of $O_2/^{\bullet}O_2^-$ (0.33 V vs. NHE) and the VB above the oxidation potential of $OH^-/^{\bullet}OH$ (1.99 V vs. NHE), promoting charge separation and catalytic redox reactions.

Upon exposure of $BaTiO_3$-TiO_2 to light (Figure B.3(c)), the photoinduced electrons transfer to $BaTiO_3$'s CB due to its more positive potential than TiO_2, while holes migrate from $BaTiO_3$'s VB to TiO_2's VB. This heterojunction inhibits charge recombination, enhancing charge density and lifetime compared to pure $BaTiO_3$ or TiO_2. Although the migration of holes facilitates oxidation, the electrons on $BaTiO_3$'s CB are insufficient to generate $^{\bullet}O_2^-$, limiting photocatalytic performance.

To address this, a viable approach is to combine piezo-electric and photocatalytic effects (Figure B.3(d)). Under both sonication and illumination, spontaneous polarization in $BaTiO_3$ induces a surface charge in TiO_2, causing band tilting and bending. This improves charge separation, suppresses recombination, and enhances electron lifetime, boosting catalytic activity.

Voltammetry analysis can assess how coupling TiO_2 with a piezo-electric material improves its photocatalytic performance. Incorporating TiO_2 with ZnS [411] increases the photoinduced charge transfer efficiency and restricts the recombination rate due to the synergistic effect of a heterojunction structure in TiO_2/ZnS and piezo-electric potential of ZnS (Figures B.3(e–g)).

Mott-Schottky plots of $BaTiO_3$ and $BaTiO_3$-TiO_2 [410] show that the piezo-photocatalytic synergy of $BaTiO_3$-TiO_2 inhibits the electron-hole pairs recombination and increases the active charge carriers generation about 20 times higher than that of $BaTiO_3$ (Figure B.3(h)). Liu et al. [410] investigated the piezo-photocatalytic synergy effect of $BaTiO_3$-TiO_2 on dye degradation, including Rhodamine B (99.5%), Methylene Blue (99.8%), and Indigo Carmine (99.7%) (Figures B.3(i–k)). Additionally, the piezo-photocatalytic rate constant of $BaTiO_3$-TiO_2 for the Rhodamine B degradation was 0.095 min^{-1} [410], which was about four times higher than that of photocatalysis and six times higher than that of piezo-catalysis.

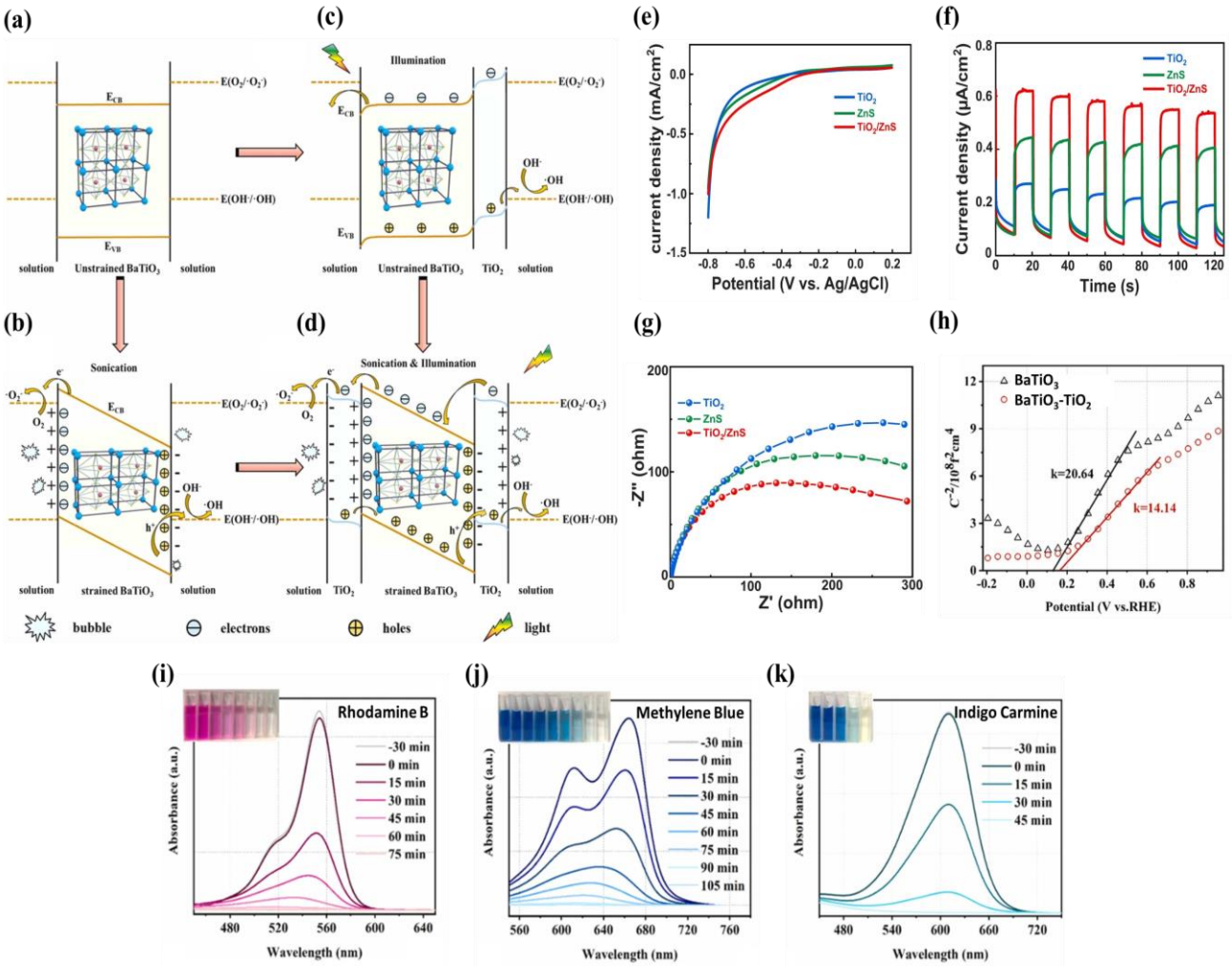

Figure B.3 Piezo-photocatalytic synergy in $BaTiO_3$-TiO_2 (a) without sonication and illumination, (b) under sonication, (c) under illumination, and (d) under sonication and illumination; (e-g) LSV curves, photocurrent responses, and EIS Nyquist plots of TiO_2, ZnS, and TiO_2/ZnS; (h) Mott Schottky plots of $BaTiO_3$ and $BaTiO_3$-TiO_2; piezo-photocatalytic synergy effect of $BaTiO_3$-TiO_2 on (i) Rhodamine B, (j) Methylene Blue, and (k) Indigo Carmine degradation

Reprinted with permission from (a-d) [410]. (e-g) [411]. (h-k) [410].

Conclusions and Prospects

The synergistic effect of piezo-electric materials and photocatalysis is a promising advancement in wastewater treatment. Piezo-electricity boosts photocatalytic activity by aligning VB and CB levels with ROS generation. $BaTiO_3$ stands out as an integrated piezo-photocatalyst capable of harnessing solar irradiation and ultrasound vibrations simultaneously. Specifically, incorporating $BaTiO_3$ with TiO_2 results in higher charge separation through band tilting and bending and enhances electron lifetime.

$BiTiO_3$ showcases another pertinent feature in this field. The crystal phase transformation of $BiTiO_3$ into $Bi_4Ti_3O_{12}$ not only enhances its piezo-electric and photocatalytic properties but also endows it with energy storage capability. This dual functionality makes $Bi_4Ti_3O_{12}$ an ideal candidate for round-the-clock wastewater treatment. Despite its potential, research remains limited, and more studies are needed to explore energy storage capabilities in piezo-photocatalysts like $Bi_4Ti_3O_{12}$.

Interest in piezo-electric materials for piezo-photoelectrochemical applications, especially in hydrogen production, is growing. However, their adaptation for wastewater treatment lags behind. Expanding research into piezo-photoelectrocatalysis can reduce electron-hole pairs recombination and enhance ROS generation, offering new methods for pollutant elimination.

Due to the piezo-electric potential and band bending, piezo-photoelectrocatalysis can facilitate the establishment of in-situ H_2O_2 generation based on the oxygen reduction reaction (ORR) or water oxidation reaction (WOR) routes. Incorporating iron into piezo-photoelectrodes can combine piezo-photoelectrocatalysis with the Fenton process, which increases ROS generation and accelerates pollutant elimination. This approach merits deeper exploration to improve wastewater treatment.

Some piezo-electric materials possess pyroelectric properties, enabling continuous wastewater treatment without light or mechanical vibration using temperature differences. This day-and-night operation has potential for future experiments but remains underexplored, needing further investigation for practical applications.

Currently, photocatalysis for wastewater treatment poses a technology readiness level (TRL) of 4-6, indicating its transition from development to demonstration. Reactors, including batch, packed

bed, continuous stirred tank (CSTR), plug flow (PFR), and bubble column, have been designed to apply powder and immobilized photocatalysts under solar light. On the contrary, the TRL of piezo-catalysis and piezo-photocatalysis has remained below 3, reflecting their current commercial immaturity as proof-of-concept and lab-scale stages. Advancing piezo-photocatalysis to TRL 4-6 requires overcoming challenges such as cost and stability of materials during prolonged mechanical stress, achieving high photoconversion and reaction efficiency for real wastewater on a large scale, and integrating low-power mechanical stress with solar irradiation for continuous wastewater treatment.

Acknowledgments

The authors thank the Velux Stiftung Foundation for the financial support through project 1381, "SUNFLOAT - Water decontamination by sunlight-driven floating photocatalytic systems". We also appreciate the support of Bourse d’excellence Neil R. Mitchell et Danièle Dumais from Polytechnique Montréal, Canada.